Sonochemical and Ultrasonic Output Analyses on Dental Endosonic Instruments

Timm Joyce Tiong

A thesis submitted for the degree of Doctor of Philosophy
University of Bath
Department of Chemistry
May 2012

Abstract

Ultrasonic instruments are used with the aid of an irrigant such as NaOCl in endodontic treatments to remove dentin debris and calculus from infected root canals. This cleaning process may be assisted by various factors, such as acoustic streaming, and the production of radicals and microjets from the collapse of transient cavitation bubbles.

The aim of this project is to understand the principal factors affecting the performance of a number of different endosonic files in order to correlate to their cleaning efficiencies. Characterisation includes detecting transient cavitation activity, mapping the areas of cavitation, assessing the file vibration movements and the streaming effects produced by the files.

Experiments to assess the cleaning efficiencies of the files include: emulsification, dye removal with a dental irrigant, ink and hydroxyapatite paste removal from model systems designed to mimic the structure of a tooth. The results show that there is a correlation between the sonochemical output and the cleaning efficiencies, and this brings in further study on the possible factors that may affect the production of transient cavitation and the vibration profiles of the endosonic files.

Lastly, a series of computational simulation of the acoustic pressure fields from different endosonic files were performed. Correlations of the simulated and experimental results showed the difference in ultrasonic output of the endosonic files is strongly related to their design. This work provides the basis and techniques necessary to perform a comprehensive study on the design of the endosonic files in order to enhance and optimise their cleaning efficiencies during clinical use and to inform future endodontic practice.

Acknowledgements

I would like to express my greatest gratitude to:

- **Prof. Gareth Price** – for his supervision, guidance and jokes he shared in the past 3.5 years.
- **Prof. Damien Walmsley** and **Dr. Simon Lea** – for the hospitality in Birmingham; and guiding me through with the SLV experiments.
- **Dr. Karen Edler** – for accommodating me in the scattering lab and for the useful comments and advices over the years.
- **EPSRC** – for funding this project *via* grant EP/F021739/1.
- **Emily Skinner** – for always being supportive, understanding and lovely lab partner/colleague and friend.
- **Elenitsa Sikou –** for the great company and laughters, and most importantly, making those late-night experiments much more bearable.
- **Daniel, David, Ilaria, Saskia** – for the great company in the lab.
- **Yeow Hong Yap** – for his patience and ever willingness to assist me when I was stuck with COMSOL and for making sure I am always well fed.
- **Prof. Stan Kolaczkowski** – for allowing me to access to COMSOL.
- **Dad, Mom** and **Mike** – for their TLC throughout the years and putting up with all my unnecessary rants.

With love, Joyce

Table of Contents

List of Tables

List of Figures

Notations /Abbreviations

Symbol	Meaning	Unit
Q	heat generated into the system	Joules (J)
m	mass	kg
C_p	heat capacity	J kg^{-1} K^{-1}
ΔT	change in temperature	K *or* ^oC
t	time	s *or* min
v *or* c	velocity	m s^{-1}
f	frequency	Hz *or* s^{-1}
λ	wavelength	m
ρ	density	kg m^{-3}
g	gravitational acceleration	9.81 m s^{-2}
p_o	static pressure	Pa
P_{total}	total pressure	Pa
A	absorbance	unitless
ε	molar absorptivity	L mol^{-1} cm^{-1}
c	concentration	mol L^{-1}
l	path length	cm
[A]	concentration at time t	mol L^{-1}
$[A_o]$	initial concentration	mol L^{-1}
k	rate constant	s^{-1} *or* min^{-1}
R	radius of the bubble at time, t	m
$\dot{R}$	radical velocity	m s^{-1}
$\ddot{R}$	derivative of radical velocity	m s^{-2}
σ	viscosity of the liquid	Pa s
p_v	vapour pressure	Pa
R_o	initial bubble radius	m
γ	polytropic efficiency	
P(t)	pressure at time, t	Pa

ω	angular frequency	s^{-1}
∇	Laplacian operator	
Φ_{KE}	kinetic energy	J
I	intensity	W m^{-2}
Z	acoustic impedance	Pa s m^{-1} *or* Rayl
SCL	Sono(chemi)luminescence	
SLV	Scanning laser vibrometry	
PIV	Particle image velocimetry	
HA	Hydroxyapatite	

1.Introduction

1.1 Ultrasound – the sound wave

Ultrasound is a type of sound wave above human's hearing range (>20 kHz) (Leighton, 2007). It is a longitudinal wave and requires a medium to travel. When ultrasound passes through a medium, the particles will vibrate parallel to the direction of the sound wave. This will give rise to the formation of acoustic pressure and the production of particle velocity in the medium (Figure 1.1).

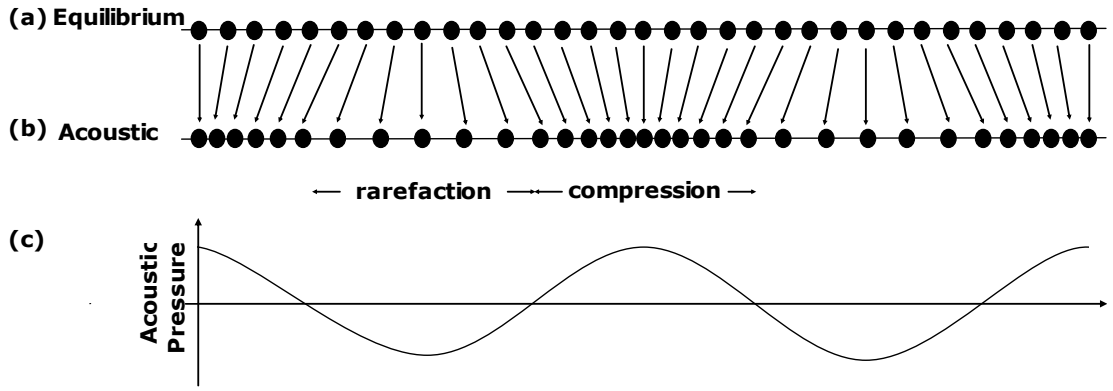

Figure 1.1: *Relationship between particle displacements with acoustic pressure along the longitudinal wave when subjected to ultrasound.*

The positive cycle of the acoustic pressure is termed 'compression' and the negative cycle is called 'rarefaction', the latter is crucial in the formation of cavitation used in sonochemistry and will be discussed more in depth later in this section (Section 1.2.1).

The wavelength of ultrasound depends on its propagating medium and frequency generated by the ultrasonic source. For example, when a sound wave of 20 kHz passes through pure water (liquid medium), it will have a wavelength of approximately 7.5 cm based on the calculation below:

From a study of the speed of sound in pure water (McSkimin, 1965),
At 298.15 K, speed of sound in pure water, v = 1496.7 m s^{-1}

$$v = f\lambda \qquad \textit{(Equation 1)}$$

$$\lambda = \frac{v}{f}$$

$$= \frac{1496.7}{20000}\ \text{m}$$

$$= \underline{\mathbf{7.5\ cm}}$$

From Equation 1, in a pure liquid medium, the frequency generated by an ultrasonic source will affect the wavelength produced. A system with higher frequency will have shorter wavelength and this will result in shorter compression and rarefaction cycles in the acoustic pressure profile.

1.1.1 Types of Ultrasound

Ultrasound can be classified into two types: power ultrasound and diagnostic ultrasound.

Power ultrasound is the sound wave within the regions of 20 kHz to approximately 1-2 MHz (Mason, 1991). At these frequencies, the expansion and contraction of the molecules in the medium may result in the formation of a void, called cavitation which, upon collapse will aid in some ultrasonic processes such as ultrasonic cleaning, erosion, emulsification, molecular degradation, sonoluminescence, chemical and biological effects (Young, 1989). Later, the term 'power ultrasound' has become known as sonochemistry covering all the processes involved, and will be discussed in Section 1.2 (Clark and Macquarrie, 2002).

Diagnostic ultrasound, on the other hand, is a non-destructive ultrasonic technique used to measure distance by utilising the reflection of a sound wave to obtain information. The range of diagnostic ultrasound is from 2 MHz up to approximately 100 MHz. The application of diagnostic ultrasound dates back to the

1940s, when Langevin first used the piezoelectric effect of producing ultrasound to detect submarines for military purposes (Rantanen, 1986). Later, **SO**und **N**avigation **A**nd **R**anging (SONAR) and sonography have been widely developed based on the principle of the echo produced by ultrasound at these ranges. In medical applications, ultrasound is used to detect lumps that occur in the soft tissues by focusing high frequency sound wave into the infected area. Dussik was the first to develop this method of detection in medicine in 1942 to diagnose cerebral ventricles (Goldberg and Kimmelman, 1988). Since then, there has been a vast development of diagnostic ultrasound for medical purposes and it is now more commonly called 'therapeutic ultrasound' for its use in the medical industry for diagnostic purposes.

1.1.2 Production of Ultrasound

Ultrasound can be produced by converting electrical energy to sound. It is first done by converting electricity to high-frequency alternating current, and then followed by conversion into mechanical vibrations, producing ultrasound. This can be done by two types of ultrasonic transducers: magnetostrictive and piezoelectric.

1.1.2.1 Magnetostrictive Transducer

The magnetostriction effect was first discovered by James Joule (1842) when observing a sample of nickel. Magnetostriction utilises the movement of the magnetic field, within a ferromagnetic material (such as nickel) which changes its shape when it is subjected to a magnetic field.

Figure 1.2 illustrates the concept of magnetostriction in producing ultrasound. Laminated strips of nickel were aligned and coiled with electrical coil. Upon providing electrical potential from the electrical source, the nickel strips will change in direction and will form oscillating magnetic field in the surroundings. The vibrations of the nickel will then be converted into high frequency sound waves, which will propagate into the sonicating medium (Wan, 2006). The advantage of magnetostrictive material is its robustness to withstand high temperatures. However, as magnetostriction converts the electrical energy to magnetic energy, and then only to mechanical energy

to produce sound wave, it will result in a lot of heat loss and hence will need significant cooling to the system (Wohlfarth, 1980). Also, the frequency produced by magnetostriction of nickel depends strongly on its size; this brings limitations to the frequency range of ultrasound that can be produced magnetostrictively. In practical uses, the frequency that can be emitted magnetostrictively can go up to 120 kHz, but the set-up of these infrequent systems is limited to 30 kHz (Luche and Bianchi, 1998).

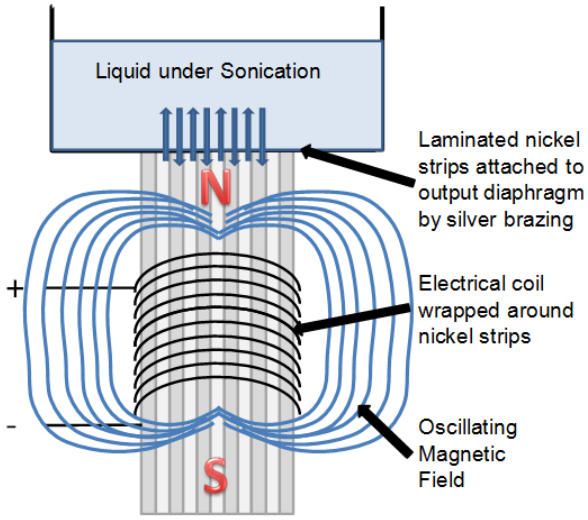

Figure 1.2: *An example of a magnetostrictive transducer, which utilises the movement of magnetic field to provide mechanical energy to be supplied to the ultrasonic source.*
Image reproduced from Fuchs (2002).

1.1.2.2 Piezoelectric Transducer

Ultrasound can also be produced using a piezoelectric transducer. The first persons to have discovered piezoelectric effects were the Curie brothers back in 1880 in crystal tourmaline (Tichý *et al.*, 2010). They noticed the effect when electrical charges proportional to the pressure applied appear on the opposite side of the crystal surfaces. A year after their discovery, based on Lippmann's prediction, they had found out that the reverse piezoelectric effect also occurs when electric potential was applied to the ceramic material, causing some slight deformation (Vives and Arnau, 2004). An illustration of a single molecule of a piezoelectric material subjected to external force is shown in Figure 1.3, where the exertion of an external force

causes slight compression of the material, resulting in a polarising effect on the surface of the material.

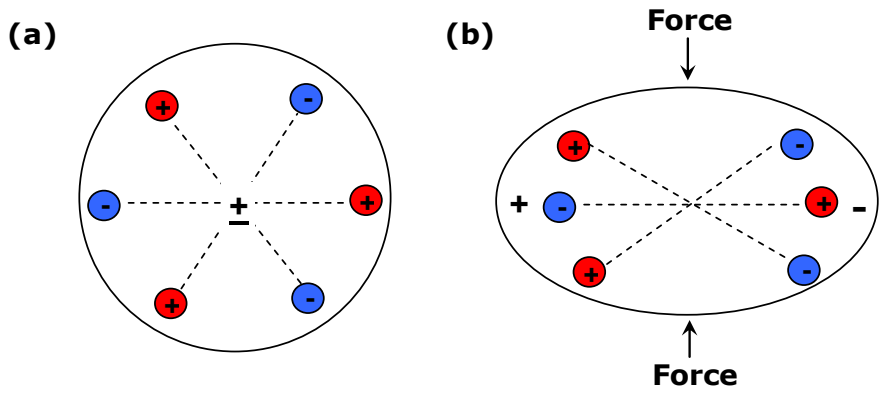

Figure 1.3: *A molecular structure to explain the piezoelectric effect. (a) A neutral molecule of a piezoelectric material when there is no external force acting to it. (b) Polarising effect due to external force on the material.*

Image reproduced from Vives and Arnau (2004).

There was no further application of the piezoelectricity effect for the next thirty years after its discovery by the Curie brothers. It was only in 1914, during World War I, that Langevin pioneered the use of the piezoelectric effect to produce ultrasonic waves (Rantanen, 1986) to detect underwater submarines. At that time, the detector consisted of a thin quartz crystal glued between two steel plates, and a hydrophone to detect the returned echo. The distance was calculated based on the time required for the echo to be bounced back from an object. The so-called Langevin transducer was the first application of piezoelectricity in ultrasound engineering (Frederick, 1965). Since then, there has been an extensive use of the piezoelectricity effect to generate ultrasound for various purposes – ranging from food processing, cleaning processes to biomedical applications (Chandrapala *et al.,* 2012, Stefanescu 2010, Suri *et al.,* 2008).

An example of a piezoelectric transducer is shown in Figure 1.4. When electric potential is supplied to the system, the piezoelectricity (PZT) element will change its shape, which will then generate ultrasonic waves through the transducer into the sonicating medium, which, in this case is shown as the 'liquid under sonication' in the figure.

Now, the piezoelectric transducer usually contains a single or double thick disc of piezoelectric ceramic material, such as barium titanate, lead metaniobate or the most commonly used lead zirconate titanate ($Pb[Zr_xTi_{1-x}]O_3$) sandwiched between electrodes which provide electrical contact (Hui and Sherkat, 2005). The ceramic assembly is sandwiched against two metal blocks, with one side being aluminium and the other being steel. When voltage is applied to the ceramic through its electrodes, the ceramic will either expand or contract according to its polarity, causing the propagation of sound waves at its resonant frequency (Vives and Arnau, 2004).

The advantage of using a piezoelectric transducer to generate ultrasound is its efficiency. There is minimum heat loss to the environment as it converts from electrical to mechanical energy. The range of ultrasonic waves generated with a piezoelectric transducer is greater than the magnetostrictive transducer as it is not size dependent. However, there are also some disadvantages of piezoelectric transducer; it is less robust compared to magnetostriction, especially under continuous usage at high temperatures, as high temperatures will degrade the ceramic materials in the piezoelectric transducers (Fuchs, 2002).

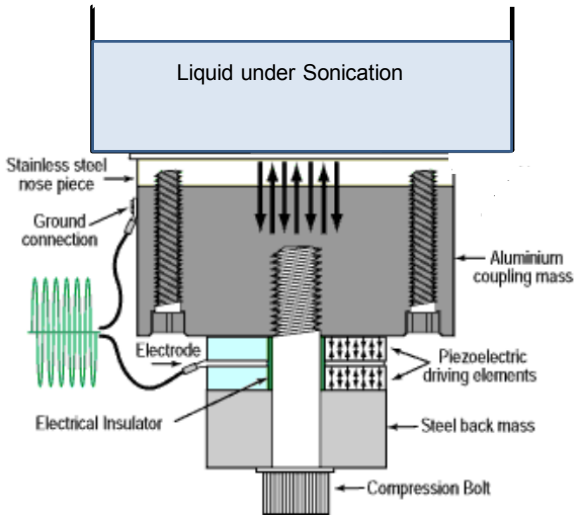

Figure 1.4: *An example of a cross-sectional view of a piezoelectric transducer, which utilises ceramic elements to produce mechanical vibrations to the ultrasonic system.*
Image adapted from Fuchs (2002).

1.1.3 Applications of Ultrasound

Ultrasound has a wide range of uses, as mentioned earlier in Section 1.1.1. In diagnostic ultrasound, the sound wave at such high frequencies was first used for detecting submarines underwater, using a technology called SONAR. Here, the distance and location of the object is measured based on the time taken to obtain the reflection of the ultrasonic wave emitted by the SONAR source (Chevalier, 2002). This technique is used widely in marine science to detect submarines and depths of the sea beds (Hilar, 1946).

Since the development of SONAR, there had been extensive developments in diagnostic ultrasound. One of them is sonography – which utilises ultrasound to detect tendons, tissues, muscles, joints and internal organs for pathology or during pregnancy (Sander *et al.*, 1996). Sonography uses ultrasound at higher frequency (7 – 18 MHz) to provide better image resolution of the tissues and internal organs. A hand-held ultrasonic probe is placed directly on the surface of the skin and moved over the patient's body (Sanders and Winter, 2006). Image is generated based on the angle and frequency shift reflected from the sound wave emitted by the internal organs (Curry and Tempkin, 2010). Ultrasonic sonography is particularly useful in medical applications as it is a non-destructive method (Azhari, 2010) of detecting the internal organs. This brings the wide range of use in medical areas such as cardiology, gynecology, neurology and so on.

Apart from the non-destructive applications, diagnostic ultrasound is also used to destruct pathogenic cells. This is performed by focusing high-intensity ultrasound *via* a lens or a curved transducer onto a small area, the sound wave will be absorbed by the tissue within the area and converted to heat, resulting in tissue ablation at the targeted area (Azhari, 2010). Medical practices adapting this method include: liposuction, cancer treatments to destroy solid tumours of the bone, brain, liver, pancreas, prostate *etc* (Suri *et al.*, 2008).

Power ultrasound, on the other hand, causes erosion to the material, and is used as a heat source to accelerate processes such as industrial welding, friction reduction, drilling and processing of liquids (Frederick, 1965, Feng *et al*., 2011). The discovery of cavitation by low frequency, high power ultrasound has broadened the applications of ultrasound. The disruption caused by cavitation is used in various areas, such as cleaning processes, chemical and biological degradation, and emulsification (Young 1989). One of the applications involving the transportation of cavitation bubbles is drug delivery. Here, ultrasonic induced cavitation bubbles creates circulating eddies around the fluid, enhancing diffusion in the fluid (Ng, 2005), hence is able to transport drugs at higher velocities. Another use of cavitation bubbles in ultrasonically driven drug delivery is by encapsulating a therapeutic agent into the ultrasonic induced cavitation bubbles and releasing it upon reaching the targeted area *via* the collapse of the cavitating bubbles (Lionetti and Paddeu, 2009).

Besides drug delivery, power ultrasound is also used in various biological and chemical processes. The shear stress and the production of radicals upon the collapse of cavitation bubbles is useful in different chemical processes – such as depolymerisation, degradation of aqueous pollutants, and so on (Mason, 1991). It is efficient for various chemical processes as it involves lesser chemicals and shorter processing times. This is why the use of power ultrasound in chemical processes (also known as 'sonochemistry') has become an important application of ultrasound (Section 1.2).

1.2 Sonochemistry

Sonochemistry is a branch of power ultrasound, where ultrasound is used for chemical processes. As mentioned earlier in Section 1.1.3, the applications of power ultrasound include cleaning, food processing and emulsification and so on – which involve chemical reactions in the process (Suslick, 1990). When power ultrasound passes through a liquid medium, the propagation of acoustic pressure results in the production of negative pressure in the system. When this negative pressure produced overcomes the tensile strength in the liquid medium (the liquid is said to have

underwent rectified diffusion) (Crum 1979), it will tear apart the liquid molecules in the system to form small voids called cavitation.

Figure 1.5 illustrates the pressure profile with respect to time when a sound wave passes through a liquid medium to form negative pressure in the system. The formation of cavitation is crucial in sonochemistry as the mechanical and chemical effects of the cavitation bubbles affect the sonochemistry processes (Leighton, 1994).

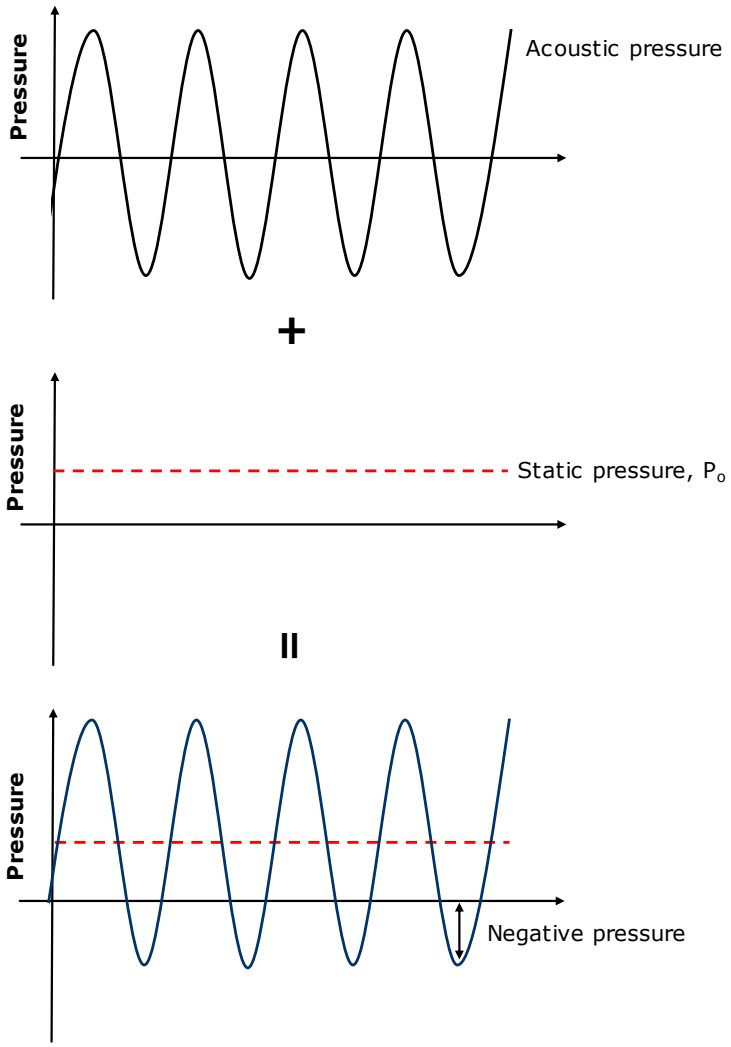

Figure 1.5: *Pressure profiles when acoustic wave passes through a liquid medium.*

1.2.1 Cavitation

The first observation of cavitation was by Sir Isaac Newton when he was examining Newton's rings formed between a convex lens and a plane glass surface. However, at that point, he did not realise the effect was the formation of air bubbles due to a reduced pressure in the liquid. After that, several scientists have observed similar effects, when they have found loose turbines on engines due to the generation of negative pressure (Euler, 1754, Reynolds, 1873) but none of them knew the actual factor affecting the loss in efficiencies in turbine engines. The more renowned case on cavitation occurred in 1893, when Barnaby and Parsons discovered a significant reduction in performance in the speed of the propeller of the destroyer HMS *Daring*, and then observed the formation of water vapour bubbles on the blades (Barnaby and Parsons, 1897). This phenomenon was then termed 'cavitation' by Barnaby and Thornycroft (1895).

The formation of cavitation is due to the formation of negative pressure when a liquid medium undergoes rectified diffusion (Crum, 1984). There are several types of cavitation: hydrodynamic, acoustic, optic and particle cavitation (Young, 1989). Lauterborn (1980) separated the types of cavitation into two categories, where hydrodynamic and acoustic cavitation are brought about by the tension in the liquid; whereas optic and particle cavitation were produced by deposition of energy.

1.2.1.1 Acoustic Cavitation

Acoustic cavitation is produced when an acoustic wave passes through a medium. There are two types of cavitation: stable and transient cavitation (Young, 1989). Stable cavitation is produced when the bubbles that oscillate along the sound field are of the approximate size of its equilibrium bubble sizes, and will often continue oscillating for many cycles of the sound pressure. On the other hand, upon

achieving the cavitation threshold[1] of the liquid system, transient cavitation is formed. It consists of bubbles with a large variety of bubble sizes, and they usually occur in less than one acoustic cycle.

Transient cavitation will sometimes expand to double in size, and upon collapsing, will disintegrate into smaller bubbles, at the same time giving out massive amount of pressure of a few hundred atmosphere and temperatures up to a few thousand Kelvin within the local collapsing region (Leighton, 1994). In these violent conditions, the energy emitted by the collapsing bubbles is able to tear apart molecules – hence breaking some molecular bonds and producing new molecular species. Figure 1.6 shows an exaggerated illustration of the growth of a cavitation bubble along a sound field and leading to eventual collapse. As seen in the figure, the cavitation is formed when there is sufficient energy absorbed from the negative acoustic pressure forming a void. There has been extensive research performed by several renowned scientists in ultrasonics regarding the phenomenon. It was found that during the cavitation collapse, the energy is so great that it could produce light (known as sonoluminescence) (Frenzel and Schultes, 1934), hydrolysis, free radicals due to pyrolysis and other chemical reactions (Miller, 1950).

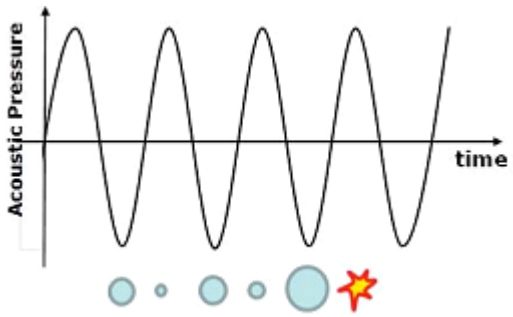

Figure 1.6: *An exaggerated illustration of the growth of a cavitation bubble when it is subjected to sound field and leads to eventual collapse.*

[1] This is also known as the Blake's Nucleation Threshold where cavitation can only be produced once it gets beyond the threshold pressure when Blake radius, R_B is achieved. (See Appendix I for the equation)

In the case of water, Weissler had discovered that, under sonication, the water molecules undergo pyrolysis to form hydrogen and hydroxyl radicals, as shown in Scheme 1.1 (Weissler, 1959).

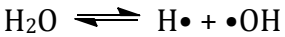

Scheme 1.1

Upon the formation of these radicals, a series of chain reactions take place in the system, as shown in Scheme 1.2.

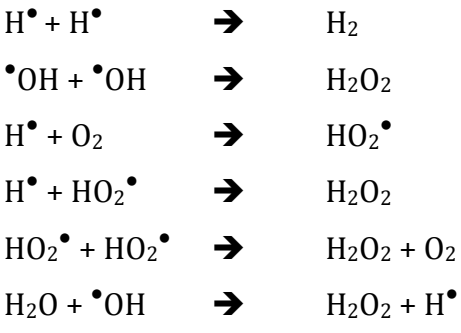

Scheme 1.2

The radicals formed in the system act as strong oxidisers and will result in various chemical effects. It was suggested that the formation of radicals upon sonication might have been produced by electrical discharges into water vapour in the cavity (Rodenbush and Wahl, 1933, Miller *et al.*, 1996) or, as a result of thermal dissociation due to adiabatic collapse of the cavitation bubbles (Fitzgerald *et al*., 1956).

In sonochemistry, the detection of radicals upon sonication has become a way to measure the sonochemical efficiencies. Among them, the radicals can be detected by performing electron spinning resonance (ESR), where the radicals formed will react with an adduct to form slightly longer life lived radical, and will be detected by ESR (Sostaric and Riesz, 2001). Alternatively, there are several chemical reactions that can be performed – such as the Fricke, iodide or the terephthalate dosimetries (Fricke and Hart, 1935, Weissler, 1959, Iida *et al*., 2005) – which utilise the oxidation properties of the radicals to react with Fe^{2+}, I^- and terephthalic acid to form detectable UV-visible or fluorescent compounds (further explanations will be given in Chapter 2).

Apart from the formation of radicals, the violent collapse of cavitation bubbles also produces shock waves (Leighton, 1994), due to the distortion in the acoustic wave pressure profile in the liquid medium when a sound wave passes through it. These shock waves will result in several physical and chemical effects in the system – causing erosion, breakage of molecular chemical bonds, producing a large amount of heat energy, contributing to various applications in sonochemistry (Section 1.2.3).

1.2.1.2 Hydrodynamic Cavitation

The other way cavitation can be formed is when a fluid flows through the system – termed hydrodynamic cavitation. The formation of hydrodynamic cavitation is strongly dependent on the velocity in the fluid. Based on Bernoulli's principle, pressure decreases when the fluid velocity increases (Young, 1989). When the decrease in pressure surpasses the tensile strength that holds the liquid together, cavitation is formed (Young, 1989).

There are some similarities between hydrodynamic and acoustic cavitation. Suslick and co-workers have demonstrated that the chemical effects produced by hydrodynamic cavitation are similar to the cavitation produced acoustically (Suslick *et al.*, 1997). When an acoustic pressure field is formed in a liquid system, fluid flow in the system may contribute to a further decrease in static pressure – which will result in the formation of hydrodynamic cavitation. A recent study by Franke *et al.* (2011) has proven the synergistic effect when combining both hydrodynamic and acoustic cavitation in degrading chloroform. Hence this may give a new insight to combine both types of cavitation to enhance chemical processes.

1.2.2 Factors affecting Sonochemical Processes

In order to understand the factors affecting sonochemical processes, one must first be introduced to the cavitation bubble dynamics that occur when a sound wave passes through the bubble.

Noltingk and Neppiras (1951) derived the Rayleigh-Plesset equation on cavitation bubble dynamics, as stated below:

$$R\ddot{R}+\frac{3\dot{R}^2}{2}=\frac{1}{\rho}\left\{\left(p_o+\frac{2\sigma}{R}-p_v\right)\left(\frac{R_o}{R}\right)^{3\gamma}+p_v-\frac{2\sigma}{R}-\frac{4\mu\dot{R}}{R}-p_o-P(t)\right\}$$ ***(Equation 2)***

Where,

R	:	radius of the bubble at time t
$\dot{R}$	:	radical velocity
$\ddot{R}$	:	derivative of radical velocity
ρ	:	density of liquid
p_o	:	static pressure
σ	:	viscosity of the liquid
p_v	:	vapour pressure
R_o	:	initial bubble radius
γ	:	polytropic efficiency
$P(t)$	:	liquid pressure at time t

As mentioned earlier in Section 1.2.1.1, the size of the cavitation bubble determines the type of cavitation that occurs, hence it is important to understand the change in cavitation bubble size with respect to time when acoustic pressure passes through it. Based on the Rayleigh-Plesset equation for acoustical bubble dynamics, it can be seen that there are several factors that will affect the size of the cavitation bubble and subsequently affecting the sonochemical processes.

Below are the summarised factors affecting the cavitation process:-

- Viscosity, σ:
  - An increase in viscosity in a liquid will result in more energy being required to overcome the cohesive forces, thus increasing the cavitation threshold.

- Vapour pressure, p_v:
  - Bubbles with a high vapour pressure will have more vapour diffusing in and out of the bubble, and act as a 'cushion' during the collapse, resulting in a less violent cavitation collapse.

- Polytropic efficiency, γ:
  - Gases with high polytropic efficiencies will result in higher cavitation collapse – more energy will be given out during the collapse.

- External pressure, p_o:
  - The application of external pressure to the system will increase the cavitation threshold (based on Figure 1.5) at the same acoustic pressure amplitude used.

- Frequency, f:
  - An increase in frequency reduces the rarefraction phase during the formation of cavitation. More energy is required to achieve the cavitation threshold during the short rarefraction phase in high frequency ultrasonic systems.

1.2.3 Applications of Sonochemistry

There are several applications of sonochemistry, as mentioned earlier in the chapter. It can be used for sonochemical cleaning, acts as a catalyst to enhance the

rate of reactions, aids in chemical processes to enhance the rate of degradation of unwanted products (pollutants, waste), aids in radical productions and so on (Suslick *et al*., 1999).

Power ultrasound is used for both its physical and chemical effects in chemical processes. Physically, the high intensity sound wave produced by the ultrasonic horn is able to create a strong mixing effect which will contribute to processes such as homogenisation of two highly immiscible liquids (Ashokkumar, 2011). This is achieved by the high shearing force produced during the collapse of transient cavitation bubbles (Behrend *et al*., 2000), which is able to break the translational motion of a liquid globule (Hinze, 1955), resulting in smaller liquid droplets which will disperse into the other immiscible liquid phase – forming emulsions in the system (Li and Fogler, 1978). Ultrasonic emulsification is widely used in various industrial applications due to its effectiveness, such as in cosmetic industry for the production of skin lotions, pharmaceutical ointments, varnishes; as well as paints for arts, lubricants and fuels for engines (Capote and Castro, 2007).

The chemical effects of power ultrasound are affected by the radicals formed during the sonication process. These radicals act as a catalyst to speed up reaction rates (Moad and Solomon, 2006). Processes involving this include organic chemical syntheses and polymerisations. Free radicals are formed when organic liquids undergo ultrasonic irradiation, resulting in end products such as hydrogen (H_2), methane (CH_4), acetylene (C_2H_2) and smaller 1-alkenes (Suslick *et al*., 1999). Suslick *et al*. (1983) have reported that the change in ultrasonic radiation conditions (such as the change in temperature and intensity) resulted in different yields of sonochemical end products. Hence this can be a useful tool in controlling the organic synthesis pathways by adjusting the ultrasonic irradiation parameters.

Sonochemistry is also used extensively for polymerisations and depolymerisations, caused by shockwaves and formation of radicals during the collapse of transient cavitation bubbles, which is crucial for the initiation of polymerisation processes. For example, homopolymers and copolymers of styrene, methyl methacrylate and *n*-butyl methacrylate are formed with the aid of the radicals

formed by ultrasonic irradiations (Price *et al.*, 1991). Ultrasound is also used to degrade polymers, forming shorter-chained polymers of relatively uniform molecular weight distributions, depending on the ultrasonic conditions (Price, 1992). The non-random nature of the degradation process of polymers enables the predictions of the molecular weights of the polymer at any time of sonication, and is used as a tool in controlling the structure during the synthesis of polymers (Price *et al*., 2002).

Another use of power ultrasound is sonochemical cleaning. Here, the collapse of transient cavitation bubbles produce high intensity shockwaves that have sufficient energy to remove (i) surface impurities – used for cleaning of jewelleries, spectacles, watches, dental and surgical equipments; or (ii) pollutants / effluents – by breaking chemical bonds to shorter, more stable molecules that are less harmful to the environment (Lifka *et al*., 2002). The latter is widely used in the textile industries and wastewater treatments where aqueous effluents are treated ultrasonically prior to discharging to the environment (Destaillats *et al.*, 2003), as well as the removal of dentin debris and microorganisms in infected teeth – which will be further explained in Section 1.3.3.

1.2.4 Sonochemical Cleaning

The main part of this project lies within the use of ultrasound for cleaning processes, also known as sonochemical cleaning. In brief, this includes both the physical and chemical effects of power ultrasound.

When the sonochemically formed cavitation bubble is close to a solid surface, it will collapse in such a way that a high velocity jet is produced in the direction of the solid surface, termed a microjet (Crum, 1979), as shown in Figure 1.7. This is particularly important in the application of sonochemistry, especially in cleaning processes, where the collapse of cavitation bubble is used to detach surface debris that is strongly bonded onto surfaces.

In conventional cleaning processes, a solvent is used to dissolve any contaminants present on the surface due for cleaning. Whilst this is an effective way of 'knocking off' the surface debris, a saturated layer will eventually form between the fresh solvent and the contaminants, limiting any further dissolution process (Figure 1.8) (Fuchs, 2002).

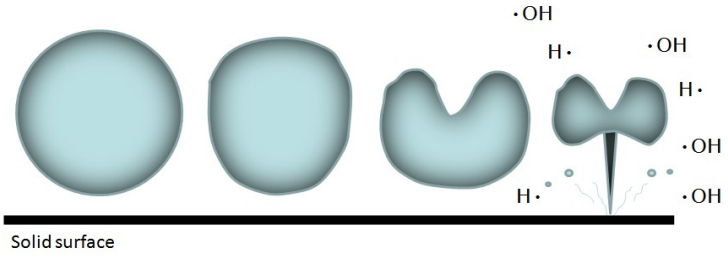

Figure 1.7: *Schematic of the collapse of a cavitation bubble close to a solid surface producing microjet and radicals.*

Image adapted from Shockwave Therapy-BC [Online].

In addition to the formation of microjets, the collapse of transient cavitation also result in the formation of radicals in a liquid system (such as the H• and •OH for the case of water), that are strong oxidising agents and will further degrade any impurities in the cleaning process by chemical reaction.

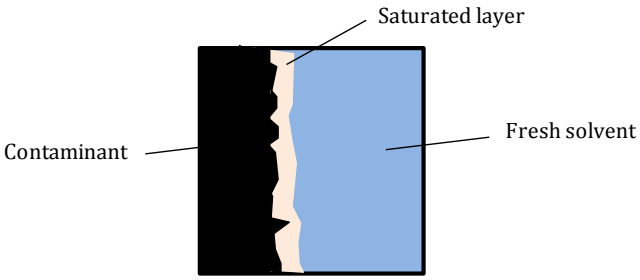

Figure 1.8: *Saturated layer formed from the dissolution of contaminants by the cleaning chemistry, limiting further cleaning process to be done.*

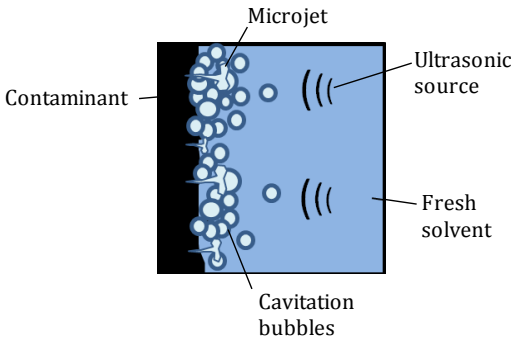

Figure 1.9: *Cavitation bubbles will attack the saturated layer, allowing fresh solvent to further dissolve the contaminants present on the surface, making the entire cleaning process more thorough.*

1.3 Endodontics

As defined by the American Association of Endodontists (2005-2006 cited in Ingle *et al.* (2002)):

> "*Endodontics is that branch of dentistry that is concerned with the morphology, physiology and pathology of the human dental pulp and periradicular*[2] *tissues. Its study and practice encompass the basic clinical sciences including biology of the normal pulp; the etiology, diagnosis, prevention and treatment of diseases and injuries of the pulp; and associated periradicular conditions*"

The origin of the word endodontics came from a Greek word, where *endo* means 'inside' and *odons* means 'tooth' (Garg and Garg, 2010). In other words, in dentistry, this term is used to describe the specialisation of study inside the tooth structure – where the root canal lies. In order to have a better understanding of the entire root canal treatment, one must first have an overview of our tooth structure.

[2] Around a root – for this case, the root of a tooth (Ireland, R. 2010).

1.3.1 Tooth Anatomy

Figure 1.10 shows a cross-sectional view of a tooth with description of each area in the tooth. It can be subdivided into two different sections: the crown and the root. The crown is the area of the tooth that can be seen, which contains part of the dentin and is covered by white layer of enamel surrounding the exterior of the tooth. The root of a tooth is where the 'bone' of the tooth lies, containing the pulp and the root canal. There are a lot of nerve endings and blood vessels, called the odontoblast (Bergenholtz *et al.*, 2010) in the pulp and the root canal that is joint to the main blood stream in the body.

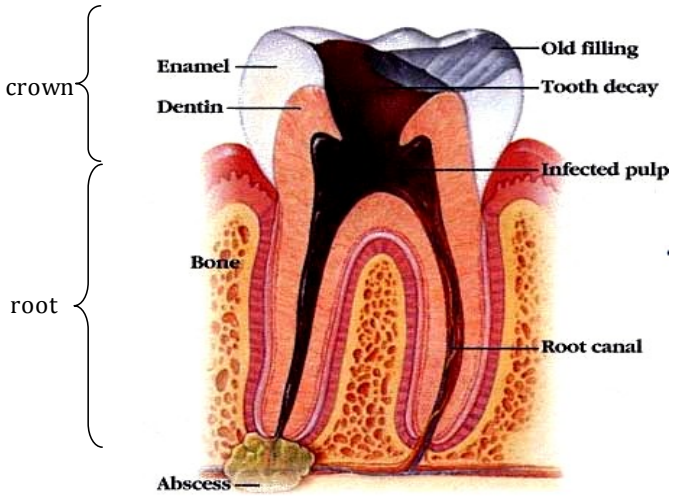

Figure 1.10: *Cross-sectional view of a tooth.*
Image adapted from Silverman (2004).

The tooth enamel contains hydroxyapatite, which gives the tooth its hardness (Park, 2008). It serves as a protective shell to cover the dentin and other components in the tooth. Due to this, the enamel is vulnerable to wear and scratches as it is subjected to the cyclic loading and involved in the mastication of food (Park, 2008). Like the enamel, dentin is also made up of mostly hydroxyapatite, but with approximately 20 – 25 % of collagen. It serves as an elastic foundation and as a protective enclosure for the pulp (Scott and Turner, 1997), acts as a necessary support to the tooth, and at the same time contains tubules which function as nutrient transporters. The pulp, as mentioned earlier, is the area of the tooth which contains all the nerve endings and blood vessels. It contains soft, gelatinous tissues (Park,

2008). The functions of the pulp include: formation of dentin, keeping the surrounding mineralised tissue supplied with moisture and nutrients; and act as a sensor to temperatures and pressures (Scott and Turner, 1997).

1.3.2 Endodontic Treatment

Most diseases in dentistry are caused by bacteria living in the mouth, and amongst them, the most commonly known disease is tooth decay (Park, 2008). As mentioned earlier, the enamel of a tooth is the part that is subjected to wear and permanent scratches. When tooth decay carries on all the way through the enamel and gets into the pulp, where the nerve endings are present, which are very sensitive, ache starts to develop in the tooth. During this process, the exposure of the pulp to the air causes infection in the pulp, and further down the root canal to form abscesses (Ingle *et al.*, 2008), or inflammation of the root canal. If this is left untreated, the infection may spread around the tissues and cause destruction of the bones and supporting tissues (Harty and Ford, 2004). This is when an endodontic treatment is needed to save the damaged pulp.

The study of endodontics (*i.e* endodontology) was practiced as early as second or third century BC, but was only in the 17th century that extensive advancements in endodontics were made (Garg and Garg, 2010). Early versions of endondontic treatments used arsenicals to treat pulpitis[3] (Ingle *et al*., 2002, Ireland, 2010). Later, between the 17th to the mid-18th century, endodontic treatments have advanced from using leeches or toasted fig poultices to treat tooth abscesses, to the generation of anesthesia and utilisation of rubber dams, *e.g.* gutta-percha[4] (Ireland, 2010) root canal points, three or four-sided tapering broaches for cleaning root canals, as well as the utilisation of antiseptics and oxyphosphate of zinc cement for root canal treatments (Ingle *et al*., 2008). Following to the discovery of x-rays in the 18th century,

[3] Inflammation of the dental pulp.

[4] A natural occurring polymer that is chemically the same as natural rubber but with a different molecular shape.

endodontology went into its renaissance, where radiographs, anesthetics and newly developed chemicals were used for medications, superseding the use of arsenics in endodontics (Ingle *et al*., 2002).

Modern endodontic treatments can be summarised into a few steps. Firstly, the infected tooth will be examined by a dentist and an evaluation is undertaken to assess the necessity of an endodontic treatment. If a treatment is needed, this will then be handed over to an endodontist, who will take a radiograph image of the surrounding teeth (including the infected tooth) (Beer *et al.*, 2006). Specialised instruments for endodontic treatments are sterilized, and anesthetic is injected into the patient's mouth which will last for the entire treatment (Ingle *et al*., 2008). The root canal is shaped with a file designed for troughing for better access into the root canal, followed by using finer files to reach into the deeper sections in the root canal to clean any abscesses in the infected root canal. The final procedure of the treatment includes a thorough rinse of the infected area, followed by crowning of the tooth either by using gutta-percha, or, in more recent times, patients can select the material of their choice such as zinc phosphate, acrylate, silicate or even a full gold crown (Hegde and Singh, 2006).

During endodontic treatments, irrigants are used to disinfect the root canal, and to increase the cleaning efficiency of the treatment. The most commonly used irrigants are: sodium hypochlorite (NaOCl), hydrogen peroxide (H_2O_2), ethylenediaminetetraacetic acid (EDTA) and saline solution (NaCl) (Zehnder, 2006). The endosonic files are used together with these irrigants to increase the cleaning effeciencies in the root canal. For cases where hand-held dental instruments are used for root canal therapies, the use of irrigants has greatly improved the performance of the entire root canal treatment. With the invention of vibratory dental files (Walmsley and Williams, 1989), the use of endosonic[5] files (either driven by magnetostrictive or PZT) coupled with these irrigants have greatly improved the entire endodontic treatment. This has brought the field of endodontics into a new horizon and ultrasound has since then been introduced into endodontics.

[5] Dental instrument used for endodontic treatment, operated by sound waves passing through it.

1.3.3 Ultrasound in Endodontics

Ultrasound was first used in dentistry for cutting by Balamuth (1963) based on a pioneering work done by Matthew C. Catuna (1953). It was used with abrasive slurry for preparation of tooth cavities prior to restoration. In the early 1960s, ultrasound technology in dentistry was repositioned and mechanical debridement (the cleaning of debridement mechanically) was introduced for the first time (McCall and Szmyd, 1960). In periodontology[6], the use of ultrasound was pioneered by Zinner (1955), who suggested the use of a modified ultrasonic instrument in conjunction with a water coolant for more effective plaque[7] and calculus[8] removal from human teeth.

Since then, ultrasound has been used in dentistry to remove calculus in the tooth, and it has been reported that adequate removal of calculus by using ultrasonic tips (Johnson and Wilson, 1957) could be achieved in a shorter time (Walmsley, 1988), as compared to conventional scaling method.

In the 1980s and 1990s, the nature of cavitation and acoustic microstreaming has begun to interest many researchers in periodontal cleaning processes in dentistry, (Walmsley *et al.*, 1984) as it was found that ultrasonic treatments on tooth descaling had also resulted in formation of sonochemical products apart from the usual mechanical cavitational effects (Kratochvíl *et al*., 2002). Further investigations were carried out by several researchers into the sonochemical effects of dental descalers, (Walmsley *et al*., 1988) and have proven that it was the sonochemical effects that aided in the cleaning process on tooth surfaces (Lea *et al*., 2005).

---

[6] Specialty of dentistry that studies supporting structures of teeth, diseases and conditions that affect them (Ireland, R. 2010).

[7] Biofilm, usually pale yellow that develops on the tooth due to colonising bacteria trying to attach themselves to the smooth surface of a tooth (Ireland, R. 2010).

[8] Also termed *tartar*, is a form of hardened dental plaque, caused by continual accumulation of minerals from saliva on plaque on the teeth (Ireland, R. 2010).

Ultrasound was introduced in endodontics for similar reasons. It was first introduced by Richman (1957) but it was only used extensively after Martin and co-workers reported that there were significant improvements in root canal debridement using ultrasonic devices (Martin *et al*., 1980). The synergistic effects produced by ultrasonic endodontic treatment due to high acoustic streaming (Plotino *et al*., 2007) and other possible effects such as possible sonochemical effects have received much attention from scientists to further investigate the possible improvements of ultrasonics into the field of endodontology.

As mentioned earlier, when ultrasonic equipment is immersed in a solvent, upon reaching a certain ultrasonic intensity, also known as the cavitation threshold, cavitation bubbles will be generated. Ultrasonic vibration of endosonic files form cavitation when a solvent runs through them. These cavitation bubbles then help to clean debris in the root canal, including side channels which are usually unreachable when performing a normal cleaning process.

Previous works on dental descalers have proven that the occurrence of inertial cavitation has an impact on the cleaning process (Lea *et al*., 2005). Similar to dental descalers, some preliminary work (Price and Walmsley, 2008) on endosonic files has shown that inertial cavitation occurs around the instrument under sonication, even though previous investigations on the occurrence of cavitation and its relevance in endodontic treatment have proved otherwise (Ahmad *et al*., 1987a, Ahmad *et al*., 1987b, Ahmad *et al.*, 1988).

Apart from the sonochemical effects, there are also several scientists investigating on the performance of different endosonic files. For example, Ahmad *et al.* (1988), Walmsley (1988) and Lumley *et al.* (2008) have performed studies on the acoustic microstreaming of the endosonic files and have found that this may contribute to the cleaning efficiencies of the endodontic treatments. Walmsley and Williams (1989) and Lea *et al.* (2004) have studied on the vibration displacements of endosonic files and found that obstruction of the vibration of an endosonic file may contribute to the streaming pattern of the fluid in a confined space, which will then affect the debridement process in a root canal. On the other hand, Roy *et al.* (1994)

have studied the hydrodynamic response on an oscillating ultrasonic file and the relationship between the file response and the physical factors of the file such as the size, curvature velocity, amplitude and so on. They have concluded that neither of the hydrodynamic properties investigated is important in the cleaning effects.

Many scientists have reported on the performances of endosonic files based on their cleaning efficiencies, such as the effectiveness in removing dentin debris or bacteria on biofilms (Martin *et al.*, 1980, Ahmad, 1989, Jiang *et al.*, 2010) and the removal of smear layer with different types and concentrations of irrigants (Cameron, 1987, Huque *et al.*, 1998). Recently, Boutsioukis *et al.* (2010b) have performed computational fluid dynamics on the streaming effects of different types of endosonic files in a confined channel, which have provided information on a better design of endosonic files for more effective cleaning efficiencies.

However, to date, there is still no conclusive analysis on the performance of the ultrasonically driven endosonic files. The literature reported showed discrepancies on the main contributing factor to the cleaning efficiency of clinical use endosonic files. Thus, series thorough sonochemical analyses of these dental endosonic files are needed in order to have a better understanding of the cleaning mechanism, with or without the presence of a dental irrigant, to have a better insight into the use of these dental endosonic files.

1.4 Aims and Objectives

The overall aim of this project is to understand the principal influencing factors affecting clinical use of endosonic instruments and to provide possible optimisation methods on scientific basis to provide a better design for the next generation of these instruments. In order to achieve this, the project is divided into two main objectives: characterisation and identification of the differences in various endosonic files, and the evaluation of their cleaning efficiencies.

1.4.1 Characterisation of Various Endosonic Files

Characterisation of various endosonic files were performed:

- To assess the cavitation distribution around various endosonic files.
- To give an *in vitro* evaluation of the vibration performances of endosonic files.
- To evaluate other factors contributing to the performances of the endosonic files: such as acoustic streaming, shapes and designs.

1.4.2 Evaluating Cleaning Efficiencies

Cleaning efficiencies of the endosonic files were assessed after characterisation:

- To give a better correlation between the characterisation techniques and the actual clinical endodontic treatment.
- To gain a better understanding of the cleaning mechanism of the endosonic files used, and to evaluate any possible improvements for a better design of files.

1.5 Structure of Thesis

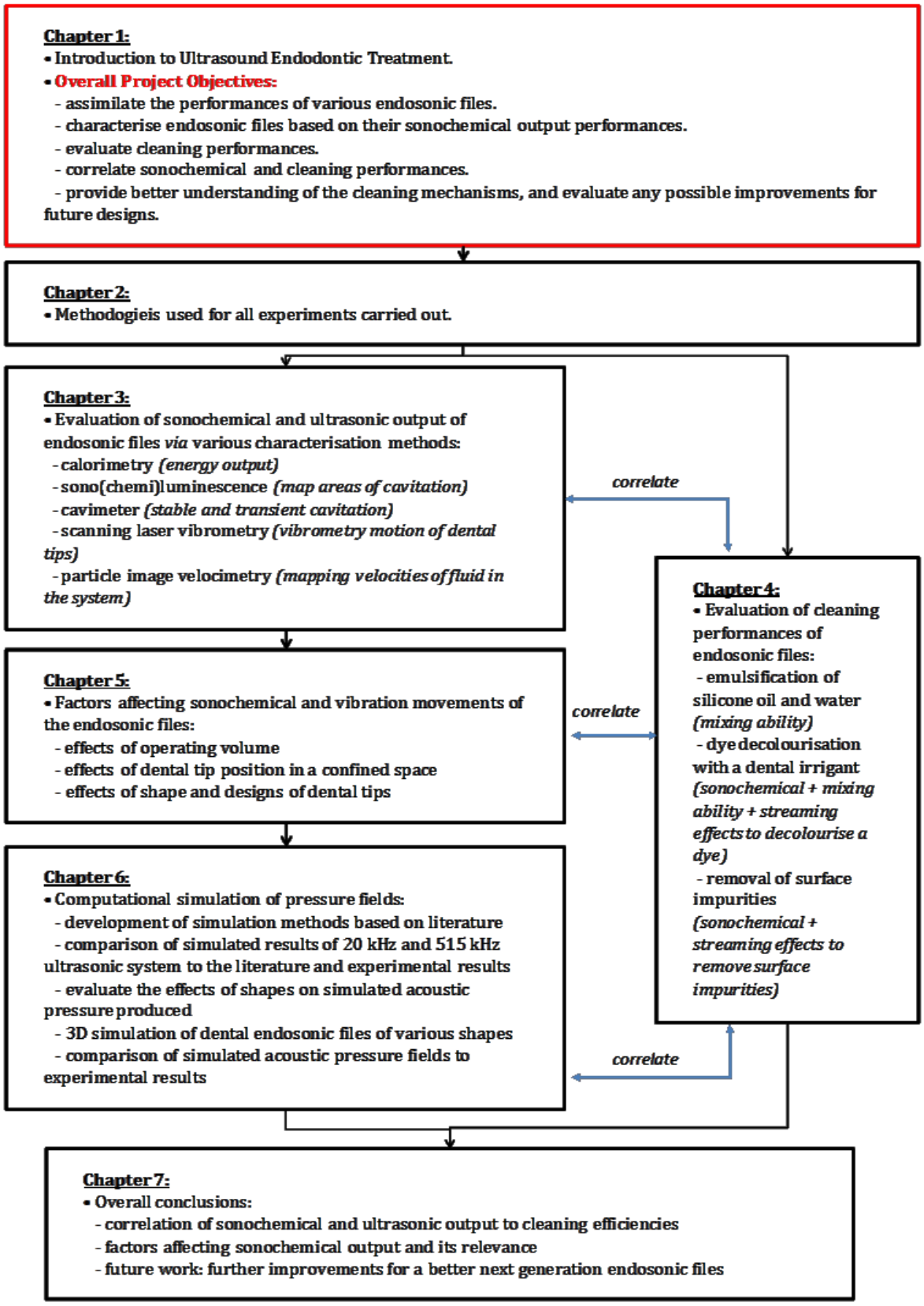

Figure 1.11: *Flowchart of the structure of the entire thesis.*

2.Methodology

2.1.1 Ultrasonic Equipment

In order to perform the objectives stated above, the experimental methods and procedures were first established by running the experiments on an ultrasonic probe at 20 kHz in order to have a comparison with the literature; followed by further comparisons with the actual endosonic files operating at 30 kHz. This strengthened the experimental methodologies used and aided a reliable experimental results when performing the experiments at a much smaller scale on the endosonic files.

The experiments described in this thesis were initially performed using a conventional ultrasonic probe (Sonics & Materials, VC 600, 600 W, 20 ± 3 kHz), hereafter referred as the 20 kHz probe. This was done to set a series of standardised methods for further experiments using the dental instruments.

Figure 2.1 shows the setup of the 20 kHz ultrasonic probe, where ultrasound is generated by the conversion of electrical energy to sound energy by a piezoelectric transducer (as explained previously in Section 1.1.2.2) housed inside the metal casing of the ultrasonic probe. Sound energy travels down the titanium probe and transfers the sound wave *via* the tip of the probe, forming an up-and-down vibration movement, providing ultrasonic energy into the sonicating medium. In a typical experimental set up, the 20 kHz ultrasonic probe is clamped at its piezoelectric housing, with part of the tip (at approximately 1 cm height) immersed into an aqueous solution.

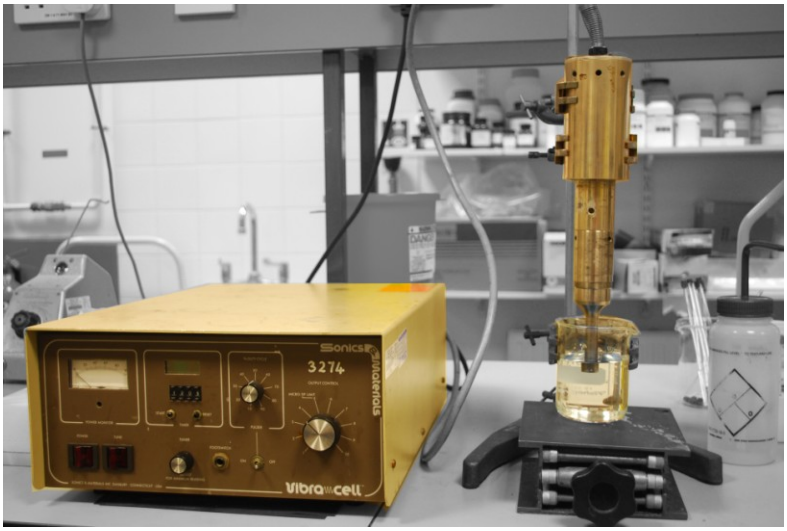

Figure 2.1: *20 kHz ultrasonic probe immersed in an aqueous solution in a beaker.*

The types of dental endosonic files used in the study were:

(i) files used for troughing during endodontic treatments (CKT-1, CKT-3, CT-4).

(ii) files used for fine root canal treatment (UT-4).

(iii) files used to shape the root canal before endodontic treatment (Start-X tips: Tip-1, Tip-2, Tip-3, Tip-4, Tip-5).

Types (i) and (ii) endosonic files fit onto an Analytic piezoelectric handpiece, whereas type (iii) endosonic files fit onto an EMS piezoelectric handpiece. All dental tips were connected onto a miniMaster ultrasound generator provided by Electro Medical Systems, Nyon, Switzerland (8 W, 30 ± 2 kHz). Figure 2.2 shows the endosonic files used for the experiments described in this thesis while Figure 2.3 shows an example of a dental tip connected to a piezoelectric handpiece, where ultrasonic energy is generated from the electrical energy supplied to it. The handpiece is connected to the generator *via* a rubber tubing housing both the electrical wires and cooling water tube separately. There are 10 divisions for the power output delivered by the generator, hereafter described as Powers 1/10 to 10/10.

Experiments on the characterisation and cleaning efficiencies of the dental endosonic files were performed on both types (i) and (ii) endosonic files described previously. Initial characterisation was performed on all the endosonic files chosen but further analyses were performed only on the CT-4, CKT-1 and UT-4(2) files as they are distinguishably different from one another as compared to the rest of the tips.

The Start-X tips (Tip-1, Tip-2, Tip-3, Tip-4 and Tip-5) were assessed to determine the effects of their individual shapes in sonochemical output.

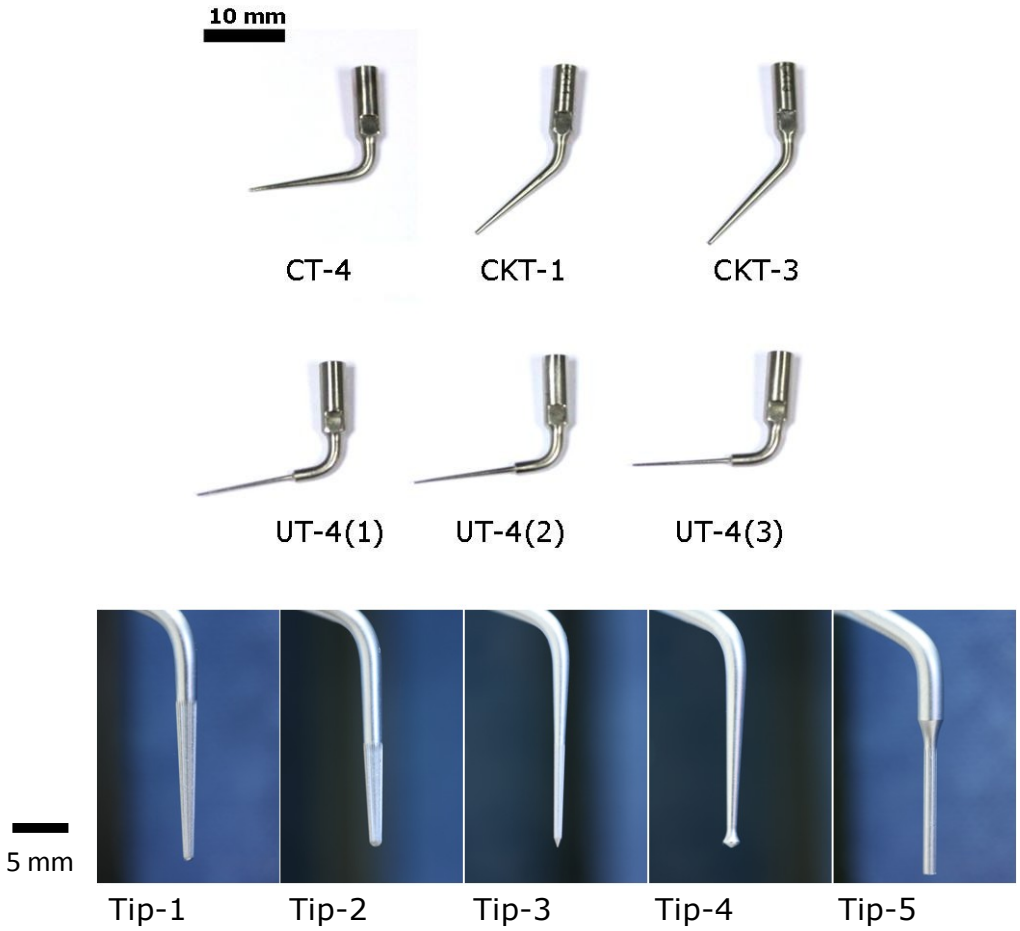

Figure 2.2: *Different endosonic files used.*

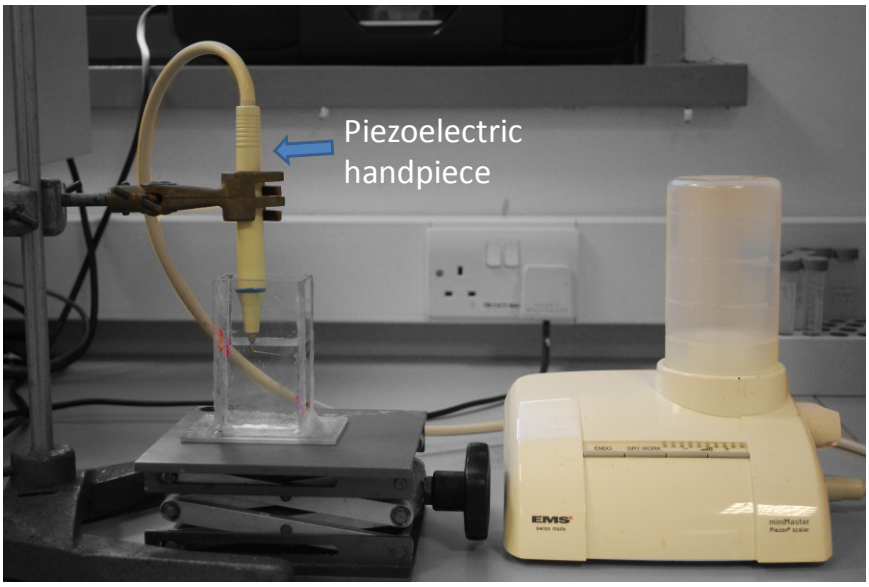

Figure 2.3: *An example of a dental tip connected to a piezoelectric handpiece, which is further connected to the MiniMaster dental generator.*

The experiments conducted using the endosonic files were performed in two sections; one in a bulk solution and another in a confined space. In the first part, the endosonic files used were fully immersed into 50 cm^3 of aqueous solution in a rectangular glass cuvette of 5 cm × 2.5 cm × 10 cm. Figure 2.4 shows an example of an endosonic file immersed in 50 cm^3 of freshly drawn distilled water in the above mentioned rectangular glass cuvette.

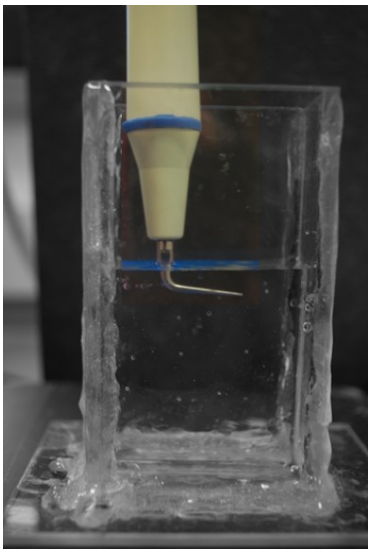

Figure 2.4: *Figure of dental tip in a glass cuvette.*

Experiments conducted in a confined space were performed in a root canal model made from silicone rubber of 25 mm × 25 mm × 3 mm, with various cut-off dimensions to form 'root canals' of various channel widths, such as 3 mm × 20 mm, 4 mm × 20 mm and 5 mm × 20 mm; depending on the experimental conditions (further elaborations will be given in Chapter 5). The silicone rubber was sandwiched tightly between two glass slides (25 mm × 25 mm × 2 mm) with four nylon bolts and nuts to ensure that there was no leakage from the system. Figure 2.5(a) and (b) illustrates the schematics of the top and front views of the described confined space system used, while Figure 2.6 illustrates the positions of a dental tip in the root canal model.

(a)

(b)

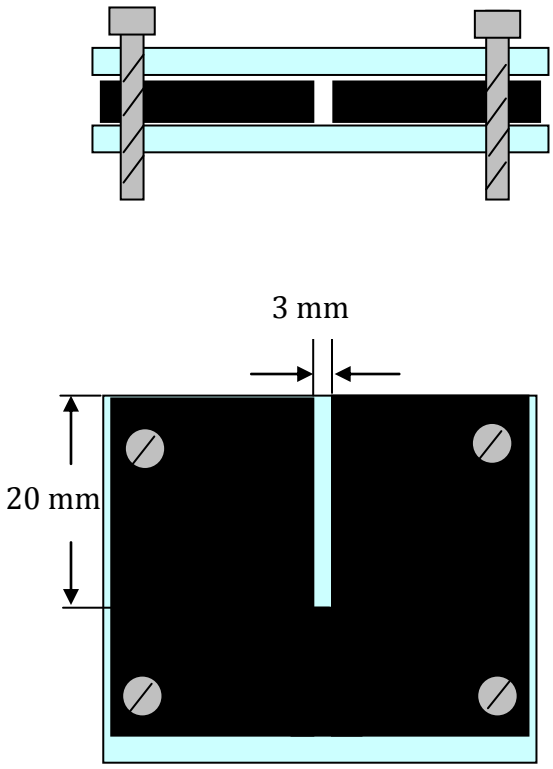

Figure 2.5: *Schematic of the model root canal made of silicone rubber sandwiched between two glass slides. (a) Top view, (b) Front view.*

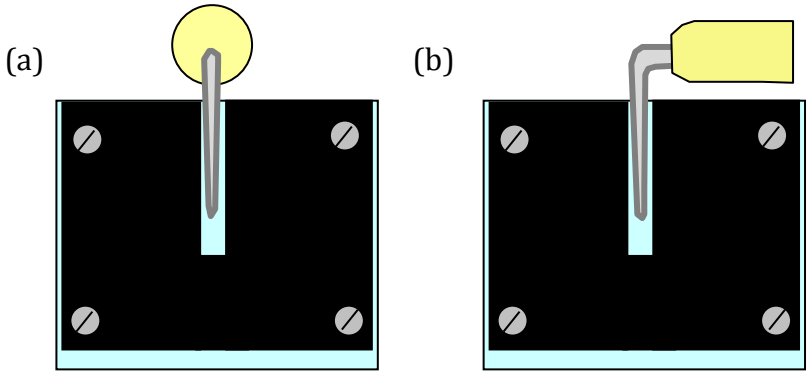

Figure 2.6: *A dental tip inserted into the channel (a) front-on and (b) side-on.*

2.1.2 Chemical Reagents

All reagents used were analytical grade, obtained from Sigma-Aldrich Co. UK, unless otherwise stated, and were used as received without further purification. All experiments were repeated three times to assess the consistencies of the experiments performed, unless stated otherwise.

2.1.3 Dimension Measurements of the Ultrasonic Devices

The dimensions of the ultrasonic devices were obtained with three different methods: with a high precision ruler (± 0.05 cm), with a vernier caliper and also by macrophotography using a digital single-lens-reflex camera (Canon EOS 500D) mounted to a Canon EF-S 60 mm f/2.8 USM Macro lens to obtain a closed focus image, followed by measuring the actual dimensions according to the ratio of the total number of pixels using ImageJ software.

2.1.4 Statistical Analysis

Statistical analyses were performed on all experiments to assess their consistencies. One-way analysis of variance (ANOVA) was performed on all comparable parameters, followed by Tukey Honestly Significant Difference (HSD) Post Hoc test to evaluate the significant difference between individual groups.

Correlation between two or more groups was evaluated using two-tailed Pearson's product-moment correlation coefficient. All statistical analyses were performed using Minitab 16 Statistical Software and were all assessed at 95 % confidence level unless stated otherwise.

2.2 Calorimetry

The importance of determining sonochemical energy output of various systems has been well established (Mason, 1991, Kuijpers *et al*., 2002). In usual practice, ultrasonic users tend to only state the maximum achievable power output as stated by the manufacturer, without taking into account all other energy dissipation. This can only give an approximate idea of the energy dissipated into the system. Thus, calibration of all ultrasonic equipments used is essential to ensure a standardised power output is obtained for comparable results (Kuijpers *et al*., 2002).

To perform this calibration, a known amount of distilled water was used. The sample water was sonicated over a fixed range of time, taking temperature readings of the sonicated sample throughout the entire process at constant intervals using a thermocouple (± 0.1 ^{o}C).

The experiment is separated into two different parts:-

- *For the 20 kHz probe*:- 100 cm^3 of distilled water was used and temperature was taken over 10 minutes at various arbitrary power settings on the ultrasonic generator (known as 20 %, 40 %, 60 % and 80 % on the power dial), noting the temperature of the water every 30 seconds.

- *For the dental tips*:- 50 cm^3 of distilled water was used and temperatures were taken over five minutes at intervals of 30 seconds, for power settings of low, medium and high (noted as Power 1/10, 5/10 and 10/10 on the generator).

The total power output of the system was then calculated based on heat generated into the system (Q) as calculated based on the equation below:-

$$Q = mC_p\Delta T \qquad \textbf{(Equation 3)}$$

where,

m is the mass of water (g),

C_p is the specific heat capacity of water (J g^{-1} K^{-1})

ΔT is the temperature difference (K)

The intensities produced by the ultrasonic equipments used $\left(\frac{Power}{Area}\right)$ was calculated by dividing the power output obtained based on the heat generated in the system (Q) by the surface area emitting ultrasonic energy divided by the total time taken (s) for both the 20 kHz probe (calculated to be 1.44 cm^2) and respective dental endosonic files - calculated using the methods stated in Section 2.1.3. The results of the calorimetry will be discussed in Section 3.1.

2.3 Fricke Dosimetry

Power ultrasonic equipment produces H• and •OH radicals in aqueous solution as a product of the collapse of cavitation bubbles (Henglein, 1987). These radicals play an important role in sonochemistry as their high reactivity may contribute to desirable changes in the sonicating system. In addition, the formation of radicals also contributes to antibacterial properties as highly reactive •OH radicals tend to destabilise bacteria, resulting in oxidative damage in bacteria and aiding in sterilisation (Liang *et al.*, 2004, Bai *et al.*, 2005, Bai and Jian, 2006). Seeing the importance of the effects of radicals to a sonicating system, quantification of the amount of radicals produced as a function of characterising one of the sonochemical

outputs of the systems has to be evaluated – and this leads to performing dosimetries to ultrasonic systems.

There are several methods of performing dosimetries to quantify the amount of •OH radicals formed in a sonicated system (Price and Lenz, 1993, Iida *et al*., 2005), among them the common ones are as follows:-

i. Iodide dosimetry:- which utilises the oxidation of I^- to form I_2 and I_3^- to detect the presence of •OH, (Scheme 2.1) measured optically by obtaining the absorbance *via* UV-visible spectrometry.

$$\bullet OH + I^- \rightarrow OH^- + I$$

$$I + I^- \rightarrow I_2^-$$

$$2I_2^- + I \rightarrow I_2 + 2I^-$$

$$I_2 + I^- \rightleftharpoons I_3^- \text{ (measured at 355 nm)}$$

Scheme 2.1

ii. Terephthalate dosimetry:- which utilises the addition of •OH onto terephthalic acid forming hydroxyterephthalic acid (Scheme 2.2) which fluoresces, measured by using fluorescence spectroscopy.

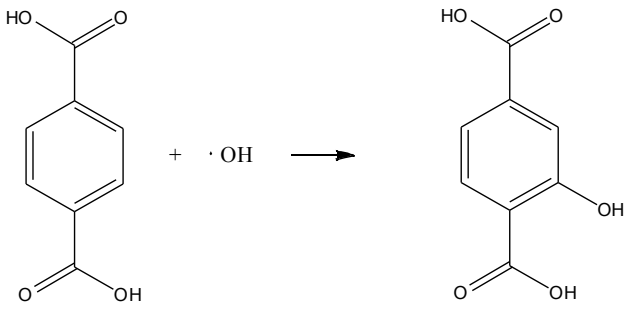

Scheme 2.2

iii. **Fricke dosimetry**:- which utilises the oxidation of Fe^{2+} to Fe^{3+} to measure the presence of •OH, (Scheme 2.3) measured optically by obtaining the absorbance *via* UV-visible spectrometry at 304 nm.

$$Fe^{2+} + {}^{\bullet}OH + H^{+} \rightarrow Fe^{3+} + H_2O$$

Scheme 2.3

In Fricke dosimetry, Fricke solution of (0.001 mol dm^{-3} $FeSO_4.7H_2O$ and 0.005 mol dm^{-3} H_2SO_4) was used. For the 20 kHz probe, 100 cm^3 of Fricke solution was placed in a jacketed vessel. Cooling water circulates the jacketed vessel, entering from the bottom and exiting from the top of the container. This provides temperature control of ± 4 ^oC (measured using a thermocouple of ± 0.1 ^oC sensitivity) throughout the length of the experiments. 1 cm of the entire length of the ultrasonic tip was immersed into the solution. Sonication was carried out at 4 arbitrary powers, similar to that performed for calorimetry (20 %, 40 %, 60 % and 80 %) over 60 minutes. 3 cm^3 of sample was pipetted out every 10 minutes into a UV cell for UV-visible measurements using an Agilent 8453 UV-visible spectrometer, obtaining the absorbance of Fe^{3+} at 304 nm.

Similar to the sonication procedures of the 20 kHz probe, sonication of the dental tips was performed in a jacketed vessel with working volume of 20 cm^3, sonicated for 30 minutes, pipetting 3 cm^3 of sample every 5 minutes for UV-visible measurements. This procedure was repeated for each different dental tip used at low, medium and high powers (P1/10, 5/10 and 10/10) respectively.

2.4 Sonoluminescence

Alongside with the formation of radicals, as mentioned earlier in Section 1.2.1.1, the collapse of transient cavitation bubbles also produce very short burst (in the range of less than a hundred nanoseconds) of high intensity light (in the range of

miliWatts) – known as sonoluminescence (Negishi, 1961, Young, 2004). Due to the extremely short lifetime of sonoluminescence, quantification of the light produced sonically becomes hard to be measured, especially for small systems like the endosonic files.

In order to obtain a clearer picture of the areas of cavitational activity based on sonoluminescence, 5-amino-2,3-dihydro-1,4-phthalazinedione (also known as luminol) was used. Luminol reacts with the •OH produced sonochemically in order to give out a more intense blue light at the areas where cavitation bubbles collapse. To achieve this, luminol solution was made up – consisting of 1×10^{-3} mol dm^{-3} luminol, 1×10^{-4} mol dm^{-3} hydrogen peroxide and 1×10^{-4} mol dm^{-3} ethylenediamine tetraacetic acid (EDTA), prepared in deionised water and made up to pH 12 by the addition of sodium hydroxide (McMurray and Wilson, 1999). Scheme 2.4 shows the excitation of luminol in the presence of •OH in the system to give out light (*hv*).

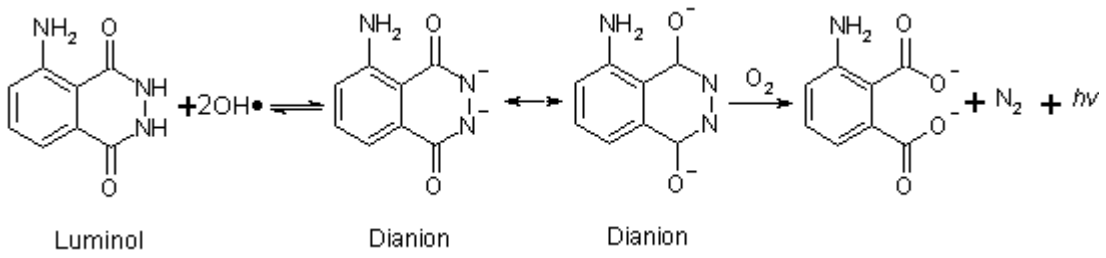

Scheme 2.4

This experiment was divided into two parts:

a) Dental tip immersed into a bulk solution

b) Dental tip immersed into a confined space

For the first part of the experiment, a dental tip was immersed in 50 cm^3 of luminol solution in a glass cuvette (5 cm × 2.5 cm × 10 cm), as shown in Figure 2.4. A digital single-lens-reflex camera (Canon EOS 500D) mounted to a Canon EF-S 60 mm f/2.8 USM Macro lens was placed aligned to the position of the tip and set to ISO 3200

for light-sensitive measurements. The focal distance was adjusted to give a 1:1 reproduction. Images were taken in a light-proof box, over exposure time of 30 seconds, both with and without sonication (silent reaction). Figure 2.7 shows the schematic of the set-up of an endosonic file immersed in luminol solution with a camera aligned to it, placed in a light-proof box.

The intensity of the luminol emission was calculated using ImageJ (Abramoff *et al.*, 2004) where the background image for the silent reaction was subtracted from the image with sonication. All further image post-processing was performed with the aid of ImageJ, which will be described and discussed further in the results section (Section 3.3). The procedure was repeated for each of the different Powers 1/10, 5/10 and 10/10, and five repetitions were taken for this experiment.

Following the first part of the experiment, a dental tip was then immersed in a confined space, mimicking the space of a root canal in a tooth. The model channels used were as described in the beginning of the chapter (Figure 2.3), with or without side channels for different experimental purposes. The duration of camera exposure depends on the nature of the experiment, ranging from 30 seconds to 5 minutes, depending on the experimental requirements. Data processing procedures of the images taken were similar to the experiments performed in bulk, which will be explained in detail in the results section (Section 3.3).

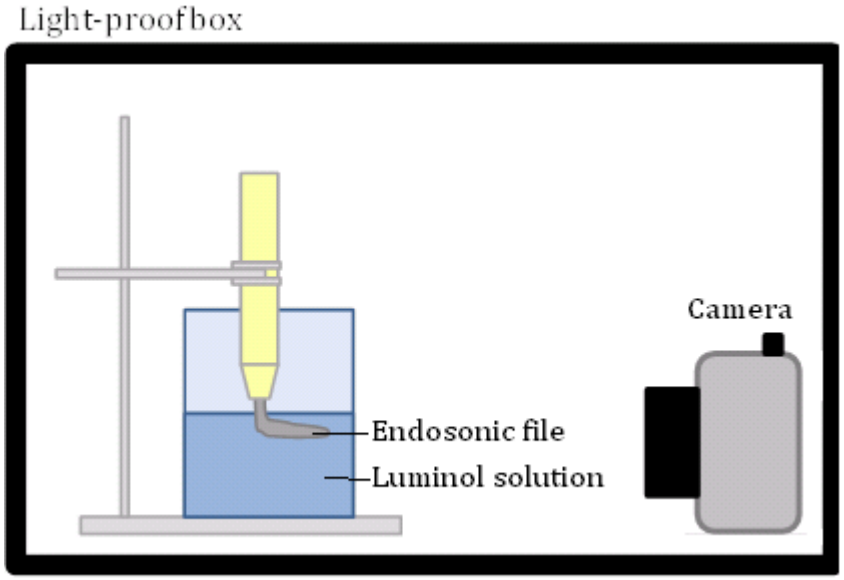

Figure 2.7: *Experimental setup of an endosonic file immersed in luminol in a glass cuvette, aligned with the camera in a light-proof box.*

2.5 Quantification of cavitation bubbles

The total amount of cavitation produced by ultrasound was measured with a CaviMeter (Figure 2.8), made up of a crescent-shaped ring, that acts as a receiver to the acoustic emissions, connected to a generator that displays the signals received in terms of arbitrary numbers (Hodnett *et al.*, 2004). The receiver contains a strip of piezoelectric material embedded onto a crescent-shaped, 4 mm thick, sound absorbing polyurethane. This design ensures the collection of acoustic signal of cavitating bubbles within the detectable area of the piezoelectric film layer and attenuates everything outside the detectable area (Zeqiri *et al.*, 2003a). The cavitation sensor measures the amount of acoustic emission produced by the sonicating system, by reading the "white noise" component of the acoustic emission spectrum associated to the occurrence of violent inertial cavitation, and displays the cavitational activity quantitatively (Zeqiri *et al.*, 2003a, Zeqiri *et al.*, 2003b).

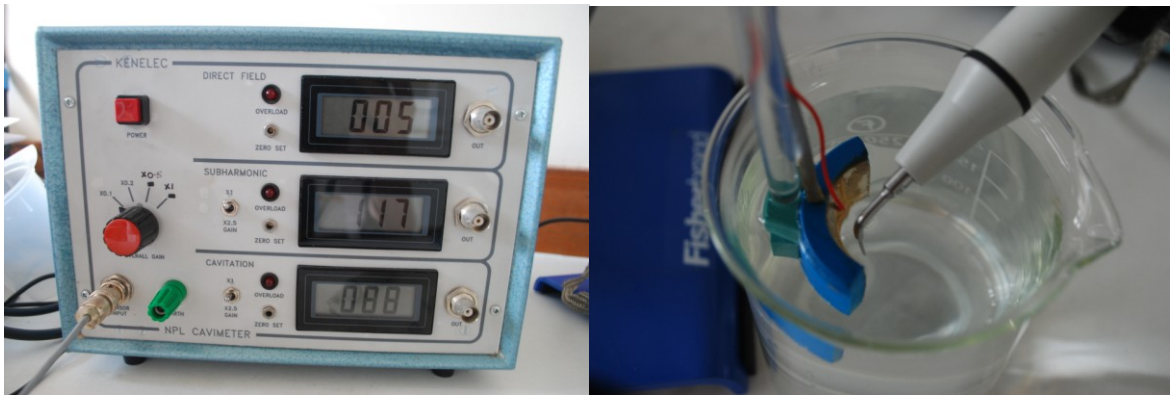

Figure 2.8: *(left) Generator of CaviMeter, stating the signal output values (from top to bottom) of the 'direct field', 'subharmonics' and 'cavitation'. (right) An example of the crescent-shaped acoustic cavitation sensor immersed in a beaker of water with an endosonic file.*

The crescent-shaped acoustic sensor was placed into a glass beaker and immersed in 50 cm^3 of freshly-drawn deionised but not degassed water. The endosonic files were positioned in the centre of the cavitation sensor ring of the CaviMeter. Background readings were taken for each experimental run in the absence of ultrasound. The handpiece was switched on for approximately 10 s, until the sensor readings were stable. An average of three successive measurements of the 'direct field' and 'cavitation' (*i.e.* high frequency output) measurements were recorded while changing the power. There were no hysteresis effects noted whilst the power was adjusted. The experiment was repeated for each file design for various power settings.

2.6 Scanning Laser Vibrometry

The Scanning Laser Vibrometry (SLV) system was used to measure the vibration movements of various dental tips, as described by Lea *et al.* (2003). The system was a PSV 300-F/S from Polytec GmbH, Polytec-Platz, Waldbronn, Germany and used as class II, He-Ne laser operating at 632.8 nm.

The SLV uses a laser beam illuminated onto a vibrating object to detect the frequency shift in the vibrating object based on the principle of Doppler's effect. Figure 2.9 shows the experiment set-up for a dental endosonic file clamped firmly, aligned vertically to the laser beam source. The housing of the laser beam source contains three beam splitters to separate the laser beams into a reference beam and an object beam – which is shone onto the object.

Figure 2.10 illustrates the structure of the SLV inside the scanning head housing. The initial laser source emitted by a beam source is separated into two sources: one acts as the reference beam, which goes through a Bragg cell to obtain a frequency shift to a lower, detectable frequency to determine the sign of the velocity, and remains in the scanning head (Polytec, 2000). The other beam passes through a wave plate, a focusing lens and two mirrors before hitting the targeted vibrating object. The wave plate creates a quarter-wavelength phase shift, polarising the laser beam from linear to circular. This was done to minimise any depolarisation loss in the process (Moshe *et al*., 2003). The lens focuses the laser beam, which then passes through two adjustable mirrors before hitting the vibrating object. The reflection of the laser beam returns *via* the same path, and gets reflected at 90^{o} at the beam splitter before joining up with the reference beam, where both frequency signals were sent to the detector. The signal detector then detects the frequency shift of the object beam, performs a Fast Fourier Transform to both the signals and produces data in terms of the velocity of the vibrating object. Further mathematical integration performed by the Polytec software provides the vibration displacements, which are used for data analyses.

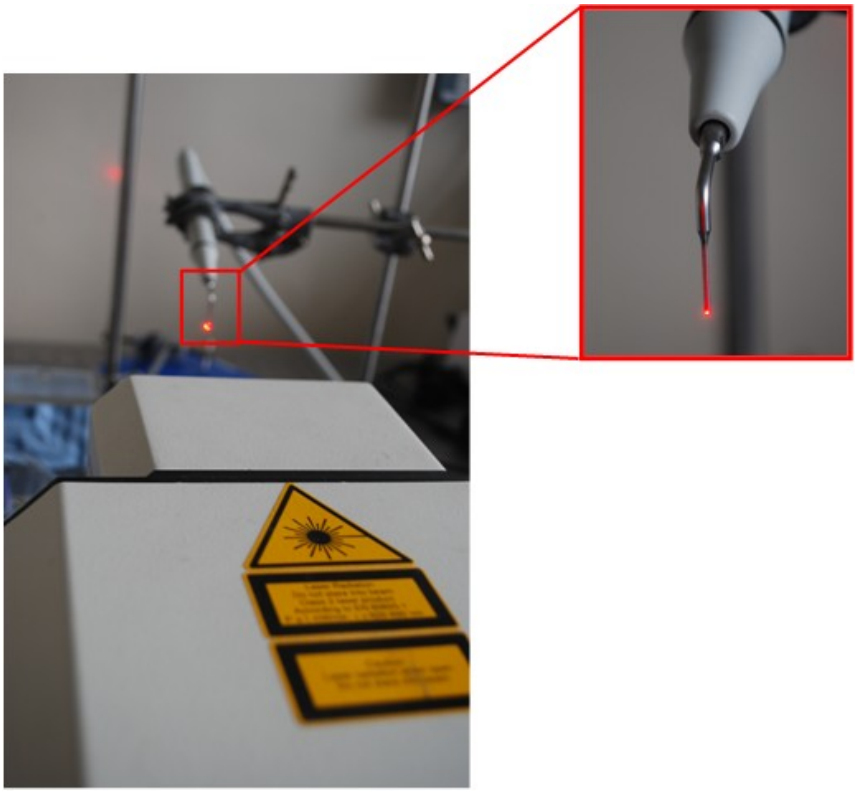

Figure 2.9: *An example of a laser beam shone onto a dental tip to obtain its vibration velocity.*

For the experimental set up, an endosonic file is clamped firmly, with the tip facing downwards, aligned to the laser beam. Scan points were spaced out equally along the working length of the dental tips (ca. 15 – 17 mm). Each scan point was measured and the average of 5 cycles was recorded for each tip, at P1/10, 5/10 and 10/10 respectively. The experiment was performed in three different conditions: in air, in 50 cm^3 distilled water and in a confined space of a root canal model (Figure 2.5).

For all the experiments, data were collected in terms of the displacement profile of various dental tips, and plotted against the scan points along the length of the files to obtain a vibration profile of a tip.

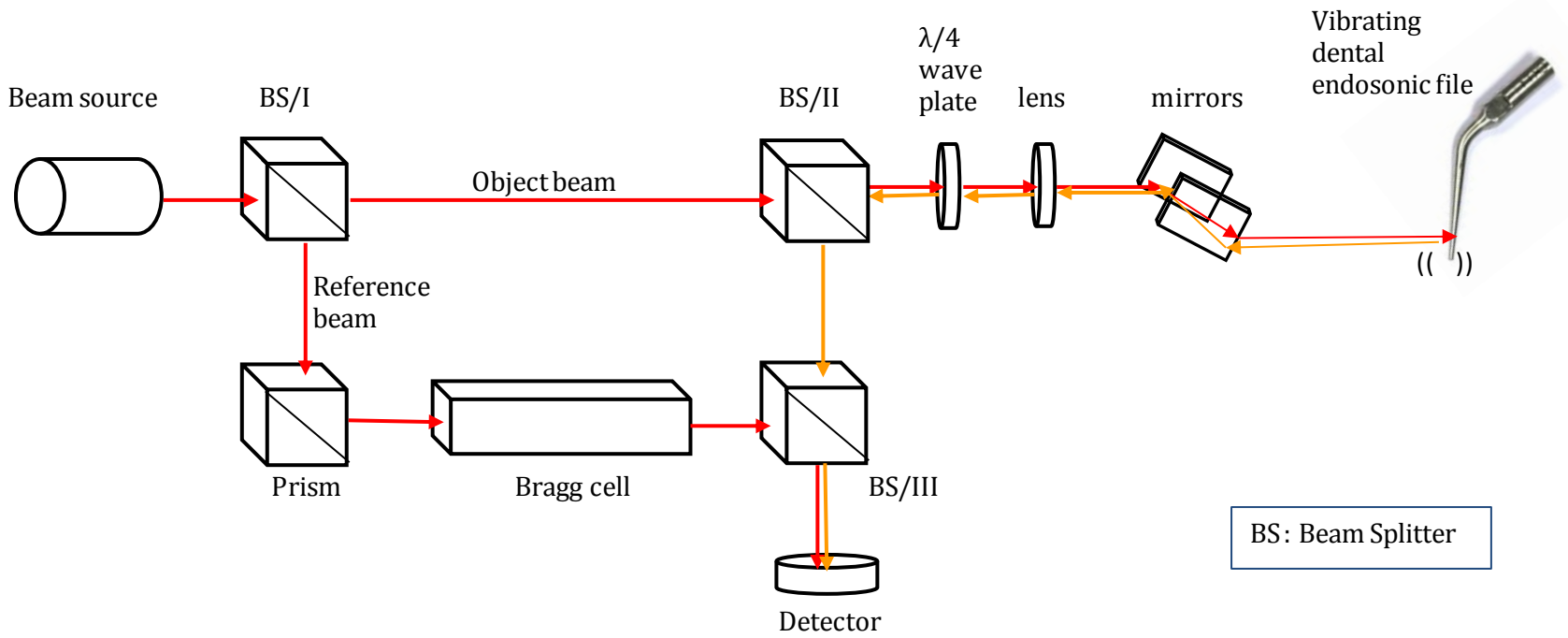

Figure 2.10: *Schematic of the system configuration of the SLV scanning head.*

Image reproduced from Polytec (2000).

2.7 Particle Image Velocimetry

Particle Image Velocimetry (PIV) is a widely used technique, where in the most common cases, a laser beam is used to illuminate seeded particles (most commonly polystyrene spheres), and the movement and the velocity of the liquid is obtained based on the movements of the seeded particles (Nowicki *et al.*, 1998, Frenkel *et al.*, 2001, Gao *et al.*, 2009, Mandroyan *et al.*, 2009).

This experiment was carried out with the courtesy of a three-month loan on the equipment from the EPSRC loan pool. In this experiment, slight modifications were made to suit the experimental equipments. Instead of using a laser beam that shines through a planar area in the liquid, a high-intensity white light connected to a fibre-optic tube was used to shine through the cuvette without giving out much heat as compared to a xenon light source. The light source used for our experiment was a Solarc®-powered metal-halide light (Everest VIT, ELSV-60 light source operating at 90 - 240 VAC 50 - 400 Hz, 1 A (@ 120 VAC). The experiments were performed by using a high speed video camera (Photron FASTCAM Digital Video Recorder (DVR)), mounted onto a Navitar 18 – 108 mm zoom lens with a aperture value of f/2.8.

In order to initiate this study, a few parameters were examined to ensure that the experimental results obtained were comparable to those reported in the literature. First of all, due to experimental constraints, all experiments on the PIV were performed in a 1 cm × 1 cm disposable polymethacrylate cuvette. The seeded polystyrene spheres used were controlled to 10 mg ± 5 % (measured gravimetrically) in 4.5 cm^3 of distilled water for each experimental runs. Polystyrene spheres of ~100 μm diameter were used in order to get a better visualisation of the particle movements on the video camera with the supplied camera lens.

A pilot study was performed on the 20 kHz ultrasonic probe, mounted with a microtip with a surface area of 0.28 cm^2, using the intensity ranges from 7 to 29 W cm^{-2} (obtained calorimetrically). The ultrasonic probe is immersed at approximately 5 mm into the polymethacrylate cuvette (filled with distilled water and seeded polystyrene spheres). The setup was aligned with the camera to have a field of view of 1 cm × 1 cm along the *x* and *y* axis on the video camera display (Figure 2.11).

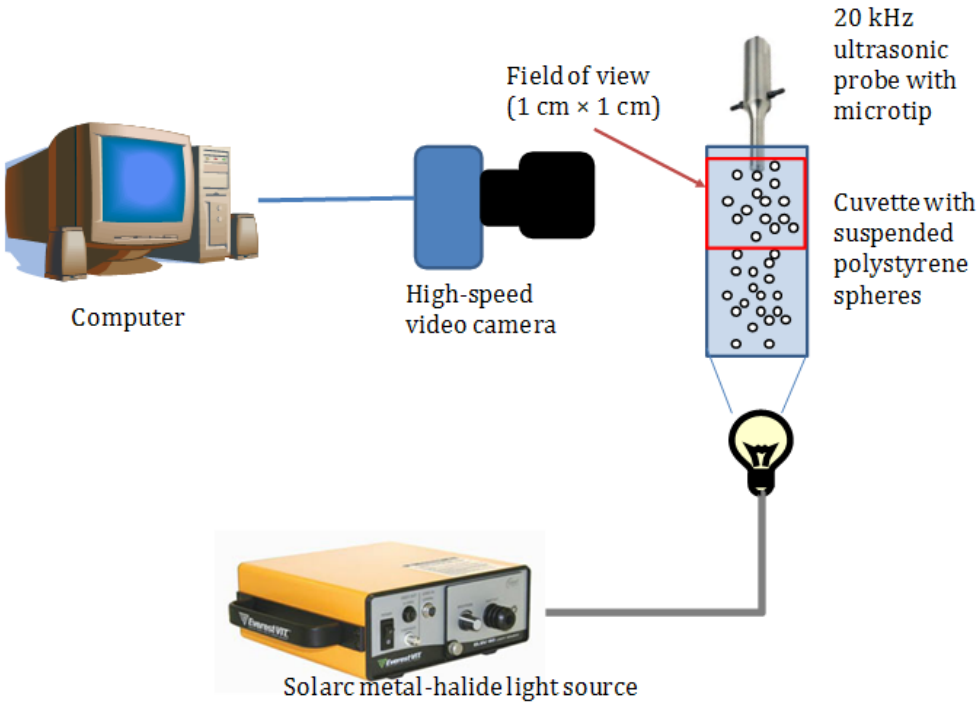

Figure 2.11: *Schematic of a 20 kHz ultrasonic microtip immersed into a polymethacrylate UV cuvette of 1 cm width with suspended polystyrene spheres in water, illuminated with a metal-halide light, aligned to a high-speed video camera.*

Video was recorded at the start of sonication for 20 s. Videos of the particle movements during sonication at those intensities chosen were carried out at various frame rates (125 fps, 250 fps, 500 fps, 1000 fps and 2000 fps) to assess the most suitable frame rates to be used for further experiments. Data from the videos taken were extracted as bitmap (.bmp) image files, which was used for post-processing analyses. Data processing were performed in a PIV software (PIV*view*, Germany) where image pairs between frames were used to assess their velocities. (Deryabin *et*

al., 2010) have found that the average velocities of the particles used for PIV stabilizes after sonicating for 10 s. Hence, for this experiment, 50 image pairs were taken after 10 s of sonication and used for analyses to assess the consistency of the experimental setup.

PIV*view* generates a velocity contour map based on an image pair, based on a calibrated length and time difference between the two images. From there, information on the maximum and average velocity across the region of interest (in this case, 1 cm × 1 cm) can be obtained from the software. Grids of 0.2 mm × 0.2 mm were used for all experiments for reliable readings on the particle movements.

Upon establishing the experimental method and compared the experimental results with literature, the experiment was performed on the endosonic files. There were a few studies carried out by other authors on the particle image velocimetry on their dental instruments. For example, de Groot *et al.* (2009) and Boutsioukis *et al*. (2010a) have performed micro-PIV on needle-type endosonic files to support their computational fluid dynamics model, whereas Jiang *et al.* (2010) have performed PIV with the aid of a high-speed camera, and have found that files which produced higher fluid velocities were better in dentin debris removal.

In order to establish correlations among the characterisation methods, PIV was performed on the endosonic files used in this study. The experimental setup for the dental files was similar to the 20 kHz ultrasonic microtip, as illustrated in Figure 2.12. For this experiment, three dental tips (CT-4, CKT-1 and UT-4(2)) were assessed at Powers 1/10, 5/10 and 10/10 respectively. Sonication was performed for 20 s, with videos taken simultaneously to the sonication. 50 image pairs after 10 s of sonication were selected, and analyses were performed in a similar manner to those for the 20 kHz ultrasonic microtip.

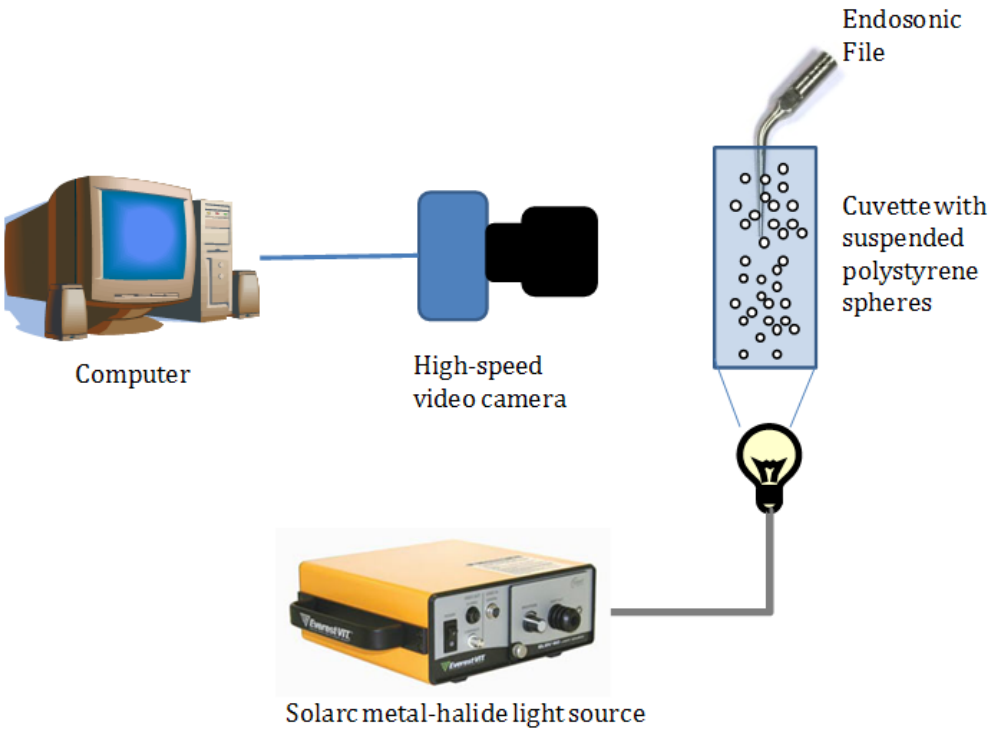

Figure 2.12: *Schematic of an endosonic file immersed into a polymethacrylate UV cuvette of 1 cm width with suspended polystyrene spheres in water, shone with a metal-halide light, aligned to a high-speed video camera.*

2.8 Cleaning Efficiencies

As mentioned earlier in Section 1.3.3, endodontic treatments aim to clean impurities in an infected root canal. Whilst characterisation of the sonochemical performances of different tips is important to give a better understanding, cleaning efficiencies also play an important role so as to determine the factors contributing to the lack of efficiency in actual clinical performances.

In this study, the cleaning efficiencies of different endosonic instruments were carried out based on different aspects:-

- The mixing ability of different endosonic files;
- The ability to decolourise a model dye in the presence of a dental irrigant;

- The ability to remove surface impurities.

2.8.1 Mixing Ability of the Endosonic Files

For this experiment, the mixing ability of different endosonic files was examined using 1:1 ratio of silicone oil (Dow Corning 50 cSt) and distilled water dyed with 1 mmol dm^{-3} of methylene blue dye. Low viscosity silicone oil was chosen for this experiment so as to match the low power input of the dental sonicating system. This study was carried out to characterise and correlate the vibration movements of the endosonic files together with the cavitation activity in terms of the ability to mix two immiscible liquids together due to high turbulence in a confined system.

An endosonic file was inserted into a root canal model channel made of silicone rubber, with a side channel to examine the mixing effect of silicone oil and water along the side direction upon sonication. Figure 2.13 shows a schematic of the experimental set up used for this experiment, with Figure 2.14 illustrating the dimensions of the channel. The experiment was performed for two minutes, at Powers 1/10, 5/10 and 10/10. Images were taken after sonication and the area of emulsion formed along the side channel was calculated with the aid of ImageJ (Abramoff *et al*., 2004). Each experiment set consists of five repeats to assess their consistency.

Further analyses on the emulsion formed were carried out using an optical microscope (GX Microscopes L3001, mounted with an Infinity Capture camera), with 100× magnification. Samples of oil-in-water emulsion were pipetted out and placed onto microscope slides. The particle droplet sizes were analysed using a method described by Scherze *et al.* (2005), using ImageJ software, where the images were treated using the following steps:

i) Images were converted to 8-bit bitmap files.

ii) Hue-saturation-intensity was adjusted to provide good contrast on the particle *vs* background.

iii) Thresholds of the images were selected, to turn the white areas black and inverse the black to white to have a better contrast on the emulsion droplets.

iv) Images were converted to a binary file.

v) Particles were analysed based on the average sizes, standard deviations and the percentage area in the images.

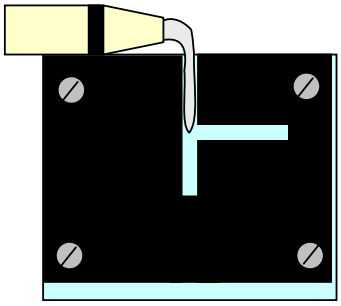

Figure 2.13: *Schematic of an endosonic file immersed into the root canal model with the end of the endosonic file facing the extended side channel.*

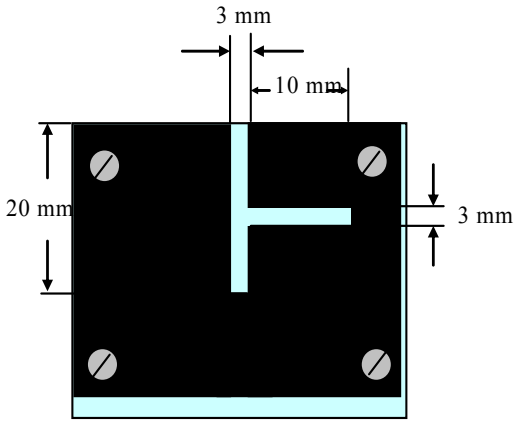

Figure 2.14: *Silicone rubber root canal model with an extended side channel used to evaluate the percentage of emulsion formed in the side channel.*

2.8.2 Dye Decolourisation with a Dental Irrigant

In endodontics, various irrigants are used as disinfectants. Studies have been carried out to evaluate the most effective irrigants used during endodontic treatments (Spencer *et al*., 2007, Driscoll *et al*., 2002, Gu *et al*., 2009, Heling and Chandler, 1998, Hülsmann and Hahn, 2000) and have found out that one of the most efficient irrigants is sodium hypochlorite, due to its antibacterial and high oxidising properties.

Sodium hypochlorite is been well known for its oxidising properties and has been used widely coupled with ultrasonic equipments to remove dye effluents, especially most well seen in wastewater treatments (Blume and Neis, 2005). Previous studies have shown sonication of a dye in the presence of small amount of sodium hypochlorite to be more effective than just having one of the parameters on its own (Pizzolato *et al*., 2002). By taking this into account, this study was conducted based on the oxidising ability of sodium hypochlorite in removing a cationic dye, such as Rhodamine B.

To initiate this study, sonication was performed with the 20 kHz probe. Experiments were conducted with 100 cm^3 of 5 μg cm^{-3} of Rhodamine B solution, with or without the presence of sodium hypochlorite. Calibration was performed on the UV-visible spectrometer at 554 nm for various concentration of Rhodamine B to obtain the extinction coefficient of the dye.

The concentration of sodium hypochlorite used varied from 0.5 % to 2.0 %, depending on the experimental conditions. All experiments with the 20 kHz probe were performed in a jacketed vessel for temperature control (20 ± 4 ºC). Sonication was performed at various intensities on the power dial (20 %, 40 %, 60 % and 80 %) for 30 minutes, pipetting 3 cm^3 of sample out every five minutes to be read from the UV-visible spectrometer at 554 nm. The change of absorbance signifies the change in

concentration of Rhodamine B which is correlated to the rate of decolourisation of the reaction.

Experiments were repeated with pH control. Sodium hypochlorite forms an equilibrium with hypochlorous acid in aqueous condition, causing the solution to be pH sensitive (Scheme 2.5). In this study, 2 wt% of hydrochloric acid (Fisher Scientific) or 2 wt% of sodium hydroxide was added to the bulk Rhodamine B and sodium hypochlorite solution to control the pH of the solution prior to sonication.

$$NaOCl + H_2O \rightleftharpoons HOCl + NaOH$$

Scheme 2.5

Similar to that performed on the 20 kHz probe, this method was adapted and modified for the endosonic files. 3.5 cm^3 of Rhodamine B was used in a UV cell, with or without the presence of sodium hypochlorite. Sonication was performed for a dental tip, at Powers 1/10, 5/10 and 10/10 respectively, for five minutes, noting the change in absorbance every 30 seconds. This procedure was repeated for all various endosonic tips to evaluate the rate of dye decolourisation of each tip.

In addition, liquid chromatography coupled with mass spectrometry (LC-MS) was performed to identify the degradation products formed upon sonication using a Daltonics micrOTOF electrospray time-of-flight (ESI-TOF) mass spectrometer (Bruker Daltonik GmbH, Bremen, Germany) coupled to an Agilent 1200 LC system (Agilent Technologies, Waldbronn, Germany). 10 µL of sample was injected into a 30:70 flow of water:acetonitrile at 0.3 mL/min. 10 µL of 5 mM sodium formate was injected after the sample as a calibrant over the mass range m/Z = 50 – 1500.

Similar experiments were also performed on the 20 kHz probe at various hydrogen peroxide concentrations to note any differences in decolourisation obtained during sonication.

2.8.3 Removal of Surface Impurities

One of the uses of power ultrasound is to remove surface impurities. This can be done when there is a very high shear stress between the surface impurities and the liquid in a closed medium when they are subjected to power ultrasound (Plesset and Chapman, 1971, Lauterborn and Bolle, 1975). Also, when cavitation bubbles collapse, high energy microjets knock off surface impurities when it is close enough to the wall, resulting in cleaning of the surface impurities (Lauterborn and Bolle, 1975).

In this study, a method was adapted from Krefting *et al.* (2004) to remove marker pen ink on a glass slide. A microscope cover slip was used for this purpose, coated with a uniform layer of black permanent marker ink spread on the cover slid (Sharpie Magnum Permanent Marker). The cover slip coated with ink was sandwiched between two glass slides with a silicone rubber model channel in between the glass slides (Figure 2.15).

Sonication was performed for two minutes, at Powers 1/10, 5/10 and 10/10 respectively for different endosonic files. An endodontic irrigant (in this case, 2 wt% of NaOCl) was inserted into the model channel with a syringe with care, making sure that no scratch is made on the microscopic cover slip. An endosonic file was then inserted into the channel, placed in the middle of the channel. A silent reaction was performed as a control with no sonication. Images of the model channel coated with ink were taken prior to and after sonication for comparison of the percentage of ink removal, calculated with the aid of ImageJ. The procedure of the image analyses is as follow:

i) Images were converted to 8-bit bitmap files.

ii) Region of interests (in this case, the entire channel area) were selected and the percentage area of the black spots were measured.

(a)

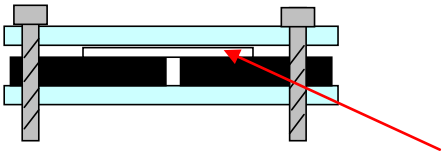

Microscope cover slip coated with permanent marker ink

(b)

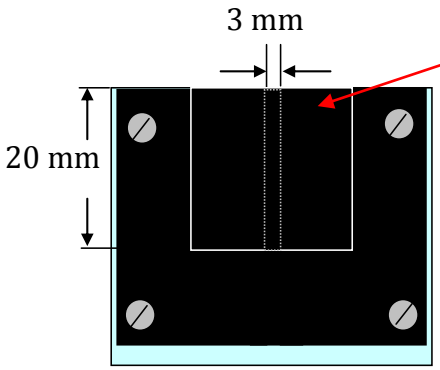

Figure 2.15: *Schematic of the model root canal made of silicone rubber with a microscopic cover slip coated with permanent marker ink, sandwiched between two glass slides. (a) Top view, (b) Front view.*

Further evaluation and comparison was made for different endosonic files for quantitative measurements on the effectiveness in removing surface impurities. In the second part of this study, hydroxyapatite paste was used to evaluate the rate of removal along the side channel in a model root canal. Hydroxyapatite, being one of the active ingredients in the tooth (Park, 2008), was used so as to show a closer correlation to the actual *in vivo* environment. The hydroxyapatite paste was mixed with distilled water at a 1:1 ratio, and packed into the side channels before it was sandwiched between the glass panels.

Sonication was performed similar to that described above, and the results obtained were evaluated based on the image before and after sonication with the aid of ImageJ – using a similar analysis method as stated above for the ink removal experiments.

3.Characterisation of Ultrasonic Instruments

In this chapter, all ultrasonic equipment (20 kHz probe and endosonic files) used were characterised based on their energy output, sonochemical output, vibration movements and their acoustic streaming properties.

3.1 Calorimetry

Calorimetry was first performed on the 20 kHz ultrasonic probe at various intensities to determine its actual energy output. Experiments with the 20 kHz probe were carried out for 10 minutes, noting the temperature every 30 seconds.

Based on Figure 3.1, the experiment was carried out for duration of 10 minutes as the temperature thereafter plateaus. The total energy given out at each intensity was then calculated by applying the equation $Q = mC_p\Delta T$ (refer to Equation 3, Section 2.1). Table 3.1 shows the collated calculations at different arbitrary powers on the 20 kHz probe, with the intensities calculated based on a probe surface area of 1.44 ± 0.01 cm^2.

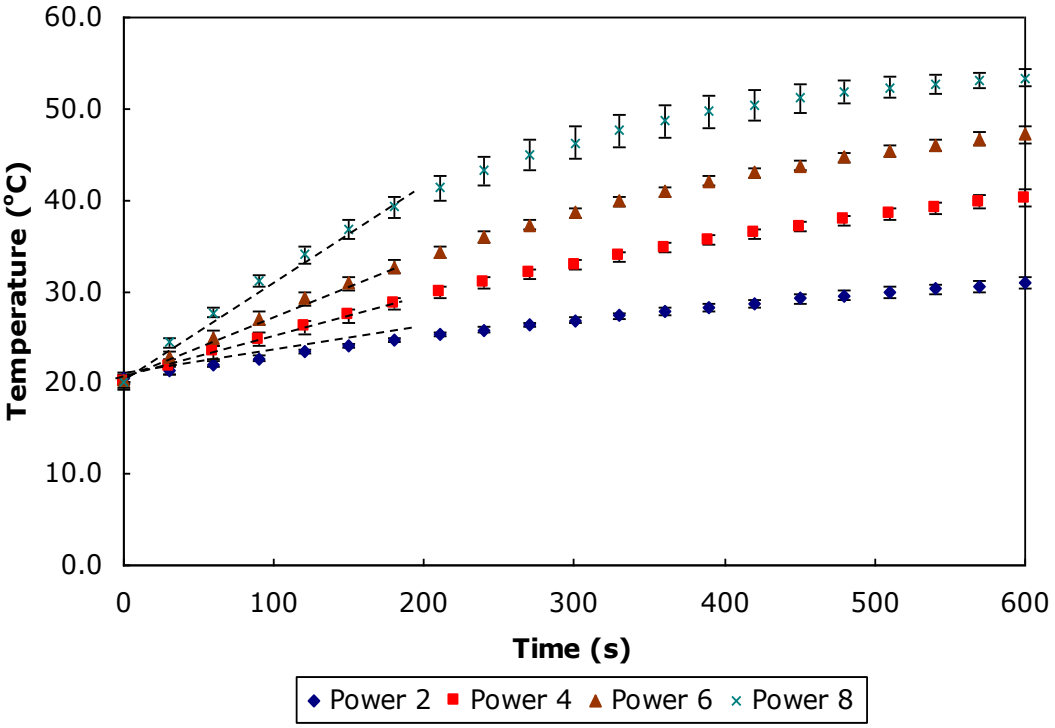

Figure 3.1: *Temperature profile upon sonication of the 20 kHz ultrasonic probe at different 'power' intensities as stated on the power dial.*

Table 3.1: *Collated energy, power and intensity at different arbitrary 'power' stated on the 20 kHz ultrasonic probe.*

Arbitrary Power	Energy (J)	Power (W)	Intensity (W cm^{-2})
2	4400	7.34	5.10
4	8400	14.0	9.72
6	1130	18.8	13.1
8	14000	23.3	16.2

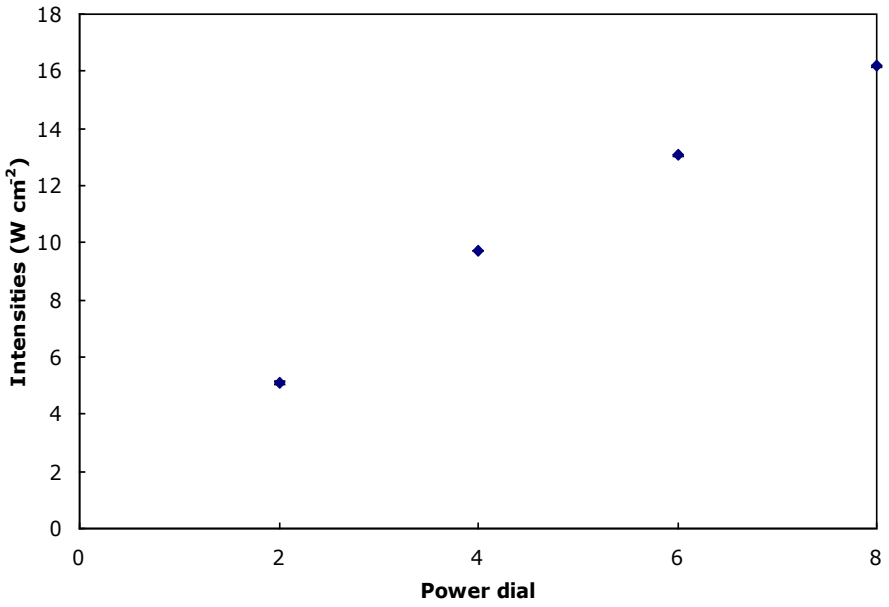

Figure 3.2: *Intensities of the 20 kHz ultrasonic probe at different 'powers' stated on the power dial. (Uncertainties obtained from triplicates of the experiment.)*

Figure 3.2 shows the relationship between the actual intensities given out by the ultrasonic probe and the arbitrary power dial on the generator. A linear relationship is obtained, suggesting that the increase in intensity increases linearly with the power dial. This gives a better illustration in terms of actual power given out per unit area of the ultrasonic probe for better quantitative measurements and comparisons than using the indicated percentage power settings on the generator.

Similar to that performed on the 20 kHz probe, calorimetry was also performed on all the dental tips described in this thesis for a better comparison among the tips. The experiment was carried out in a smaller volume of 50 cm^3, recording the temperature rise in the water over five minutes. The results obtained are tabulated below.

Table 3.2: *Collated energy, power and intensity of different endodontic tips (operating at 30 kHz) at different arbitrary power settings.*

Tips	Surface area (cm^2)	Arbitrary Powers (1-10)	Energy (J)	Power (W)	Intensity (W cm^{-2})
CT-4	0.47	1	21.1	0.07	0.149
		5	63.4	0.211	0.446
		10	464	1.55	3.27
CKT-1	0.50	1	21.0	0.07	0.141
		5	126	0.421	0.847
		10	474	1.58	3.182
CKT-3	0.44	1	20.9	0.07	0.159
		5	76.7	0.256	0.581
		10	451	1.50	3.41
UT-4(1)	0.20	1	21.1	0.07	0.353
		5	160	0.535	2.67
		10	432	1.44	7.22
UT-4(2)	0.18	1	21.6	0.07	0.39
		5	151	0.505	2.77
		10	628	2.09	11.50
UT-4(3)	0.20	1	20.9	0.07	0.354
		5	41.8	0.140	0.708
		10	167	0.558	2.83

Based on Table 3.2, we can conclude that the difference in power (W) and intensity (W cm^{-2}) at low 'power' setting is insignificant (ANOVA, p-value > 0.05) for all dental tips. As the power increases, the variation in power output increases, depending on different shapes of the endosonic files, as shown in Figure 2.2.

Figure 3.3 shows the collated power output for different endosonic tips at Powers 1, 5 and 10; which corresponds to low, medium and high power settings on the EMS generator.

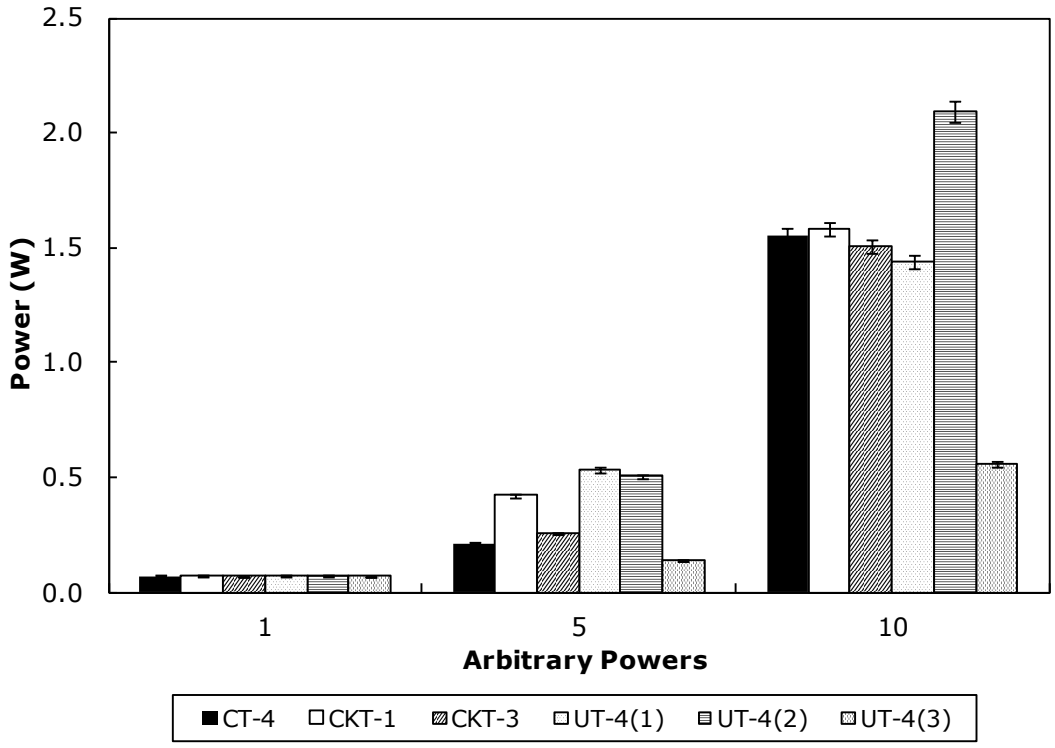

Figure 3.3: *Collated power output for all endodontic tips at different arbitrary powers.*

It can be seen that the output power at Power 1/10 is about the same for all dental tips as the recorded temperature rise in the system is almost insignificant over a prolonged period of sonication. The difference becomes more obvious at medium and high power settings, as the temperature rise in the system becomes more variable among the dental tips. This gives an indication of the various power outputs and corresponds to different levels of energy dissipation for individual tips during sonication.

The total power calculated *via* calorimetry does not take into account the shape of each endosonic files used. In order to have a uniform measurement of the power output, the surface areas of the working lengths of the endosonic files were

calculated. Upon achieving this, the intensities of each endosonic files were collated in Figure 3.4.

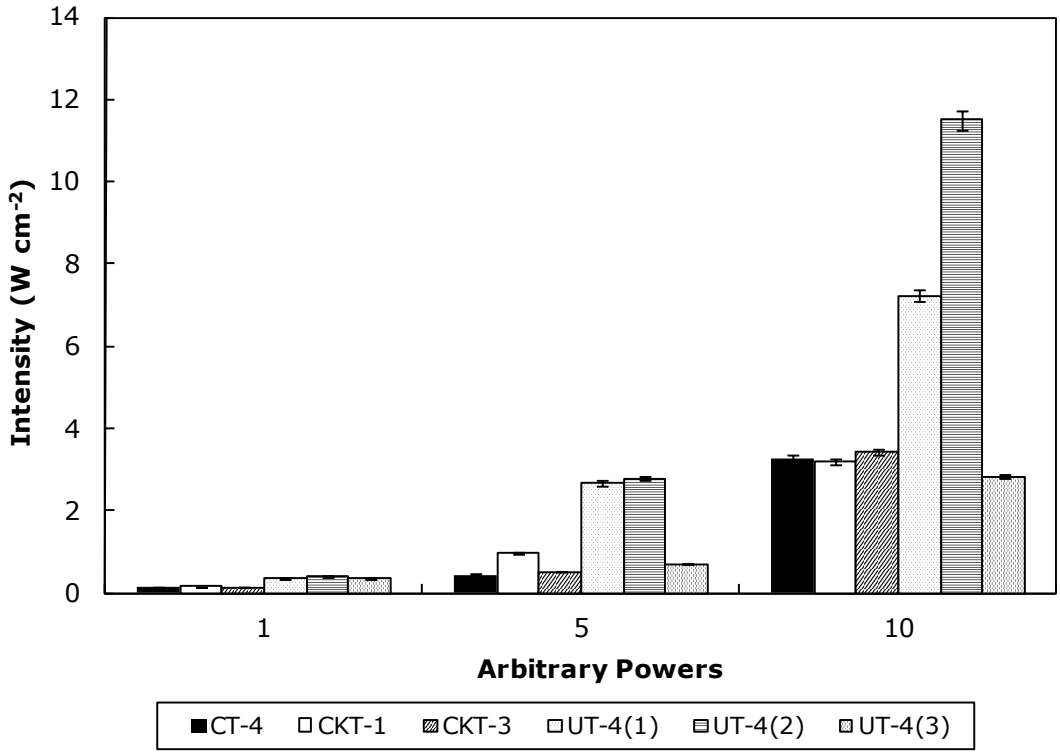

Figure 3.4: *Collated intensity given out for all endodontic tips at different arbitrary powers.*

The intensity profile for different endosonic tips shows that apart from UT-4(3), in general, UT-4 tips give out more intensity than the rest of the tips (Figure 3.4). The main reason for this being that UT-4 generally has a smaller surface area (Table 3.2), and that gives a smaller mass to the tip compared to the rest of the tips, which in turn give a smaller resistance to oscillations when force is applied to the tip. This agrees with Newton's second law of motion: where it was described that the net force of an object depends on the rate of change of its linear momentum in an inertial reference frame.

When the mass of an object increases, its inertia increases, resulting in lower kinetic energy towards the surrounding liquid. Hence, less energy is transferred into the liquid system, causing a lower intensity output for those tips.

However, it is still ambiguous to see why the total intensity and energy output of UT-4(3) differs so greatly from the other UT-4 files even though they have about the same surface area and material properties. This can only be explained as a possible manufacturing fault in the particular endosonic tip where it does not connect to the hand-piece properly.

On the other hand, the CT-4, CKT-1 and CKT-3 tips have similar intensities after dividing by the total surface area of each tips. This is most probably because of the similarities in the design of these tips. Whilst CT-4 differs from the CKT tips in terms of the angle of the tip, all other dimensions and the shape of the tip are quite similar to one another, which might be the reason why they have similar intensities.

This experiment enabled us to gain a better understanding of the actual energy output of each endosonic tip, giving a standard quantitative measurement for all of them, which will be very useful in comparing further results in terms of various experimental parameters.

3.2 Fricke Dosimetry

As mentioned in Section 2.3 earlier, there are several types of dosimetry for quantifying radical production of power ultrasonic systems. Among them, Fricke dosimetry appears to be one of the most straight forward dosimetries to perform as it can be measured directly on the UV-visible spectrometer.

Fricke dosimetry utilises the oxidation of Fe^{2+} to Fe^{3+} which is optically active and can be detected *via* UV-visible spectrometry at 304 nm. There are several ways of oxidising Fe^{2+} through sonication, as shown in the scheme below.

$$H_2O \xrightarrow{)))} H\bullet + \bullet OH$$

$$\bullet OH + Fe^{2+} + H^+ \rightarrow Fe^{3+} + H_2O$$

$$H_2O_2 + Fe^{2+} + H^+ \rightarrow Fe^{3+} + H_2O + \bullet OH$$

$$O_2 + H\bullet \rightarrow \bullet OOH$$

$$\bullet OOH + Fe^{2+} + H^+ \rightarrow Fe^{3+} + H_2O_2$$

Scheme 3.1

Different products formed from the radicals produced sonichemically are able to oxidise Fe^{2+}. This causes the measurement of Fe^{3+} to consist of a mixture of different source of oxidation species. Whilst this experiment is not able to give a good quantification of the amount of radicals produced, it still gives the oxidation characteristics of different ultrasonic instrument used, which will be particularly useful for the endosonic instruments as our main interest lies on the oxidising efficiencies of different endosonic instruments.

Fricke Dosimetry was performed on the 20 kHz ultrasonic probe at four different intensities obtained calorimetrically. Based on Figure 3.5, the formation of Fe^{3+} increased with ultrasonic intensity and sonication time. The initial reading of Fe^{3+} production is not very apparent upon 10 minutes of sonication but a noticeable increase after sonication for an hour can be observed. Based on the absorbance of Fe^{3+} obtained, the concentration of Fe^{3+} produced can be calculated, noting the molar extinction coefficient of Fe^{3+}, ε, as 2197 $dm^3\ mol^{-1}\ cm^{-1}$ (Iida *et al.*, 2005). The total production of Fe^{3+} turns out to be around 12×10^{-5} mol dm^{-3} at the highest intensity used, as tabulated in Table 3.3. The relationship between Fe^{3+} production and ultrasonic intensity is not linear (Figure 3.6, $R^2 = 0.94$), as suggested by the values obtained. This can be due to cavitation threshold at lower intensities of the ultrasonic probe, resulting in lower radical production at those intensities. As the intensity increased to 13.1 W cm^{-2}, the production of Fe^{3+} doubled compared with 9.72 W cm^{-2}, therefore it can be said the transient cavitation dominates the reaction, causing more radical production and oxidation to occur.

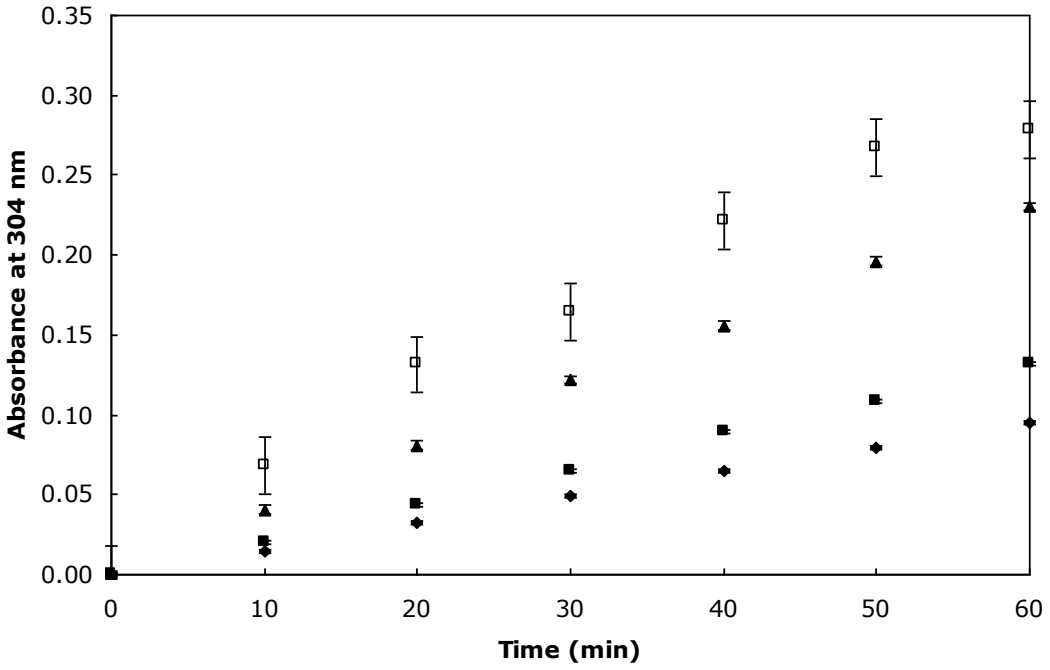

♦ 5.10 W cm^{-2} ■ 9.72 W cm^{-2} ▲ 13.1 W cm^{-2} □ 16.2 W cm^{-2}

Figure 3.5: *Absorbance at 304 nm of Fe^{3+} upon sonication with the 20 kHz ultrasonic probe for 60 minutes at different intensities.*

Table 3.3: *Absorbance of Fe^{3+} upon sonication for an hour and their corresponding concentrations at different ultrasonic intensities.*

Intensity (W cm^{-2})	**5.10**	**9.72**	**13.1**	**16.2**
Absorbance of Fe^{3+} at 304 nm	0.095	0.132	0.230	0.278
Concentration × 10^{-5} (mol dm^{-3})	4.34	5.99	10.5	12.7

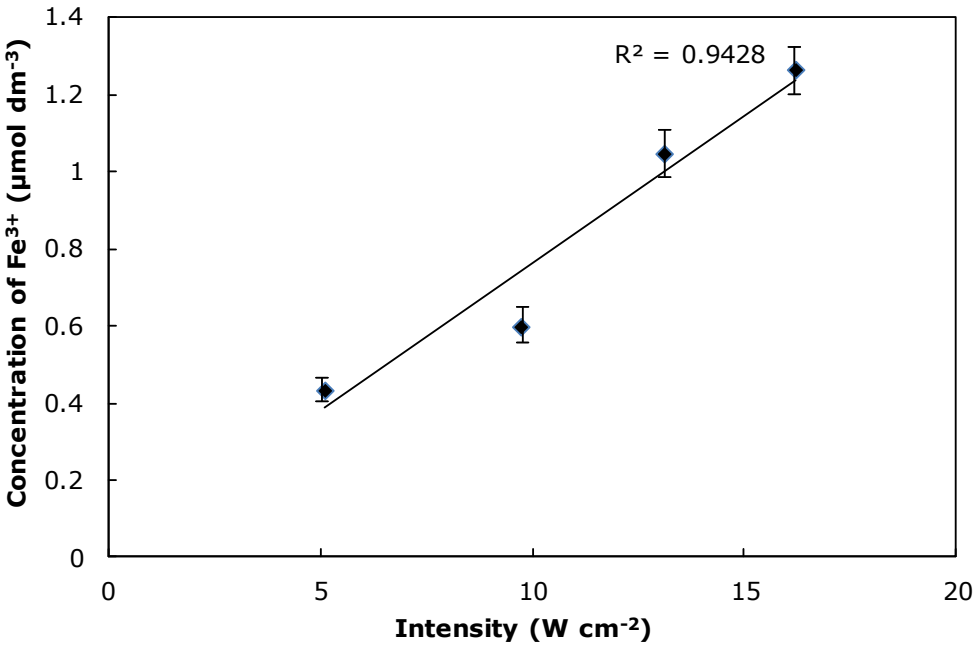

Figure 3.6: *Final concentration of Fe^{3+} upon sonication using the 20 kHz ultrasonic probe for 60 minutes at various intensities. (as tabulated in Table 3.3)*

Similarly, Fricke Dosimetry experiments were performed for all different dental tips to determine the amount of radicals production upon sonication with the tips at various intensities. Here, sonication was performed at three arbitrary power settings, similar to that in Section 3.1. Due to time constraints for the sonication of endosonic files, experiments were performed for five minutes in order to prevent overheating and to minimise hysteresis effect on the PZT hand piece.

An example of the absorbance of Fe^{3+} over the five minutes of sonication is shown in Figure 3.7. As expected, increasing the arbitrary power on the power dial resulted in more cavitation, producing more Fe^{3+} upon sonication.

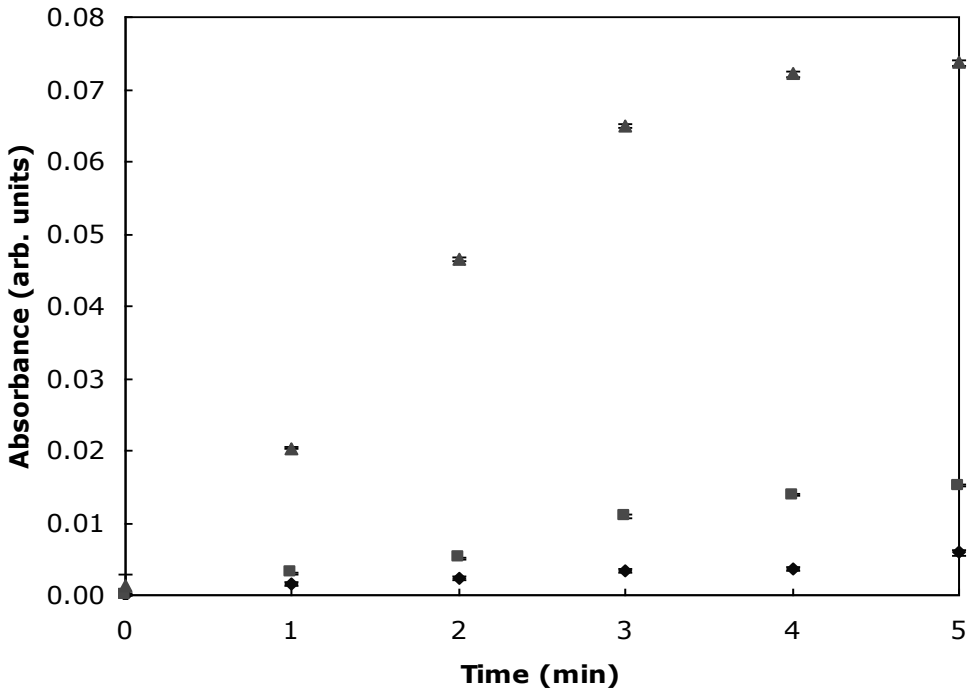

♦ Power 1 (0.15 W cm^{-2}), ■ Power 5 (0.45 W cm^{-2}), ▲ Power 10 (3.27 W cm^{-2})

Figure 3.7: *Absorbance of Fe^{3+} at 304 nm upon sonication of CT-4 for five minutes at different arbitrary powers. (Uncertainties obtained from triplicate of the experiment.)*

It has to be noted that the increase in arbitrary powers on the power dial is not linear, where Power 10 on the power dial appears to be much higher in actual power compared to the other powers, as shown in Table 3.2 in Section 3.1. Due to this, there is a more abrupt increase from Power 5 to Power 10. Figure 3.8 illustrates the relationship of the absorbance of Fe^{3+} at 304 nm after five minutes with the actual intensity obtained calorimetrically.

Similar experiments were performed for each different tip and the results were collated in Figure 3.9. Once again, there is a big variation in absorbance of Fe^{3+} for the different endosonic files, indicating that they all perform very differently, with the CT-4 and CKT tips generally producing more Fe^{3+} than the UT-4 tips. As the UT-4 tips are generally much thinner than the rest of the tips (Table 3.2), it is understandable that they are not very efficient in displacing the surrounding liquid in order to obtain a high enough negative pressure to produce cavitation, resulting in

low Fe^{3+} production. As for the comparison of CT-4 and the CKT tips, it is clear that they both have similar characteristics in terms of cavitation production at low and medium powers. This, however, is not the case at the highest arbitrary power (Power 10), where CT-4 overtook the CKT tips in its performance, showing the highest amount of Fe^{3+} production among all the tips, suggesting that it produces the most amount of cavitation.

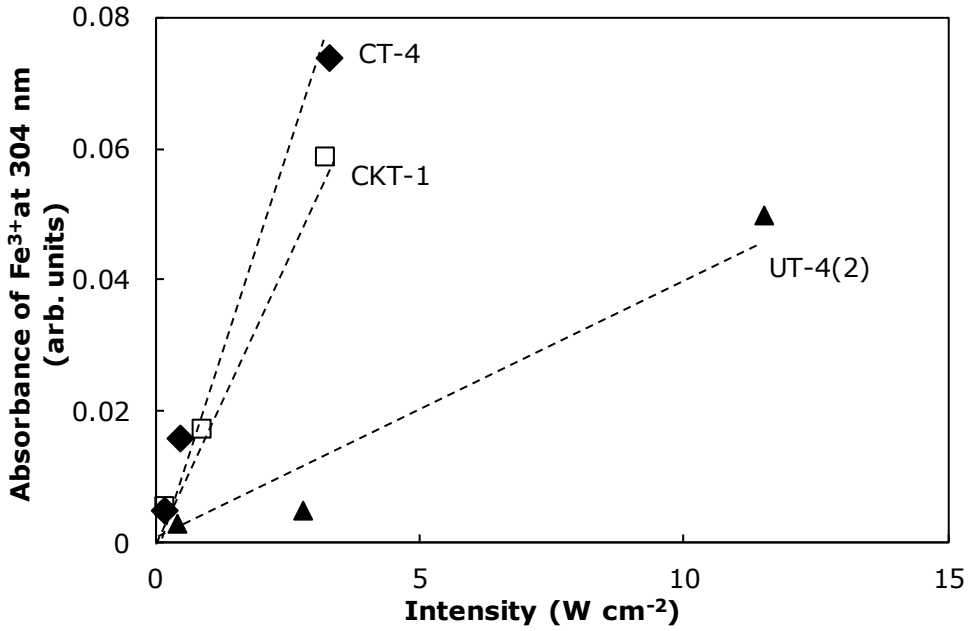

Figure 3.8: *An example of the absorbance of Fe^{3+} at 304 nm after sonication for 5 minutes for three selected endosonic files, at their respective intensities (equivalent to arbitrary 1, 5 and 10).*

With the results obtained in this section, it can be concluded that different tips performed very differently in terms of the ability to oxidise Fe^{2+} to Fe^{3+} in the presence of ultrasound. This brings the need to have a more thorough study of all the dental tips used in order to identify the cause of cavitation production so that further modification of the tips can be made for a better next generation endosonic files.

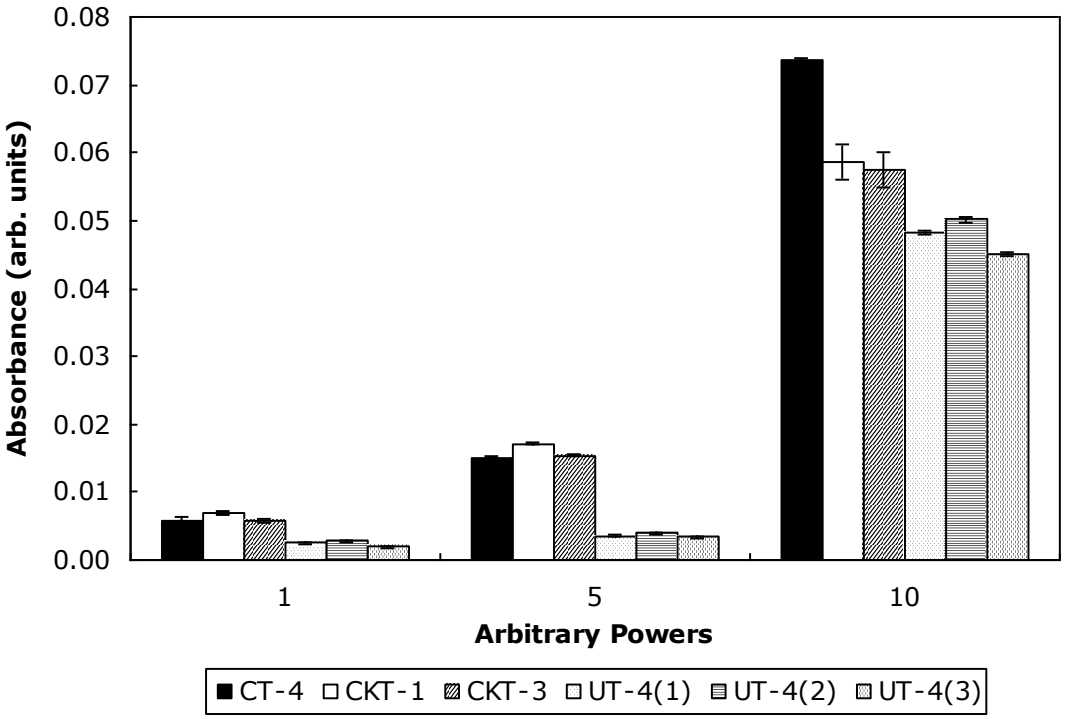

Figure 3.9: *Collated results of absorbance of Fe^{3+} at 304 nm upon sonicating for five minutes for all various endosonic files at low, medium and high arbitrary powers (Powers 1, 5 and 10).*

3.3 Sono(chemi)luminescence

Sono(chemi)luminescence (SCL) was used to detect radical production by measuring the intense blue light produced when luminol reacted with radicals generated by cavitation collapse. Photographs of the SCL produced were taken with a digital Single-lens-reflex (dSLR) camera over a certain exposure time upon sonication. This was performed in a light proof box, where the sonicated sample was kept with the ultrasonic source, and the camera was monitored remotely during the sonication. The results obtained were calculated in terms of light pixels produced in the photographs, after subtracting each image with a darkframe image (or a silent reaction photograph over the same exposure time).

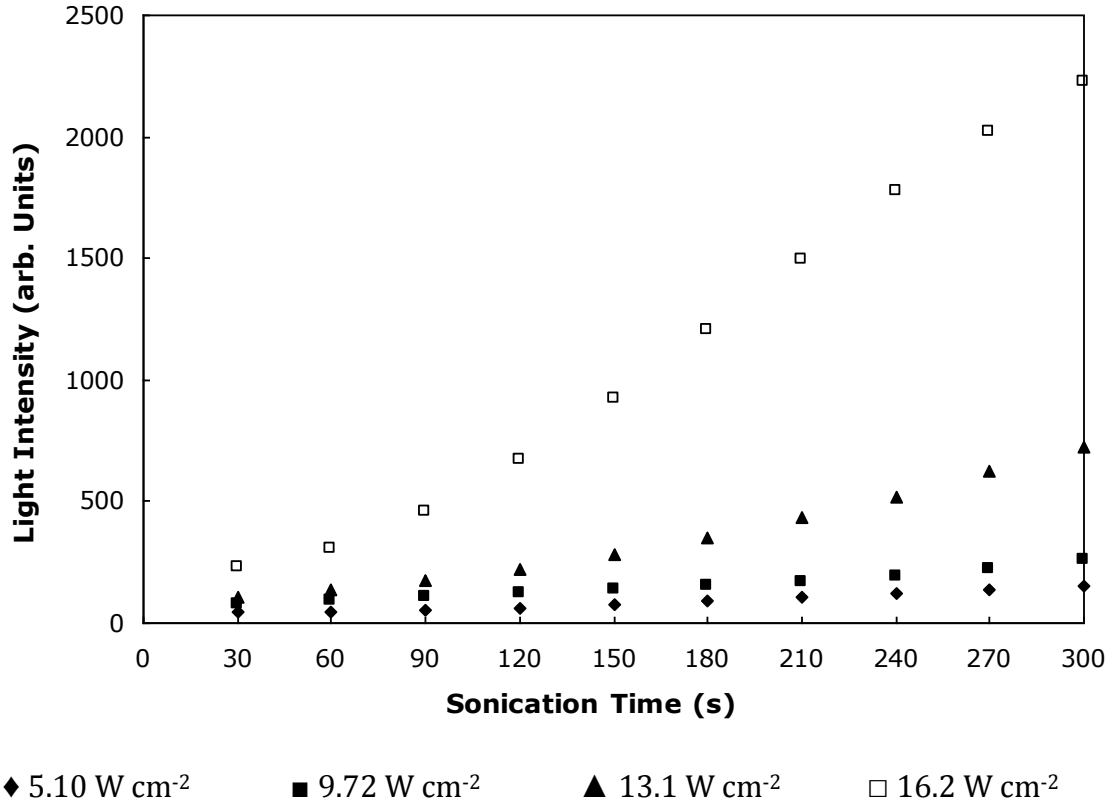

Figure 3.10: *Collated chemiluminescence intensity counts over five minutes of sonication time with the 20 kHz ultrasonic probe at different intensities.*

For the 20 kHz ultrasonic probe, sonication was performed for five minutes, taking readings every 30 seconds at four different intensities. Figure 3.10 shows the results of the mean light intensity obtained from the photographs, which picks up light intensities at each pixel point. From the results obtained, it can be seen that there is a general increase in sono(chemi)luminescence intensity as the ultrasonic intensity increases. A non-linear increase is obtained, with a gradual increase in light intensities at the two lower ultrasonic intensities followed by exponential increase at higher ultrasonic intensities, which again can be explained by the cavitation threshold at lower intensities causing lesser inertial cavitation to form at such intensities – supported by the results showed in Fricke Dosimetry in Section 3.2.

Sono(chemi)luminescence measurements were performed for each endosonic files at low, medium and high powers respectively over a sonication time of five minutes. The results obtained from the images were processed using an image

analysing software, ImageJ (Abramoff *et al.*, 2004). A dark-frame image was taken each time in order to subtract background thermal noise from the images. This was done by taking a photograph in the exact same conditions as the sonoluminescence image, in the absence of ultrasound. From there, the dark-frame image was subtracted from the sonoluminescence image to obtain a true value of sonoluminescence for analysis. For all images, a known dimension of region of interest (ROI) was selected. This is obtained from the region at 3mm below the end of the tip, and spread to 5mm on either side in front and behind the tip, as shown in Figure 3.11.

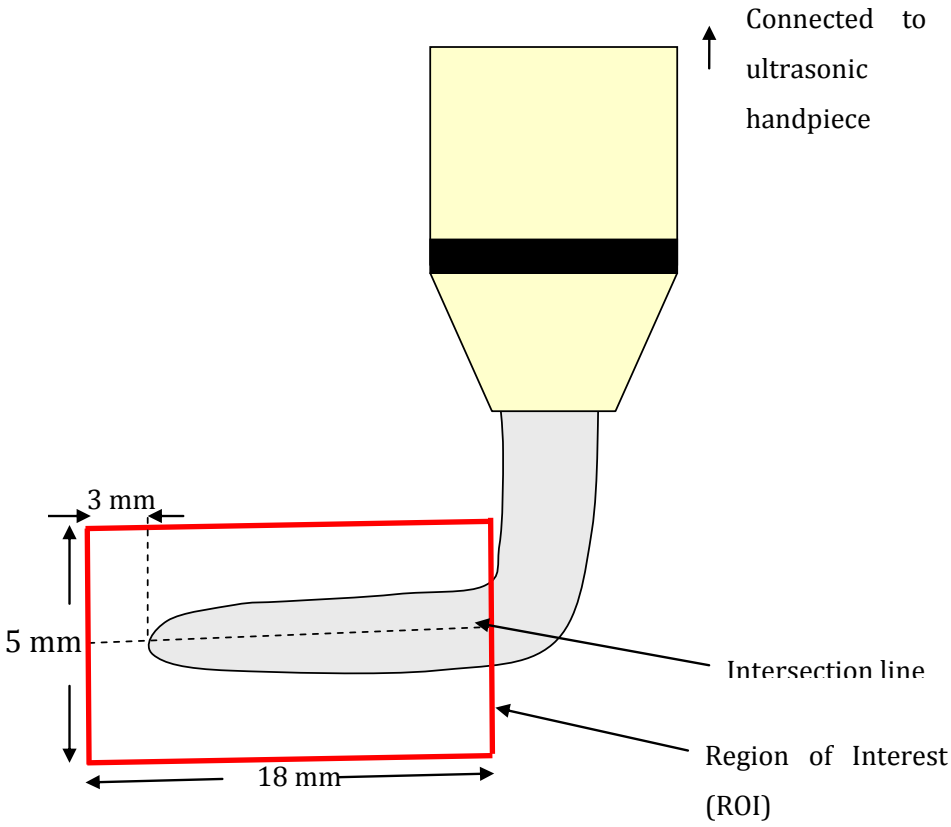

Figure 3.11: *Dimensions of the region of interest (ROI) with respect to an endosonic file.*

Upon setting up the ROI, an average light intensity is calculated in terms of 'grey pixels' by ImageJ. This was done by converting each colour pixel throughout the

entire ROI into a 'grey pixel'[9]. ImageJ then generated a mean 'pixel value' for the entire region of interest based on the formula stated above. The mean 'pixel value' calculated will then serve as an arbitrary indicator of the light intensity given out by the dental tip, which corresponds to the amount of radicals formed during sonication.

Figure 3.12 shows the collated results of the average light intensity given out over the entire ROI. In general, CT-4, CKT-1 and CKT-3 produce more sono(chemi)luminescence than the UT-4 tips at each power setting. This might be due to the lack of surface area of the UT-4 tips, having approximately half the surface area of CT-4, CKT-1 and CKT-3 tips. CKT-3 appeared to have the most sono(chemi)luminescence produced at Power 5 but remained about the same at Power 10. Whilst the reason behind this remains ambiguous, it shows that it can achieve its maximum sono(chemi)luminescence and/or cavitation at a lower power, and is also at a comparable state with CT-4 at the highest power (Power 10). Referring back to Figure 3.4 on the intensities of the endosonic files, it can be seen that the intensities produced by the endosonic files do not directly correlate to the amount of sono(chemi)luminescence produced, suggesting that other factors are also at play.

Though there is a slight variation in the mean light intensity produced for all UT-4 tips at each powers settings assessed, the analysis of variance (ANOVA) showed that there is no significant difference of the light intensity produced for the three tips at 95 % confidence level (ANOVA, p-value > 0.05).

[9] Grey pixel = 0.299R + 0.587G + 0.114B; where RGB values were obtained from the images taken (Abramoff *et al.*, 2004)

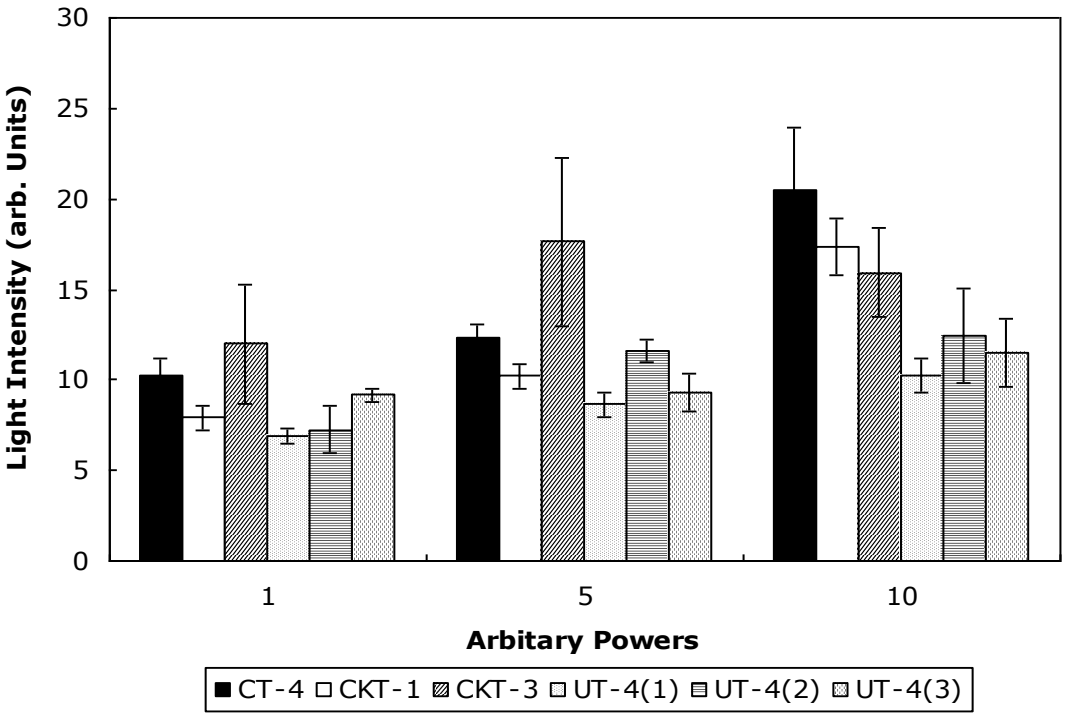

Figure 3.12: *Collated mean light intensities obtained upon five minutes sonication at various arbitrary powers for all dental tips used.*

Figure 3.13(b) shows an image of a tip producing sono(chemi)luminescence upon capturing the light photons emitted by the sonicating dental tip for five minutes at Power 10/10. The image shows that areas where cavitation occurs are localised at certain areas, with most cavitation occurring at the bend of the dental tip, which is highly due to the change of wave direction when travelling down to the tip from the ultrasonic hand piece. In order to have a better illustration on cavitation occurring at various parts of the dental tip, a detailed analysis was carried out on three different tips: CT-4, CKT-1 and UT-4.

Analyses of these three tips were done based on the same ROI as illustrated in the inset image of Figure 3.14. The red boxes below indicate the region of interest in the images, where data were taken for analysis. The distance along the ROI was calibrated based on the actual length of the tip, which was 15 mm throughout the working length of the tip. A plot of light intensity across the entire ROI was then obtained from ImageJ, as illustrated in Figure 3.14. From there, three peaks were

separated out for analysis, where peak 1 ranges from 0 – 4 mm; peak 2 from 4 – 12 mm and peak 3 which is > 12 mm, depending on the tip. The total intensity produced at each area was then obtained by integrating the area under each peak with the aid of MATLAB, in order to give a better comparison of the light intensity at different areas along the dental tips.

(a) (b)

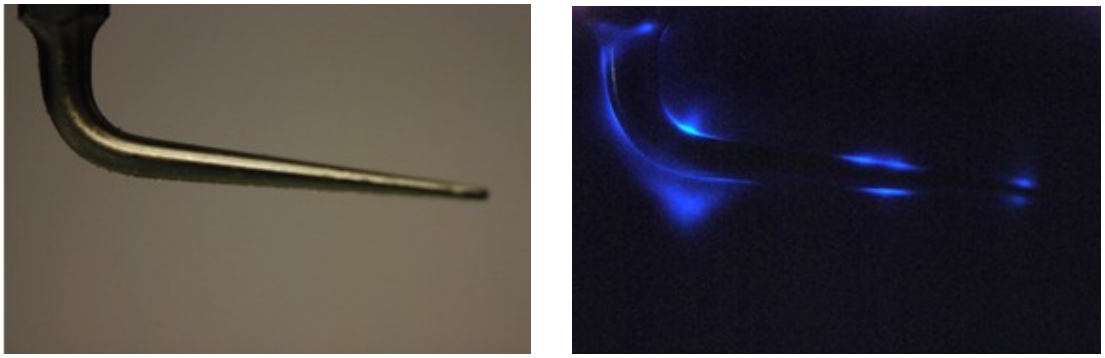

Figure 3.13: *(a) photograph taken in light of a dental tip immersed in luminol; (b) the same tip upon long camera exposure in a light-proof box upon sonication in luminol.*

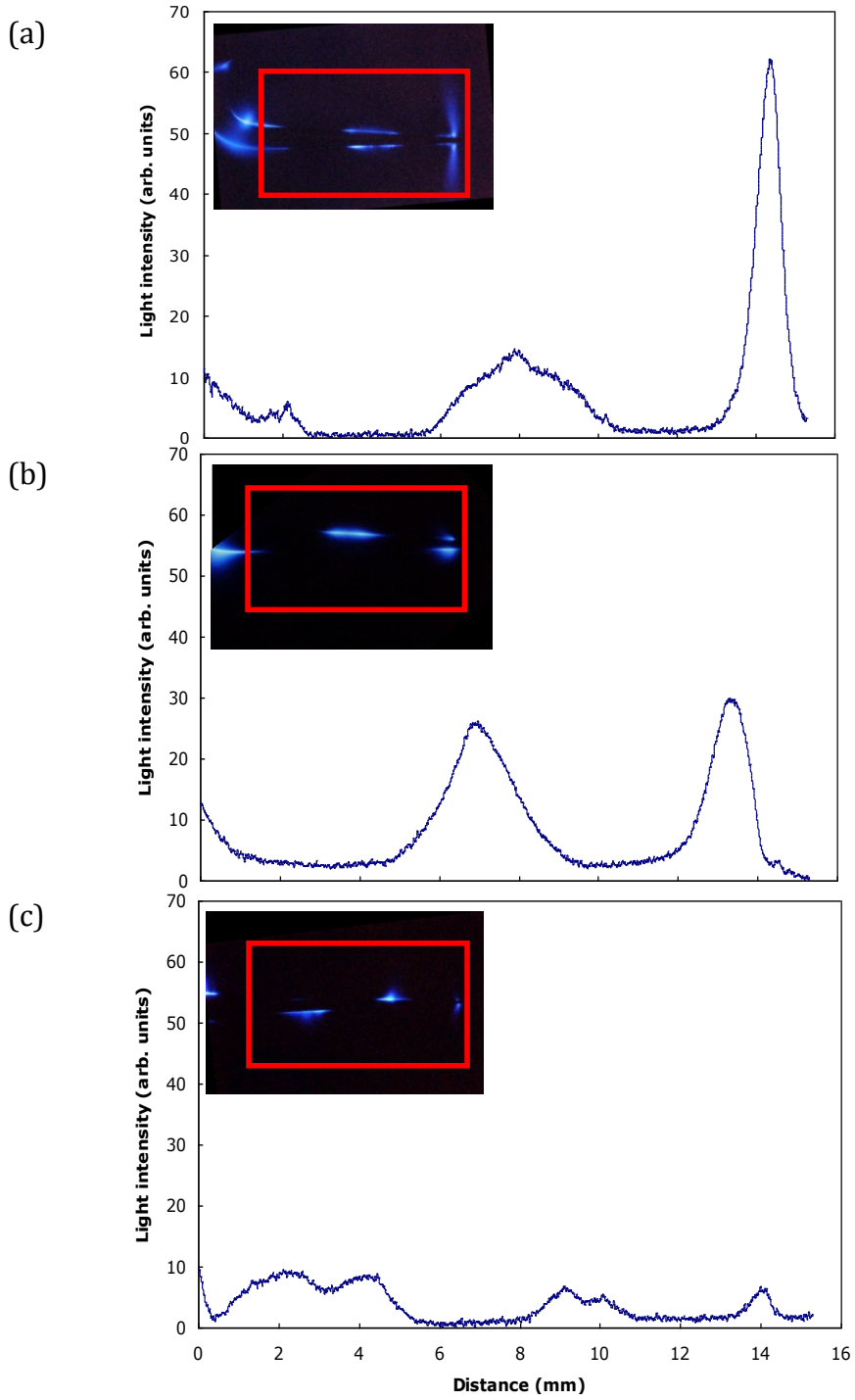

Figure 3.14: *The total light intensity produced across the working length of the tip; (inset) A sono(chemi)luminescence image of CT-4 together with its region of interest (shown with the red box) used for analysis: (a) CT-4; (b) CKT-1; (c) UT-4(2).*

Similar analyses were performed for CKT-1 and UT-4, which show very different distributions of light intensity for each tip, as illustrated in Figure 3.14(b) and 3.14(c). Integration of the area under each peak was performed to obtain a

breakdown quantity of light intensities produced at different areas of the dental tip, as shown in Figure 3.15.

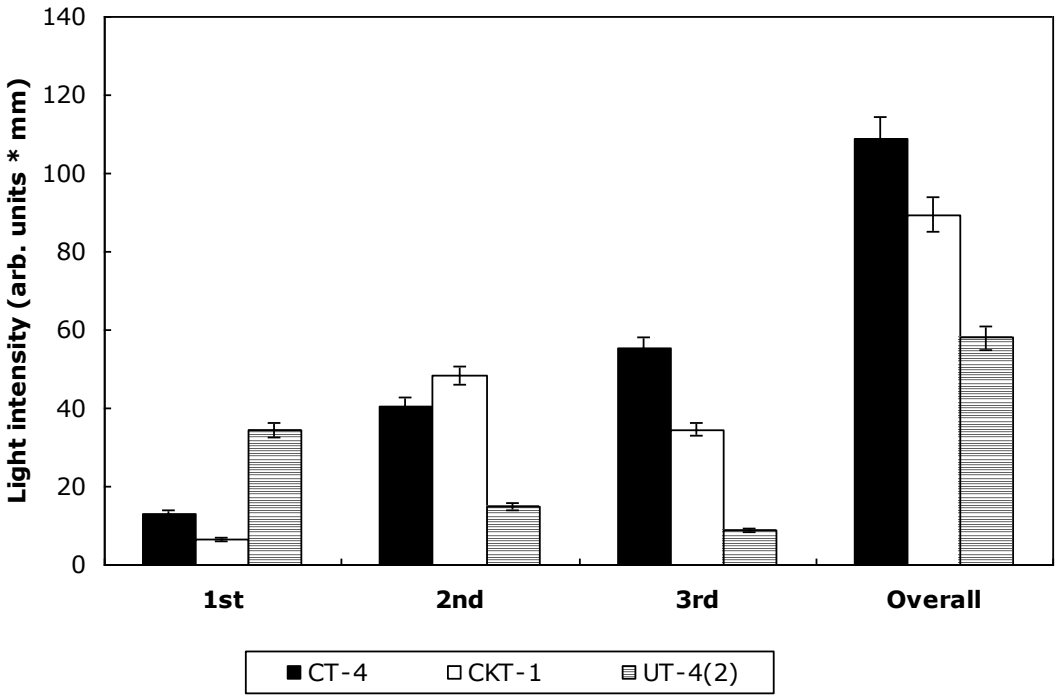

Figure 3.15: *A break-down of total light intensity emitted by different dental tips at different areas, noted as 1st, 2nd and 3rd peak respectively.*

Based on Figure 3.14, it can be seen that CT-4 gives out the highest light intensity, especially towards the end of the tip. However, this trend is not consistent with UT-4(2), where the highest amount of light is given out near the bend of the tip, and gradually decreases as it goes down along the dental tip. On the other hand, CKT-1 showed a maximum light emission at the middle of the tip, and appeared to give out the highest amount of SCL at that area compared with the two other tips. Though it is not possible to draw any conclusion on the performances of these different dental tips, it can be said that the nature of CT-4 tip is the most favourable dental tip, as it not only gives out the most SCL, but also the distribution of SCL produced is such that it produced large amounts of cavitation at the end of the tip, which is deduced to aid in cleaning processes.

Table 3.4: *Calculated results of light intensity produced at Power 10/10 per unit area of each dental tip.*

Tips	**CT-4**	**CKT-1**	**CKT-3**	**UT-4(1)**	**UT-4(2)**	**UT-4(3)**
Surface area (cm^2)	0.474	0.44	0.497	0.2	0.182	0.197
Light intensity (a.u.)	20.44	17.32	15.91	10.27	12.41	11.52
Intensity per area (cm^{-2})	43.13	39.37	32.01	51.39	68.20	58.51

As the results above showed that different dental tips give out very different amounts of SCL, and this can be due to their difference in design. Another way of analysing the performances of the tips was to obtain the amount of light intensity produced by each dental tip based on their surface areas. The calculated 'average light intensity per unit area of dental tip' is collated in Table 3.4. This was done in order to have a better comparison in light intensity – which corresponds to radicals produced in the sonicating systems, for the different dental tips. Care must be taken that the amount of SCL produced is not solely based on the surface area of the dental tips. It can only be suggested that dental tips with relatively higher surface area, such as CT-4, CKT-1 and CKT-3, stand a higher chance of displacing the liquid around them hence achieving a higher negative pressure around them, which is crucial for the formation of cavitation, which will be explained further in Chapter 6.

Upon dividing the light intensity into the surface area of each dental tip, the UT-4 tips appear to be producing more cavitation per unit area, calculated based on the light intensity produced. Whilst this illustration is not able to draw any conclusion, it does indicate that the surface area plays a role in producing cavitation, as oscillatory movements will be affected by the dimensions of the dental tips, which will be discussed later in Section 3.4.

From the results obtained in this section, we can conclude that the amount of sono(chemi)luminescence produced by each endosonic file is very different from one

another, with CT-4, CKT-1 and CKT-3 tips producing more SL compared to the UT-4 tips. This might be attributed to the shape and the surface area of the tips, affecting the ability to produce sufficient negative pressure at the areas around the dental tips, to allow cavitation. Also, the luminol photography taken shows that areas of cavitation are localised at various areas along the tip, suggesting that there might be areas of acoustic pressure antinodes. Further characterisation is needed to support the conclusion in this section, which will be discussed later in Section 3.5 and in Chapter 6.

3.4 Cavimeter

Cavitation counts were performed with a cavimeter developed by the National Physical Laboratory (NPL). The device detects the direct field, which, in this case would be the 30 kHz signal produced from the transducer; the sub-harmonic signal at one-half and one-quarter of the fundamental frequency; and the total amount of cavitation produced by the system (Felver *et al.*, 2009) in terms of arbitrary numbers displayed on the cavimeter generator (as shown in Figure 2.7).

In this experiment, three different dental tips (CT-4, CKT-1 and UT-4) were chosen for evaluation at Powers 1 to 5 and Power 10 due to their distinct differences in shape; and the results were correlated with the SCL results obtained from the previous section. Figure 3.16 shows the collated cavitation counts obtained for the CKT-1, CT-4 and UT-4 tips at different power settings. The results showed that CT-4 produced much more cavitation than the other two at lower power settings, with a cavitation threshold at approximately Power 3. Upon increasing the intensity to Power 10, UT-4 appeared to have more cavitation than CT-4 and CKT-1. This, however, was not what was obtained from the luminol photography shown in Section 3.3, where UT-4 produced only very little cavitation – resulting in low luminol emission. This brings the need for further evaluation of the results obtained from the cavimeter to have a better understanding in the cavitation regime.

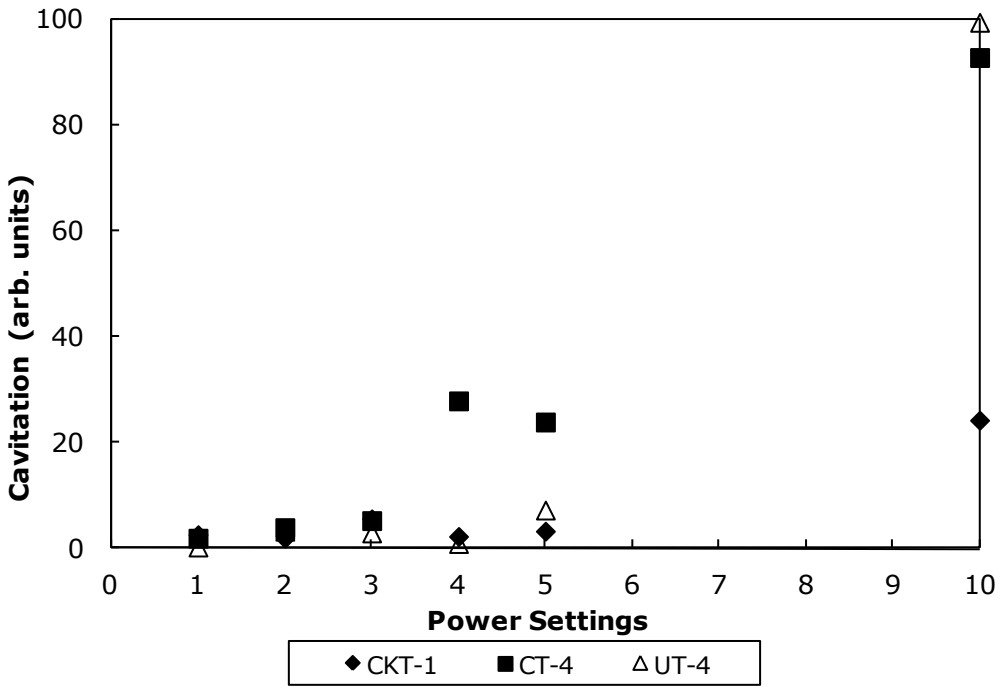

Figure 3.16: *Cavitation counts for the CKT-1, CT-4 and UT-4 tips at various power settings.*

Frohly *et al*. (2000) have previously explained that the presence of sub-harmonic signals arises due to cavitation of bubbles double the size of the resonance bubble size. They further explained that this result is an indication of stable cavitation. However, this was then further argued by (Ashokkumar *et al*., 2007) that the presence of sub-harmonic signals might also give rise to some transient cavitation. Based on this, the sub-harmonics and the cavitation counts obtained for the three tips studied were assessed.

Figure 3.17 shows the sub-harmonic and the cavitation signal for CKT-1 at the power settings studied. Though there is no clear correlation between the sub-harmonic and the cavitation counts, it can be seen that the sub-harmonic signals were high at lower power settings, and reduced slightly when the cavitation count increased. A better illustration of the scenario can be seen for CT-4, shown in Figure 3.18, where the sub-harmonic signal is significantly lower at the highest power setting, even when the cavitation counts were highest. This suggests that the cavitation counts produced when there is a significantly high sub-harmonic signal was due to the presence of stable cavitation.

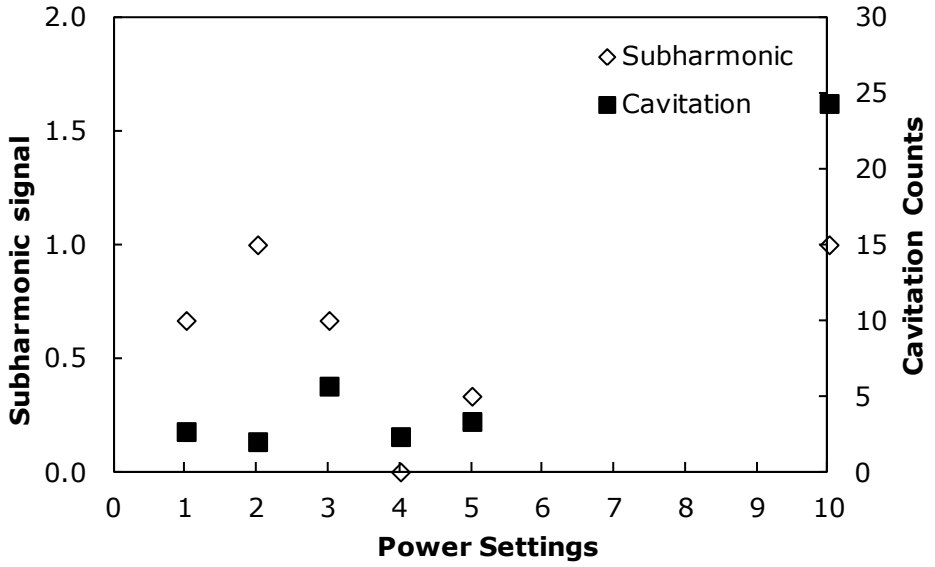

Figure 3.17: *Sub-harmonic signal and cavitation counts obtained from cavimeter at various power settings for CKT-1. All axes were plotted with arbitrary units.*

This phenomenon is even more prominent in UT-4 (Figure 3.19) where the sub-harmonic signal was constantly high compared to the other tips, resulting in a 'false' cavitation count at the highest power setting suggesting that high cavitation counts are in actual fact made up of mostly stable cavitation – which was not visible in the luminol photography shown in the previous section.

The cavitation signal indicates the total amount of cavitation produced (both stable and transient) from the dental tips, resulting in a poor correlation between the cavitation counts and the light emission results from SCL, shown in the previous section (Section 3.3). However, when the sub-harmonic signals were taken into consideration, a better classification of the types of cavitation present in the system can be seen, and with that information, a better correlation can be obtained.

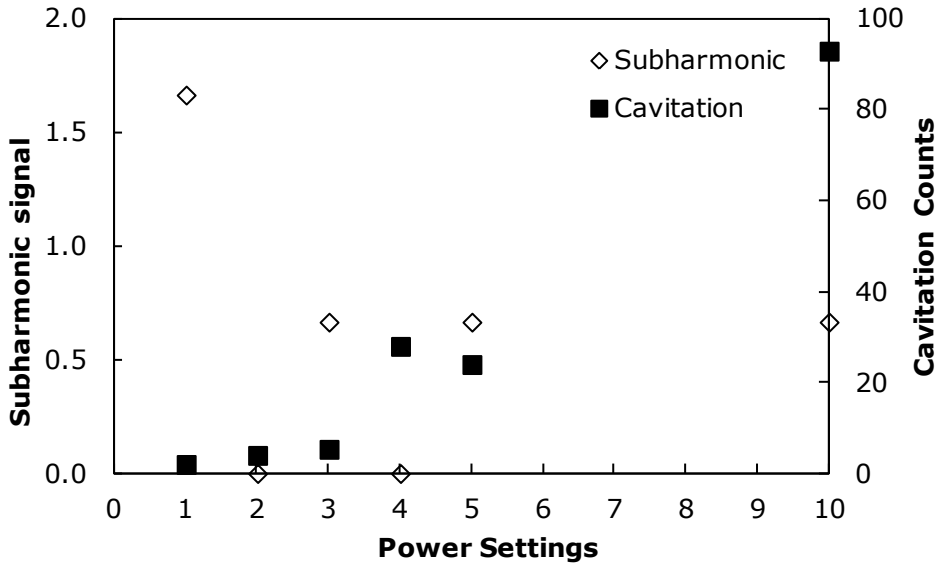

Figure 3.18: *Sub-harmonic signal and cavitation counts obtained from cavimeter at various power settings for CT-4. All axes were plotted with arbitrary units.*

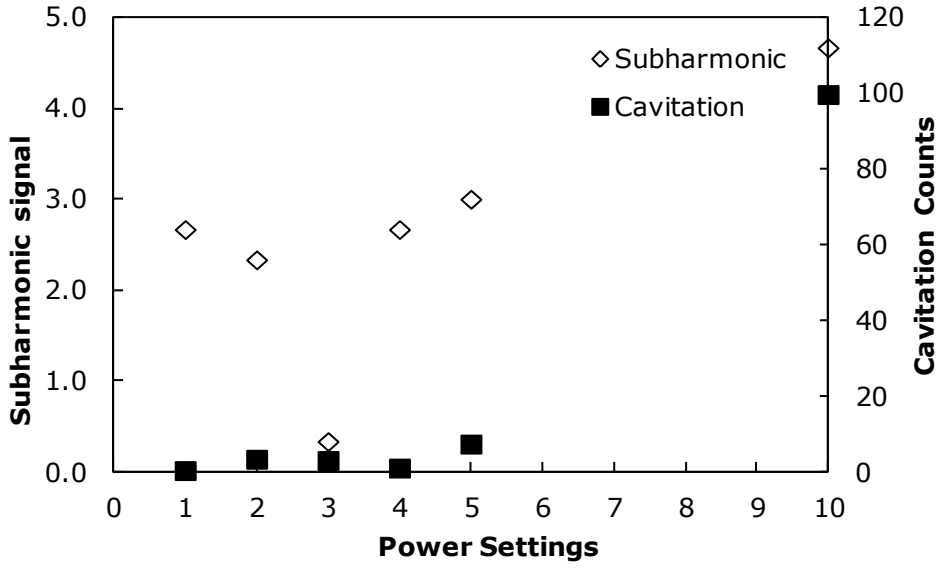

Figure 3.19: *Sub-harmonic signal and cavitation counts obtained from cavimeter at various power settings for UT-4. All axes were plotted with arbitrary units.*

For example, by comparing signals at Power 10 for all the three dental tips, when both the cavitation and sub-harmonic signals were at the maximum, the total SCL produced is low. On the other hand, when cavitation count is high and the sub-harmonic signal is low, the total SCL produced will be higher (Figure 3.20). This

indicates the relationship between the production of transient and stable cavitation in the system – hence shows the importance of the relationship between both parameters when interpreting the reading shown on the cavimeter.

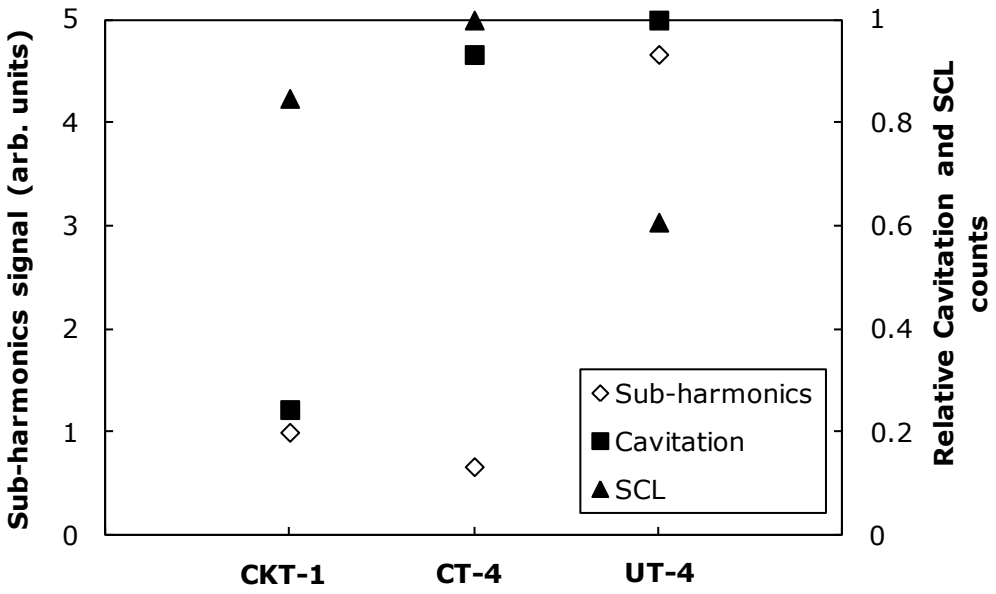

Figure 3.20: *Relative signal of the sub-harmonic, cavitation and SCL produced by the three different tips (CKT-1, CT-4 and UT-4) at Power 10.*

3.5 Scanning Laser Vibrometry

Scanning Laser Vibrometry (SLV) was performed in three different conditions:-

i) In air;

ii) In water (50 cm^3 of distilled water);

iii) In a silicone rubber channel of 3 mm, 4 mm or 5 mm width – which will be discussed in Chapter 5.

Figure 3.21 shows a typical displacement profile produced by the Scanning Laser Vibrometry (SLV) for a dental tip at various power settings, both in air and water. The dental file shows maximum displacement points at the end of the tips, with a second highest displacement (in terms of magnitude), in the middle of the tip, at approximately 7 mm along the file. The pattern of the vibration displacement profile for a particular dental tip is the same for each power settings used and it is independent of the medium it is in (air or water). The change in power settings and travelling medium will only change the magnitude of the vibration displacements, and is valid for all the other dental tips used for this study.

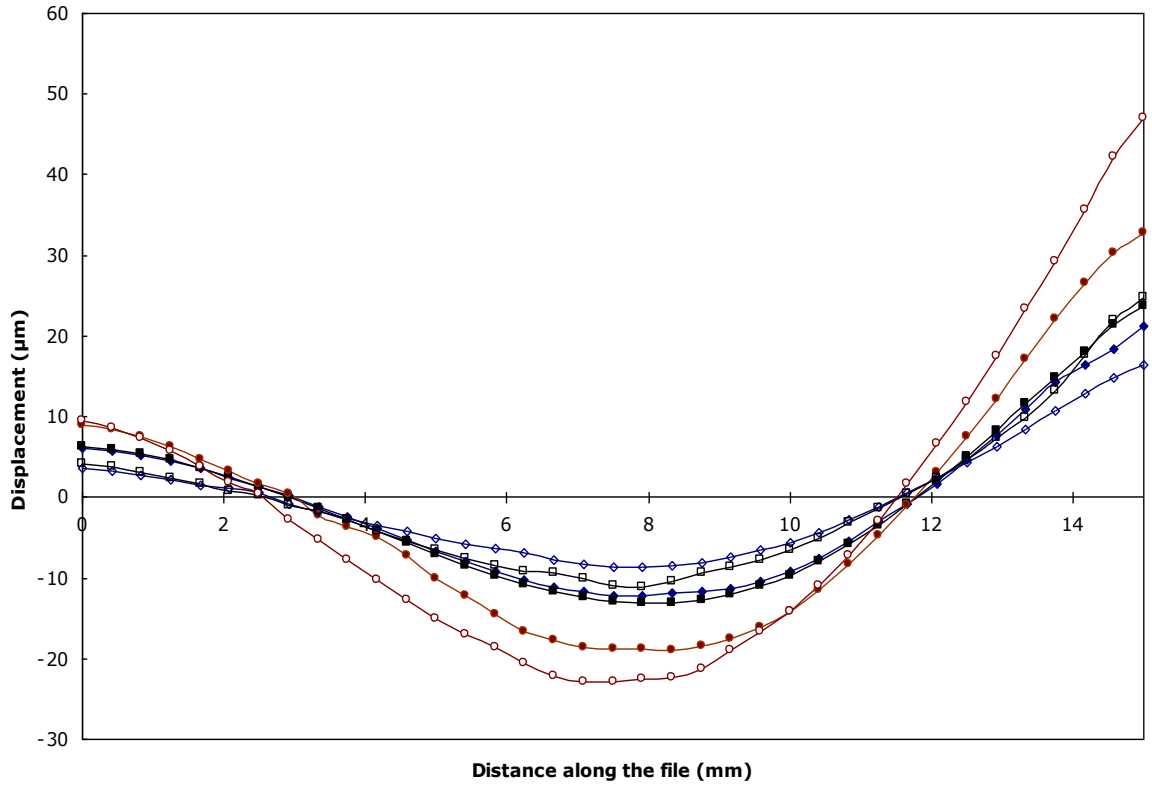

♦,◊ Power 1/10 ■,□ Power 5/10 ●,○ Power 10/10

Closed symbols (♦,■,●): in water Opened symbols (◊,□,○): in air

Figure 3.21: *Displacement profile along a dental tip in air and water, at Powers 1, 5 and 10 respectively for UT-4(2).*

A comparison of the maximum vibration displacements for each dental tip in both air and water was performed (Figure 3.22). It can be seen that apart from UT-4(1), there is a 30 % decrease in maximum displacement of the tip upon oscillating in water. All the tips showed a significant difference (ANOVA, p-value < 0.05) between the air and water oscillatory profile, apart from UT-4(1). It has to be noted that the formation of cavitation bubbles during the SLV measurements taken in water will obstruct the laser beam from taking a precise reading of the vibration frequency of the dental tips, and this might be a contributing factor to the discrepancy in UT-4(1) from the rest of the UT-4 tips. In order to have an unbiased comparison on the vibration displacements among the endosonic files, further analyses on the SLV results from hereon will be based on the vibration movements in air.

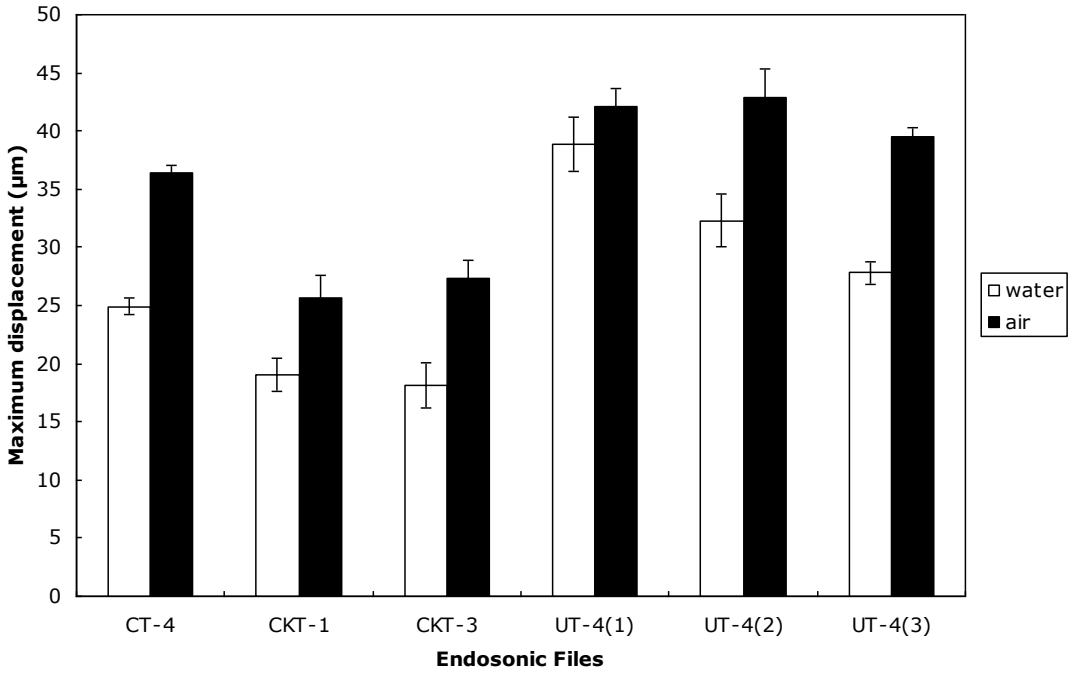

Figure 3.22: *Collated maximum displacement of all different endosonic files at Power 10/10.*

Vibration displacement profile of the dental tips are plotted on the positive axis to give a better illustration on the displacement magnitudes. Figure 3.23 shows the vibration displacement profile varies among the three endosonic files chosen. The CT-4 and CKT-1 tips give similar vibration profile patterns, showing two vibration

antinodes at approximately 3 mm and 12 mm along the working length of the files. On the contrary, the UT-4(2) tip showed the vibration antinodes at approximately 6.5 mm and 12.5 mm along the working length of the tip.

Referring to the shapes of the dental endosonic files used (Figure 2.2), it can be seen that the CT-4 and CKT-1 tips have similar file thicknesses along their working lengths – *i.e.* almost similar surface areas (Table 3.2), whereas the UT-4(2) is much thinner. Ultrasonic energy is delivered through vibration movements of the stainless steel molecules in the dental files, resulting in standing wave-like vibration profiles. The differences in vibration profiles between the CT-4 / CKT-1 and the UT-4 tips can be explained using an analogy of a vibrating string to produce sound waves – where the frequency of the sound wave produced by a string is inversely proportional to the linear density[10] of the string. Comparing two strings of the same length and material, where the diameter of string number two is double of that of string number one; string number one will produce higher sound frequency than string number two as it is 'lighter' (*i.e*. lower linear density). Similarly, the UT-4 tips, which are thinner than the CT-4 and CKT-1 tips, will produce higher sound frequency – hence producing shorter vibration wavelengths. On the other hand, as the CT-4 and CKT-1 tips have similar diameters, the sound frequency produced by these two dental files will be very similar, resulting in similar vibration displacement profile patterns.

Transient acoustic cavitation is formed during the negative acoustic pressure cycle, when cavitation threshold is achieved (Figure 1.5). As explained earlier, the sound energy is delivered through vibration movements of the molecules in the dental files. This means that the vibration profiles of the dental files have a close correlation to the acoustic pressure produced in the conducting medium (air or water), which in turn affects the production of transient cavitation.

[10] Mass per unit length.

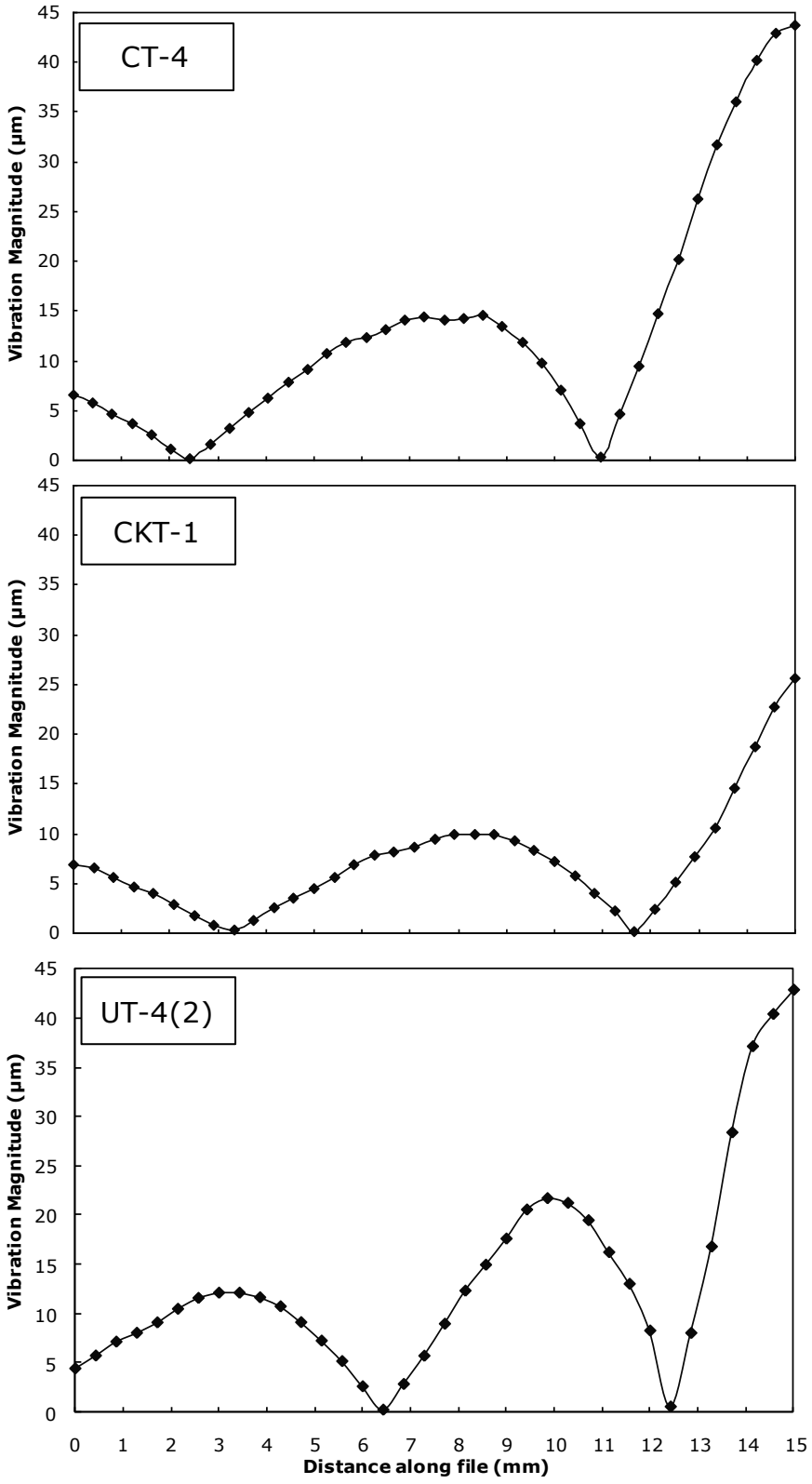

Figure 3.23: *Vibration magnitude along the working length of the endosonic files at Power 10.*

By combining the results obtained for the sono(chemi)luminescence (Section 3.3) and the vibration displacement profiles of the dental tips at the same settings, based on Figure 3.24, it can be seen that the areas of cavitation always occur at the vibration antinodes along the tips. The increase of power only increases the magnitude of the vibration movements and the intensity of luminol emission at those specific areas, as illustrated in Figure 3.25.

Though higher vibration magnitudes contribute to more cavitation, as the ability to displace the surrounding liquid is much higher, the size of each dental tips also have to be taken into consideration. Thicker files (with a larger surface area) were able to displace more liquid at a same displacement magnitude compared to a thinner file. This will then result in higher counts of cavitation produced for thicker tips compared to the thinner tips of the same length. This explains why the UT-4 tips, which have higher average displacement, did not seem to produce much sono(chemi)luminescence.

Figure 3.26 shows the collated maximum displacement produced by different dental tips at various intensities. It can be concluded that, in general, UT-4 produces the most displacement amplitude, followed by CT-4, CKT-1 and CKT-3. It can be seen that of the UT-4 tips, UT-4(3) appeared to produce smaller vibrations, even though they have similar designs. Though it can be said that up till this point, the factor contributing to this result remains ambiguous, the results shown in Figure 3.26 seem to tally with the calorimetry results obtained in Section 3.1 (in Figure 3.4).

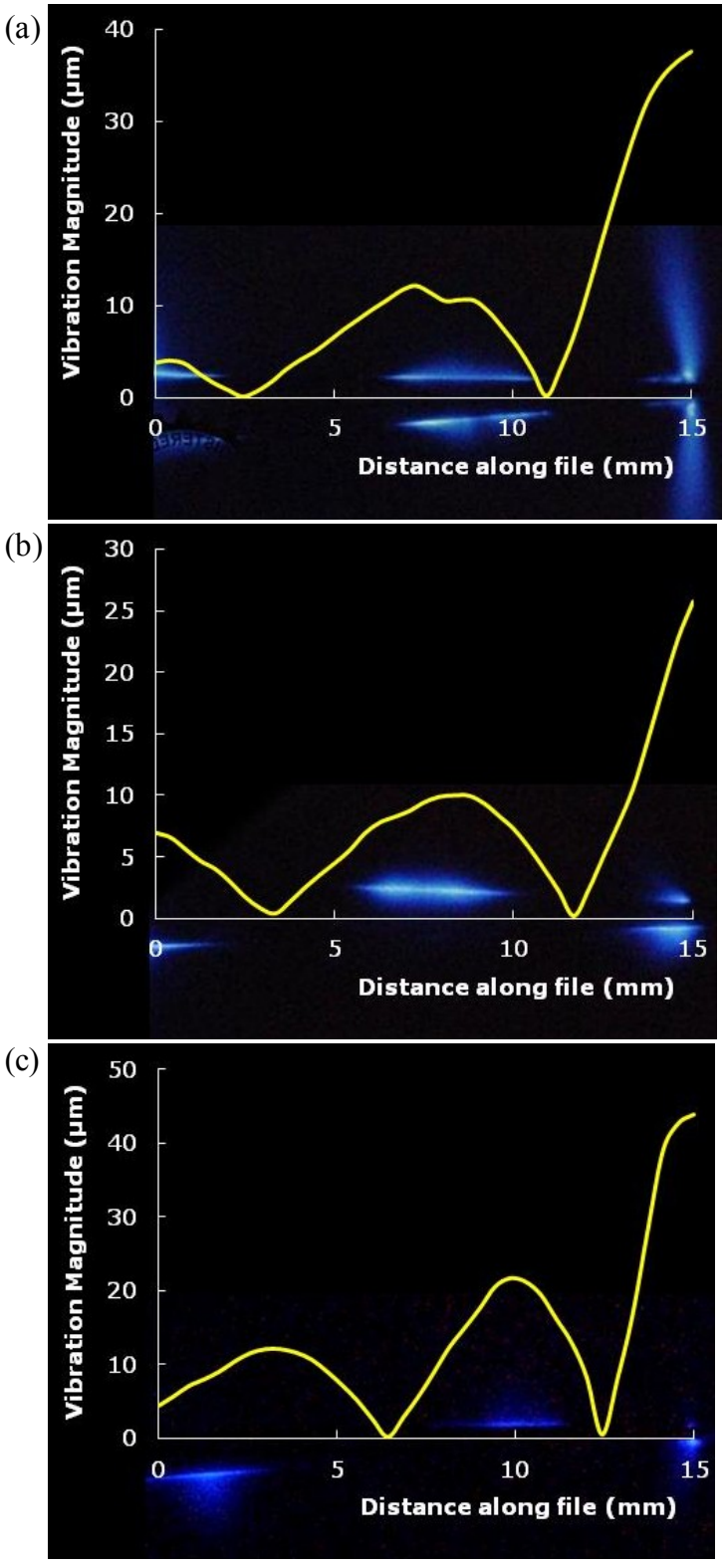

Figure 3.24: *Superimposed luminol photographs of (a) CT-4; (b) CKT-1 and (c) UT-4(2) and their vibration magnitudes at Power 10/10 in air.*

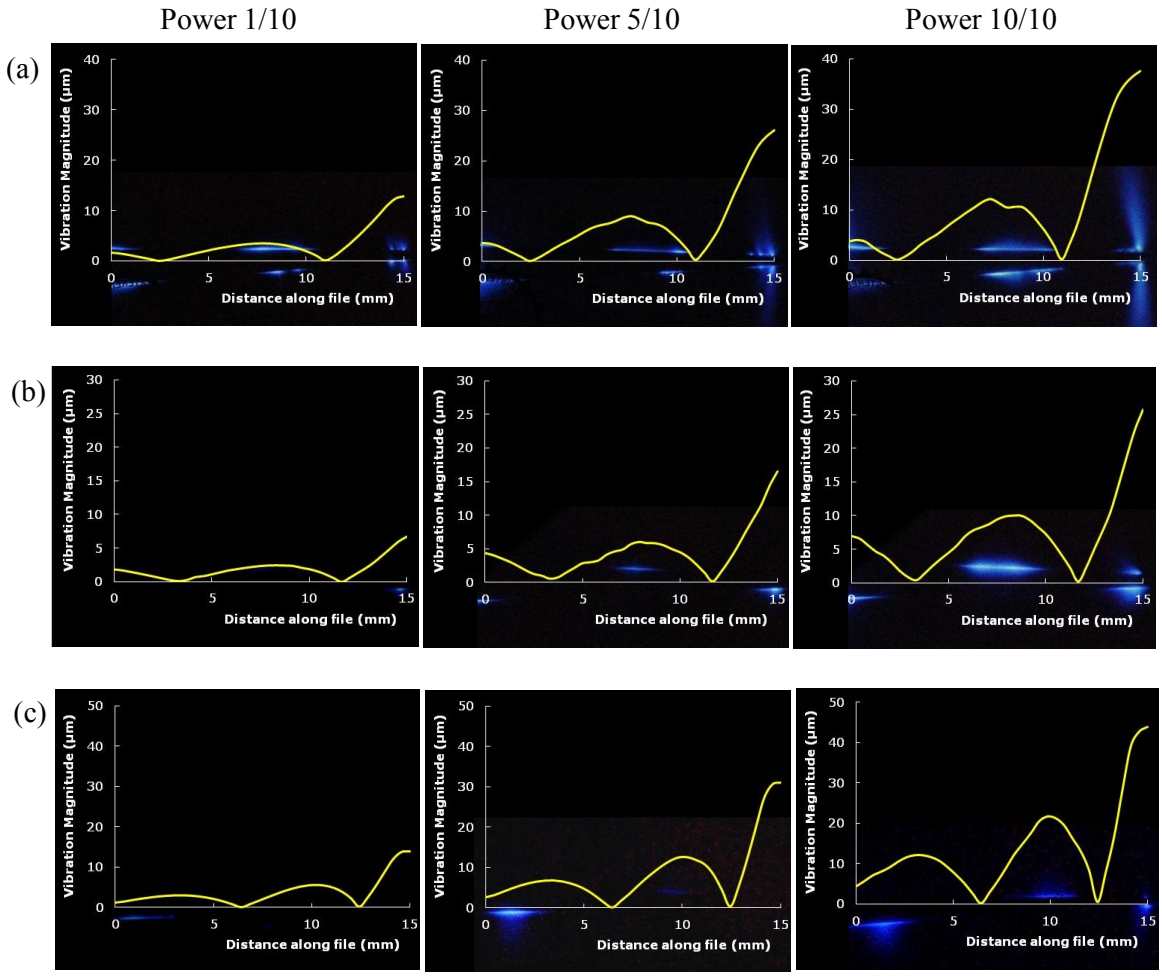

Figure 3.25: *Superimposed luminol photographs of (a) CT-4; (b) CKT-1 and (c) UT-4(2) and their vibration magnitudes at Power 1, 5 and 10 in air.*

The results for the vibration movements of the tips correlate with the energy output of the tips, obtained calorimetrically in Section 3.1. This proves that energy transfer to the tip plays an important role in producing high vibration displacement as proven by the law of conservation of energy. However, there are also other factors that contribute to the vibration movements, such as the contact angle of the dental tip to the handpiece. For example, in Section 3.1, Figure 3.5, CKT-1 seemed to have slightly higher intensity compared to CT-4. But this is not the case for the vibration movements of the tips. It can be argued that this is due to their different contact angle, with CT-4 connected to the handpiece in a 90^{o} angle while CKT-1 was connected at a 135^{o} angle (Figure 2.2), it would be easier for CT-4 to oscillate at its

resonance amplitude when it is connected in a 90^{o} angle to the handpiece compared to CKT-1 connecting at such a wide angle.

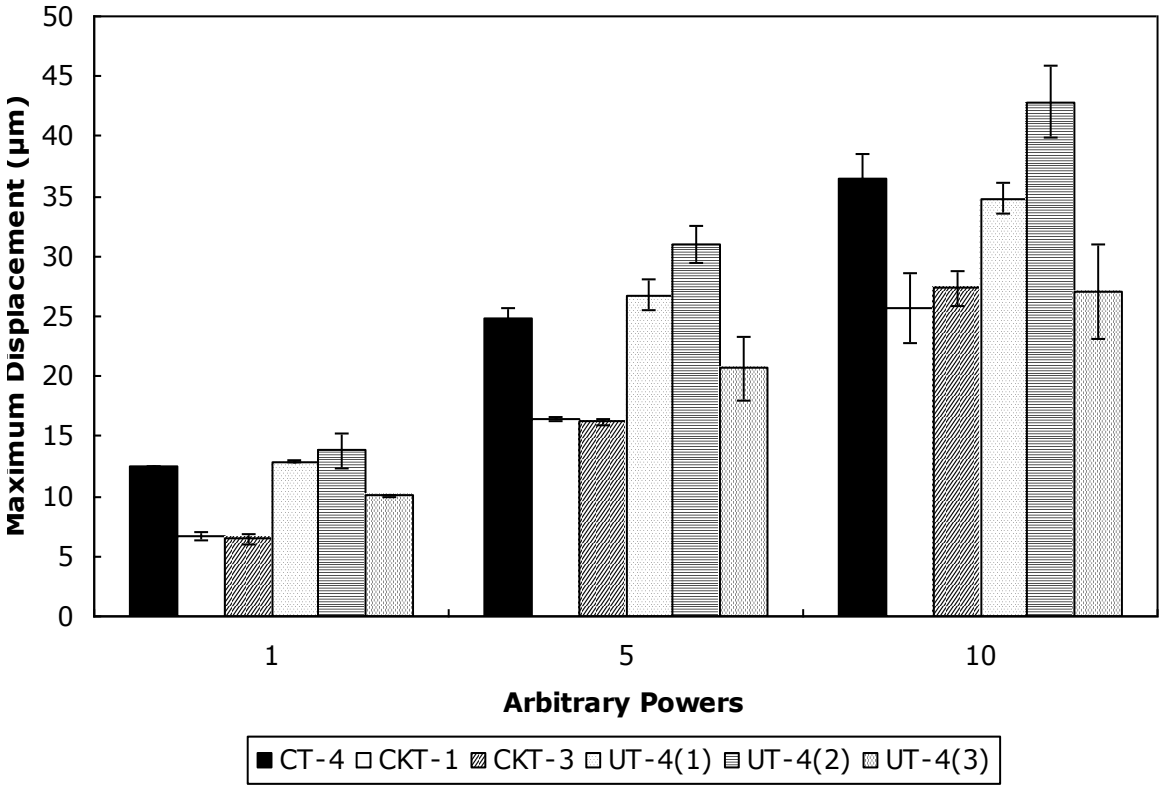

Figure 3.26: *Collated maximum vibration displacement of different dental files at low, medium and high intensities respectively in air*

As mentioned earlier in the chapter, there is a correlation between the vibration magnitude profile and the intensity of the sono(chemi)luminescence produced for the thicker endosonic files, such as the CT-4 and the CKT-1. Further analyses were performed on these tips, similar to that performed on the sono(chemi)luminescence, where the vibration displacements were divided to three maximum peaks, one at the beginning of the tip, one in the middle of the tip (which is the antinode), and the other one at the end of the tip (Figure 3.27).

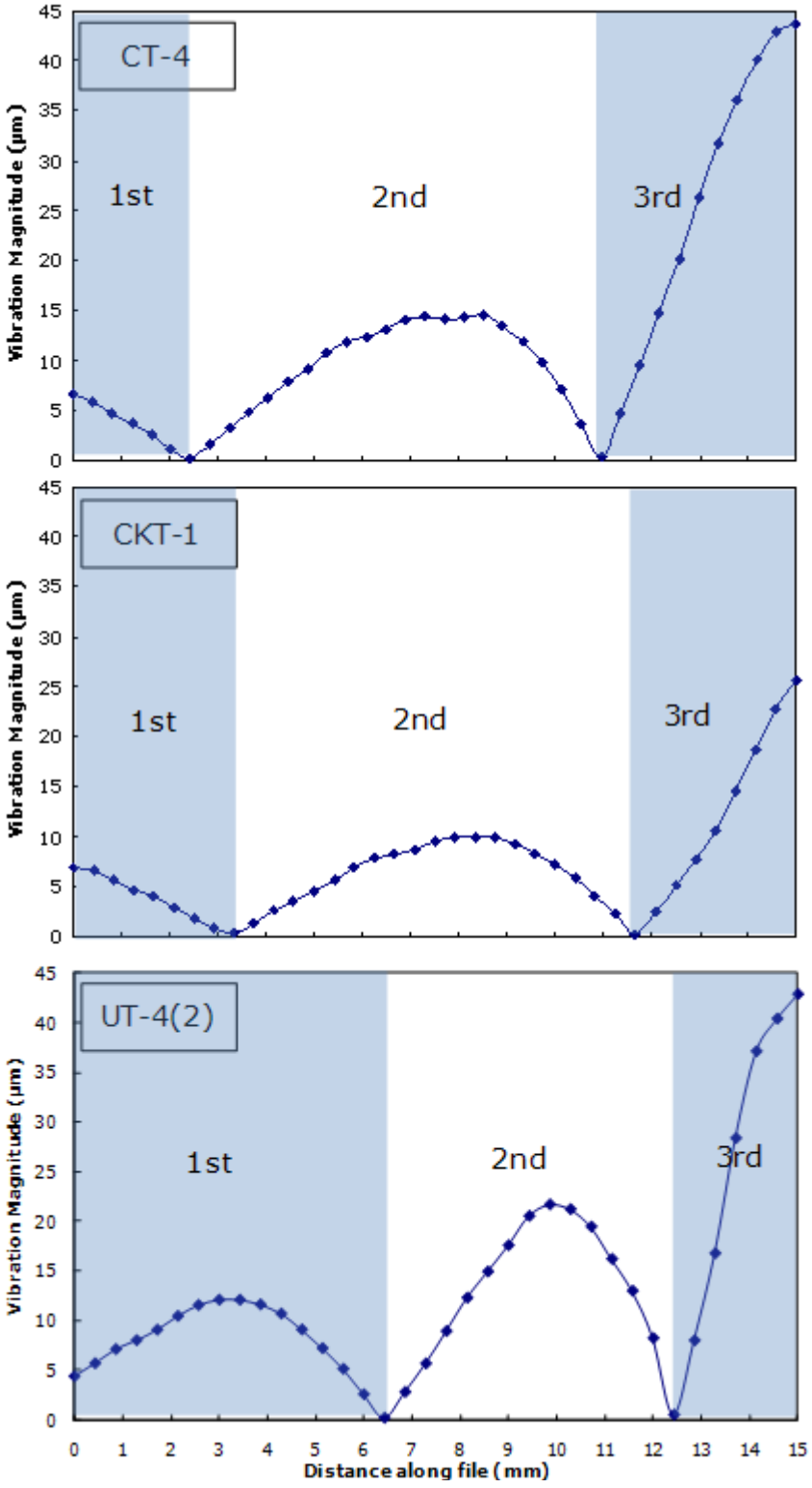

Figure 3.27: *Vibration displacement magnitudes of CT-4, CKT-1 and UT-4(2) with shaded areas indicating the 1st, 2nd and 3rd peaks of maximum vibration displacements used for analyses.*

Based on Figure 3.24(a) and (b), it can be seen that the areas of sono(chemi)luminescence were localised to certain areas and they coincide with the antinodal areas of the vibration displacement profiles, for CT-4 and CKT-1. Further analyses were performed at specific points where sono(chemi)luminescence (SCL) was produced, and the results showed that the individual peaks showed a fairly good correlation in the vibration displacement and the amount of SL produced, shown as a comparison between Figure 3.28 and Figure 3.29.

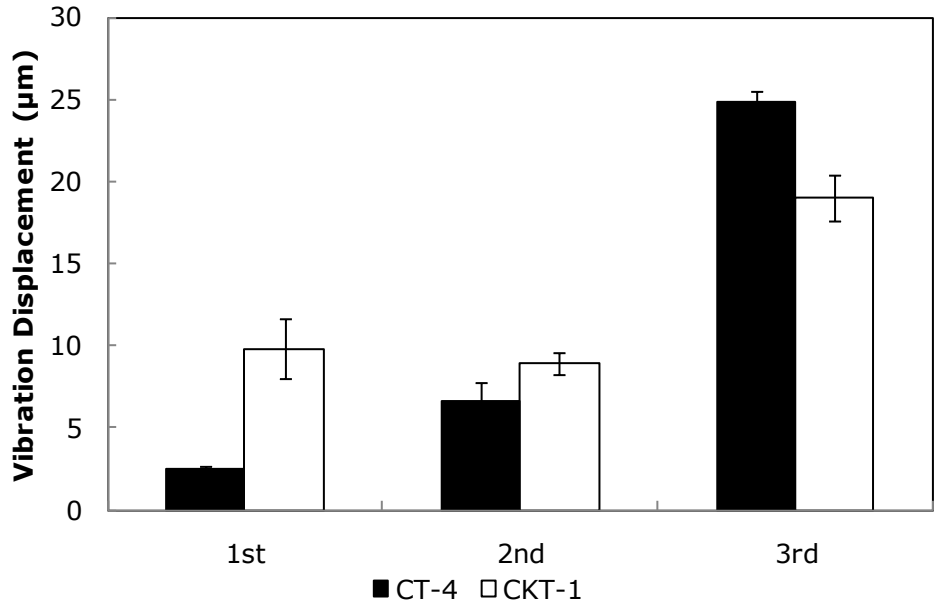

Figure 3.28: *Maximum vibration displacement at different areas (noted as 1st, 2nd and 3rd peaks) along the endosonic file at Power 10/10 for CT-4 and CKT-1 tips.*

The correlation between the SL produced at those specific areas and the vibration displacement magnitude is high, giving a Pearson's correlation coefficient, r above the critical value at 95% confidence level, as shown in Table 3.5. This shows that the two parameters are closely linked to each other, where places with higher displacement amplitude increase the probability of production of cavitation. However, this is not the case for the first peak of analysis. In the case for CKT-1, the high displacement amplitude did not result in high production of cavitation. However, it has to be noted that the shape of CKT-1 is such that it is bent at a 135° angle, causing a lot of energy loss at the bend of the tip, resulting in a huge reduction in SL production at the antinodal points.

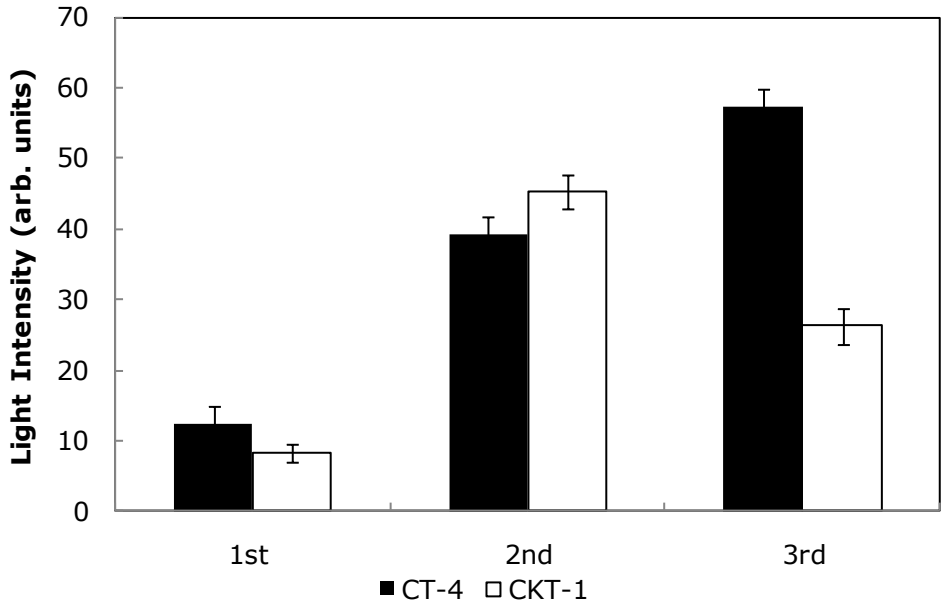

Figure 3.29: *Light intensity at different areas (noted as 1st, 2nd and 3rd peaks) along the endosonic file at Power 10/10 for CT-4 and CKT-1 tips.*

Based on Figure 3.26, it can be seen that the maximum displacement produced by all the UT-4 tips differ from one another even though they have very similar designs. Further analyses were done on the three UT-4 tips, taking their vibration magnitude at three different areas along the tip at the highest oscillating power (Power 10/10).

Table 3.5: *Pearson's correlation coefficient of CT-4 and CKT-1 for the SL and SLV results at specific areas along the tip.*

Tip	CT-4	CKT-1
Sample size, N	9	
Critical value	0.582	
Confidence level	95 %	
Pearson's correlation coefficient, r	0.984	0.909

By using the maximum displacements of the three UT-4 tips at the 1st, 2nd and the 3rd antinodal points along the tips (as illustrated in Figure 3.27), it can be seen that, in Figure 3.30, there is a significant difference in the vibration magnitude at all the antinodal points (ANOVA, p-value < 0.05), suggesting that they have a very

different vibration displacement profile. However, in Section 3.3, none of the UT-4 tips showed any significant difference in the mean intensity of sono(chemi)luminescence produced. Upon further analyses, it was found that the overall vibration magnitude produced (the summation of all the maximum vibration displacements) showed no significant difference for all the three UT-4 tips; and this might be the reason supporting the results in Section 3.3. Table 3.6 below shows the statistical analysis results for the results collated in Figure 3.30.

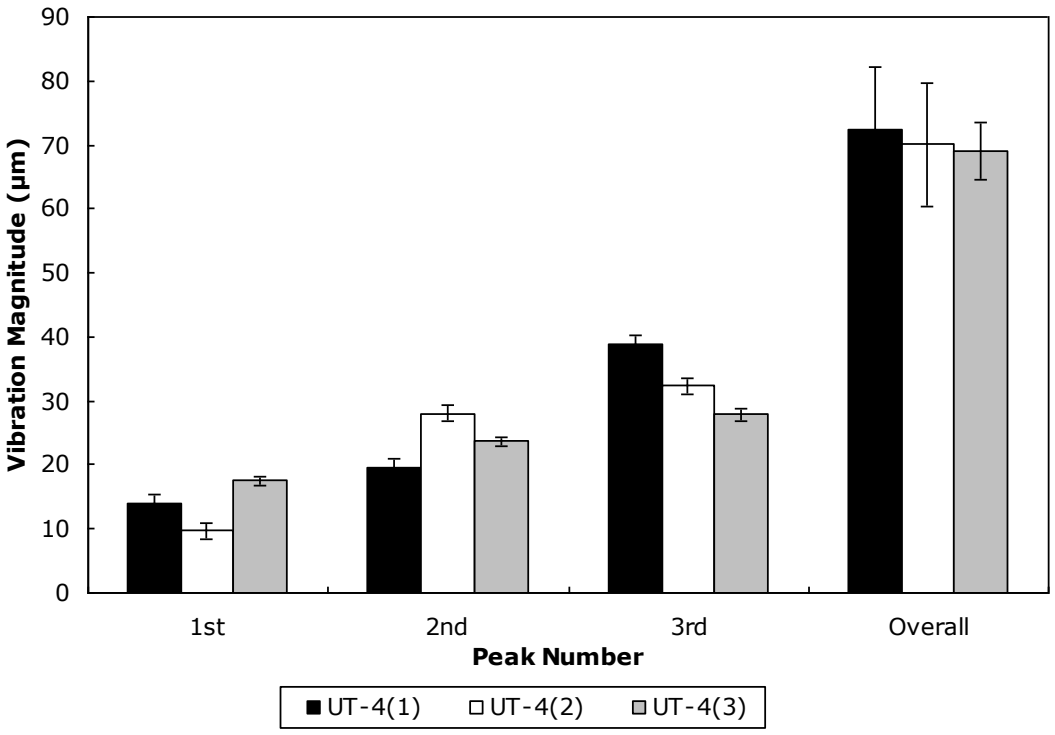

Figure 3.30: *Maximum vibration magnitude at three different areas (as explained in Figure 3.27) and the summation of the 'overall' vibration magnitude along the three UT-4 tips at Power 10 in water.*

Table 3.6: *Analysis of Variance for all the UT-4 tips at Power 10 at their respective peaks and their significant difference at 95 % confidence level.*

Peak number	ANOVA, P-value	Significant Difference
1st	0.008	Yes
2nd	0.001	Yes
3rd	0.001	Yes
Overall	0.867	No

This section enabled us to study the vibration displacement profile of each endosonic file used. It can be concluded that some of the thicker endosonic files such as the CT-4, CKT-1 and CKT-3 tips showed correlation between the vibration displacement and the amount of sono(chemi)luminescence produced, suggesting that the magnitude of the displacements give rise to the production of negative pressure in the surroundings, producing cavitation. However, for UT-4, there is little or no correlation found in the vibration profile and its production of sono(chemi)luminescence. This might be due to the shape of UT-4, which is thinner and has a much smaller surface area, resulting in big oscillation amplitude but failed to produce sufficient negative pressure in the surrounding areas. The areas of maximum displacement for all the tips coincide with the wavelengths of the harmonic frequencies, and the antinodal points correspond to the areas of sono(chemi)luminescence. This further strengthens the argument that there is a relationship between vibration movements and the production of cavitation.

With these conclusions, it brings the need for us to further characterise the fluid properties when the endosonic files are immersed in order to have a better understanding of the performances of the tips used.

3.6 Particle Image Velocimetry (PIV)

3.6.1 PIV on 20 kHz Ultrasonic Microtip

A pilot study was performed on the 20 kHz ultrasonic microtip to assess the validity of the experimental method based on velocity values obtained from the literature.

Experiments were performed at ultrasonic intensities of 7 W cm^{-2}, 14 W cm^{-2} and 29 W cm^{-2} (obtained calorimetrically) respectively, recorded at frame rates ranging from 125 fps to 2000 fps. However, discrete particle movements can only be seen at 7 W cm^{-2} at the highest frame rate used (2000 fps), limiting down the pilot study intensity to 7 W cm^{-2}. The frame rates were limited to 1000 fps to give a good field of view and resolution in the videos taken.

The particle movement traces were identified by the PIV*view* software developed by PIVtech, Germany. It was performed based on the comparison of two images, where the distance of the image was calibrated based on a known value taken with a high precision ruler, and the velocity of the particle movements were taken based on the time difference in between the frames.

Figure 3.31 shows the velocity contour map obtained for sonication using a 20 kHz ultrasonic microtip at 7 W cm^{-2}. The position of the ultrasonic probe is drawn in black in the figure for better illustration. It can be seen that 'hot spots' of turbulent flow occur in the regions under the ultrasonic probe, which might be due to both the formation of cavitation bubbles and acoustic streaming effects. Table 3.7 collates the average and maximum velocities obtained from the experiment, compared with the values obtained from the literature. It can be seen that the velocities obtained from this pilot study are comparable to those in the literature, though it has to be noted that the experimental conditions and equipment used vary from one another, resulting in slight discrepancies in the calculated velocities.

After performing the 'proof of principle' experiment on the 20 kHz ultrasonic microtip, a similar PIV method was applied to obtain a comparison in the velocity profiles in different dental endosonic files, which will be discussed in the next sub-section (Section 3.6.2).

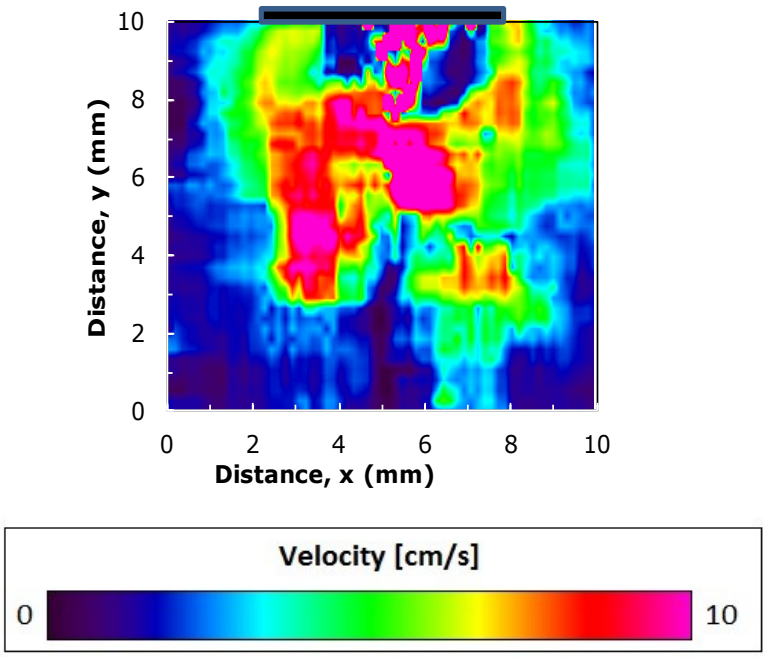

Figure 3.31: *Velocity contour map of the sonication of 20 kHz ultrasonic microtip (drawn as a black block) at 7 W cm^{-2}.*

Table 3.7: *List of average and maximum velocities obtained from experimental results compared with those reported in the literature.*

	Frequency / kHz	**Intensity / W cm^{-2}**	**$\langle v_{avg} \rangle$ / cm s^{-1}**	**$\langle v_{max} \rangle$ / cm s^{-1}**
Experimental Result	**20**	**7**	**46.5**	**127**
Mandroyan *et al.* (2009)	20	13.9	22.7	63.9
Laborde *et al.* (2000)	28	N/A	65	N/A
Tsochatzidis *et al.* (2001)	20	N/A	31.8	100

3.6.2 PIV on Endosonic Files

An endosonic file was immersed front and side-on to obtain velocities of the fluid at *x*, *y* and *z* axes for the experiment based on the displacements of the suspended polystyrene spheres. A tip was first inserted into the middle of a disposable polymethacrylate cuvette of 1 cm × 1 cm width and depth, with a front-on position as shown in Figure 3.32. Videos were recorded at 1000 frames per second upon starting the sonication for 30 seconds.

A similar analysis method was applied to the images as to those described previously for sonication of the 20 kHz ultrasonic probe (Section 3.6.1). A velocity contour map of the particle movements was obtained from the analysis done from the software. An example of the velocity contour map obtained for an endosonic file immersed in the middle of a cuvette is illustrated in Figure 3.33. As it can be seen in the figure, the highest velocity areas always occurred around the surroundings of the oscillating endosonic file. Based on Figure 3.33(b), it can be seen that the highest velocities in the region of interest occur near the tip of the endosonic file, suggesting that the oscillatory movements of the file cause the displacement of the fluid, resulting in high fluid velocities around the area. A non-uniform fluid velocity profile is obtained for all power settings, but they all show a general trend of higher fluid velocities at the areas surrounding the endosonic files. As the intensity increases from Power 1 to Power 10, the fluid velocity around the tip increases tremendously, causing a highly turbulent flow in a cuvette upon increasing to Power 10.

From the contour maps generated, information about the fluid flow can be obtained and the influences of the oscillating endosonic file on the fluid displacement under comparable operating conditions can be examined. Table 3.8 illustrates the average velocities of the fluid flow at the *x*, *y* and *z* direction as well as the maximum velocity obtained for each power settings, where the velocities at the *z* direction were obtained when the endosonic files were immersed with a side-on position. It can be seen that the CT-4 tip exceeds all the other tips in terms of the average and maximum

velocities. It achieved a maximum velocity of 12.2 cm s^{-1} at Power 1, which was more than twice the maximum velocity of UT-4(2).

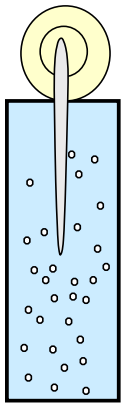

Figure 3.32: *Schematic of an endosonic file immersed into a cuvette filled with suspended polystyrene spheres in water in a front-on position.*

Table 3.8: *Average and maximum velocities along the x, y and z axes at different power settings for three endosonic files used.*

	Middle position								
Velocity	**$\langle v_{avg,\,x,y} \rangle$ / cm s^{-1}**			**$\langle v_{avg,\,y,z} \rangle$ / cm s^{-1}**			**$\langle v_{max} \rangle$ / cm s^{-1}**		
Power Settings	1/10	5/10	10/10	1/10	5/10	10/10	1/10	5/10	10/10
CT-4	8.5	17.5	62.0	2.2	2.0	5.1	12.2	25.6	110.9
CKT-1	0.8	1.4	31.5	0.8	1.0	10.2	1.0	1.8	53.7
UT-4(2)	2.6	3.0	2.9	3.5	3.6	3.6	5.2	4.9	7.1

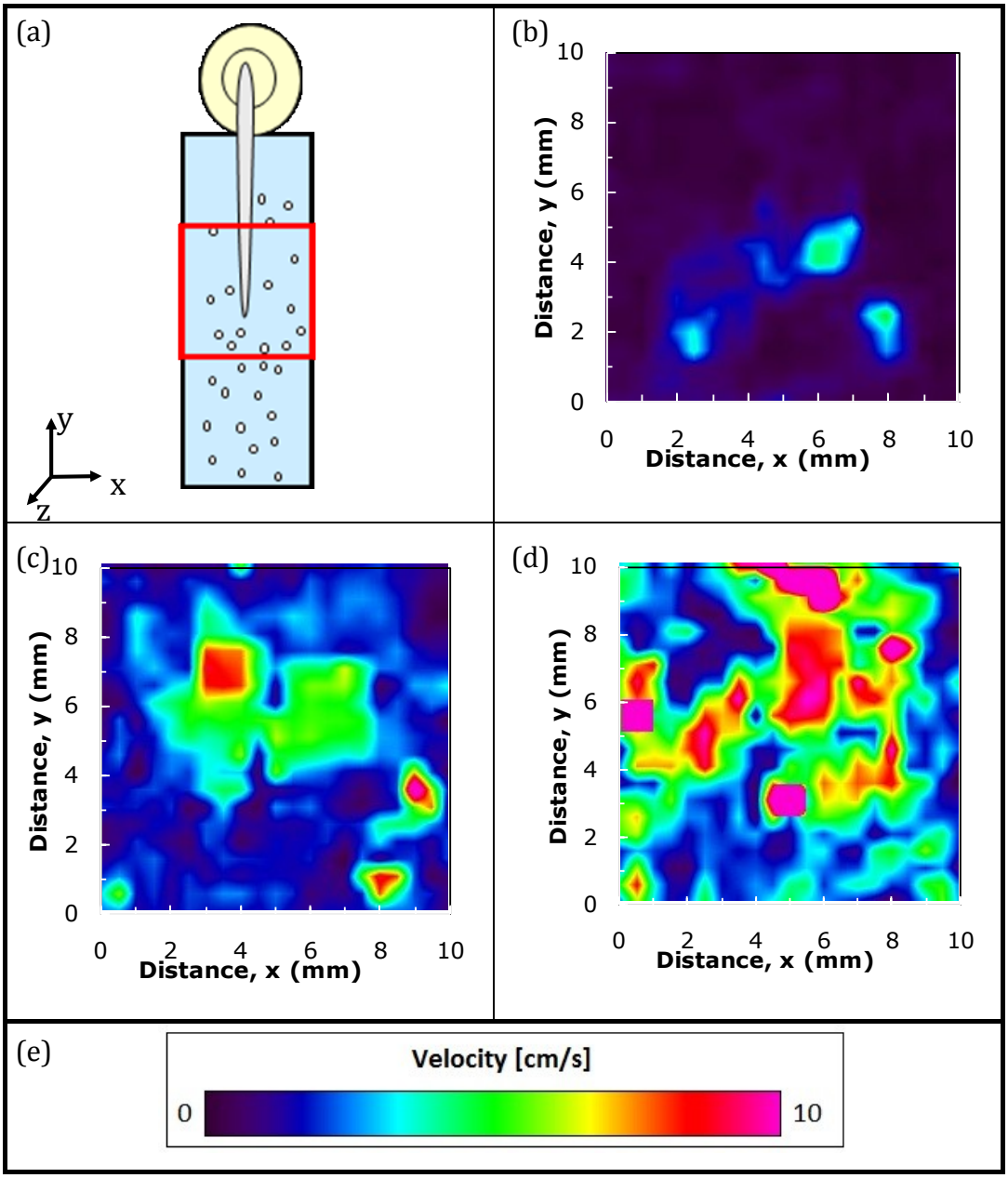

Figure 3.33: *(a) Schematic of a dental tip immersed in a front-on position into a polymethacrylate cuvette, high-lighted in red with the region of interest stating the areas of where PIV was conducted; (b) PIV contour map of the region of interest of CT-4 at Power 1/10; (b) PIV contour map of the region of interest of CT-4 at Power 5/10; (d) PIV contour map of the region of interest of CT-4 at Power 10/10; (e) Velocity colour bar for the contour maps.*

In general, the velocity profile in the *x* and the *y* axes were much greater than that on the *z* axis (Table 3.8). Hence, more studies on the velocity when the tips were immersed in the front-on position were done as the most significant changes in the fluid velocities is obtained at this configuration.

Table 3.9 shows the collated velocity contour maps for the three endosonic files at various power settings, with Figure 3.34 giving a better illustration. It can be seen that CT-4 has the highest maximum velocities at all power settings whereas UT-4(2) gives a very much lower velocity even at the highest arbitrary power. This has further strengthened the results in Section 3.3 on the sono(chemi)luminescence (SCL) produced on each dental tips, where endosonic files producing more SCL showed higher fluid velocities in the PIV experiments. This is because high fluid velocity prevent cavitation bubbles from coalescing and clustering, which in turn increased the intensity of SCL (Hatanaka *et al.*, 2006). It was also reported in the literature that acoustic cavities accumulate at high fluid velocity areas and do not form clusters due to the presence of secondary Bjerknes force (Franke *et al*., 2011), which was observed in the experimental results (Table 3.9), where the areas with high fluid velocities correlates to the areas of SCL (Figure 3.14).

Table 3.9: *Collated velocity contour maps for all three endosonic files at various power settings.*

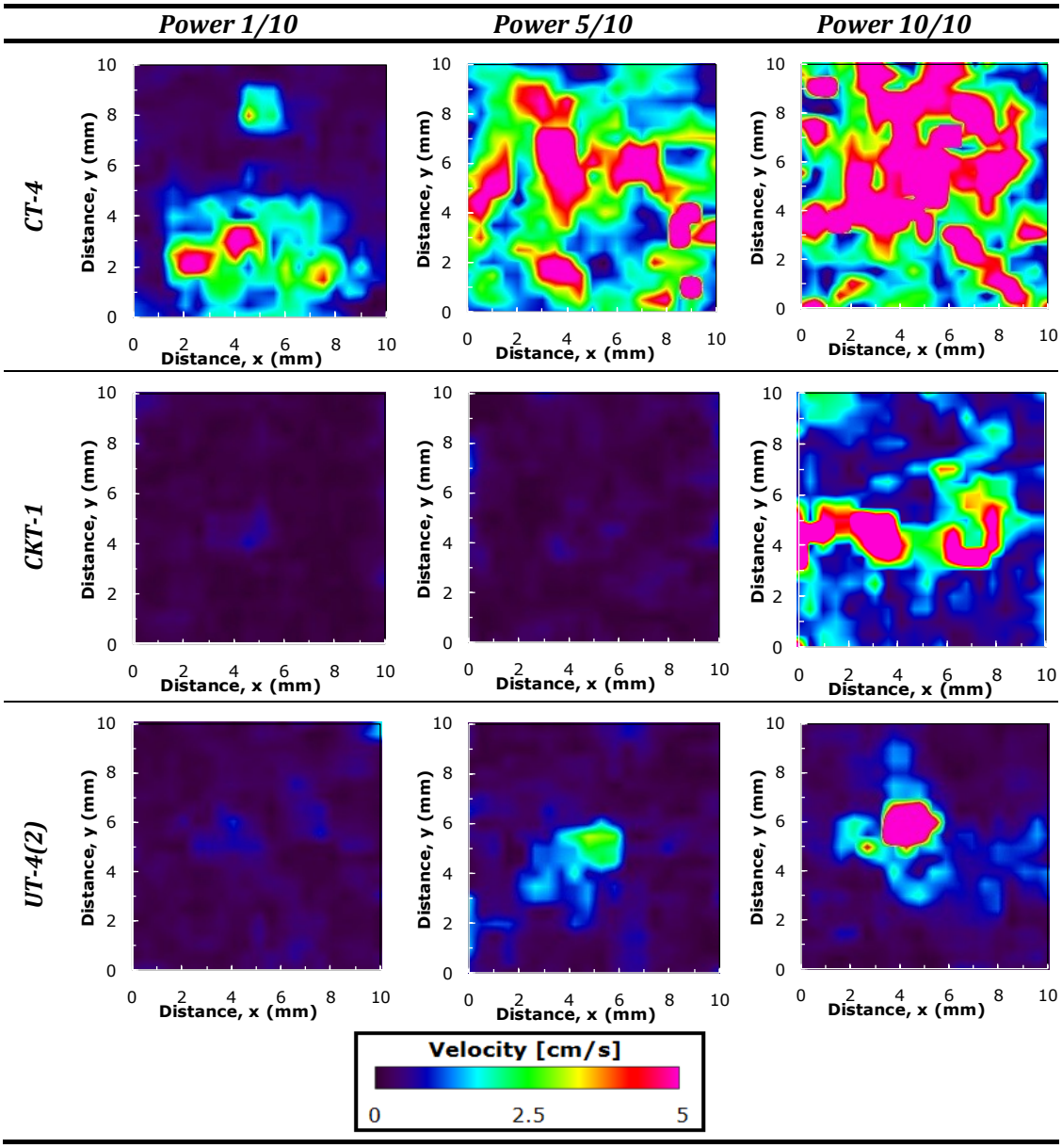

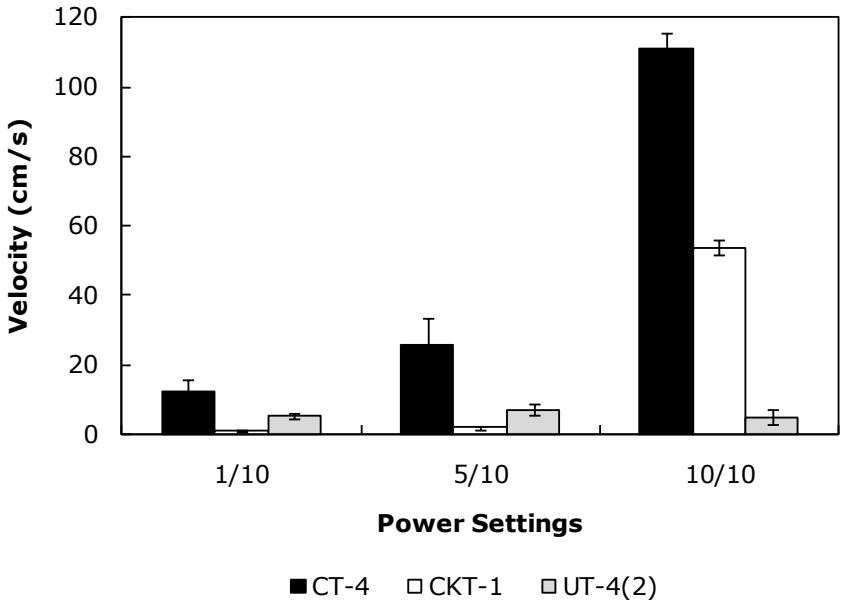

Figure 3.34: *Maximum velocities at various power settings for CT-4, CKT-1 and UT-4(2). (data extracted from Table 3.8)*

The results obtained from the velocity profile of the fluid strengthen all the previous conclusions on the production of SCL at the vibration antinodes along the dental tips. It shows that the ability of the endosonic files to produce high acoustic streaming is crucial in the formation of cavitation, which in turn will contribute to the formation of microjets and •OH radicals, believed to increase the cleaning efficiencies in the dental procedures.

3.7 Conclusions

In this chapter, a series of characterisation methods were covered to identify the difference among all the endosonic files used. The characterisation methods used have given us a good overview of the performances of all the endosonic files studied. A better picture of the correlations of all the different techniques is illustrated in the scheme below (Scheme 3.2).

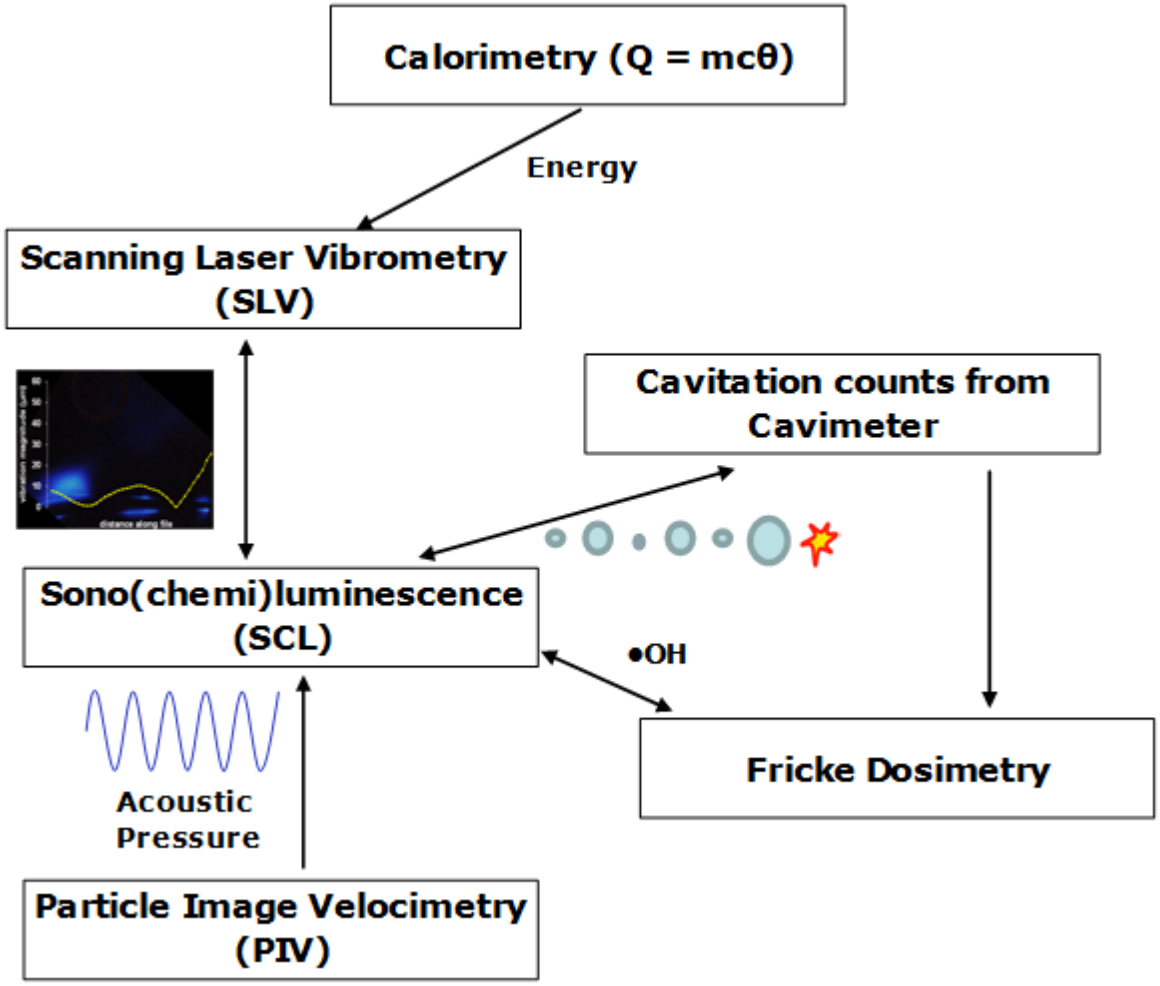

Scheme 3.2: *Relations of all the characterisation methods performed.(Arrows indicate the influencing parameter)*

Based on Scheme 3.2, we can summarise:-

i) **Calorimetry** results give the total energy output of all the different tips, where tips with greater energy output result in higher vibration oscillation amplitude, shown in the **SLV** results.

ii) The areas where maximum vibration magnitudes in the oscillation movements produced from **SLV** were the areas where transient cavitation happens – producing **SCL**.

iii) Cavitation counts produced from the **Cavimeter™** were able to quantify the total amount of both stable and transient cavitation. Cavitation counts on the meter correlated with the intensity of **SCL** produced.

iv) Similarly, the amount of cavitation produced, measured by the **Cavimeter™** functions as an indicator of the total amount of stable and transient cavitation produced in the system – when there is more transient cavitation, more radicals were produced and resulted in higher Fe^{3+} production as detected by the **Fricke Dosimetry**.

v) **PIV** results showed that endosonic files which produce high velocity streaming tended to result in higher **SCL**. This suggests that the high streaming effects in the system contributes to the production of higher acoustic pressure in the system, hence resulting in more transient cavitation – producing more SCL.

4.Cleaning Efficiencies of Dental Tips

Endosonic files are used to clean any impurities or debris in an infected root canal. Upon performing a series of characterisations on various endosonic files in Chapter 3, which showed very different characteristics depending on the shape of the endosonic file, the cleaning efficiencies of these files were studied in order to obtain a better comparison and if possible correlate the cleaning effeciency to the sonochemical effects.

A series of experiments were carried out in order to have an idea of their cleaning performances based on their ability to produce an emulsion, degrade dye and also to remove surface impurities.

4.1 Mixing Ability of the Endosonic Files

Power ultrasound can be used to form emulsions (Abismail *et al.*, 1999) due to the high shearing force produced during sonication (Behrend *et al*., 2000), as mentioned earlier in Section 1.2.3.

Adapting the idea from Behrend *et al*. (2000) experiments on ultrasonic emulsification were conducted with low viscosity (50 cSt) silicone oil and water on the endosonic files. This gave an indication of the presence of transient cavitation from these files, and at the same time provide an illustration of the streaming effects taking place in the system – in terms of the ability to form emulsions in a model channel.

For this experiment, equal amount of silicone oil to water ratio was used. The endosonic files were immersed into a root canal model made of silicone rubber with

an extended side channel for examination of the emulsion formed at the side channel of the dental tip. Figures 2.12 and 2.13 show the schematic and the dimensions of the system used for the experiments.

The water used for this experiment is distilled water with 1 mM of methylene blue dye in order to give a better colour contrast. At the ratio of silicone oil to water of 1:1, it turned out to be that the oil-water (o/w) interface was at end of the endosonic tip when it was immersed into the model channel. Figure 4.1 illustrates the silicone oil and water locations in the model channel prior to the start of the experiment.

Upon sonication for two minutes at various power settings for all the dental tips, the percentage of area of the emulsion formed was evaluated based on image analysis, where emulsion is classified according to a range of coloured liquid formed in the side channel. This process was done with the aid of ImageJ software (Abramoff *et al*., 2004).

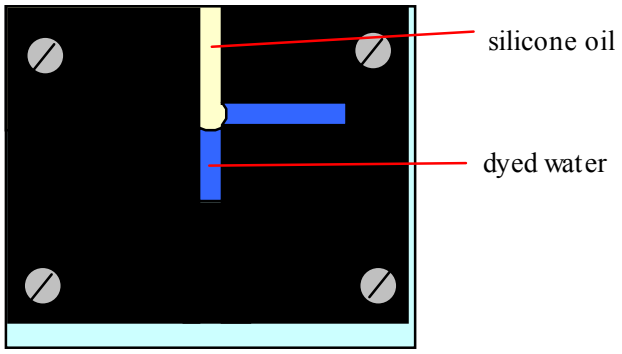

Figure 4.1: *Positions of silicone oil and water upon inserting into the model channel.*

Table 4.1 shows the results of the percentage area of emulsion formed in the side channel upon sonication for two minutes. Based on the results, sonication at the highest power setting (Power 10/10) showed that almost the whole of the side channel was filled with emulsion after sonication. CT-4 was the only tip to form some emulsion at the side channel at Power 5/10. Though it was stated that the formation of emulsion indicates the formation of cavitation bubbles in the system (Gaikwad and

Pandit, 2008), care must be taken that other factors also take place in emulsification, such as the high stirring rate of the system upon sonication. As for the case in this experiment, it has to be noted that the formation of emulsion also depends on the ability of the vibrating endosonic file to break the surface tension of the oil-water interface at the side channel.

Table 4.1: *Pecentage area of emulsion formed at the side channel upon sonication for two minutes.*

Power Setting	**1/10**	**5/10**	**10/10**
CT-4	NDE	23.5	100.0
CKT-1	NDE	NDE	95.5
CKT-3	NDE	NDE	89.0
UT-4(1)	NDE	NDE	86.3
UT-4(2)	NDE	NDE	88.6
UT-4(3)	NDE	NDE	83.5

NDE: No Detectable Emulsion

Based on the oscillatory movements of the endosonic files (Section 3.4), it was expected that the oscillatory movements of the tips would break the oil-water interface in order to promote the formation of emulsion in the side channel. This however was not the case even at medium powers, suggesting that the force formed by the oscillatory movements of the tips was not strong enough to tear apart the surface tension of the o/w interface. High ultrasonic irradiation power results in a high percentage of emulsion formed. This can be explained by the large amount of cavitation produced, resulting in a high collapse intensity, which will then result in an increase in interfacial instability, causing the temperature of the system to increase dramatically. Due to this, the interfacial tension of the oil-water interface decreases, resulting in better penetration of the oil to water interface and thus forming more emulsion.

Figure 4.2 shows the percentage of emulsion formed in the side channel upon sonication at Power 10 for two minutes. It can be seen that the CT-4 and CKT tips

have achieved more than 90 % of emulsion in the side channel, and that there is no significant (ANOVA, p-value > 0.05) difference between the percentage of emulsion formed between the CT-4 and CKT-1 tips. However, the UT-4 tips showed slightly less emulsion formed compared to the other tips. Though the differences between the UT-4 tips were not great, it still gives a rough idea of the streaming effects of the dental tips which will eventually affect the cleaning efficiencies of the tips.

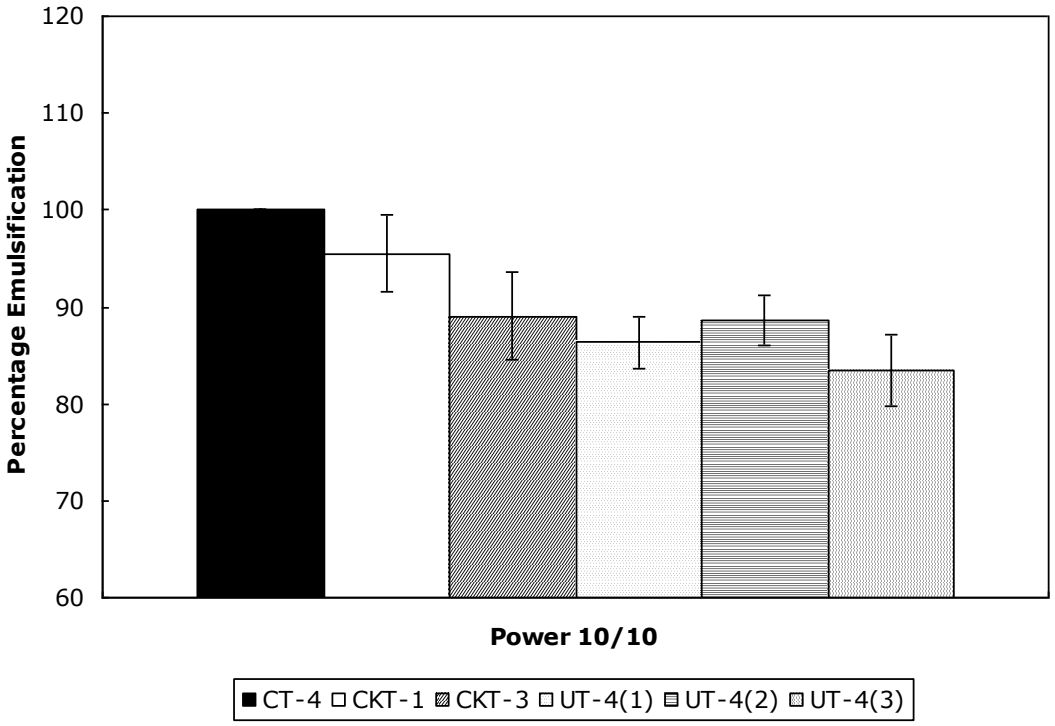

Figure 4.2: *Percentage of emulsion formed upon sonication for two minutes at Power 10 for the endosonic files used. (data extracted from Table 4.1)*

Further image analyses were performed on the microscopic images with the aid of ImageJ, using the method by (Scherze *et al*., 2005), as described in Section 2.8.1, where the average particle diameter of the emulsion and the percentage area of oil formed in the water emulsion is calculated. An example of the steps of image analysis to obtain the mean particle diameter is illustrated in Figure 4.3.

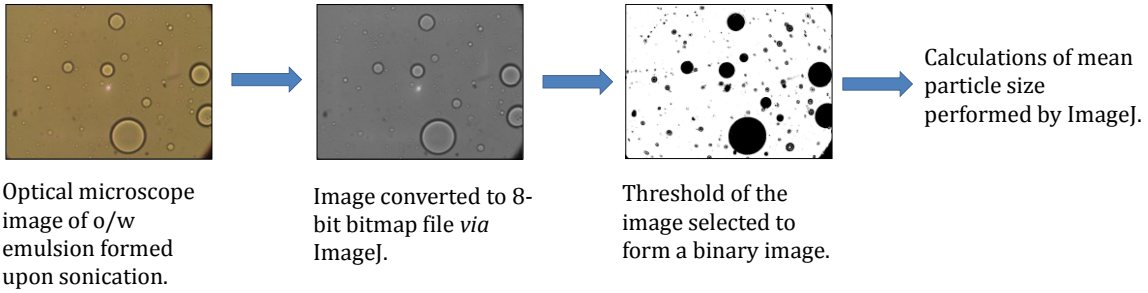

Figure 4.3: *An example of image analysis performed on the microscopic image of o/w emulsion to obtain the mean particle diameter from ImageJ.*

Samples of the oil-in-water (o/w) emulsion were taken out to be analysed under an optical microscope (GX Microscopes L3001, mounted with an Infinity Capture camera). Figure 4.4 illustrates the emulsion formed upon sonication for two minutes at Powers 1/10, 5/10 and 10/10 for CT-4, CKT-1 and UT-4(2). It can be seen that the emulsions formed by the sonication using CT-4 at Power 10/10 has smaller oil droplet sizes compared to the emulsion formed upon sonication with the CKT-1 and UT-4(2) tips.

Table 4.2 tabulates the average oil droplet sizes in the o/w emulsion and the percentage of o/w emulsion formed, as calculated by imageJ. It can be seen that the oil droplets formed upon sonication at low intensities have bigger average diameters as compared to those sonicated at higher ultrasonic intensities. It is well known that the o/w droplet size affects the creaming rate of emulsions, where emulsions with smaller droplets cream more slowly (Horozov *et al.*, 2007). This indicates that the emulsion formed at low ultrasonic intensities is less stable compared to those at high intensities. Emulsions formed from the sonication with CT-4 have lower average particle diameter, indicating that it forms the most stable emulsion among the three endosonic file assessed, while UT-4(2) on the other hand, formed the least stable emulsion.

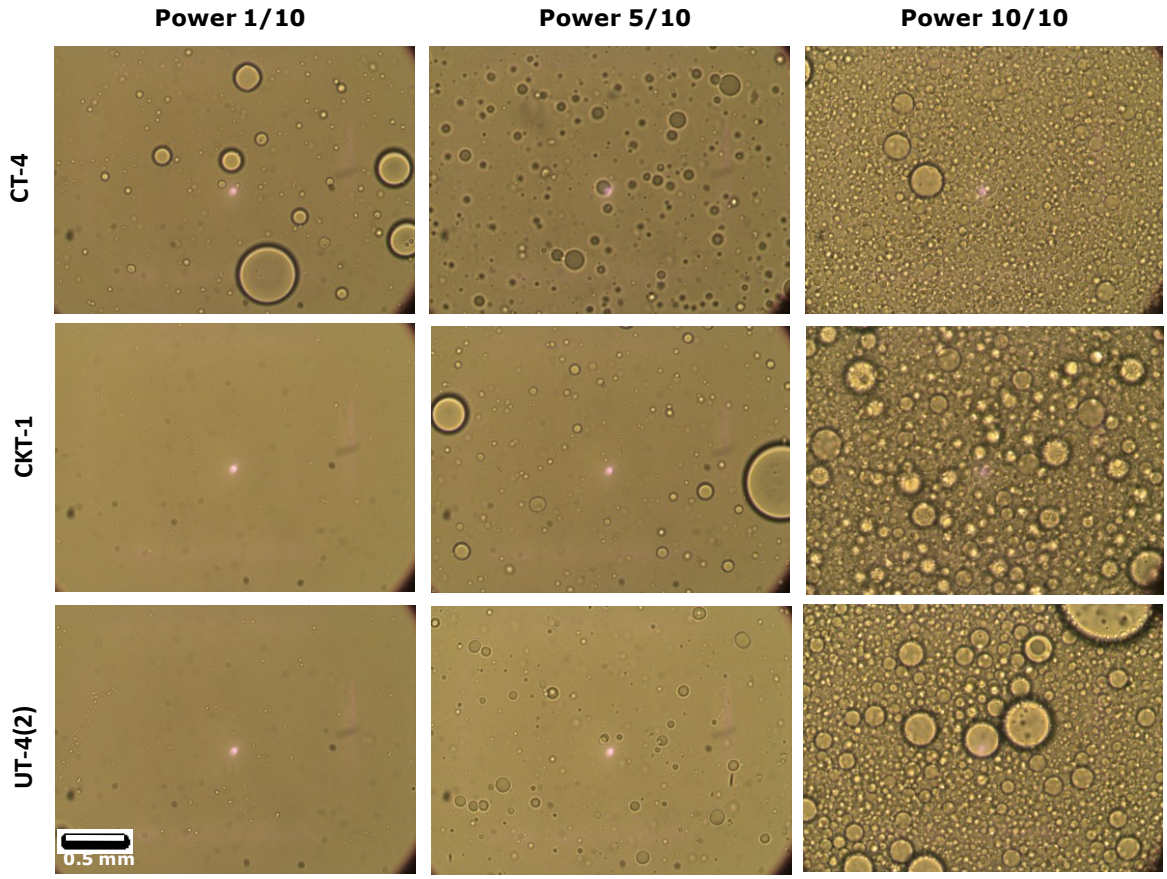

Figure 4.4: *Microscopic images of the oil-in-water emulsion formed upon sonication for two minutes with CT-4, CKT-1 and UT-4(2) at Powers 1/10, 5/10 and 10/10.*

The percentage area of oil in water of the samples analysed showed that emulsion formed upon sonication at Power 10/10 has almost 1:1 ratio of oil to water in the samples, indicating that well-dispersed emulsion is formed upon sonication with the dental tips at Power 10/10.

The results obtained from the ultrasonic-assisted emulsification has proven that an emulsion can be formed upon sonication with various endosonic files and that they all produce different sized oil particles, differentiating the stability of the emulsions formed from one another. This provides an indication of the mixing ability of the endosonic files caused by various factors: such as acoustic streaming and the production of shockwaves due to violent collapse of transient cavitation. This may be a contributing factor to the cleaning efficiency of the endosonic files, which will be assessed and discussed more in the next section.

Table 4.2: *Average particle diameter and the percentage area of o/w emulsion formed upon sonication at Powers 1/10, 5/10 and 10/10 for CT-4, CKT-1 and UT-4(2) tips.*

	CT-4			CKT-1			UT-4(2)		
Power	**1/10**	**5/10**	**10/10**	**1/10**	**5/10**	**10/10**	**1/10**	**5/10**	**10/10**
Average Particle Diameter, d_p (mm)	0.586 ± 0.3	0.238 ± 0.03	0.167 ± 0.04	N/A	0.279 ± 0.15	0.186 ± 0.1	N/A	0.236 ± 0.02	0.301 ± 0.12
Percentage area of oil droplet in water (%)	3.7	11.5	51.8	N/A	4.4	49.3	N/A	2.0	47.1

4.2 Dye Decolourisation with a Dental Irrigant

As mentioned earlier in Section 2.8.2, sodium hypochlorite is a strong oxidising agent, and is capable of decolourising dyes by breaking the chromophores of the dye structures.

In this study, the rate of reaction was determined by the absorbance of Rhodamine B, measured with a UV-visible spectrometer (Agilent 8453) at 554 nm under various sonication conditions. Comparison of the performances of each endosonic file used were assessed based on the rate of reaction of Rhodamine B. Studies were also carried out with hydrogen peroxide for comparison of the cleaning efficiencies of these two different irrigants.

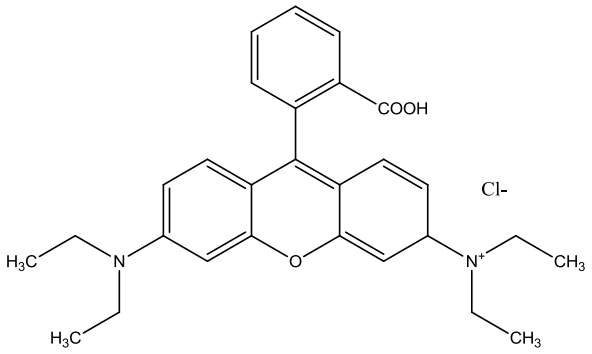

Scheme 4.1: *Structure of Rhodamine B*

4.2.1 Removal of Rhodamine B with Sodium Hypochlorite

To initiate the study, calibration of Rhodamine B solutions was performed at various concentrations in order to obtain the molar extinction coefficient of the selected cationic dye, as shown in Figure 4.5.

From the equation stated in Beer-Lambert's law of absorption:-

$$A = \varepsilon cl \qquad \textbf{(Equation 4)}$$

where,

A : absorption (unitless)

ε : molar extinction coefficient (L μmol^{-1} cm^{-1})

c : concentration (mol L^{-1})

l : path length (set to be 1 cm)

The gradient in Figure 4.5 shows the molar extinction coefficient, ε of 0.1022 L μmol^{-1} cm^{-1} at 554 nm on the spectrometer. This enables us to calculate the concentration of Rhodamine B in the solution upon sonication based on the absorption of the dye. However, care must be taken that a slight change in Rhodamine B structure would still cause a similar absorption band, but in this case, degradation of Rhodamine B would still have occurred. Thus, the degradation products were

confirmed by performing liquid chromatography coupled with mass spectrometry (LC-MS) in order to strengthen the results obtained.

Sonication of Rhodamine B was first performed on the 20 kHz ultrasonic probe at different conditions, and thereafter compared to the performances of the endosonic systems.

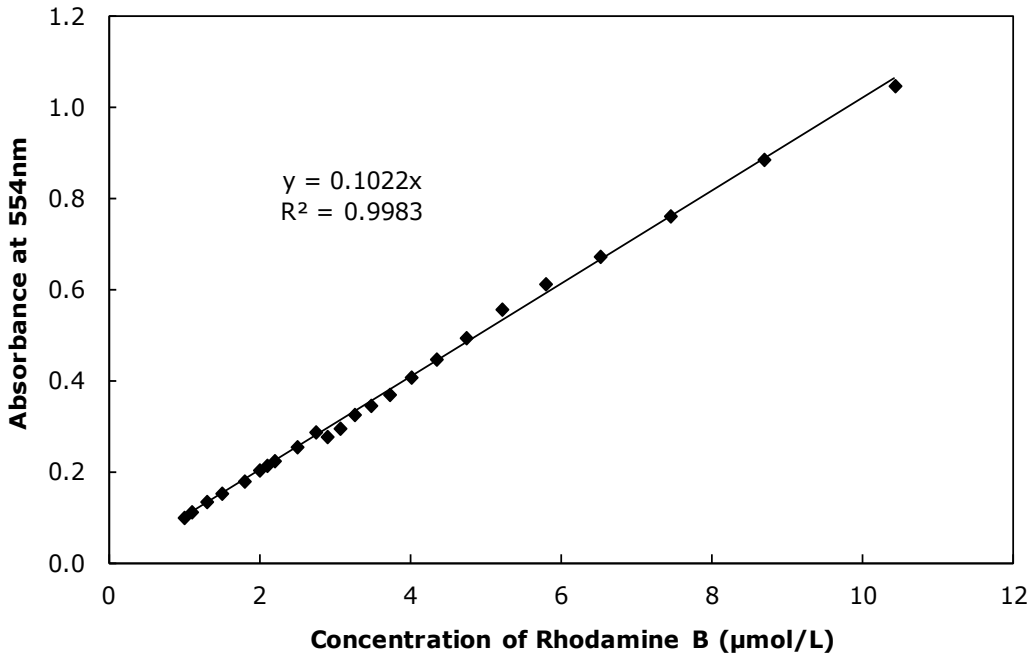

Figure 4.5: *Calibration absorbance curve for different concentrations of Rhodamine B at 554 nm.*

4.2.1.1 20 kHz Ultrasonic Probe

Sonications of Rhodamine B were performed with and without sodium hypochlorite at various ultrasonic intensities under different conditions to evaluate the differences in the presence or absence of a certain parameters.

Based on the absorption coefficient curve of Rhodamine B, 5 μg cm^{-3} (*ca.* 1 × 10^{-5} M) of Rhodamine B was chosen for the purpose of these series of experiments as it gives an absorbance of approximately 1.

Experiments were first performed for 100 cm^3 of 5 μg cm^{-3} of Rhodamine B in a jacket vessel to regulate the temperature of the solution to be at 21 ± 4 ^oC. The 20 kHz ultrasonic probe was immersed 1 cm below the surface of the solution and was sonicated for 30 minutes, taking a sample for UV-vis measurements in five-minute intervals. Figure 4.6 shows the rate of degradation of Rhodamine B upon sonication at different intensities for 30 minutes. Significant degradation can be observed, with an expected trend of increase by degradation (lower final concentration of Rhodamine B) at higher intensities.

This degradation (due to the breakage of the chromophore of the dye) proceeds as a result of the formation of free radicals during water sonolysis as well as the high pressure and temperature generated in the cavitation (Sivakumar and Pandit, 2001). Given the structure and, in solution, ionic nature of Rhodamine B (Scheme 4.1), it is unlikely that it will enter the cavitation bubble to undergo pyrollysis and so a degradation process in solution will be favoured (Ashokkumar *et al.,* 2007). This is also supported by the product analysis discussed later.

Upon plotting the rate of degradation of Rhodamine B on a first order reaction plot, based in the equation:-

$$\ln \frac{[A]}{[A_o]} = -kt \qquad \textbf{\textit{(Equation 5)}}$$

where, $[A]$: concentration of Rhodamine B at time, t (mol L^{-1})

$[A_o]$: initial concentration of Rhodamine B (mol L^{-1})

k : rate constant (min^{-1})

t : time (min)

A straight line is obtained for all reactions at various intensities used, suggesting that the reaction follows a first order kinetics, as shown in Figure 4.7. They all produced a good fit for the first order reaction with an R^2 value of > 0.9 for all cases, as collated in Table 4.3.

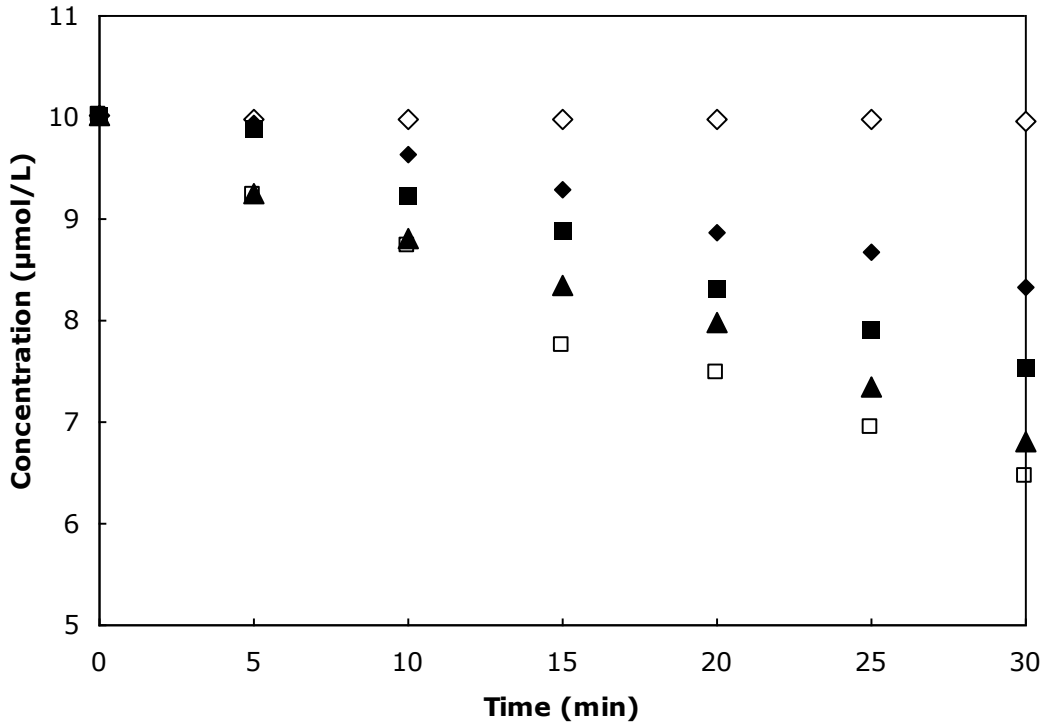

◊ control (absence of ultrasound)

◆ 5.10 W cm^{-2} ■ 9.72 W cm^{-2} ▲ 13.1 W cm^{-2} □ 16.2 W cm^{-2}

Figure 4.6: *Decomposition of Rhodamine B upon sonication for 30 minutes with the 20kHz ultrasonic probe at various intensities.*

Figure 4.8 shows the first order rate constants of the degradation of Rhodamine B upon sonication at various ultrasonic intensities. A straight line relationship is obtained, suggesting that the degradation of Rhodamine B is highly dependent on the ultrasonic intensities, and that they are directly proportional to one another, up till the highest sonication intensity of 16.2 W cm^{-2}. This further strengthens the argument of the order reaction of the degradation of Rhodamine B.

Table 4.3: *First order rate constants of the degradation of Rhodamine B with the 20 kHz ultrasonic probe at various intensities and their respective R^2 values.*

Intensity (W cm^{-2})	**5.10**	**9.72**	**13.1**	**16.2**
Rate constant (min^{-1})	0.006	0.009	0.013	0.015
R^2	0.96	0.98	0.99	0.99

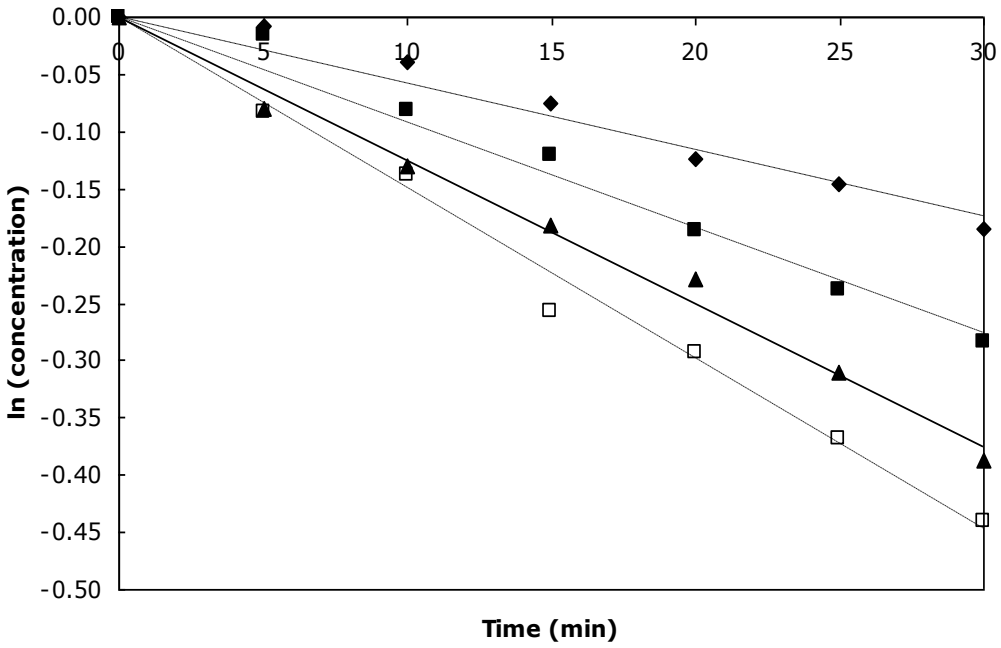

Figure 4.7: *First order plot of the degradation of Rhodamine B in the presence of ultrasound upon sonication with a 20 kHz ultrasonic probe at various intensities.*

Following the experiments performed for the degradation of Rhodamine B upon sonication, 2 wt% of sodium hypochlorite was added to the bulk Rhodamine B solution to evaluate the effects of NaOCl on the reaction. Here, 2 wt% of NaOCl was chosen for this study as it was the most commonly used concentration of irrigant in endodontics. Further studies of different concentrations of the irrigant were also performed, which will be discussed later on in the chapter. Sodium hypochlorite, known as a strong oxidising agent, was able to bleach the pink colour of Rhodamine B

solution upon continuous stirring. Hence, a control experiment was set at various stirring speeds on an IKAMAG hotplate for 30 minutes, similar to the total experimental times.

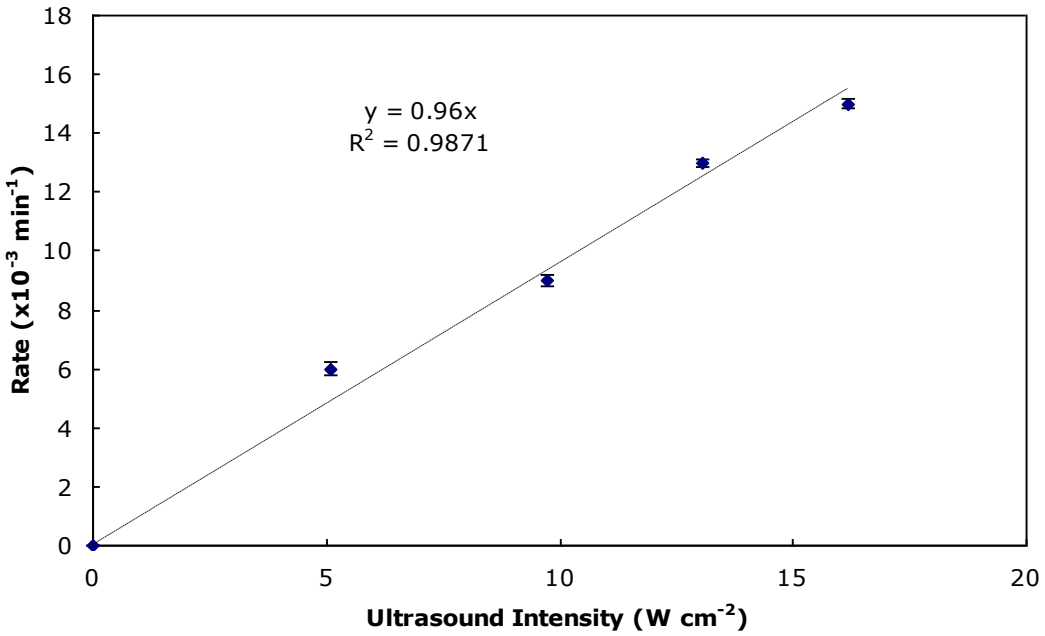

Figure 4.8: *First order rate constants of the degradation of Rhodamine B upon sonication at various ultrasonic intensities.(uncertainties based on triplicates of experiment)*

The percentage degradation of Rhodamine B in 2 wt% of NaOCl with different stirring speeds is shown in Figure 4.9. A slight increase in percentage degradation is noted as the stirring speed increases from 200 to 800 rpm. However, repetition of the experiments showed that the difference in the degradation is insignificant (ANOVA, p-value > 0.05).

Experiments were carried out at various ultrasonic intensities for 30 minutes. The results obtained for the percentage of degradation is shown in Figure 4.10. As expected, the increase in ultrasonic intensity drastically increases the rate of reaction, with almost 100% degradation achieved at 12 minutes of sonication at 16.2 W cm^{-2}.

The difference in percentage degradation between stirring and sonicating at the lowest intensity, 5.10 W cm^{-2} seemed small, one-tailed *t*-test statistical analysis of the two experimental results showed significant differences with P-value < 0.05.

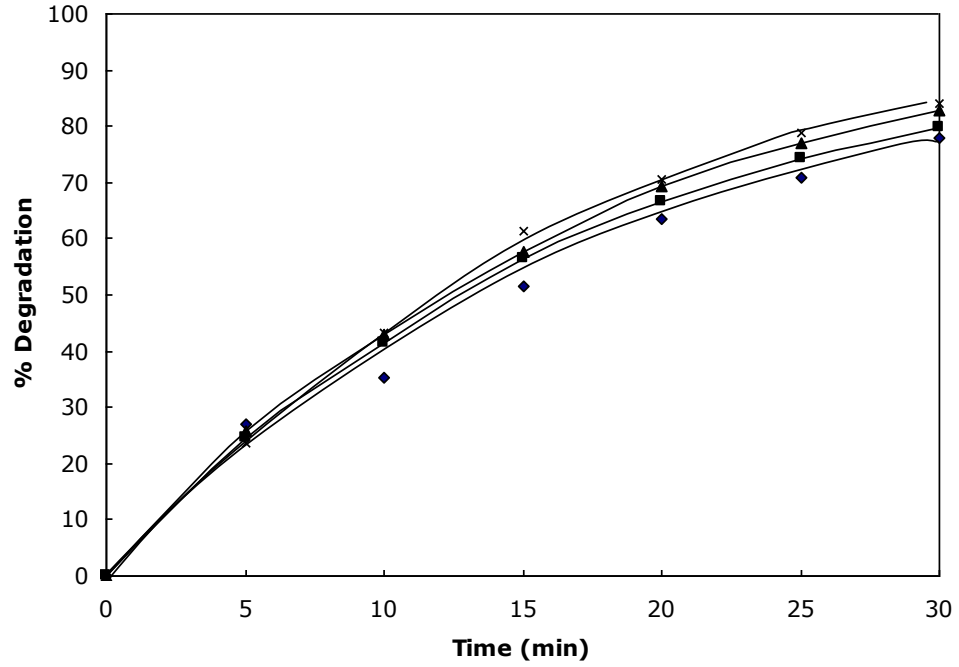

◆ 200 rpm ■ 400 rpm ▲ 600 rpm × 800 rpm

Figure 4.9: *Percentage degradation of Rhodamine B in 2 wt% NaOCl upon stirring for 30 minutes at different stirring speeds.*

Given the relative concentrations of NaOCl and dye, the former is in vast excess so that a *pseudo*-first order reaction might be expected. Figure 4.11 shows the first order reaction plot for the percentage degradation of Rhodamine B in 2 wt% NaOCl.

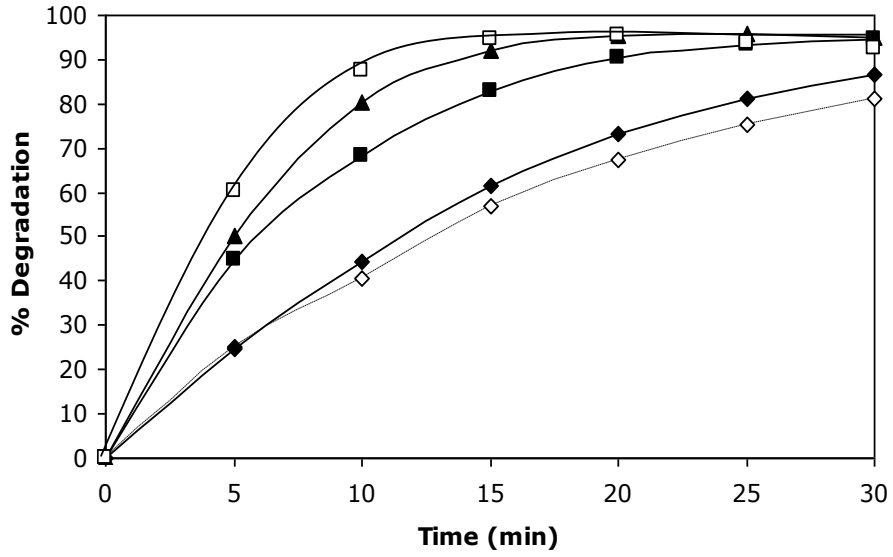

◊ control (absence of ultrasound)

◆ 5.10 W cm^{-2} ■ 9.72 W cm^{-2} ▲ 13.1 W cm^{-2} □ 16.2 W cm^{-2}

Figure 4.10: *Percentage degradation of Rhodamine B in 2 wt% NaOCl upon sonication at various ultrasonic intensities.*

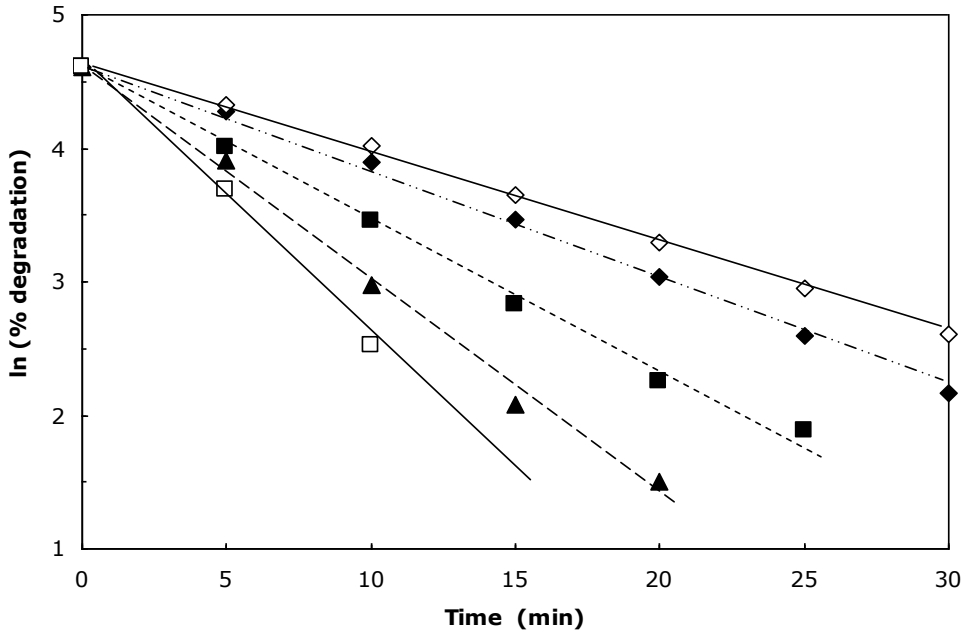

◊ control (absence of ultrasound)

◆ 5.10 W cm^{-2} ■ 9.72 W cm^{-2} ▲ 13.1 W cm^{-2} □ 16.2 W cm^{-2}

Figure 4.11: *First order reaction plot for the percentage degradation of Rhodamine B in 2 wt% NaOCl upon sonication at various ultrasonic intensities.*

Aqueous sodium hypochlorite forms an equilibrium with hypochlorous acid, as shown in Scheme 4.2, which causes reactions with sodium hypochlorite solution to be pH dependent (Bitton, 2005). The native pH of NaOCl solution is basic (measured at 11.7 for 2 wt% NaOCl solution) due to the presence of a strong base (sodium hydroxide, NaOH) and a weak acid (hypochlorous acid, HOCl) at equilibrium.

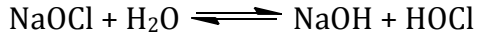

Scheme 4.2: *Equilibrium of sodium hypochlorite in water.*

Hypochlorous acid is a stronger oxidising agent compared to hypochlorite (OCl^-) ion (Paulus, 2005). At basic pH, the equilibrium reaction of NaOCl solution favours the OCl^- ion, resulting in a less effective reaction. Based on Figure 4.12, when a small amount of hydrochloric acid (HCl) was added to the solution, resulting in pH 10 in the solution, a significant increase in the rate of degradation of Rhodamine B was obtained. Further decreases in pH to pH < 7 were too fast to conveniently measure. Behnajady *et al.* (2008) showed that the decolourisation rate of Rhodamine B solely using ultrasound was accelerated at low pH but that it was essentially constant above pH 6. Hence, the results shown here can be attributed to the effect of pH on the hypochlorite equilibrium.

Table 4.4 shows the difference in rate constants at two different pHs, with and without sonication. It is very clear that lowering the pH of the solution accelerates the reaction, which can be explained by the nature of sodium hypochlorite in a solution, as shown in Scheme 4.2.

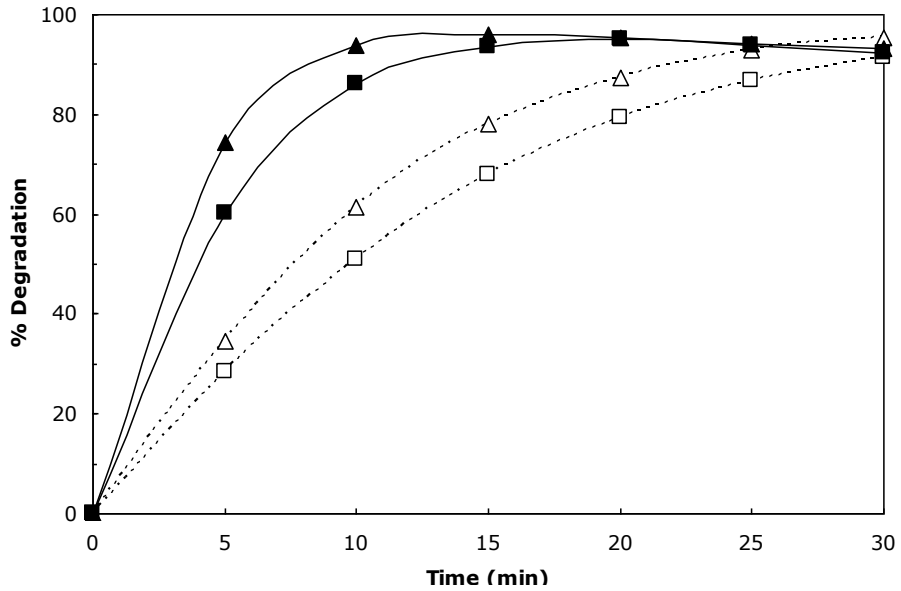

No ultrasound: □ non-buffered; Δ pH=10

Sonochemical reaction (13.1 W cm^{-2}): ■ non-buffered; ▲ pH=10

Figure 4.12: *Effects of pH on the degradation of 5mg/L Rhodamine B with 2% of NaOCl, with and without the presence of sonication.*

Based on Scheme 4.3, addition of hydrochloric acid will result in a reaction with sodium hydroxide to form sodium chloride, causing the concentration of sodium hydroxide to decrease. This will shift the equilibrium of NaOCl (Scheme 4.2) to produce more NaOH, which will also result in more HOCl in the solution, which is the active oxidising agent in the decolourisation of Rhodamine B (Zeng *et al.*, 2009).

Table 4.4: *First order rate constants of the degradation of Rhodamine B with and without 20 kHz sonication at pH 10 and pH 11.7, and their respective R^2 values.*

	No Sonication		**With Sonication**	
pH	11.7	10.0	11.7	10.0
Rate (min^{-1})	0.079	0.103	0.183	0.227
R^2	0.99	0.99	0.99	0.97

$$NaOH + HCl \rightarrow NaCl + H_2O$$

Scheme 4.3

The effects of various concentrations of NaOCl were also studied. Figure 4.13 shows the percentage degradation of Rhodamine B upon sonication at 13.1 W cm^{-2} at various NaOCl concentrations. It can be seen that the rate of reaction increases with the concentration of NaOCl. Significantly, the sonochemical reaction at 0.5 wt% hypochlorite gives a bleaching rate equivalent to 2 wt% in the absence of ultrasound. This shows that the use of NaOCl can be reduced in the presence of ultrasound, which will be beneficial in enhancing the safety of the use of NaOCl and for optimisation of the combination of sonication and bleaching, for various applications – including dental practices.

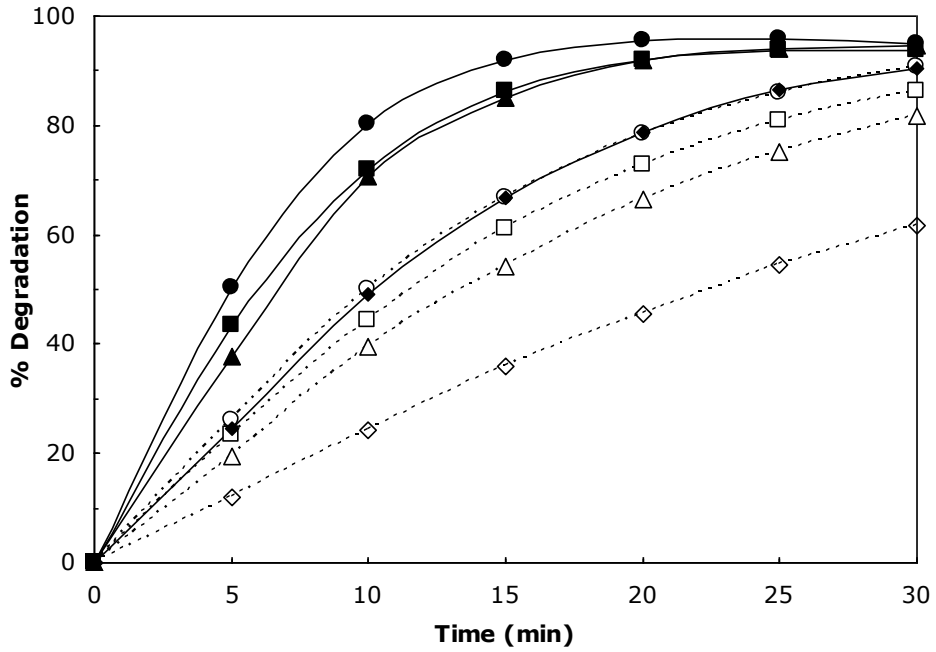

◊, ◆ 0.5 %; Δ, ▲ 1.0 %; □, ■ 1.5 %; ○, ● 2.0 % of NaOCl.
Closed symbols - sonochemical reactions (13.1 W cm^{-2}); open symbols – no ultrasound

Figure 4.13: *Effects of hypochlorite concentration on the bleaching of 5 μg cm^{-3} Rhodamine B.*

Table 4.5 shows the first-order rate constants as a function of ultrasonic intensity and concentrations of sodium hypochlorite in Figures 4.10 and 4.13. The rate constants are comparable with those reported in earlier literature (Behnajady *et al*., 2008, Mehrdad and Hashemzadeh, 2010) although care must be taken in ensuring that the frequency, intensities and experimental conditions are similar.

As expected, the reactions proceed faster with higher energy input. It is clear that the rate of the sonochemical reaction is not simply the sum of the rate of the separate reactions in the absence of ultrasound and the absence of hypochlorite. This suggests that the presence of both creates a synergistic effect and accelerates the rate of reaction due to the presence of both physical (advance mass transfer and local heating due to shockwaves from cavitation) and chemical (production of radicals) effects.

Table 4.5: *First order rate constants for the degradation of Rhodamine B with the 20 kHz ultrasonic probe under various conditions.*

Ultrasound intensity (W cm^{-2})	**2 wt% NaOCl unbuffered**	**2 wt% NaOCl pH = 10**	**No NaOCl**
0.0	0.082	0.105	0.0001
5.10	0.068	0.093	0.006
9.72	0.112	0.127	0.009
13.1	0.170	0.191	0.013
16.2	0.199	0.279	0.015

Concentration of NaOCl / wt%	**Ultrasound 13.1 W cm^{-2}**	**No ultrasound**
0.5	0.081	0.032
1.0	0.129	0.058
1.5	0.129	0.068
2.0	0.170	0.081

Sonolysis of water in the presence of ultrasound to produce hydroxyl radicals is a well known effect (Makino *et al.*, 1983). Undissociated hypochlorous acid could also evaporate into a cavitation bubble and undergo sonolysis, also (Scheme 4.4) producing •OH radicals resulting in higher concentrations of these highly oxidising species, contributing to the acceleration of the degradation process. It was also suggested that the presence of HOCl could result in the production of more hydroxyl radicals to accelerate the degradation of aqueous dyestuffs (Zeng *et al.*, 2009).

$$H_2O \xrightarrow{)))} H^{\bullet} + {}^{\bullet}OH$$

$$HOCl \xrightarrow{)))} {}^{\bullet}OH + Cl^{\bullet}$$

Scheme 4.4: *Sonolysis of water and hypochlorous acid.*

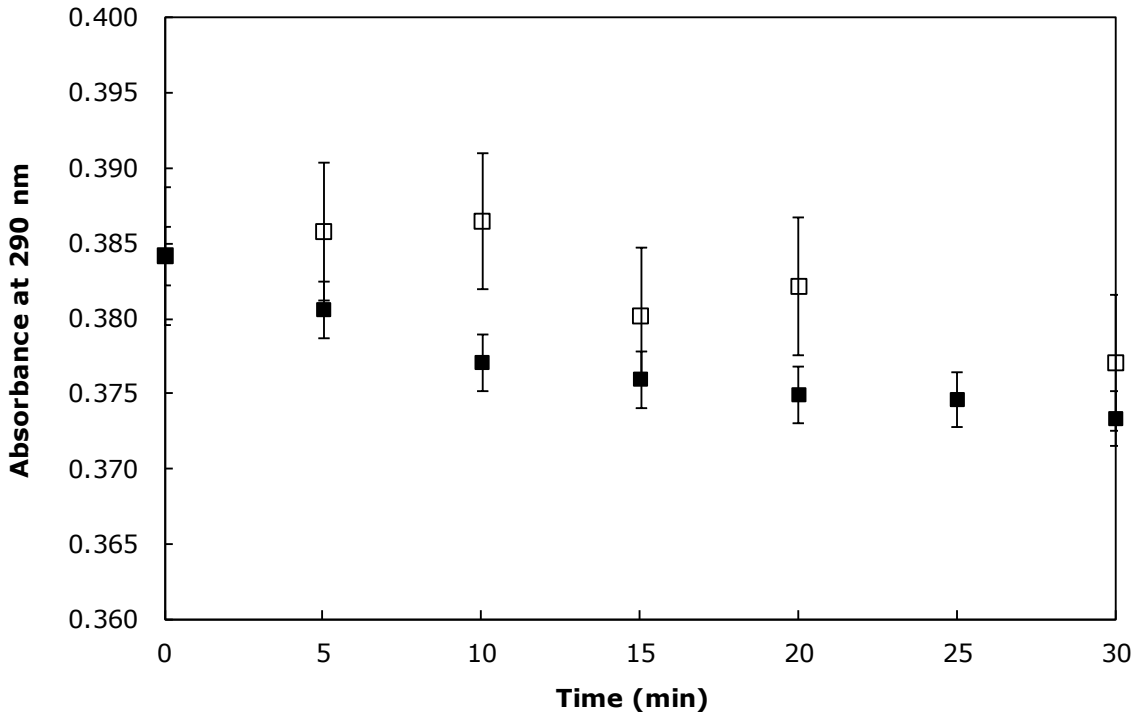

■ without sonication □ with sonication at 13.1 W cm^{-2}, 20 kHz

Figure 4.14: *Absorbance of OCl^- at 290 nm over time.*

To further investigate the reasons for the acceleration, measurements of the concentration of OCl^- in solution were undertaken. The absorbance of a hypochlorite

solution at 290 nm is mainly due to OCl^- (ε_{OCl^-} = 350 $dm^3\,mol^{-1}\,cm^{-1}$; ε_{HOCl} = 30 $dm^3\,mol^{-1}\,cm^{-1}$) (Morris, 1966). Though the results obtained for the absorbance of OCl^- change only slightly, it acts as a good indicator as to what is happening in the reaction. Rhodamine B loses colour when it reacts with HOCl and OCl^-. The concentration of OCl^- therefore falls during the reaction as shown in the absence of ultrasound in Figure 4.14.

On the other hand, the absorbance of OCl^- fluctuates in the presence of ultrasound but remains higher than in the "silent" reaction. The difference in concentration is around 1×10^{-5} mol dm^{-3} which, although small, is similar to the concentration of the dye. The $H^{\bullet}$ and $^{\bullet}OH$ radicals formed during sonolysis, will continuously react with the free chlorine and chloride present in the solution to form OCl^- and HOCl leading to higher concentrations and hence a faster reaction.

In order to better understand the reaction pathway, intermediate products formed were investigated using liquid chromatography coupled with mass spectrometry (LC-MS) for reactions conducted for 30 min with and without NaOCl, taking samples every 5 minutes. As noted above, in the absence of hypochlorite, the reaction is relatively slow and proceeds only to a limited extent. Here, the products detected were derivatives of Rhodamine B (Scheme 4.5) arising from deethylation processes. The initial stages of the sonochemical reaction are therefore similar to those reported for catalysed photodegradations (Chen *et al.*, 2003, Zeng *et al.*, 2009). Even though the deethylation process can be seen clearly, cleavage of the chromophore of Rhodamine B also takes place at the same time, forming new compounds with lower molecular weights which were not detected in our system. An open system was used so that volatile products would be lost.

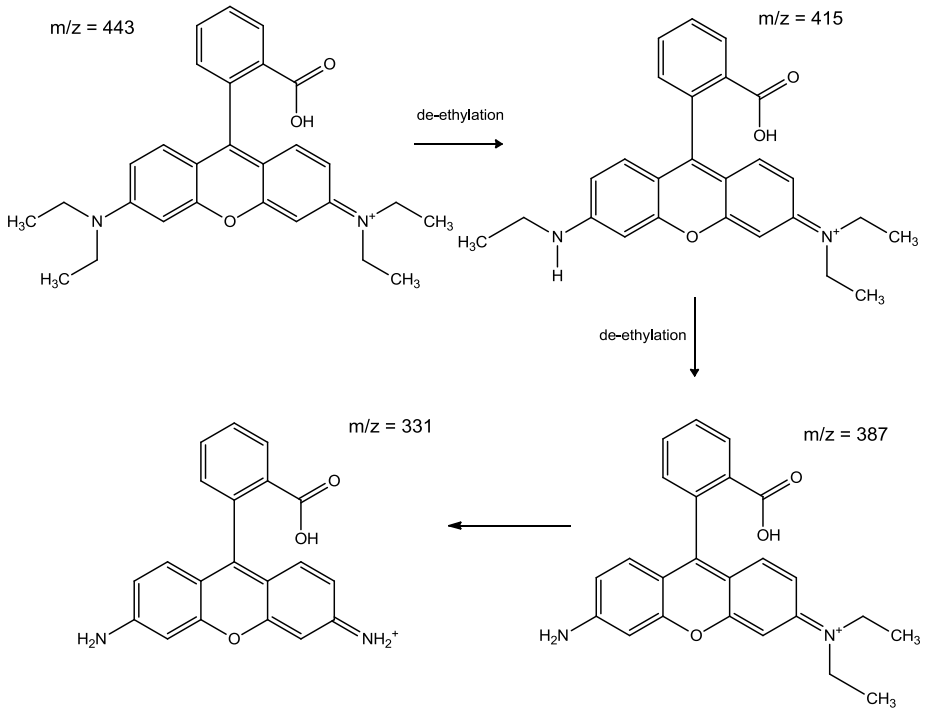

Scheme 4.5: *Proposed reaction pathway of the degradation of Rhodamine B upon sonication, without NaOCl.*

A more complex reaction mixture resulted when the solution was sonicated in the presence of NaOCl. As expected from the spectrophotometric results in Figure 4.10, reaction of NaOCl with Rhodamine B in the presence of ultrasound was very fast and only very small concentrations (*i.e.* 0.2 % w/v of the singly de-ethylated product with m/Z = 415) remained after 30 minutes. Table 4.6 illustrates the molecular weights detected from the mass spectrometer and their intensities (converted into percentages). It can be seen that the results obtained from LC-MS showed various unidentifiable products, with molecular weights ranging from 191 to 511, suggesting that total decolourisation of Rhodamine B occurred during the sonicating process and new, stable products were formed.

In conclusion, the degradation of Rhodamine B seems to be a good indicator of the effects of NaOCl, due to the strong oxidising nature of sodium hypochlorite. The results showed that the presence of NaOCl accelerates the rate of reaction. Also, the effects of pH and concentration play a vital role in the rate of degradation of Rhodamine B, and this can be incorporated into the endosonic source as a suggestion to improve the cleaning efficiencies for root canal treatments. Further to that, mass

spectrometry results showed that the degradation pathway for Rhodamine B is very much accelerated in the presence of NaOCl in such that there is no structure related to the core structure of Rhodamine B that can be detected even after a short sonication time.

Table 4.6: *Molecular weights of the degradation products and their percentage intensities upon sonication of Rhodamine B with NaOCl after 30 minutes sonication at 5.10 W cm^{-2}.*

Molecular weight (m/Z)	Percentage intensity (%)
191	15.0
214	5.78
236	23.9
415	0.18
443	8.57
483	1.36
511	45.2

4.2.1.2 Endosonic Sources

As mentioned in the beginning of the chapter, irrigants were used in endodontic treatment as a disinfectant to kill any bacteria present in the infected root canal. With sodium hypochlorite being one of the most commonly used irrigant, sonication of Rhodamine B in the presence of NaOCl was performed under different conditions in order to compare the results to the sonication using the 20 kHz ultrasonic probe.

An example of the percentage degradation by an endosonic file is shown in Figure 4.15. It can be noted that there is a slight increment in the percentage of degradation of Rhodamine B upon sonication in the absence of sodium hypochlorite, and the results have shown a similar trend to that observed on the 20 kHz ultrasonic probe shown in Section 4.2.1.1.

Similar experiments were carried out for each different endosonic files, and the final percentage degradations were collated in Figure 4.16. It can be seen that low power sonication has little to no effect on the degradation of Rhodamine B as compared to the control experiments when sonication is absent. This may probably be due to cavitation threshold of the endosonic instruments, where there is insufficient energy produced during the sonication at such a low power to produce useful cavitation which will aid in the formation of •OH radicals to accelerate the rate of reaction.

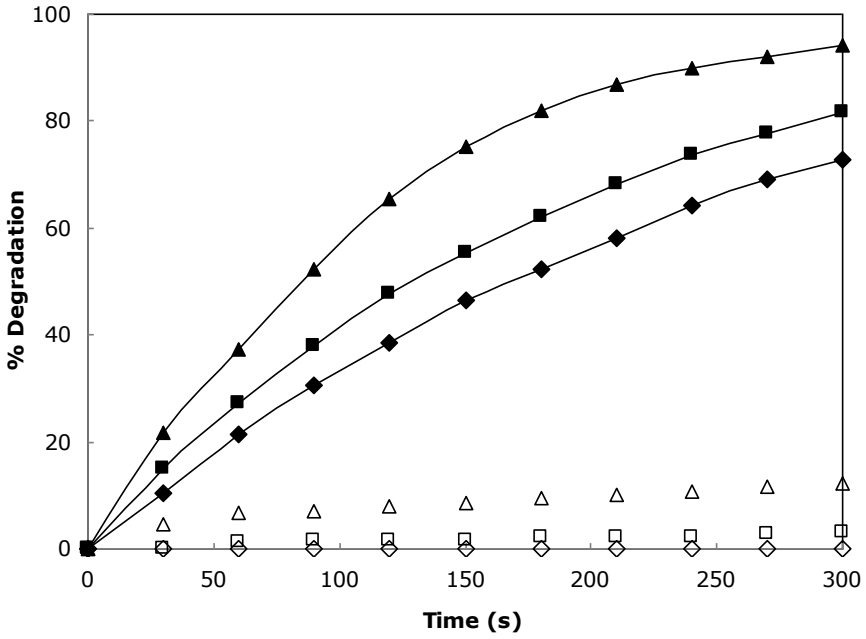

Δ, ▲ no ultrasound; □, ■ Power 5/10; ◊, ◆ Power 10/10

Closed symbols – 2.0 wt% NaOCl solution ; open symbols – no NaOCl

Figure 4.15: *Percentage degradation of Rhodamine B in the presence of 2 wt% NaOCl at various arbitrary powers for CT-4.*

In general, the UT-4 tips showed lower percentage degradation at the highest sonicating power (Power 10/10). This, has once again proven the fact that the insufficient surface area of the tips have resulted in lack of efficiency in producing sufficient negative pressure, producing many fewer •OH radicals. This is supported

by the results shown in Chapter 3 for the oxidation of Fe^{2+} to Fe^{3+} in Fricke Dosimetry (Section 3.2), the production of sono(chemi)luminescence (Section 3.3) as well as the ability of the endosonic file to produce high velocity flow in the surrounding fluid (Section 3.5).

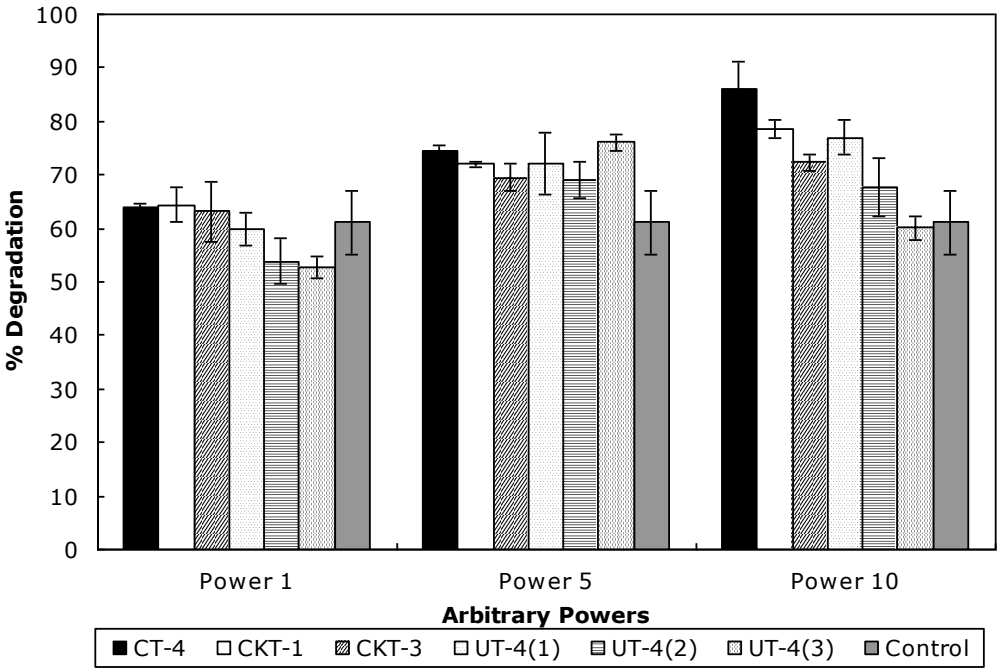

Figure 4.16: *Collated percentage degradation of Rhodamine B in the presence of 2 wt% NaOCl upon five minutes sonication at various arbitrary powers for all endosonic files.*

At low and medium powers (Power 1/10, 5/10), there seemed to be no significant difference in the percentage degradation of Rhodamine B for all the endosonic files (ANOVA, p-value > 0.05). This suggests that there are other factors playing in the degradation of Rhodamine B apart from the production of cavitation, such as the ultrasonic stirring effect of the dental tips, accelerating the rate of degradation.

CT-4 appeared to be more effective in degrading Rhodamine B in the presence of NaOCl compared to all the other dental tips at the highest sonicating power (Power 10/10). This is consistent with all previous experiments performed on the

characterisation of the endosonic files, suggesting that even if cavitation is not the sole factor contributing to the cleaning efficiency; it plays an important role in accelerating the cleaning process.

Similar to the experiments performed on the 20 kHz ultrasonic probe, a *pseudo*-first order reaction was expected due to the vast excess of NaOCl for the sonication using the endosonic files (Figure 4.15). Figure 4.17 shows the first order rate plot of the degradation of Rhodamine B in 2 wt% NaOCl for CT-4.

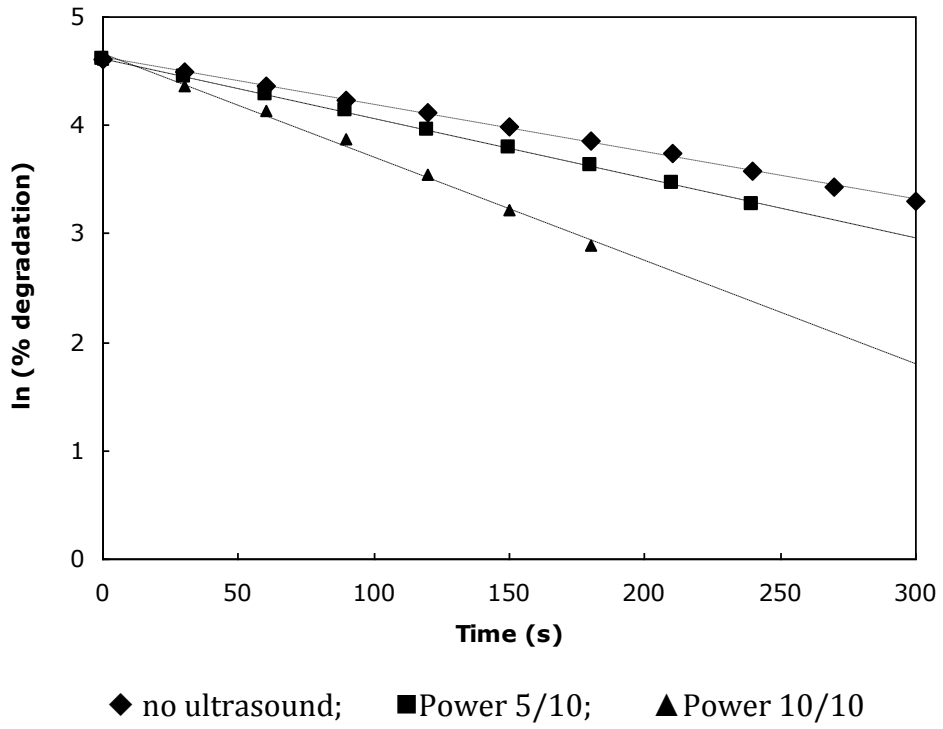

Figure 4.17: *First order rate plot of the degradation of Rhodamine B in the presence of 2 wt% NaOCl upon sonication under different conditions for CT-4.*

The rate constants for the degradation of Rhodamine B with and without NaOCl were collated in Table 4.7 for three different endosonic file designs (CT-4, CKT-1 and UT-4(2)). As expected, the presence of sodium hypochlorite accelerated the reaction by more than ten-fold upon sonication. Sonication of Rhodamine B in the absence of NaOCl did not show much sign of degradation, suggesting that the ultrasonic intensities of the endosonic systems are not strong enough to show

significant changes in the absorbance of Rhodamine B. However, the results have clearly shown that sonication of NaOCl with Rhodamine B have proven to be a good indicator of the ultrasonic cleaning efficiencies of the endosonic files used, and this can be further correlated to the characterisation results of the files.

Table 4.7: *First order rate constants of the degradation of Rhodamine B with and without 2 wt% NaOCl under different conditions for CT-4, CKT-1, and UT-4(2).*

	Rate Constants ($\times 10^{-3}$ min^{-1})					
	CT-4		**CKT-1**		**UT-4(2)**	
	With 2 wt % NaOCl	Without NaOCl	With 2 wt % NaOCl	Without NaOCl	With 2 wt % NaOCl	Without NaOCl
No Ultrasound	3.48	0.00	3.48	0.00	3.48	0.00
Power 5/10	5.42	0.09	4.10	0.03	3.50	0.004
Power 10/10	9.07	0.60	5.01	0.30	3.90	0.01

In conclusion, this series of experiments have proven that sonication accelerates the rate of cleaning and that the reactions follow a *pseudo*-first order reaction rate in decolourising Rhodamine B with and without sodium hypochlorite. This may be due to both the presence of physical (improved mass transfer) and chemical (production of radicals) effects of ultrasound. Different conditions will affect the rate of sonication, such as the concentration of NaOCl and the operating pH of the system. Also, different endosonic files have different rates of degradation of Rhodamine B at the highest sonication power, with CT-4 having a higher percentage degradation compared to the other endosonic files. The results tally with previous characterisation of the endosonic files and have strong relation to the shape of the files.

4.2.2 Removal of Rhodamine B with Hydrogen Peroxide

Hydrogen peroxide, being a non-chlorine oxidising agent, is the second most commonly used irrigant used in endodontics after sodium hypochlorite. Similar experiments were performed using various concentrations of hydrogen peroxide, to degrade 5 μg cm^{-3} of Rhodamine B. Reviews on endodontics state that the maximum percentage of H_2O_2 used is 3 wt%, higher concentrations of H_2O_2 are carcinogenic and dangerous for oral use (Marshall *et al.*, 1995).

To initiate the experiment, 3 wt% of H_2O_2 was chosen. The experiments were run in a similar way to those for the sodium hypochlorite, and were divided into two sections: with the 20 kHz ultrasonic probe and with the endosonic files.

4.2.2.1 Removal of Rhodamin e B with the 20 kHz Ultrasonic Probe

Sonication was performed using the 20 kHz ultrasonic probe to decolourise 5 μg cm^{-3} in the presence and absence of 3 wt% H_2O_2 for 30 minutes with different intensities.

Figure 4.18 shows the percentage of Rhodamine B degradation upon sonication of 3 wt% H_2O_2 at various ultrasonic intensities. There is a clear threshold between intensities 9.72 W cm^{-2} and 13.1 W cm^{-2} where the percentage of Rhodamine B degradation has doubled, suggesting that the cavitation threshold of the system lies in that range. The stated results obtained correlate with previous results using the 20 kHz ultrasonic probe – both for the SCL (Section 3.3) as well as the degradation of Rhodamine B with sodium hypochlorite (Section 4.2.1.1). Increasing the ultrasonic intensity from 13.1 W cm^{-2} to 16.2 W cm^{-2} did not further increase the dye decolourisation any further, and this phenomenon is also seen in the previous section – which confirms that the process has come to the limit of the ultrasonic probe.

Further to this experiment, a comparison between the presence and absence of H_2O_2 was conducted. Figure 4.19 shows the final percentage dye degradation after

30 minutes of sonication at various ultrasound intensities with and without 3 wt% of H_2O_2. The results show that the presence of H_2O_2 greatly decreases the dye degradation by approximately 10 to 15 percent, suggesting that the presence of hydrogen peroxide inhibits the dye degradation process – although the main factor causing this still remains ambiguous at this stage. This brings the need to further investigate the situation in order to draw conclusions on the cleaning properties of hydrogen peroxide.

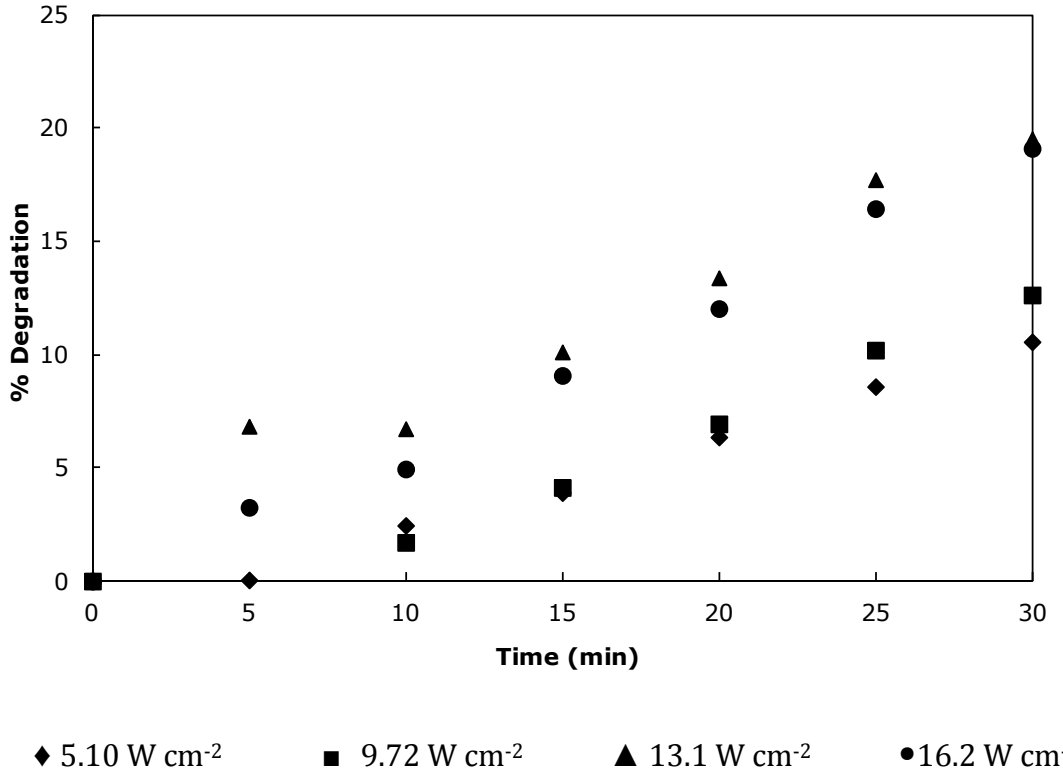

Figure 4.18: *Percentage degradation of 5 μg cm^{-3} of Rhodamine B in the presence of 3 wt% H_2O_2 upon sonication for 30 minutes of sonication using the 20kHz ultrasonic probe.*

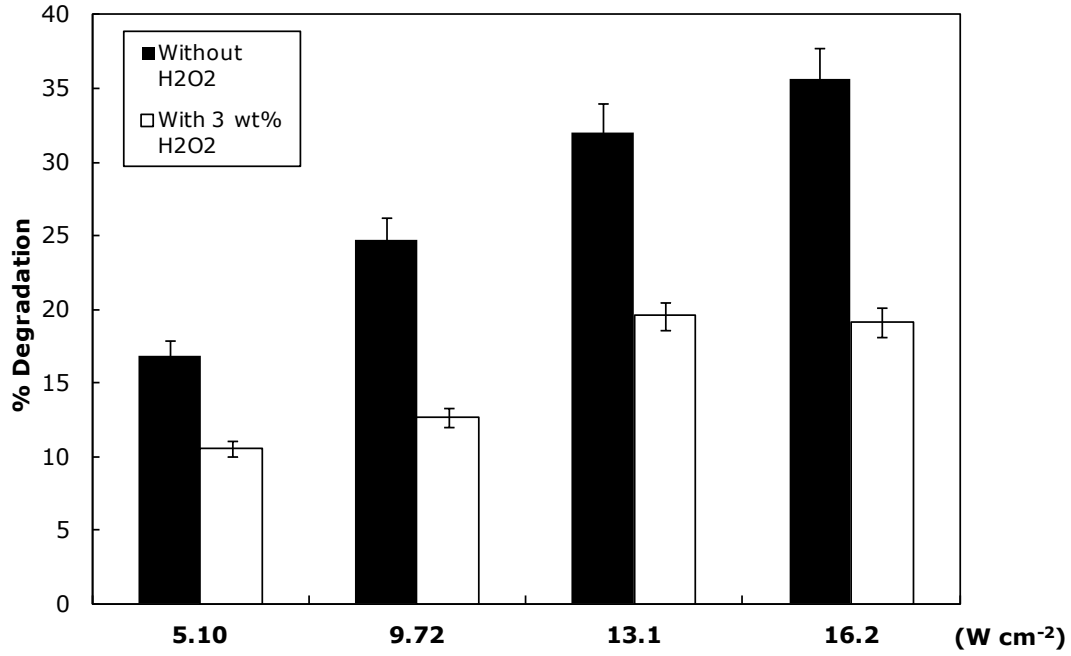

Figure 4.19: *Percentage dye degradation upon sonication for 30 minutes with the 20kHz ultrasonic probe at various intensities with and without 3 wt% H_2O_2.*

Similar to the experiments performed on the degradation of Rhodamine B with NaOCl, due to vast excess of H_2O_2 present in the solution, a *pseudo*-first order reaction is obtained (Figure 4.20). Following sonication of 3 wt% H_2O_2 at various ultrasonic intensities, a control experiment was conducted to investigate the effects of sonication on hydrogen peroxide. Experiments were performed at different concentrations of hydrogen peroxide, with and without sonication. For all concentrations of H_2O_2 used, there is no dye degradation without any form of sonication. On the other hand, there is a significant amount of dye degradation when sonication was performed on the dye and peroxide mixture, with results collated in Figure 4.21, where first-order rate constants were plotted.

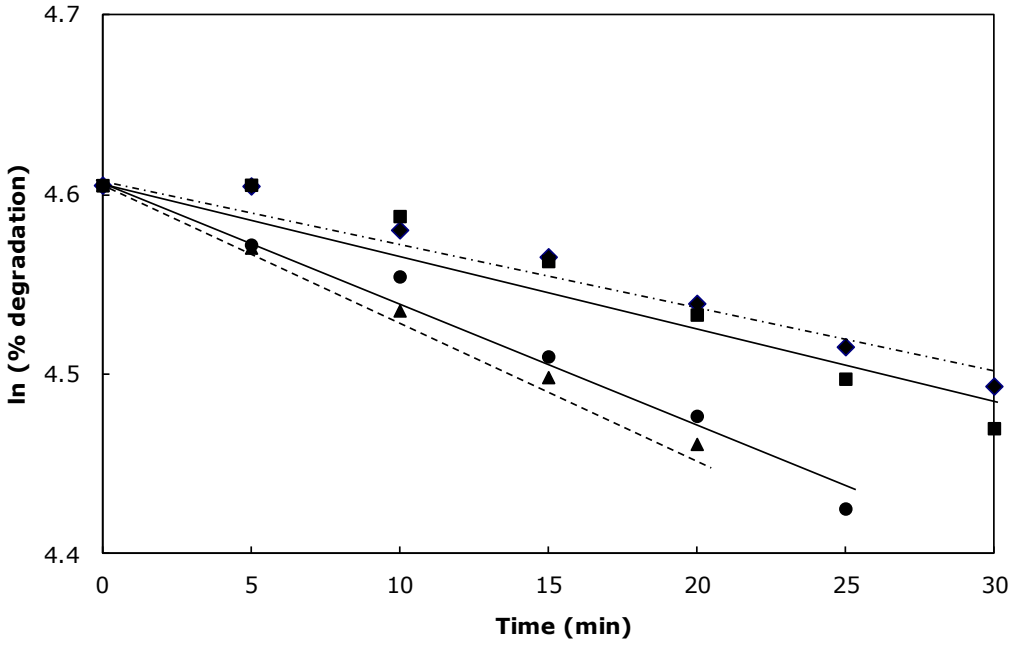

♦ 5.10 W cm^{-2} ■ 9.72 W cm^{-2} ▲ 13.1 W cm^{-2} ● 16.2 W cm^{-2}

Figure 4.20: *Percentage degradation of 5 μg cm^{-3} of Rhodamine B in the presence of 3 wt% H_2O_2 upon sonication for 30 minutes of sonication using the 20 kHz ultrasonic probe.*

Once again, it can be seen that when the presence of hydrogen peroxide greatly reduce the dye degradation process. There is an initial significant (ANOVA, p-value < 0.05, based on triplicate experiments) increase in the rate of removal of the dye at approximately when 0.005 wt% H_2O_2 is present, but has thereafter reduced the rate of removal significantly upon further addition of the peroxide. To clarify this phenomenon, sonoluminescence photographs were taken at the same intensities in the presence of the same series of hydrogen peroxide concentrations to verify the results obtained, which will be presented in Section 4.2.2.2.

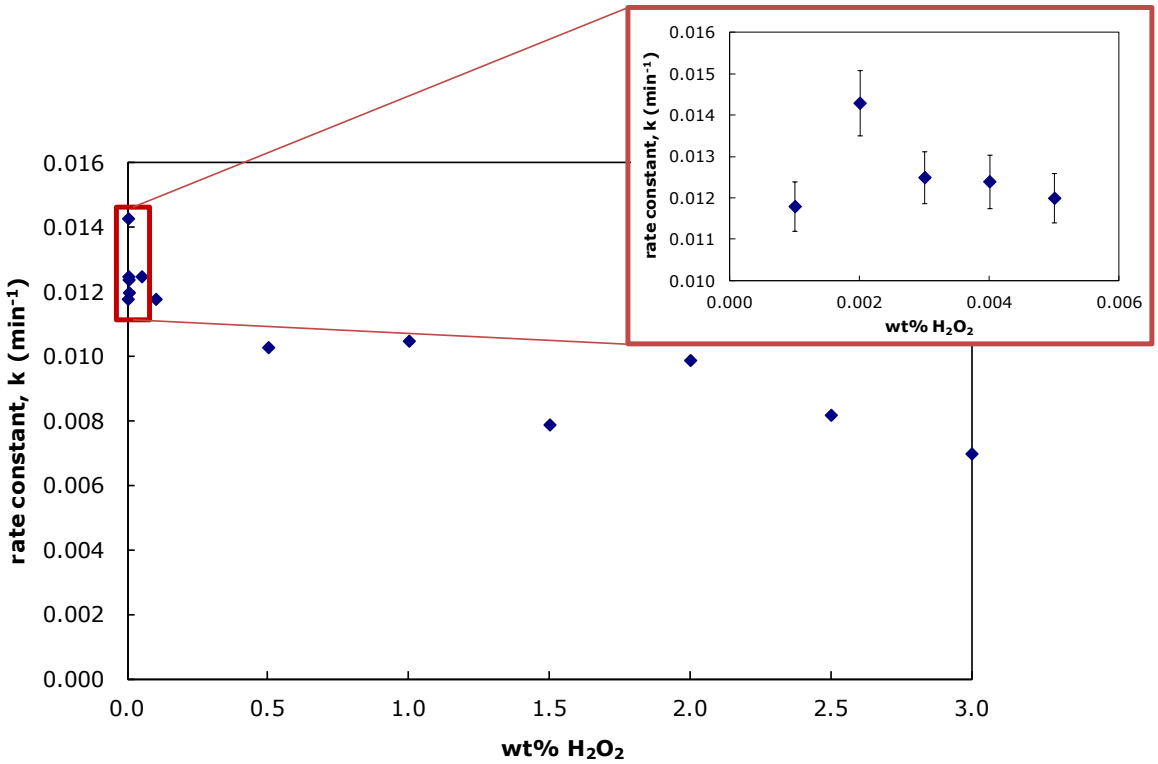

Figure 4.21: *First order rate constants for the degradation of Rhodamine B in the presence of various concentrations of hydrogen peroxide upon sonication for 30 minutes at 13.1 W cm^{-2}.*

4.2.2.2 Sonoluminescence of the 20kHz ultrasonic probe in the presence of H_2O_2

In order to gain a better understanding and to clarify the findings obtained from the dye removal experiments in the previous section, sonoluminescence (SL) was performed on the 20 kHz ultrasonic probe in the presence of various concentrations of hydrogen peroxide. As the sonoluminescence signal is relatively much lower compared to the SCL signal, the solutions of deionised water were pretreated with argon for 30 minutes prior to the experiments. Images were captured in a light-proof box, with the image to object ratio of 1:1.5, at an exposure time of 30 seconds.

Sonoluminescence of deionised water in the presence of various concentrations of hydrogen peroxide shows an initial increase in SL produced, and then continued to decrease as the concentration of H_2O_2 increased (Figure 4.22). The approximate concentration threshold of H_2O_2 for the increment in SL produced was found to be 0.005 wt% H_2O_2, and the sonoluminescence activity declined after the said concentration. One way ANOVA and Tukey Post-Hoc tests on the experimental results showed that the light intensity produced by SL can be grouped into two different groups: (i) 0 to 0.05 wt% H_2O_2 and; (ii) 0.1 to 3 wt% H_2O_2. Light emission showed no significant difference (ANOVA, p-value > 0.05) for sonication of H_2O_2 from 0 to 0.05 wt%, but is significantly different (ANOVA, p-value < 0.05) for concentrations 0.1 wt% to 3 wt% H_2O_2.

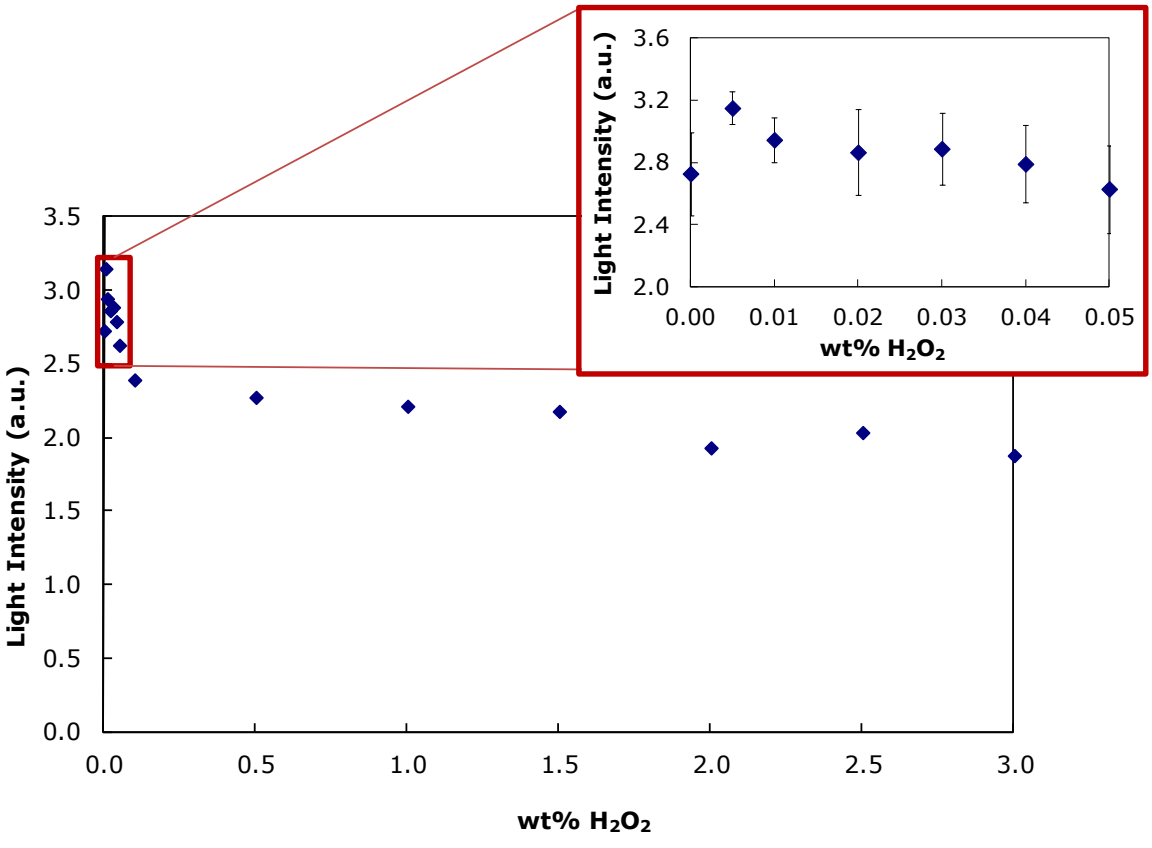

Figure 4.22: *Soluminescence light intensity upon sonication at 13.1 W cm^{-2} on the 20 kHz ultrasonic probe in the presence of various concentrations of hydrogen peroxide.*

4.2.2.3 Effects of sonication in the presence of H_2O_2

From the results obtained – both from dye removal and sonoluminescence, we can come to a conclusion that there is an upper limit of hydrogen peroxide to act as an oxidising agent in the sonication process. In the presence of ultrasound, the addition of high concentrations of peroxide inhibits the cavitation activity, which will in turn affects the cleaning efficiency in endodontic treatments. Merouani *et al*. (2010) have recently performed a series of experiments on the sonochemical degradation of Rhodamine B in the presence of various concentrations of hydrogen peroxide using a 300 kHz ultrasonic plate transducer, and has obtained similar results, where the rate of dye removal had increased up to the addition of 100 μg cm^{-3} H_2O_2 (Merouani *et al*., 2010), and decreased thereafter. Similar results have also been reported by Behnajady *et al*. (2008) and Mehrdad *et al*. (2010), which further strengthens the results obtained above.

This phenomenon, as described by Merouani *et al*. (2010), is due to the scavenging properties of hydrogen peroxide. Behnajady and co workers (2008) pointed out that there is a certain concentration threshold for hydrogen peroxide to produce •OH radicals – which, in our system – was found to be at 0.005 wt% H_2O_2. They have proved that sonication of hydrogen peroxide at this concentration will result in more •OH radical production, which will then aid in the dye removal process. Similarly, when there are sufficient radicals present in the system, there had to be high amount of transient cavitation in the system to produce sonoluminescence.

Above the concentration threshold, hydrogen peroxide will act as a radical scavenger in the system, where it will tend to react with the •OH radicals present in the system to produce superoxide radicals (•OOH), as shown in Scheme 4.6 below. The reactivity of superoxide radicals is much lower than hydroxyl radicals, hence this reduces the rate of reaction due to the absence of sufficient quantities of •OH radicals when a high concentration of H_2O_2 is present.

$$H_2O_2 + \bullet OH \rightarrow H_2O + HO_2\bullet$$

Scheme 4.6: *Hydrogen peroxide as a radical scavenger to produce superoxide radicals.*

Hydrogen peroxide becomes very unstable in high temperatures, with a heat of formation of -187.9 kJ mol^{-1} and heat of decomposition of -98.3 kJ mol^{-1} (Clarke, 2009), resulting in higher tendency of decomposition into water and oxygen (Scheme 4.7). It was noted that the rate of decomposition increases with temperature at about 2.3 times for every 10°C rise (Clarke, 2009). Shockwaves of high pressure and temperature produced during the collapse of transient cavitation may increase the decomposition rate of hydrogen peroxide, resulting in more water and oxygen in the solution, which will then reduce the amount of 'active' hydrogen peroxide present in the solution. Oxygen formed will then diffuse into the cavitation bubbles formed, resulting in less violent cavitation collapse, reducing the amount of •OH radicals formed, hence reducing the rate of decomposition of Rhodamine B.

H_2 (g) + O_2 (g)	⟶	H_2O_2 (l)	- 187.9 kJ mol^{-1}
H_2O_2 (l)	⟶	H_2O (l) + 0.5 O_2 (g)	- 98.3 kJ mol^{-1}

Scheme 4.7: *Heat of formation and decomposition of liquid hydrogen peroxide.*

Sonication of hydrogen peroxide with the endosonic source did not show significant changes out due to the relatively low amount of dye removal, resulting in inconsistencies in the rate of reaction as recorded from the UV-visible absorption spectra due to equipment constraints. However, from this study on the 20 kHz ultrasonic probe, there is a very clear indication of the implications of various concentrations of hydrogen peroxide present during sonication.

There have been reviews on the different irrigants used in endodontic treatment, and they have all concluded that hydrogen peroxide is a less effective irrigant in comparison to sodium hypochlorite, even at much higher concentrations (Vijaykumar *et al.*, 2010). This series of experiments performed might be able to explain the reason behind the entire process. Hydrogen peroxide acts as an oxidizing agent due to its due to its instability in the compound, and will reduce to water

compound – which is a much more stable molecule. However, in the presence of ultrasound, the production of radicals in the sonication system will inhibit the oxidizing properties of hydrogen peroxide, hence reducing the rate of reaction. With this, it should give a better clinical insight of the use of irrigants and their reactions that occur when sonication is present at the same time.

4.3 Removal of Surface Impurities

Clinical endodontic treatments are performed to remove dentin debris in the infected root canal. This debris includes surface impurities on the walls of the infected root canal, bacteria, dead tissue, and so on. Clinical research on cleaning efficiencies is most commonly performed using extracted root canals (Brown *et al*., 1995, Zmener *et al*., 2005, Aasim *et al*., 2006, Passarinho-Neto *et al*., 2006, Singla *et al*., 2010) – and this increases the inconsistencies in the experiments due to different structures in the human's root canal.

In this study, two methods were used to determine the cleaning efficiencies of the endosonic files. Here, we have used two different approaches to determine the efficiencies of the endosonic files in removing surface impurities by evaluating the percentage of permanent marker ink removed on a microscope cover slip and the percentage of hydroxyapatite paste removed in a channel upon sonication.

4.3.1 Removal of Permanent Marker Pen Ink

Ink removal experiments were performed by coating a layer of permanent marker ink onto the surface of a microscope cover slip of 22 mm × 22 mm, as shown in Figure 2.7 in Section 2.6.3.

There have been studies on various methods used to determine the cleaning efficiencies of an ultrasonic source. Gaquere-Parker *et al*. (2009) have used a 20 kHz

ultrasonic horn for ink removal on paper while Krefting *et al*. (2004) used high-speed imaging to examine the ink removal on a glass sheet upon sonication using a 40 kHz ultrasonic bath. They have observed that the ink was removed at the pressure antinodal points when the glass sheet is inserted perpendicularly into the ultrasonic bath. By applying the similar concept, permanent marker ink was coated onto a microscope cover slip, and then placed into the silicone rubber model channel to evaluate the areas of ink removal in a confined space.

Figure 4.23 shows the video frames taken using a high-speed video camera (refer to Chapter 2, Section 2.7 for specifications) of the ink removal at various time intervals upon sonication at Power 10/10 with CT-4 in a 3 mm silicone rubber channel. The areas of ink removal coincide with the areas where cavitation occurs – which happens to be the antinodal points for the vibration movement of the tip. Similar results of ink removal at the antinodal points were obtained upon sonication for 30 seconds for all the endosonic files used in this study (CKT-1, CT-4 and UT-4(2)), as shown in Figure 4.24.

With the aid of ImageJ, the percentage of ink removal after 30 seconds of sonication can be obtained from the digital images obtained from both the high-speed video camera and a CCD digital SLR camera (Canon 500D). The collated results of the percentage ink removed are shown in Figure 4.25.

Results showed that CT-4 removed permanent ink most effectively, followed by CKT-1 and UT-4(2). This gives a fairly good correlation with the SCL (Section 3.3), PIV (Section 3.6) and dye degradation (Section 4.2) experiment results. As mentioned earlier, there is no particular way to determine which of the parameters is particularly important and plays the most important role in sonochemical cleaning. Up to this point, it can be concluded that all factors play an equal importance in sonochemical cleaning – the presence of transient cavitation also comes with high acoustic streaming, production of microjets and radicals during cavitation collapse.

The absence and/or limitation of any of the above factors could result in great reduction in the cleaning efficiency – an example of what is shown in UT-4.

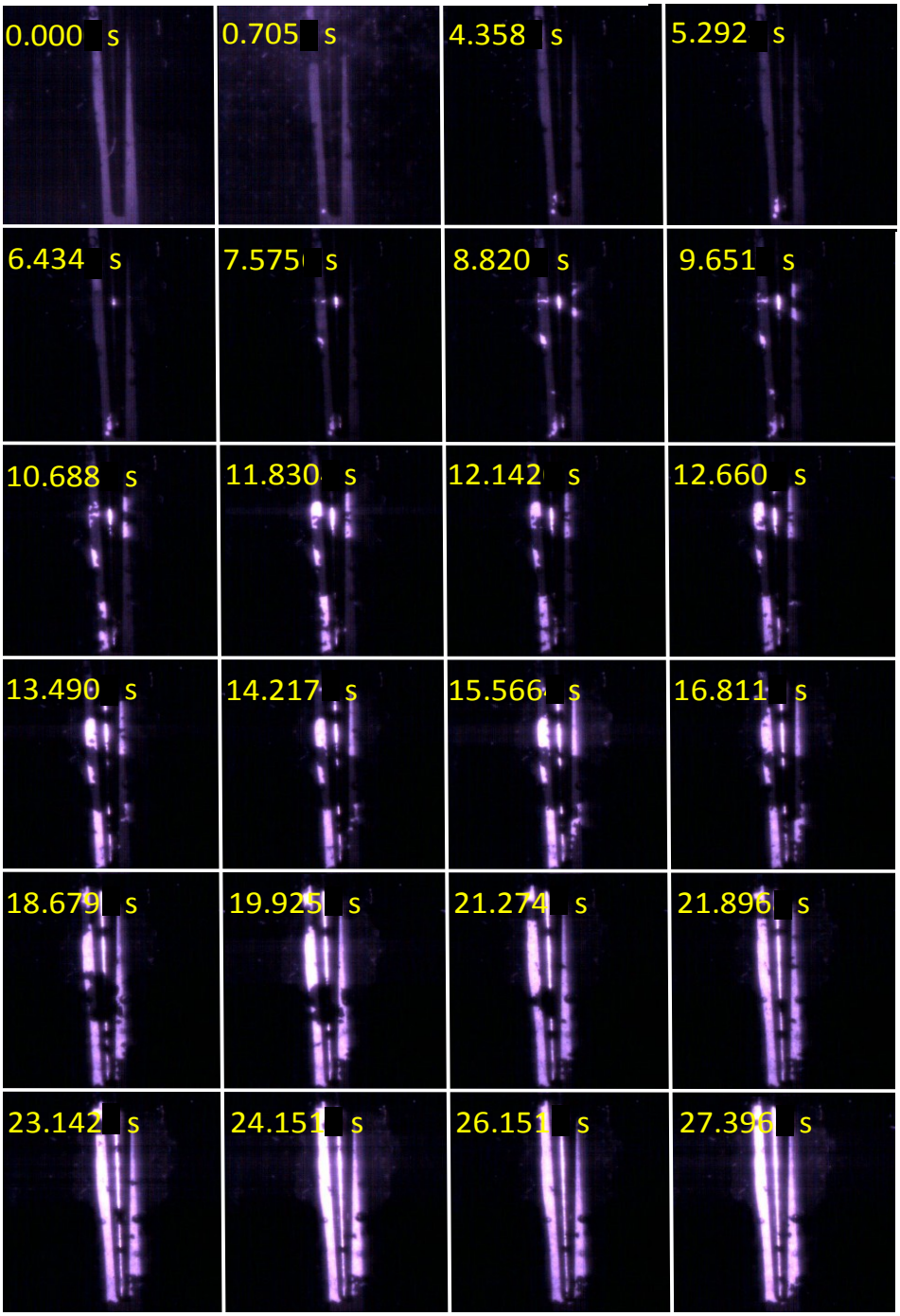

Figure 4.23: *High-speed video frames at different time intervals showing the ink removal in a model channel for CT-4 at Power 10/10.*

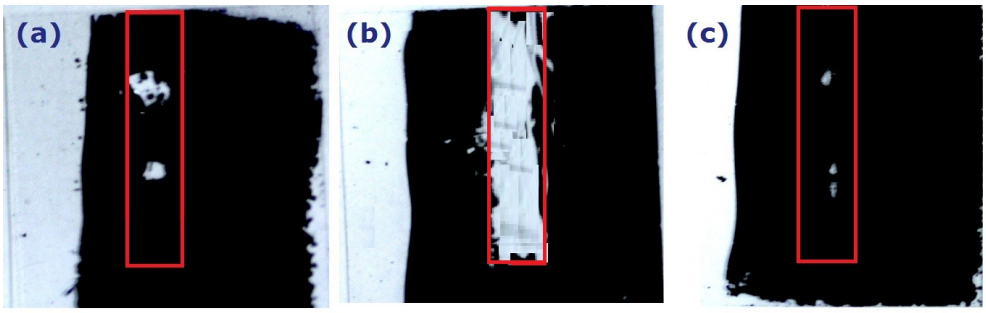

Figure 4.24: *Areas of ink removal upon sonication for 30 seconds at Power 10/10 for: (a) CKT-1; (b) CT-4; and (c) UT-4(2).*

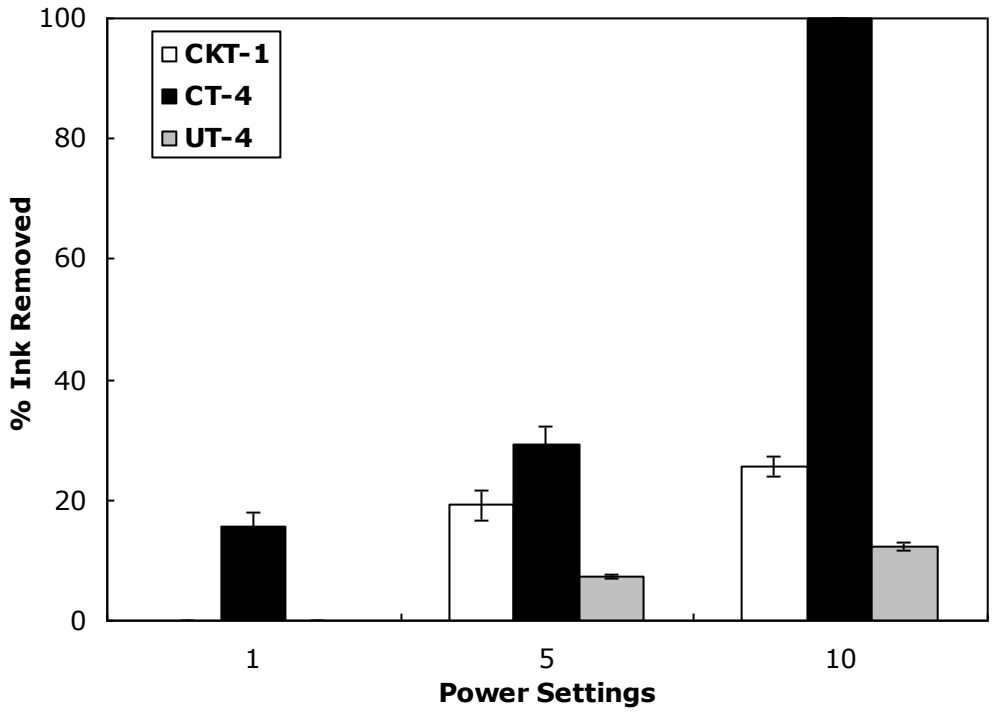

Figure 4.25: *Percentage of permanent marker ink removed upon sonication for 30s in distilled water for the three endosonic files.*

On a separate observation, it was interesting to find out that, from the frames captured using a high-speed video camera (Figure 4.23), the ink removal during sonication always starts at the free end of the dental tip, and is then followed by the other vibration antinodal point in the middle of the tip – and this scenario is also seen in CKT-1 during sonication. Though these two areas are the places where cavitation occurs, it is interesting to know the reason behind this finding.

In a coincidental event, looking at the cavitation clouds on a dental tip during sonication using a high-speed video camera at 1000 frames per second, we found an interesting observation – where the cavitation clouds gets generated at the free end of the tip upon initiating the sonication, followed by the generation of cavitation clouds at the other vibration antinode approximately 200 milliseconds later. Figure 4.26 illustrates the video frames obtained during the sonication of CT-4 at Power 10 in silicone oil of viscosity of 50 cSt for better illustration of the cavitation clouds, as observed by Skinner (Skinner, 1904).

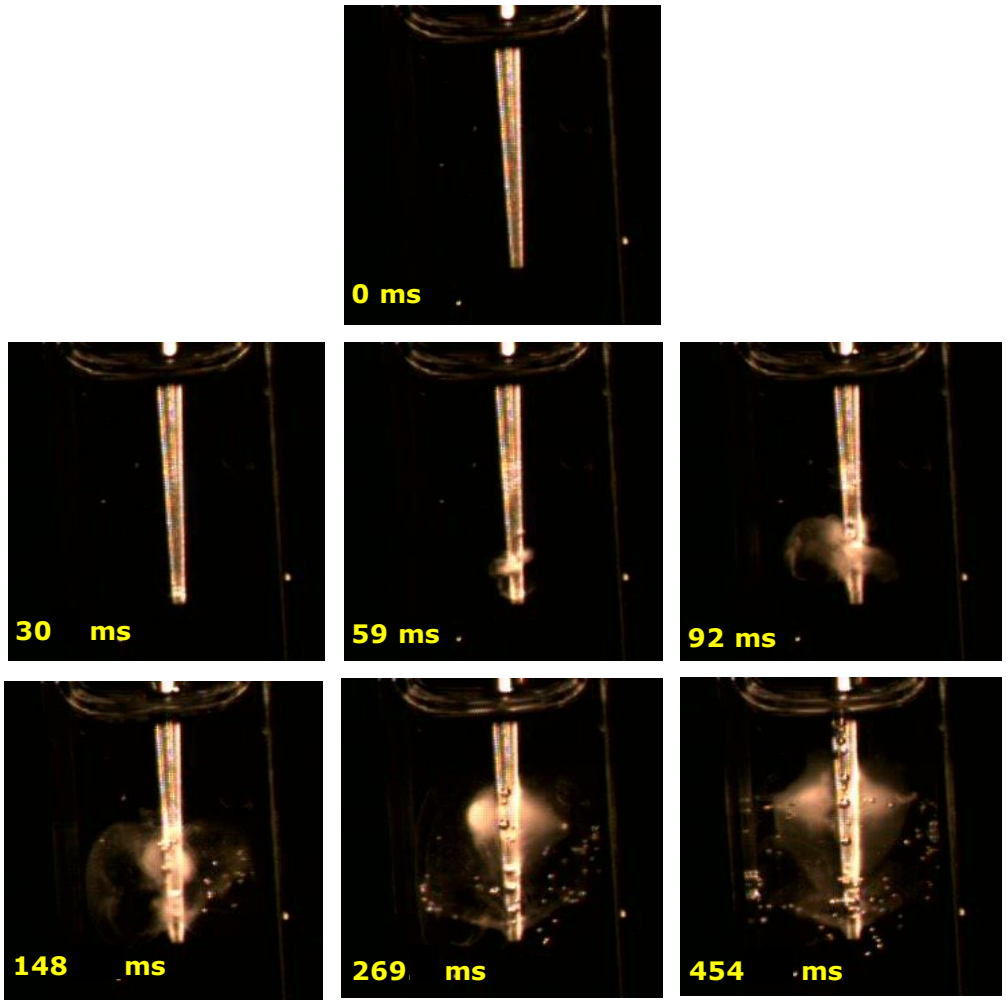

Figure 4.26: *High-speed video frames at different time intervals to illustrate the formation of cavitation clouds during sonication of CT-4 at Power 10/10, performed in a 1 cm × 1 cm polymethacrylate cuvette.*

From this, we can suggest that the initiation of the jets of cavitation clouds at the bottom end of the tip might be the contributing factor to the ink removal in the

channel. Both Figure 4.23 and 4.26 show comparable time frames of both the ink removal and the production of visible cavitation clouds at the two vibration antinodal areas. This result also correlates well with the SCL image obtained for the CT-4 (Figure 3.14), where the SCL produced has the greatest light intensity at the end of the tip, with a wide spread of SCL emission in the luminol solution – hence contributing to the cleaning efficiency.

4.3.2 Removal of Hydroxyapatite Paste

Hydroxyapatite is one of the major contents in the bone structure in the teeth. Tooth enamel, dentin and calculus (tartar) are largely made up of hydroxyapatite (Park, 2008). Several scientists have previously performed experiments on the removal of impurities to assess the cleaning efficiencies of the endosonic files used. For example, Jensen *et al.* (1999) have used image analysis method to evaluate the percentage of debris present in molar root canals upon sonication, while van der Sluis and co-workers (2007b) have studied the percentage removal of calcium hydroxide ($Ca(OH)_2$) paste packed into an artificial groove to evaluate the cleaning efficiencies of various irrigation methods used, and showed that passive ultrasonic irrigation with 2 wt% of NaOCl was more effective in removing $Ca(OH)_2$ compared to syringe delivery irrigation.

Jiang *et al.* (2010) have also performed studies on the cleaning efficiencies of various endosonic devices by evaluating the percentage of artificial debris removed upon sonication. They have then compared their results of the final percentage of debris removal to the velocimetry of the endosonic files in a confined space, and have concluded that there is a correlation between the acoustic streaming and the cleaning efficiencies.

By adapting the experimental methods performed previously in the literature, in this experiment, a known amount of hydroxyapatite (HA) paste was packed into a model channel to mimic more closely the contents of the root canal, and the

percentage of hydroxyapatite removed upon sonication with the endosonic files was recorded. The model channel used was similar to the ones used to evaluate the percentage of emulsion formed in a side channel. The HA paste was packed into the side channel and the bottom of the channel, as shown in Figure 4.27. Sonication was performed for 2 minutes on three dental tips: CKT-1, CT-4 and UT-4(2), at Powers 1/10, 5/10 and 10/10 respectively.

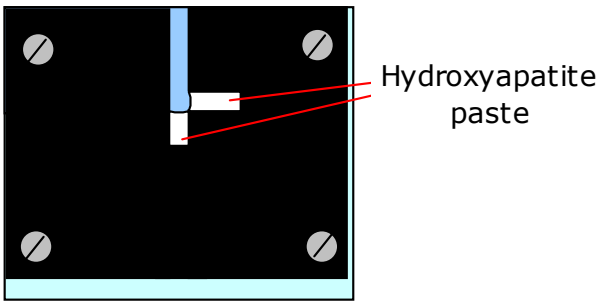

Figure 4.27: *Hydroxyapatite packed into a model channel.*

The evaluation of the percentage hydroxyapatite removed was done by image manipulation, comparing the percentage areas of hydroxyapatite remaining in the channel and the colour intensity along the channel, taking into account the following assumptions:

i) HA paste is uniform and will have the same colour.
ii) Removal of HA paste is based on some dissolution into the solution but it is assumed to be insignificant in comparison to sonication.
iii) Reduction in colour intensity indicates the reduction in the amount of HA in the channel.

The final results presented in this experiment are based on the percentage removal of HA paste in both the side and at the bottom of the channel after normalizing both the percentage of area and the colour intensity in the region of interest studied. Figure 4.28 illustrates the experimental setup with an endosonic file inserted into the model root canal packed with HA paste, before and after sonication.

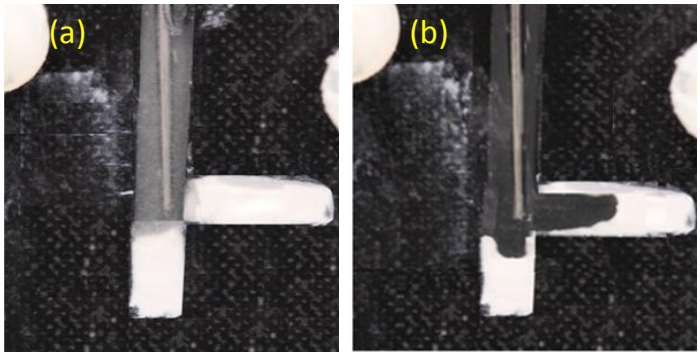

Figure 4.28: *An example of the experimental setup with hydroxyapatite paste packed into the model channel: (a) before sonication; (b) after sonication with CT-4 at Power 10/10 for 2 minutes.*

Figures 4.29 and 4.30 showed the percentage of HA paste removal upon sonication at different power settings for the three endosonic files respectively. It can be seen that, in comparison, the percentage of HA paste removed along the side channel is much higher than that removed at the bottom. This might be due to the projection of the cavitation clouds for all the tips producing a streaming effect in the direction of the vibration movement. On the other hand, there is not much happening along the direction of the tip, with merely 25 % of HA paste removed at the maximum power setting. This suggests that the streaming effects happening in a confined space is still not great enough to produce sufficiently turbulent flow in the root canal to knock of dentin debris.

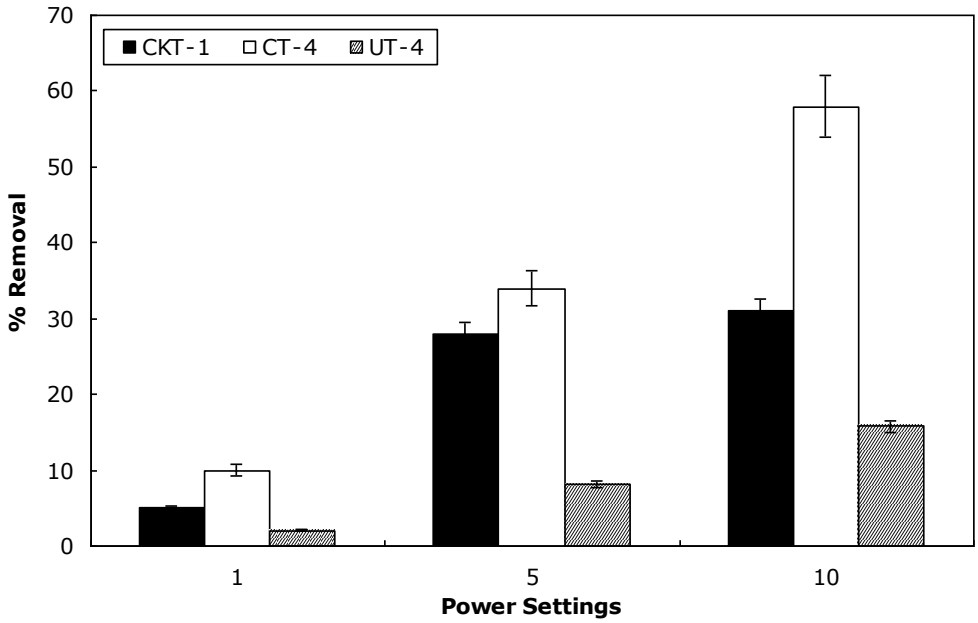

Figure 4.29: *Percentage of hydroxyapatite paste removed along the side channel upon sonication at various power settings for three different endosonic files.*

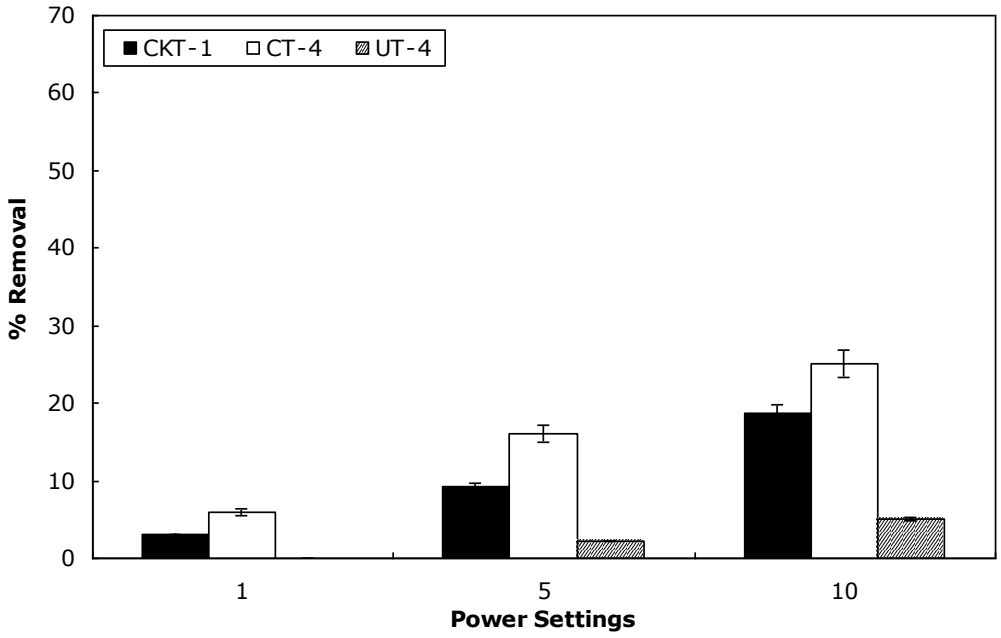

Figure 4.30: *Percentage of hydroxyapatite paste removed at the bottom channel upon sonication at various power settings for three different endosonic files.*

The downfall in clinical endodontic treatments lies here, where there is insufficient flow travelling down the channel and restraining further cleaning treatments. Boutsioukis *et al.* (2010b) have performed a series of computational fluid dynamics modelling to see the effects of the flow pattern for different endosonic files with different size of vented holes to increase the streaming effects. It was claimed that with an increase in flow along the vertical direction down the root canal increases the removal of dentin debris during root canal treatment (Vinothkumar *et al.*, 2007). In this work, due to equipment constraints, experiments were not performed on the effects of irrigant flow in a channel on the cleaning efficiencies, but it is worth considering this factor in designing the next generation endosonic files.

From this experiment, we can conclude that the cavitation activity and the streaming effects have a strong contribution in the removal of HA paste, which further strengthens our hypothesis on the importance of sonochemical effects in root canal treatments.

4.4 Conclusions

i) Ultrasonic-assisted emulsification has shown that silicone oil-water emulsion can be formed upon sonication using the endosonic files for two minutes, with CT-4 forming emulsion with the smallest average particle droplet size, followed by CKT-1 and UT-4(2).

ii) Ultrasound can be used to accelerate the process of dye decolourisation, and decolourisation can be used as an indication of the ultrasonic cleaning efficiency based on the rate of removal of a model dye (Rhodamine B) upon sonication with a dental irrigant under various conditions.

iii) Sonication of H_2O_2 has shown that the concentration of H_2O_2 affects the rate of dye decolourisation due to its volatility and scavenging properties, which will affect the cleaning process in the endodontic treatment when it is used as a dental irrigant.

iv) Permanent ink and hydroxyapatite paste removal upon sonication showed good indication of the cleaning efficacy of the endosonic files assessed.

v) Assessments of the cleaning efficiencies of the endosonic files (emulsification, dye decolourisation, ink removal, hydroxyapatite paste removal) have shown good correlation, with CT-4 showing the best performance in each experiment performed.

5.Factors Affecting Sono(chemi)luminescence and Vibration Movements

In this chapter, a few potential factors affecting sono(chemi)luminescence and the vibration movements of the dental tips were studied. Firstly, the effects of the size of the channel were assessed by having three model channels of different widths. Following, the position of the dental tips in the channel was evaluated. In the last section in this chapter, a series of differently designed endosonic files (Start-X) was used and compared based on the amount of SCL they produced and was then compared with their vibration movements as well as their cavitation counts.

5.1 Effects of Channel Width and Position in Sonoluminescence

In order to have a better illustration of the dental tips performance in actual dental practices, the sono(chemi)luminescence experiments were repeated in a confined space, made of silicone rubber cut-out of 3 mm, 4 mm and 5 mm respectively, as illustrated in Figure 5.1. This is to study the effect of confinement on the cavitation production for different tips.

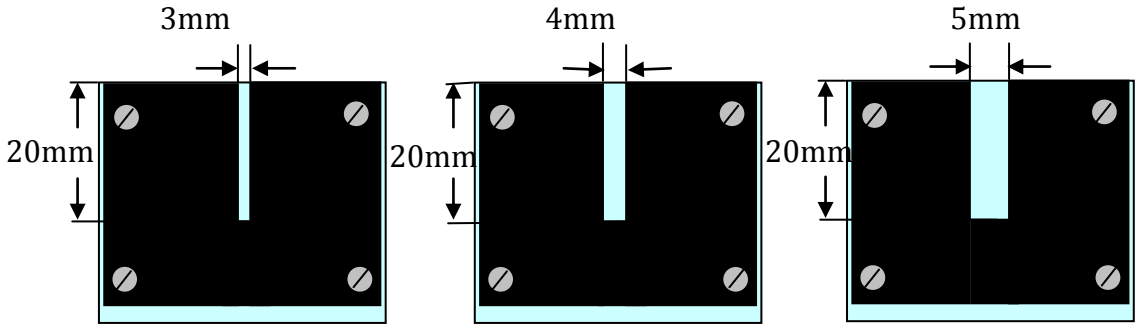

Figure 5.1: *Silicone rubber channels of different width for comparison.*

Figure 5.2 shows the average light intensity emitted with different channel width (measured using similar method to those in Section 3.3) with CT-4 inserted into the channel front-on position (Figure 2.6(a)). The results showed no significant difference in light intensities emitted at low and medium powers (Power 1 and Power 5) (ANOVA, p-value > 0.05). A big difference can be detected at Power 10, with 4 mm and 5 mm channels showing twice as much light intensity compared to that in the 3 mm channel. It is suggested that this could be due to confinement restricting liquid movements which will then obstruct the formation of sufficiently high transient cavitation. An optimum confined space was then needed to achieve the cavitation threshold, which, in this case, would be in the 4 mm channel, resulting in approximately twice as much cavitation produced as compared to that in the 3 mm channel. Similar trends were obtained for CT-4 performed with the tip inserted into the channel side-on (Figure 2.6(b)).

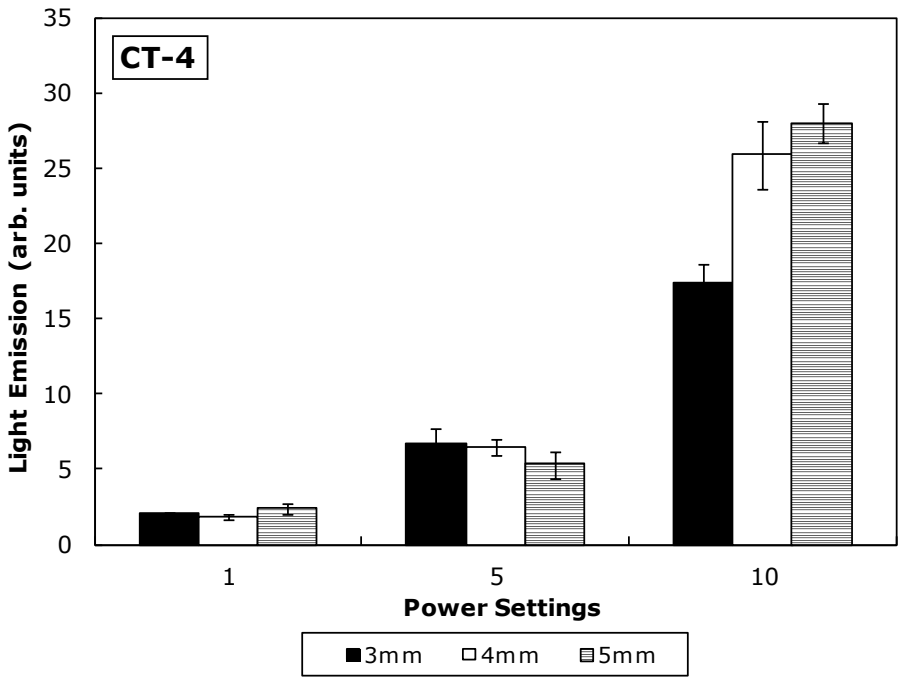

Figure 5.2: *Average light intensity emitted at different powers for CT-4 inserted into the channel with front-on position, with different channel width.*

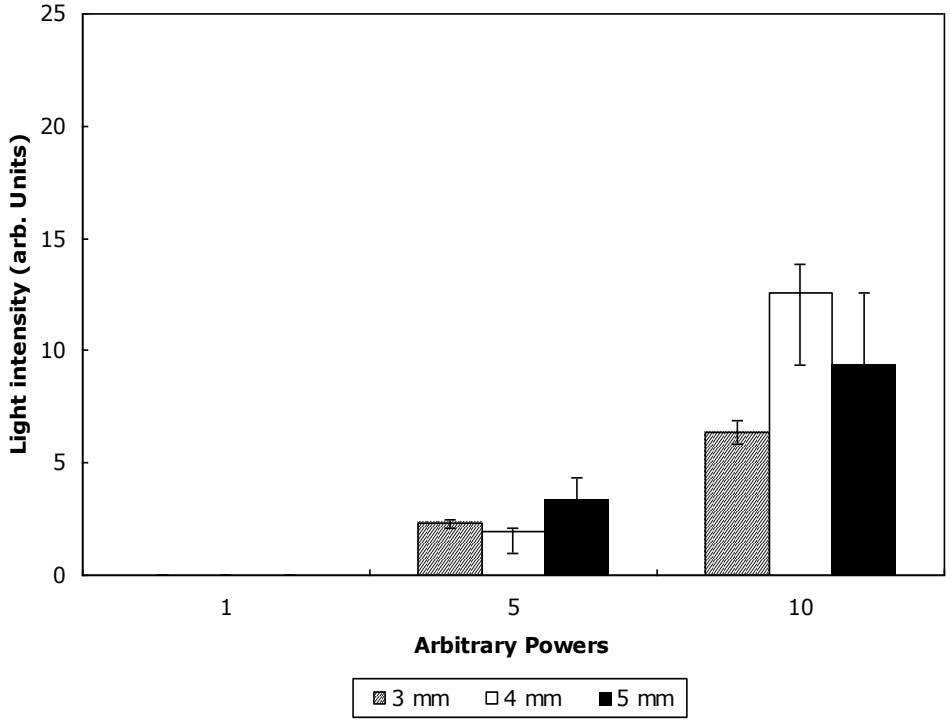

Figure 5.3: *Average light intensity emitted at different powers for CT-4 inserted into the channel with side-on position, with different channel width.*

Based on Figure 5.3, when CT-4 was inserted into the channel with side-on position, there is no detectable SCL at Power 1, and there is no significance difference in Power 5, regardless of the width of the channel used (ANOVA, p-value > 0.05). At Power 10, SCL appears to be much higher in the 4 mm channel compared to the 3 mm channel. Discrepancies in the light intensity produced for both 4 mm and 5 mm channel may be due to the position of the tip in the channel (placed side-on), obstructing some light to be detected.

Similar experiments were performed on the CKT-1 and UT-4 tip in different channels, but different trends were obtained for the tips assessed. For example, Figure 5.4 shows the average light emission produced from the luminol photography produced at different power settings. Increasing the channel width in this case reduces the amount of SCL produced in the channel. At the highest power, SCL was the highest in a 3 mm channel, but reduced as the channel width increases. On the other hand, referring to Figure 5.5, channel confinements have no significant difference on UT-4(2) (ANOVA, p-value > 0.05). The variance that arise in the results may suggest that different tips give rise to a different response in SCL under different conditions, and there is a certain optimum condition for each tip in order to produce sufficient transient cavitation. For example, it can be suggested that the CT-4 performs better in wider channels, followed by CKT-1 in a 3 mm channel, and probably narrower channels for a more optimum performance for UT-4.

When different tips were inserted into the 3 mm channel to test the effects of confinements on the amount of SCL given out, it showed a similar trend obtained compared to the tips in a bulk solution. For the purpose of this experiment, only three dental tips were used – which comprises of a CKT, CT and an UT tip.

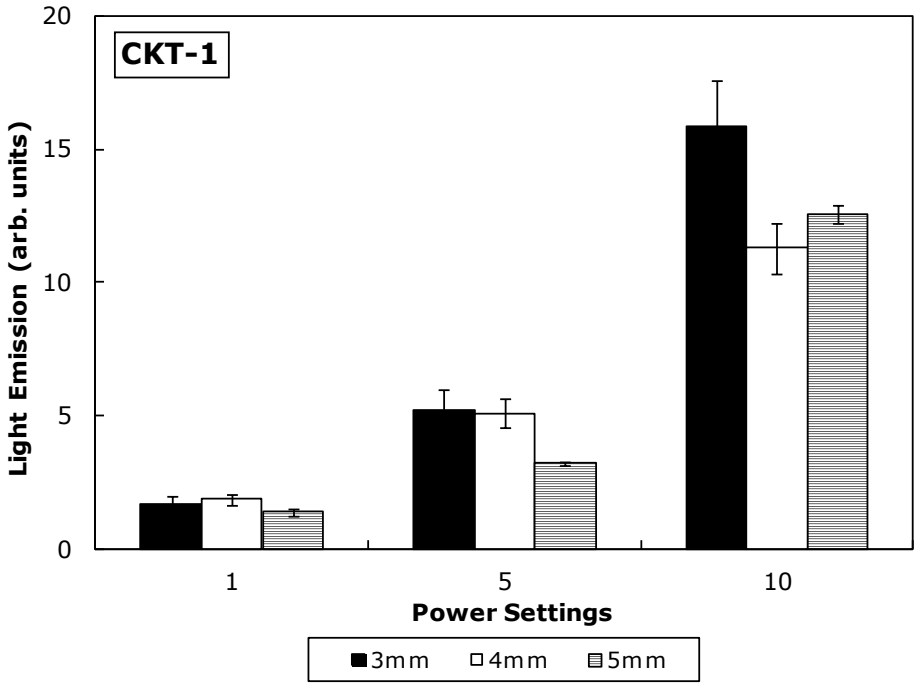

Figure 5.4: *Average light intensity emitted at different powers for CKT-1 inserted into the channel with front-on position, with different channel width.*

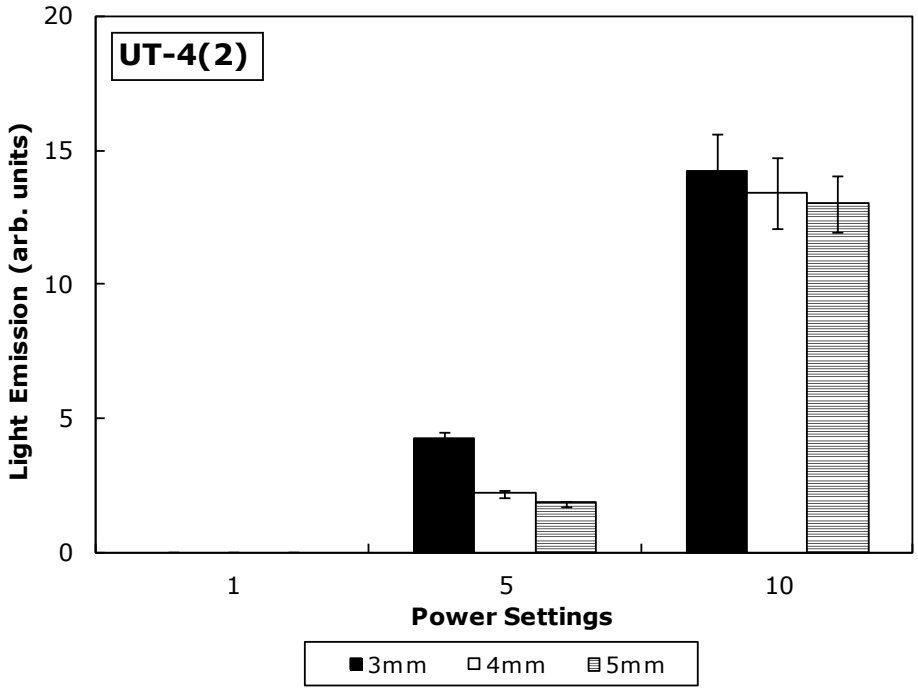

Figure 5.5: *Average light intensity emitted at different powers for UT-4(2) inserted into the channel with front-on position, with different channel width.*

Figure 5.6 shows the results of the mean light emission of three of the aforementioned tips with at different powers in a confined space of 3 mm silicone rubber and in a bulk solution when the dental tips were immersed in a cuvette. Both results showed similar trends for the different tips, with CT-4 giving out the most SCL, followed by CKT-1 and UT-4(2). However, in the 3 mm channel, variations in readings were much greater, probably due to higher deviations in data collection when measured at a smaller scale. Results have shown that the light emission produced in confined space is much higher than those in bulk solution. The discrepancies in the data suggests that more activity happens in a confined space, producing more violent cavitation collapse, resulting in more SCL produced.

Often in clinical practices, the endosonic file inserted into the root canal is not placed in the middle of the root, and will often be in contact with some/part of the root canal walls. An experiment was performed to investigate the effects on SCL produced when a dental tip is placed at different positions in the root canal. For the purpose of the experiment, it was done in a 3mm channel at 'medium' power – Power 5/10. The positions of the tips were divided into three different parts – placed in the middle, side of the channel and touching the silicone rubber wall, as illustrated in Figure 5.7.

In general, the position of the tip in the channel does not make a significant difference to light emission, especially for CT-4 (Figure 5.8). However, the UT-4 tip is affected the most, where the oscillatory movements were obstructed when the tip is touching the silicone rubber channel, resulting in absolutely no light emission detected. It can be speculated that this might be due to the course of UT-4 depending on higher oscillatory movements to produce sufficient negative acoustic pressure to form cavitation compared to the other tips which have larger surface areas to displace the liquid surrounding them to form higher negative pressure with lower oscillatory movements.

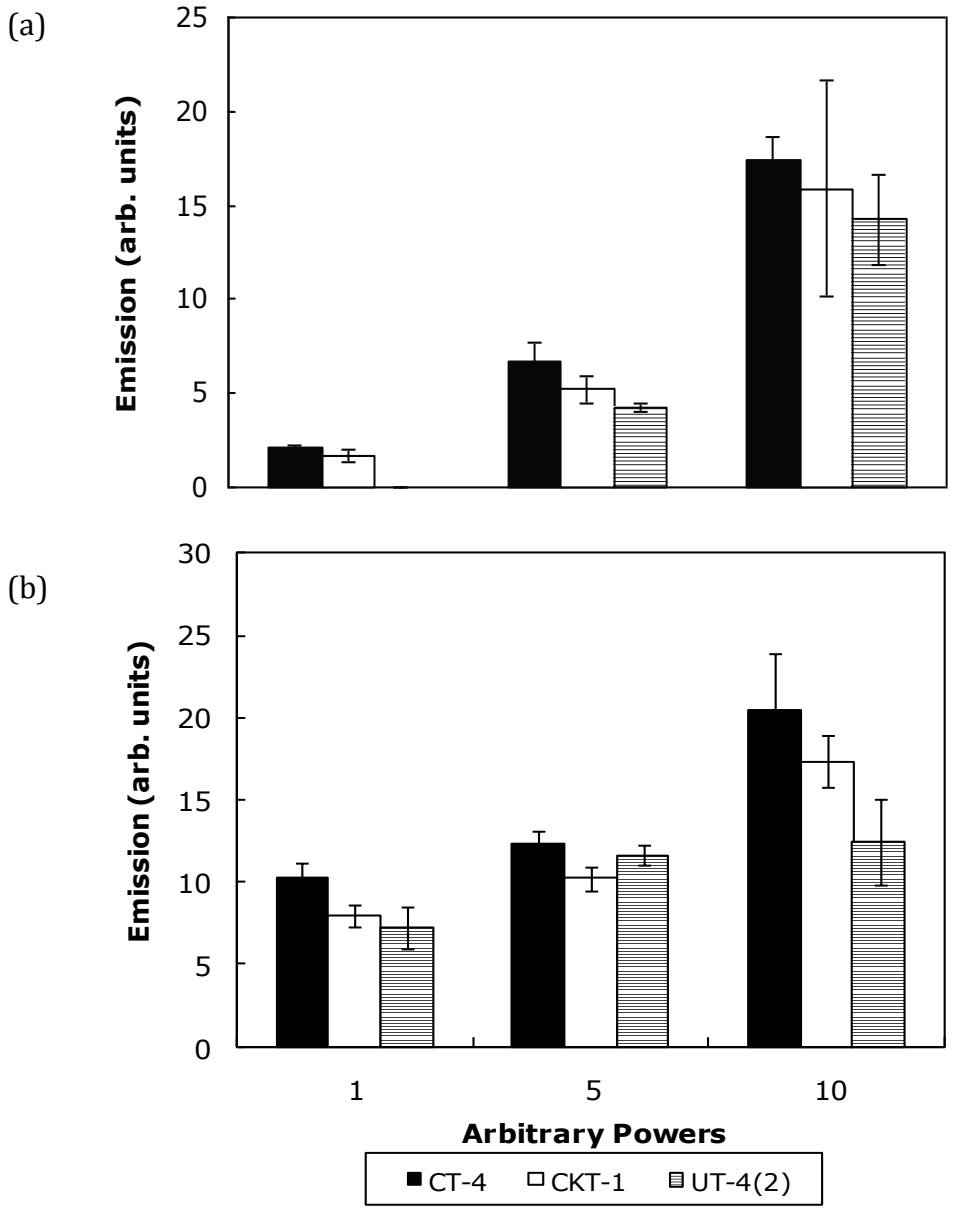

Figure 5.6: *Mean emission obtained when different dental tips were placed in a (a) 3mm silicone rubber channel and (b) in a bulk solution; at low, medium and high (1/10, 5/10 and 10/10) powers respectively.*

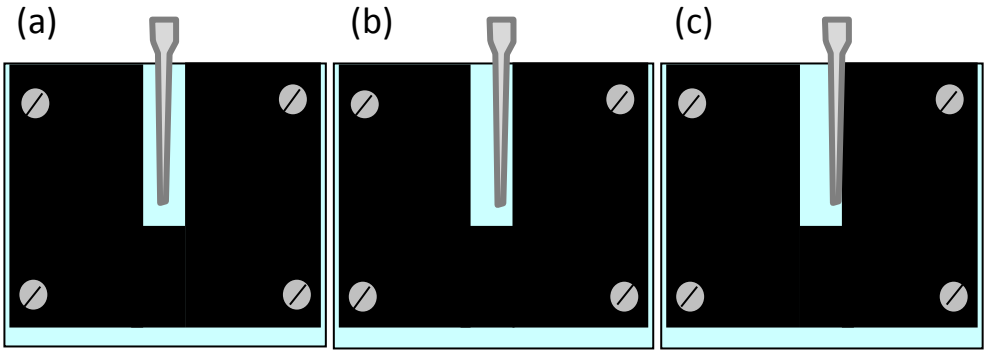

Figure 5.7: *Illustration of the positions where different dental tips were inserted in a silicone rubber channel: (a) middle; (b) side; (c) touch.*

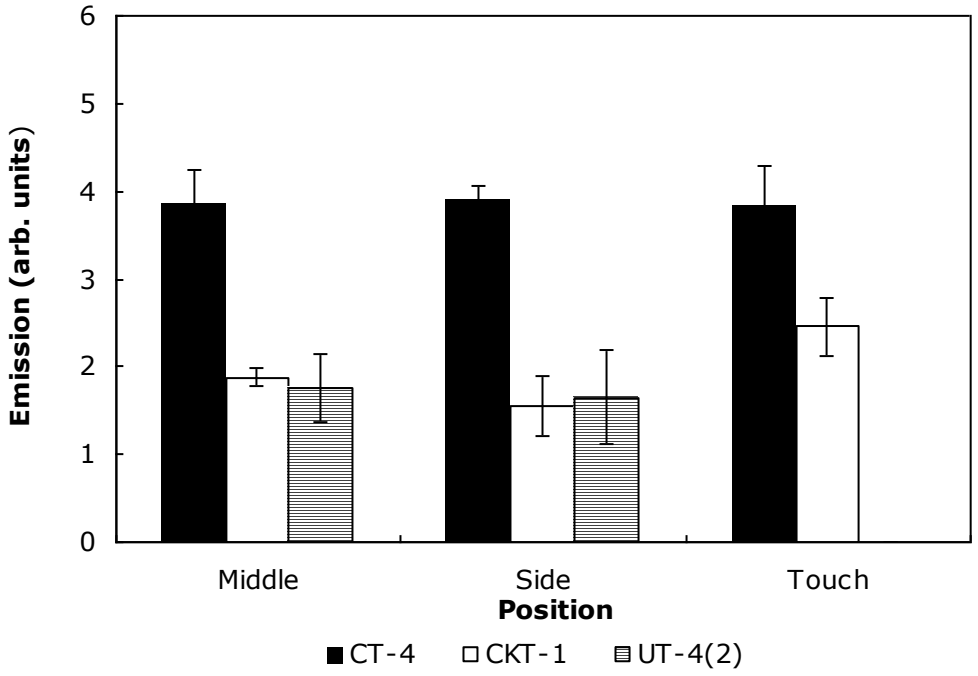

Figure 5.8: *Mean light emission produced by sono(chemi)luminescence in a 3 mm silicone rubber channel at Power 5 when dental tips were inserted at different positions.*

The production of sono(chemi)luminescence depends on the cavitation produced during the rarefaction in an acoustic cycle. The higher negative pressure produced during rarefaction, the more cavitation produced, which will then collapse to form more radicals to react with luminol. It can be concluded that the formation of negative acoustic pressure depends on the surface area of the dental tip, where tips

with bigger surface area displace more of the surrounding liquid, hence producing higher negative acoustic pressure around them.

As for tips with smaller surface areas such as the UT-4 tips, formation of cavitation is dependent on its high oscillatory movements (driven by high energy output calculated in Section 3.1) to achieve more cavitation as compared to the other tips. This will be verified in Section 3.4, where the oscillatory movements of different tips will be discussed.

5.2 Effects of Channel Width and Position in Vibration Movements

Vibration movements of the dental tips were evaluated in a similar way to that discussed in Section 3.4, but in a confined space in a model root canal made of silicone rubber of different channel width, as shown in Figure 5.1. Measurements were performed for CKT-1, CT-4 and UT-4(2) tips, similar to those performed for the SCL in Section 5.1.

An example of the displacement profile of a dental tip (CT-4) in a channel of different widths is shown in Figure 5.9. As it can be seen, the general displacement profile remains the same regardless of the channel width, showing the same nodal and antinodal points along the file. However, there is a slight change in the maximum displacement of the file at the free end of the tip.

Based on the example above, a statistical study was carried out by performing an analysis of variance (ANOVA) followed by a Tukey post-hoc test on the three different channel widths. The example above on CT-4 at Power 5/10 showed that even though there is a slight difference in the maximum displacement obtained, it is

not significantly different (ANOVA, p-value > 0.05). This, however, cannot be generalised for all the other dental tips at different settings. Appendix II shows all the vibration displacement profiles of the dental tips at various conditions, with tabulated results of statistical significance of the samples obtained shown in Table 5.1.

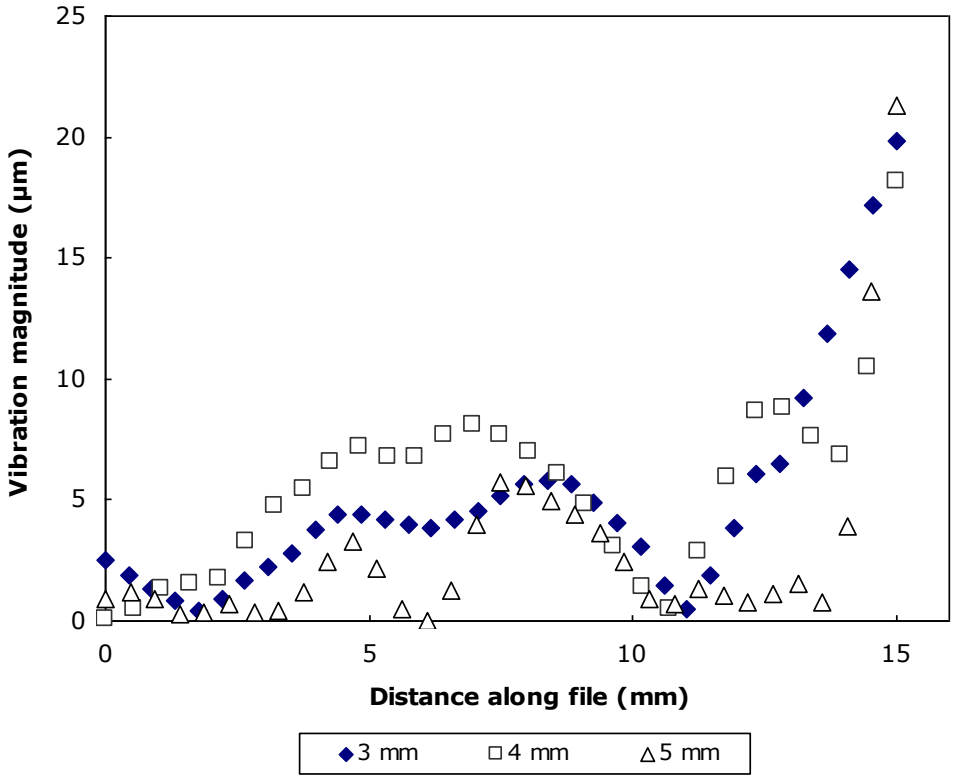

Figure 5.9: *Vibration displacement magnitude along the length of CT-4 in a confined channel of different widths at Power 5/10.*

Based on Table 5.1, there is no general conclusion that can be made on the effects of channel widths to the vibration displacements. However, it can be said that there is a significant difference (ANOVA p-value < 0.05) at low powers, indicating that the channel width plays as a factor in contributing to the oscillatory movements of the dental tips at those settings. This effect becomes less prominent as the sonicating power increases.

Similarly, a study on the effects of the dental tip position on the vibration movements was carried out. Experiments were carried out similar to those for the sono(chemi)luminescence, where a dental tip was placed in the middle, side or touching the wall of the model channel, as illustrated in Figure 5.7.

Table 5.1: *Collated results of ANOVA and Tukey Post-hoc test on maximum displacements of the three endosonic files used in a 3mm, 4mm and 5mm wide channels.*

	ANOVA P-value*			Tukey post-hoc*		
Power setting	**P1/10**	**P5/10**	**P10/10**	**P1/10**	**P5/10**	**P10/10**
CT-4	0.000	0.149	0.294	Significantly different from one another	N/S	N/S
CKT-1	0.001	0.004	0.151	3mm is significantly different from 4mm and 5mm	3mm is significantly different from 4mm and 5mm	N/S
UT-4(2)	0.016	0.700	0.026	3mm is significantly different from 5mm but there is no significant difference in 3mm & 4mm, 4mm & 5mm.	N/S	3mm is significantly different from 4mm and 5mm

Key * : At 95% CI, significant if p-value < 0.05

N/S : No significant difference

Table 5.2: *Collated results of ANOVA and Tukey Post-hoc test on maximum displacements of the three endosonic files placed in the middle, size and touching the model channel at Power 5/10.*

	ANOVA P-value*	Tukey post-hoc*
CT-4	0.000	Significantly different when tip is touching the wall.
CKT-1	0.000	Significantly different from one another
UT-4(2)	0.674	N/S

Key * : At 95% CI, significant if p-value < 0.05

N/S : No significant difference

Table 5.2 illustrates the statistical results of the effects of the file position on the vibration movements of the three endosonic files studied. It can be seen that there

is a significant difference for CT-4 and CKT-1 when the dental tip touches the wall of the model channel, reducing the vibration movement of the tip (Appendix II, Figure 8.10 and 8.11). However, the vibration movements of UT-4 were not hindered by the position of the tip. This has been proven by both the high p-value obtained on Table 5.2 as well as the vibration profile of the tip in Appendix II, Figure 8.12. With this information, we can then correlate the vibration movements and the amount of sonoluminescence produced in different channel conditions, which will be discussed further in Section 5.3.

5.3 Correlations of Sono(chemi)luminescence and Vibration Movements

It has been shown previously in Chapter 3, Figures 3.24 and 3.25 that the areas where SCL is produced along the endosonic files correlates to the areas of maximum vibration amplitude.

In this section, the correlations between the vibration amplitudes and the SCL is studied by performing statistical analyses on the results obtained in Sections 5.1 and 5.2. The results were assessed by obtaining the Pearson's product-moment correlation coefficient for both the vibration amplitudes and the light intensity (from SCL). The outcome of the statistical analyses are tabulated in Table 5.3.

Here, the correlation between the two parameters was assessed based on 99 % level of confidence for sample size of 9. It can be seen that the vibration amplitude of the endosonic files (CT-4 and CKT-1) has strong relationship with the amount of light intensity produced for each parameters studied. This means that the vibration movements of the endosonic files have aided in the production of transient cavitation, resulting in more SCL produced upon sonication in luminol solution. However, this correlation does not apply for the UT-4(2) tip, where, out of four separate studies on the correlation, only two showed positive correlation at 99 % confidence level. Once

again, this suggests that other factors may also contribute to the formation of transient cavitation, such as the shape of the endosonic files – which will be discussed further in the next section (Section 5.4).

Table 5.3: *Pearson's product-moment correlation coefficients, R between the vibration movement amplitudes and the light intensity produced from SCL for the endosonic files used in a confined space of different widths and placed at different positions.*

Factors / ***Width***	**CT-4**	**CKT-1**	**UT-4(2)**
3 mm	0.917 *yes*	0.990 *yes*	0.719 *no*
4 mm	0.842 *yes*	0.941 *yes*	0.889 *yes*
5 mm	0.904 *yes*	0.805 *yes*	0.926 *yes*
Position (middle, side, touch)	0.858 *yes*	-0.999 *yes*	0.000 *no*

For sample size of 9, degree of freedoms = 7
No correlation if , - 0.798 < R < 0.798

5.4 Effects of the shapes of the tips to Sonoluminescence and Vibration Movements

It has been mentioned previously in this thesis that the sonochemical activities of the endosonic files assessed are strongly related to the shape of the files. In order to further clarify the effects of the shapes on the sonochemical activities, a series of Start-X tips (Dentsply-Maillefer, Balaigues, Switzerland) was used.

Figure 5.10 shows all the Start-X tips used for this study. Each Start-X tips was designed for a specific use in endodontic treatments (Dentsply, 2010), where:

i. Tip-1 : used to access cavity in the walls of an upper molar, with micro milled ends to minimise potential grit loss in the patient's mouth.

ii. Tip-2 : used to remove dentine that often conceals access in upper molars, with micro milled ends to minimise potential grit loss in the patient's mouth.

iii. Tip-3 : used as a canal openings scouter – to remove obstructions that prevent a straight access to the canal.

iv. Tip-4 : used to remove metal post in the upper molars of the tooth.

v. Tip-5 : used to reveal the original pulp chamber floor anatomy, in order to locate the canal orifice more easily and with good visibility.

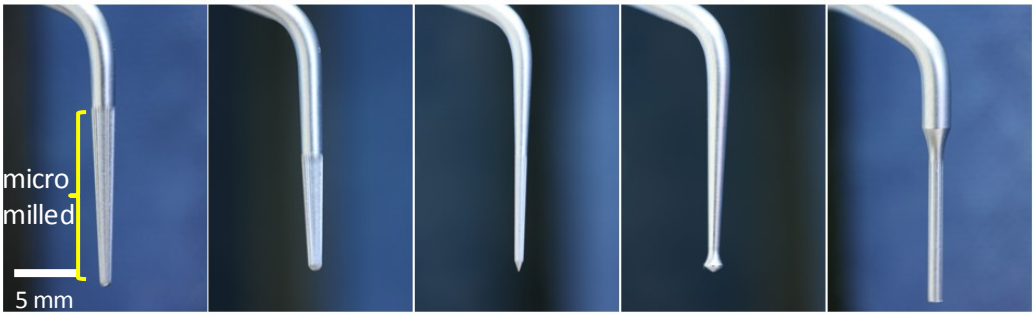

Figure 5.10: *All the Start-X dental tips used. From left to right: Tip-1, Tip-2, Tip-3, Tip-4 and Tip-5.*

The tips were assessed and evaluated based on the following methods:

i. Sono(chemi)luminescence in a polymethacrylate UV cuvette of dimensions (10 mm × 10 mm × 45 mm), with image exposure length of 30s for each run.

ii. Cavitation counts with the aid of a CaviMeter™.

iii. Vibration movements of the tips using the Scanning Laser Vibrometry technique.

In these experiments, the endosonic files used were assessed in Powers 1/10, 5/10 and 10/10. In addition to that, experiments were also carried out at Powers 2 to 4 to identify the cavitation threshold intensity of the system.

5.4.1 Sono(chemi)luminescence on the Start-X Tips

SCL on the Start-X tips were performed in a light-proof box, similar to those performed in the previous sections. Luminol images taken for all different tips are attached in Appendix IV, Table 8.4.

The luminol images were analysed in a similar way to the ones treated previously (Section 3.3), with the aid of ImageJ. From there, the average light intensity across the entire region of interest in the images can be evaluated and a quantification of the amount of light intensity produced can be obtained. Figure 5.11 shows the collated light emission of various Start-X tips at different power settings. Apart from Tip-5, there is a general increase in light intensity with the increase of power. There is a big leap in light intensity from Power 3 to 4 for most of the dental tips (Tip-1, Tip-2 and Tip-4) indicating that a possible cavitation threshold might lie in that range. Tip-5 had a surprising trend of producing almost constant amount of light intensity at all power settings.

Overall, the results showed that Tip-1 produces the most SCL at medium at high powers, suggesting that it might be a well-designed endosonic file in maximising the production of cavitation. It can be noted that the presence of the ridges around the tip aids the amount of negative acoustic pressure produced, which then increases the production of SCL. A better illustration of comparison is shown in Figure 5.12, where CT-4 was used in this case to compare with Tip-1 at Power 1. The ridges around the dental tip increase the possibility of producing SCL at the antinodal points of the dental tip. This results in a huge decrease in cavitation threshold and a good production of SCL can be seen at lower power settings.

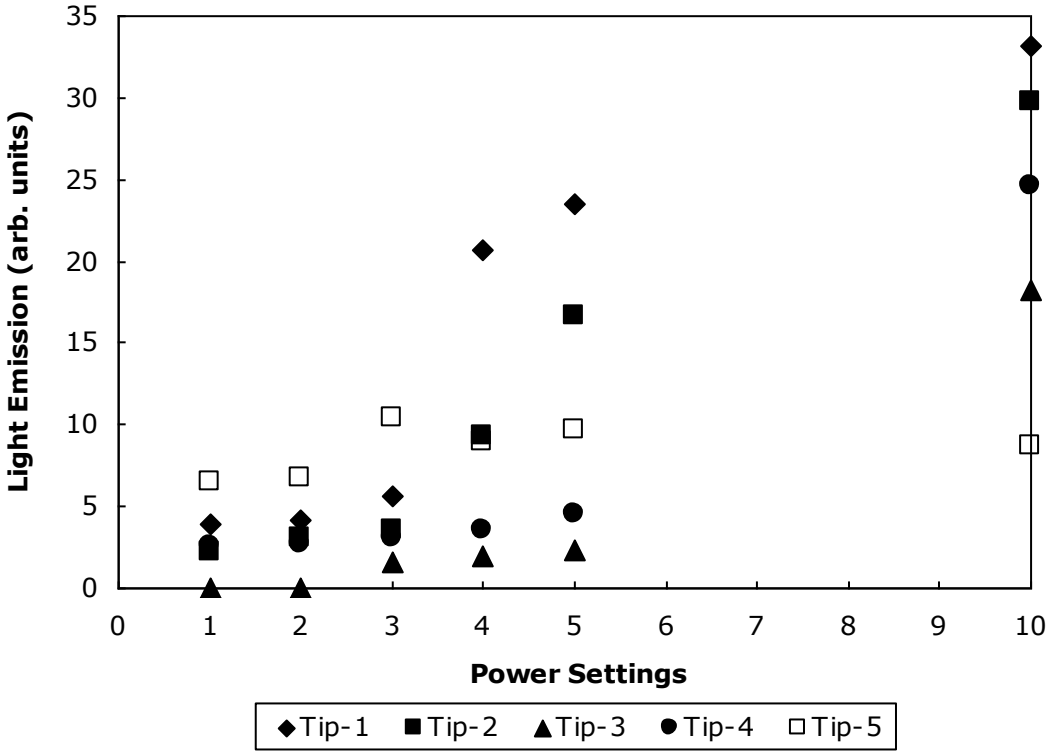

Figure 5.11: *Light emission of Tips 1, 2, 3, 4 and 5 at various power settings upon sonication for 30 s in a polymethacrylate UV cell filled with luminol solution.*

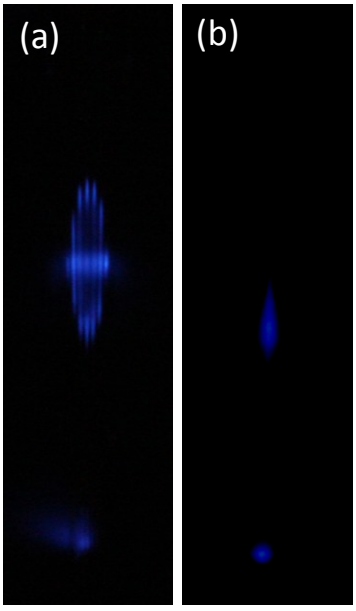

Figure 5.12: *Luminol photograph of (a) Start-X Tip-1 and (b) CT-4; both at Power 1.*

In the case of Tip-2, the presence of ridges around the dental tip did not aid much in the production of the SCL, which might be due to the position of the ridges along the tip. An early hypothesis of this phenomenon is that the position of the ridges along the tip did not fall on the antinodal point when sound wave passes through the tip. Further analyses are needed to identify the factors affecting the production of SCL, which will be discussed in detailed in Sections 5.4.2 and 5.4.3.

Tip-3 turned out to be the least effective tip in producing SCL, a result which is similar to the UT-4 tips mentioned earlier in Section 3.3. The presence of minor ridges along Tip-3 did not in any way aid in the production of SCL in this case, suggesting that the improvements of the amount of SCL produced is not solely dependent on the design and the presence of uneven surfaces along the tip but also depends on other factors in the design of the endosonic file – such as the minimum surface area needed to produce the required acoustic pressure amplitude to overcome the cavitation threshold.

Tip-4 is very different from all the other dental tips that have been used previously due to its special design with a diamond-shaped ball in the end of the tip, used for the removal of metal from a previous crowning[11] (Dentsply, 2010). Results showed that the presence of this enhanced the amount of SCL produced at low power settings, even though the amount of light emission along the entire tip averages out to lie in the middle range amongst the five dental tips. Figure 5.13 shows the photograph of Tip-4 taken as it was during experimental setup and compared with a luminol photograph of the tip taken at Power 1. As shown, the amount of SCL produced does not total up to be as much as the other tips like the Tip-1 which has ridges along the dental tip. However, there is clear, bright SCL produced at the end of the tip, suggesting that the presence of the diamond-shaped ball at the end of the tip has some effects on the SCL produced even at such a low power setting.

[11] A type of dental restoration used to completely cover a tooth or dental implant.

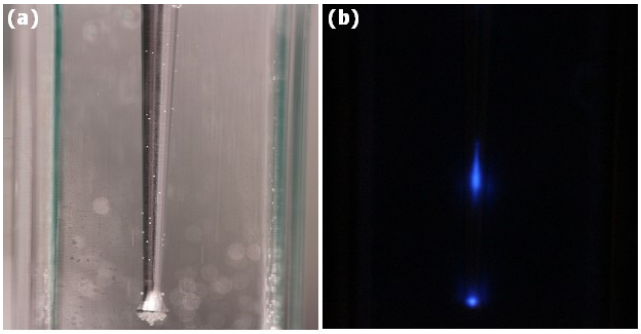

Figure 5.13: *(a) Photograph of Tip-4 immersed in luminol in a cuvette; (b) Luminol photograph of Tip-4 at Power 1.*

Tip-5 was among the tips that produced the most SCL at low power settings. This could be due to the design of the tip, in that there was a good energy transfer throughout the entire length of the tip. But, as the input power increases, the tip has come to a plateau in the maximum SCL it can produce under sonication. Further proofs on this are needed for better explanation and will be discussed in more detailed in Sections 5.4.2 and 5.4.3 respectively.

5.4.2 Cavitation counts with the aid of a CaviMeter™

Cavitation counts of all the Start-X tips were evaluated in a similar way as to how it was performed previously (Section 3.4), where the signal of the total cavitation was obtained in terms of arbitrary units from the CaviMeter™. An average from five repeats was taken for all the Start-X tips upon obtaining a background reading of the system in the absence of sonication.

Figure 5.14 shows the cavitation counts for all the Start-X tips at different power settings. An example of the correlation between the cavitation counts obtained together with the light emission counts from luminol photography is shown in Figure 5.15, with the two parameters plotted on the same figure.

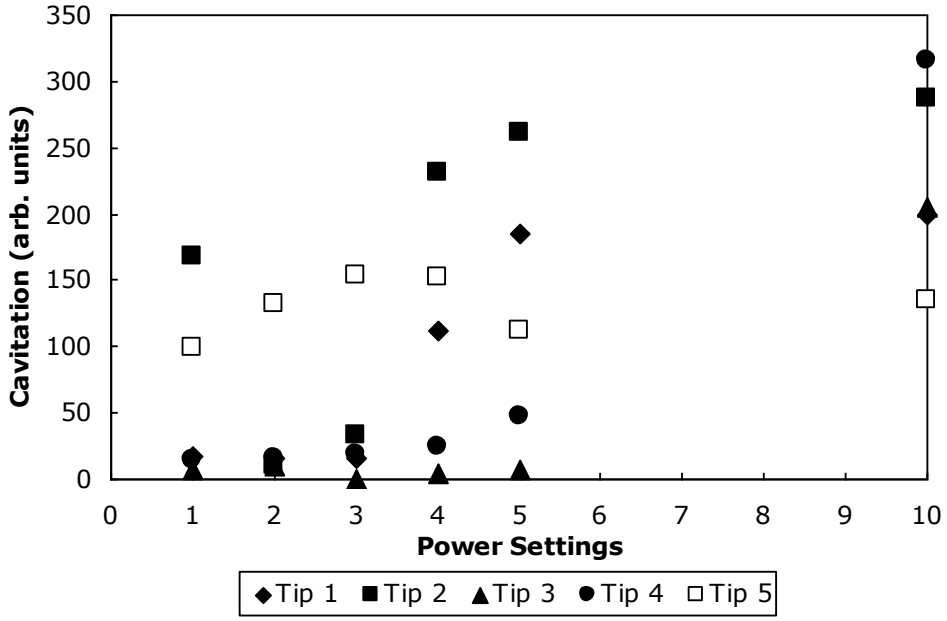

Figure 5.14: *Cavitation counts for all the Start-X tips at different power settings.*

There is a very clear correlation between the cavitation counts obtained from the cavimeter and the light emission counts obtained from luminol photography, as seen in Figure 5.15. Once again, it can be seen that there is a clear leap from Power 3 to 4 in cavitation counts, where it is suggested that the cavitation threshold lies. This gives a potential suggestion to clinical endodontic practices to adjust the power setting to that required setting in order to give rise to approximately three times as much cavitation, which may contribute to the cleaning efficiencies in clinical practices.

Similar data treatment was performed for all the other Start-X tips, and the results were collated in Figure 5.16. There is a generally good correlation in the SCL and the cavitation produced in the tips, with some small discrepancies in the results, especially for Tip-2 (Figure 5.16(a)). It has to be noted that these discrepancies that arise might be due to the presence of both stable and transient cavitation. The cavimeter measures both stable and transient cavitation in the system whilst the light emitted from SCL is a result from the collapse of transient cavitation. Hence, the slight discrepancies shown in the results are considered as within our experimental uncertainty. Previous work on comparison of cavitation counts and SCL emission on dental descalers by Felver *et al.* (2009) also showed slightly higher acoustic cavitation signal compared to the light emission obtained from SCL.

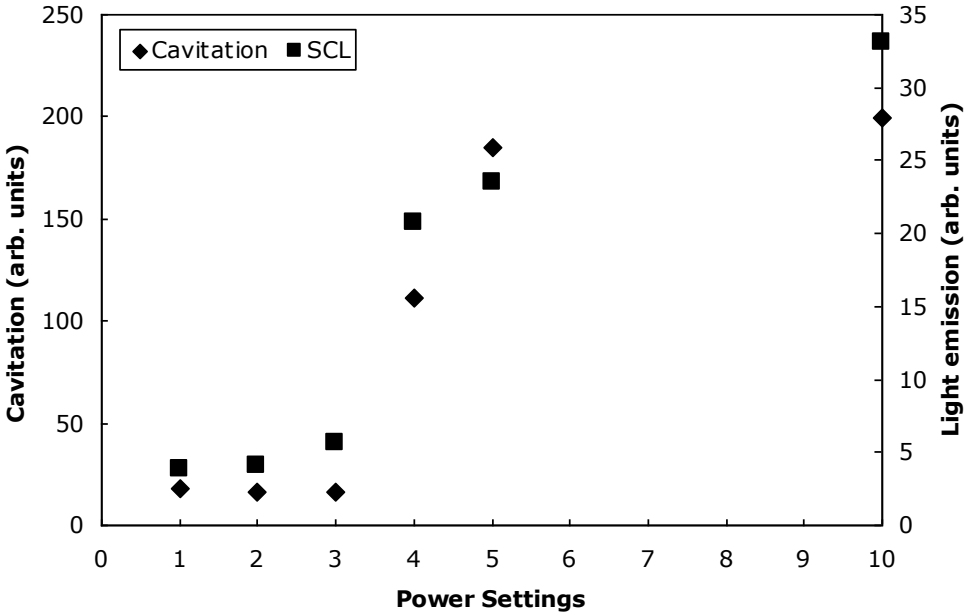

Figure 5.15: *An example of the cavitation counts obtained from a cavimeter in comparison with the light emission counts obtained from luminol photography for the Start-X Tip-1 at various power settings.*

To further evaluate the dissemblance of the results, the sub-harmonics signal obtained for Tip-2 was studied. The sub-harmonics signal obtained from the cavimeter records the one-half and one-quarter of the fundamental frequency (in this case ~ 30 kHz), giving rise to the onset of transient cavitation (Frohly *et al*., 2000). According to Frohly *et al*., the presence of sub-harmonic oscillations appears at low intensities in a randomly distributed bubble field, and suggests the presence of stable cavitation in the system. This agrees with the results obtained, where a generally high sub-harmonic signal was obtained at low intensities as a result of the presence of stable cavitations, as shown in Figure 5.17.

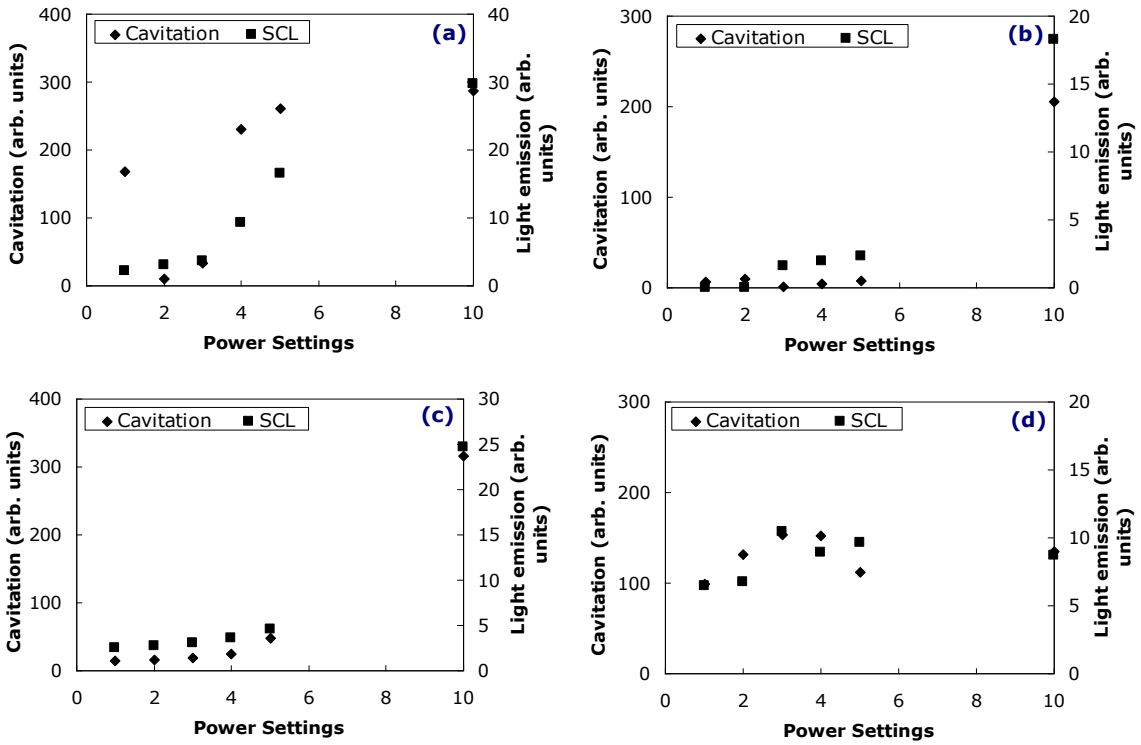

Figure 5.16: *Correlations between the amounts of cavitation produced obtained from a cavimeter and the light emission produced from luminol photography at each power settings for (a) Tip-2; (b) Tip-3; (c) Tip-4; and (d) Tip-5 respectively.*

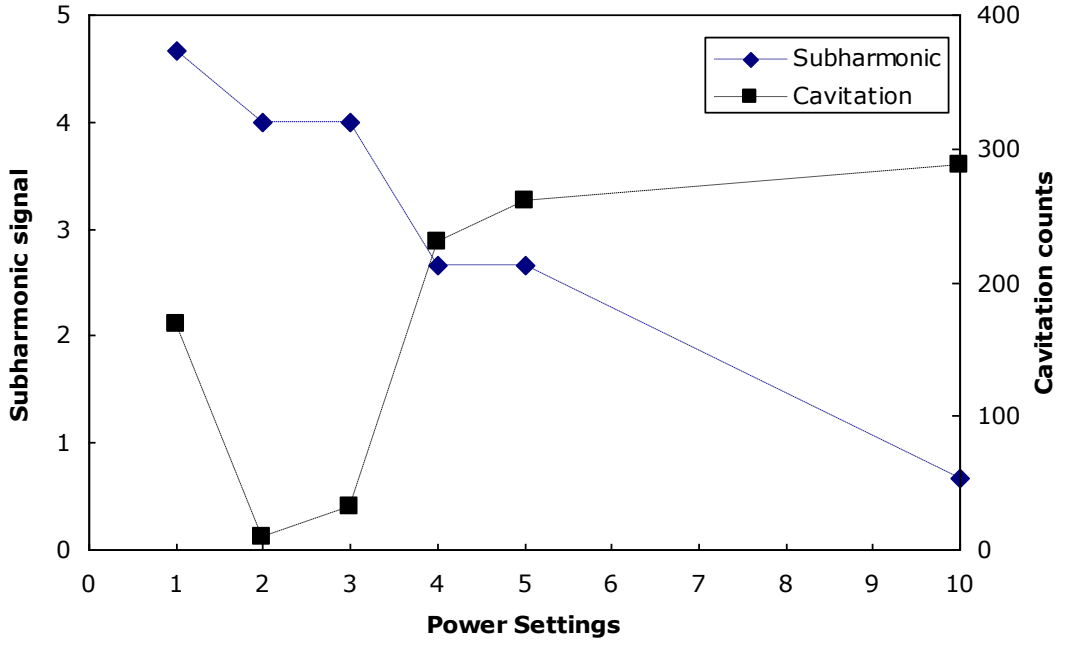

Figure 5.17: *Sub-harmonic signal and the cavitation counts for Tip-2 at various power settings. Results were all based on arbitrary units.*

5.4.3 Vibration movements of the Dental Tips

Vibration movements of the Start-X tips were evaluated using a Polytec Scanning Laser Vibrometer, similar to the ones assessed in Section 3.5. The vibration profile of the dental tips were performed at Powers 1, 3, 5 and 10 and were all collated in Appendix IV, Figures 8.14, 8.15, 8.16, 8.17 and 8.18 respectively.

In general, the vibration patterns of the files were similar to those discussed previously in Section 3.5. The areas with maximum vibration magnitude correspond to the areas where SCL was produced. Figure 5.18 illustrates the vibration magnitude profile superimposed with the SCL photographs taken upon sonication at Power 10/10 for each Start-X tips used.

Figure 5.19 shows the maximum displacement results collated for all the Start-X tips at various power settings, whereas Figure 5.20 shows the average light emission produced for the tips at the same settings. It can be noted that there is little to no correlation between the maximum displacements produced on the dental tips to the amount of SCL produced. It can be suggested that even though the antinodal points of the vibration movements were the places where it produces cavitation, the magnitude of the vibration amplitude has little to no correlation to the amount of cavitation produced. This suggests that the design and the shape of the dental tips plays an important role in cavitation production rather than the vibration movement amplitude itself.

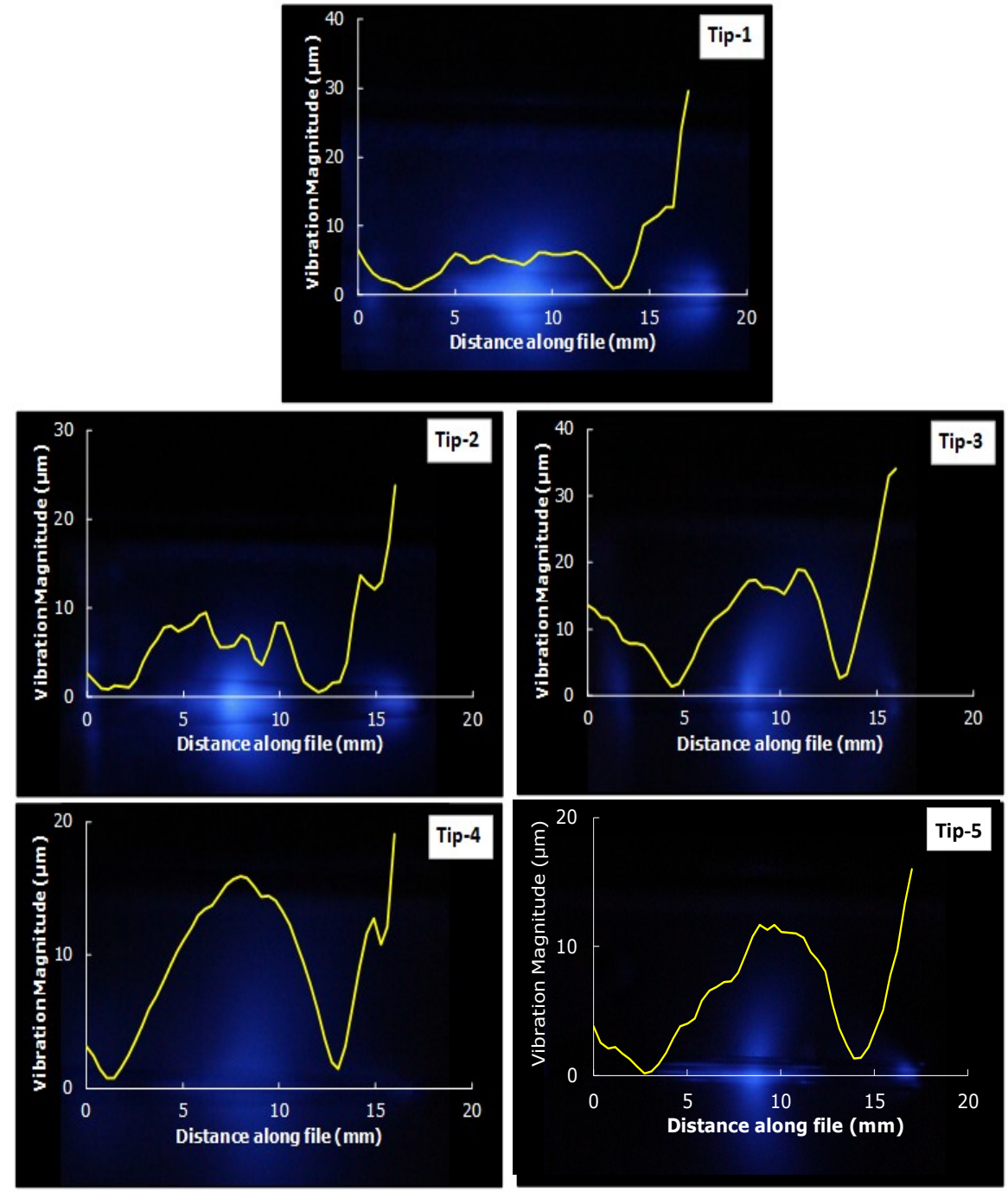

Figure 5.18: *Superimposed luminol photographs of the Start-X tips and their vibration magnitudes at Power 10/10 in water.*

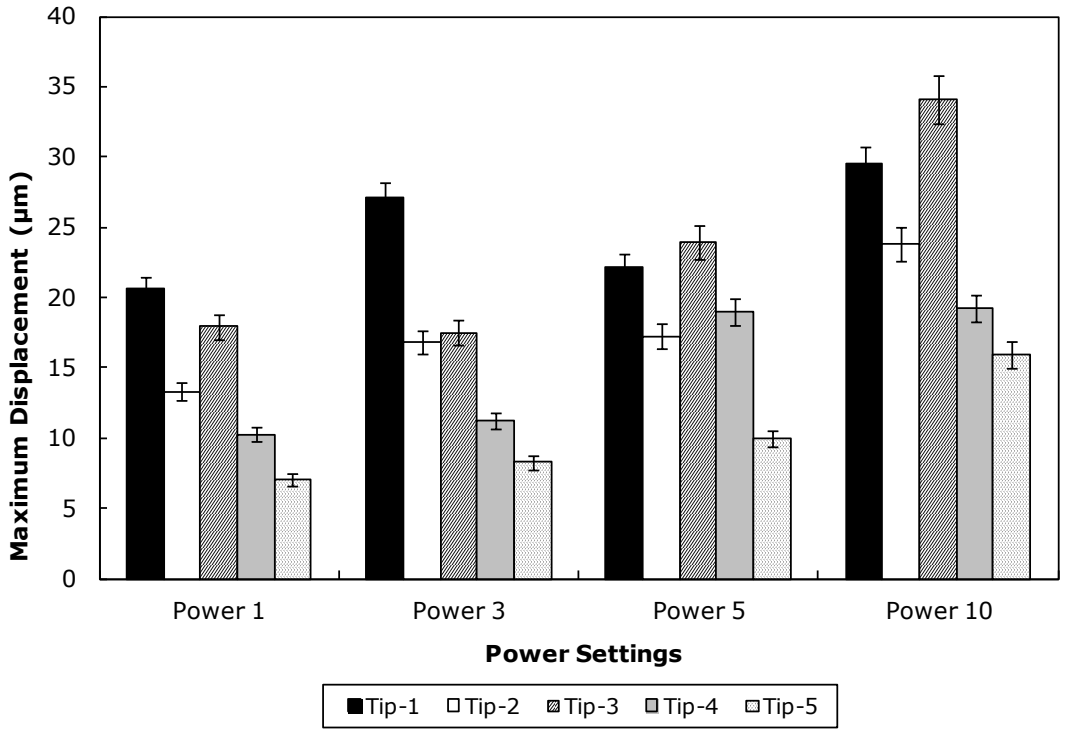

Figure 5.19: *Maximum displacement of all the Start-X tips at various power settings.*

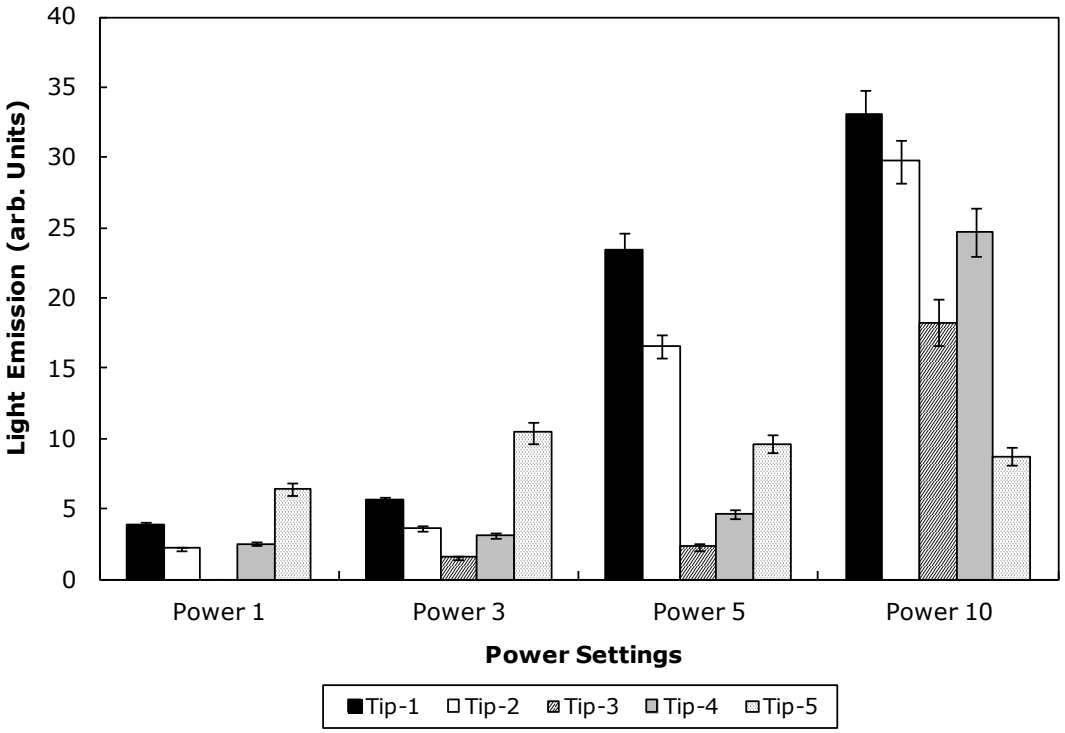

Figure 5.20: *Average light emission produced from sono(chemi)luminescence of all the Start-X tips at various power settings.*

5.4.4 Correlations among the SCL, Cavitation and Vibration Movements

Correlations between the parameters investigated on the Start-X tips were assessed statistically – by obtaining the Pearson's product-moment correlation coefficient, R value between the samples. Table 5.4 shows the respective R values between two parameters studied for each Start-X tips, and the overall correlation between the parameters at 99 % confidence level for a sample size of 10.

Table 5.4: *Pearson's product-moment correlation coefficients, R between the vibration movement amplitudes and the light intensity produced from SCL and the Cavitation counts for the Start-X endosonic files.*

	SCL *vs* vibration movements	**Vibration movements *vs* Cavitation**	**SCL *vs* Cavitation**
Tip-1	0.498 *no*	0.312 *no*	0.973 *yes*
Tip-2	0.924 *yes*	0.529 *no*	0.808 *yes*
Tip-3	0.950 *yes*	0.933 *yes*	0.993 *yes*
Tip-4	0.653 *no*	0.669 *no*	1.000 *yes*
Tip-5	0.184 *no*	0.311 *no*	0.766 *yes*
Overall	**no**	**no**	**yes**

For sample size of 10, degree of freedoms = 8
No correlation if, - 0.765 < R < 0.765

Based on Table 5.4, it can be seen that apart from Tip-3, the other tips showed little correlation between the vibration movement to the SCL and cavitation produced, indicating that the vibration movement amplitudes has only slight correlation to the production of cavitation, and that other factors such as the shape of the individual endosonic files may also influence the production of transient cavitation in the system.

On the other hand, there is a very strong correlation between the SCL and the cavitation counts, indicating that the two parameters have a strong relationship between each other. This strengthens the experimental results and verifies the experimental methods used in assessing the sonochemical activities of the endosonic files.

5.5 Conclusions

This chapter can be concluded into a few points:

i) SCL produced in a confined space is more intense than that in a bulk solution, but the total area of the confined space does not seem to show much difference in the production of SCL.

ii) For CT-4 and CKT-1, SCL is not affected by the position of the endosonic files in the model root canal, but has a strong effect on UT-4(2) – where there is no SCL detected when the file touches the wall of the channel.

iii) The vibration movements of the endosonic files are generally not affected by the space.

iv) The shape of the endosonic files have a strong effect on the SCL formed.

v) SCL showed a strong correlation ($R > 0.9$) with the cavitation counts, but poor correlation with the vibration movement amplitudes of the files. This indicates that files that vibrates at the highest amplitude does not necessarily produce the most SCL.

6. Computational Simulation of the Acoustic Pressure Fields

Despite all previous experiments performed in Chapters 3, 4 and 5 on characterisation, cleaning efficiencies and the effects of various factors on the areas of SCL and SLV patterns, there is still lack of information in the acoustic pressure fields – which acts as an important factor in producing transient cavitation bubbles.

Computational modelling has been widely used on ultrasonic systems to predict the violent conditions in the sonicating systems (Huang *et al*., 2004, Vanhille *et al*., 2004, Gao *et al*., 2009, Louisnard, 2012) – including the study on cavitation and bubble dynamics. On the other hand, some authors have used this method to predict the acoustic pressure fields in their sonicating systems. For example, Saez *et al.* (2004), Raman *et al*. (2006) and Klíma *et al*. (2007) have used the acoustic module in finite element analysis modelling (in COMSOL Multiphysics™) to predict the intensities and acoustic pressures around their sonicated sample using a 20 kHz ultrasonic probe. All these studies performed share the same aims – which is to have a better understanding on their ultrasonic systems used, correlate the result to the experimental results, and also to provide better optimisation on the experimental conditions for more efficient and reliable results.

Simulation was performed for the ultrasonic systems described in this thesis for the same reasons. Here, the acoustic pressure fields of various ultrasonic devices used (*i.e* 20 kHz ultrasonic probe, 515 kHz ultrasonic plate transducer and dental endosonic files) were modeled by using COMSOL Multiphysics™ (version 4.2a). The following exercises were performed:

i) Identifying the acoustic pressure fields of a 20 kHz ultrasonic probe and compared to the models performed in the literature. (2-Dimensional)

ii) Identifying the acoustic pressure fields of a 515 kHz ultrasonic plate transducer, compared to the sonoluminescence images obtained for the same system. (2-Dimensional)

iii) Building up the dental tip model using a 2-Dimensional acoustic pressure model system.

iv) Building up the dental tip model in 3-Dimensional acoustic pressure model system.

6.1 Simulation/Modelling Methods

To initiate this study, a few assumptions were made:

i) It is assumed that the sound wave propagates linearly[12].

ii) The sound wave travels as a sinusoidal wave profile and when time-harmonic domain is used in the software, it reduces the Helmholtz's equation to a second order ordinary differential equation.

iii) The sound wave propagates only in the longitudinal direction and shear stress is therefore neglected. (In this case, a plane wave is assumed in the models used)

iv) The ultrasonic devices simulated were all symmetric and operate at the frequency stated by the manufacturer, and remain constant throughout the length of study.

These assumptions are valid for acoustic pressure modelling using the acoustic module on COMSOL Multiphysics™ (version 4.2a). Saez *et al.* (2004), Raman *et al*. (2006) and Klíma *et al*. (2007) have used the same acoustic module on COMSOL Multiphysics™ for acoustic pressure modelling on power ultrasonic systems successfully. With these assumptions, it has to be noted that pressure values obtained from the simulated results can only be used for comparison but not for quantitative measurements, as there are other components such as: the effect of shockwaves from

[12] The sound wave system which responds only to the driving frequency.

the collapse of transient cavitation, presence of cavitation bubbles and streaming effects resulting in formation of dynamic pressures in the system – which are all not considered in this computational model.

Computational modelling on acoustic pressure predictions is based on the general equation of the wave profile (Comsol, 2011):

$$\frac{1}{\rho_o c^2}\frac{\partial^2 p}{\partial t^2} + \nabla\left(-\frac{1}{\rho_o}\nabla p\right) = 0 \qquad \textbf{(Equation 6)}$$

Where,

ρ_o : density of the fluid

c : speed of sound in the fluid medium

p : pressure

∇ : Laplacian operator

For time harmonic wave profiles, where,

$$p = p_o\, e^{(i\omega t)} \qquad \textbf{(Equation 7)}$$

p_o : pressure amplitude

ω : angular frequency ($2\pi f$)

f : frequency

This reduces the wave equation to:

$$\nabla\left(-\frac{1}{\rho_o}\nabla p\right) - \frac{\omega^2}{\rho_o c^2}\, p = 0 \qquad \textbf{(Equation 8)}$$

which is also known as the Helmholtz equation.

COMSOL performs finite element analysis based on meshes generated around domains. For this study, predefined tetrahedron mesh was used.

6.1.1 20 kHz Ultrasonic Probe

For the 2-dimensional 20 kHz ultrasonic probe model;

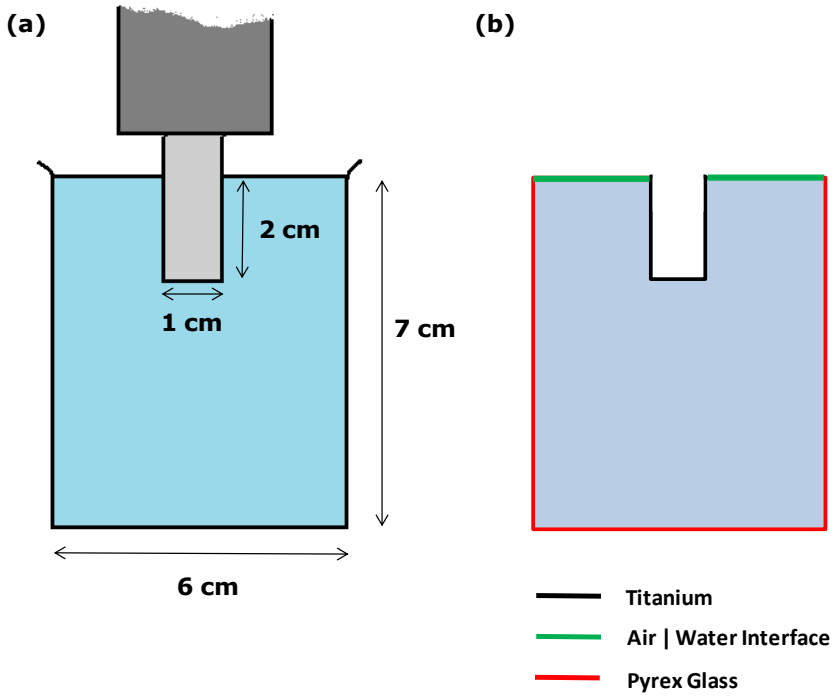

Figure 6.1: *(a) Dimensions of the ultrasonic probe immersed into a Pyrex beaker containing water. (b) Model dimensions built in COMSOL with different boundary conditions.*

In order to check the validity of the model, different boundary conditions were examined:

i) All boundaries were hard boundary walls[13].

ii) Soft boundary[14] at the air | water interface, and hard boundaries everywhere else.

---

[13] Hard wall boundary assumes all sound wave gets reflected at constant velocity, where $\delta p/\delta n = 0$; where p is the acoustic pressure and n is the normal vector to the boundary surface. (Refer to Appendix I for explanation)

[14] Soft wall boundary assumes all sound wave gets reflected entirely at the boundary and that $p = 0$ at the boundary. (Refer to Appendix I for explanation)

iii) Soft boundary at the air | water interface, impedance of titanium at the walls of the ultrasonic probe (27.3 MPa s m^{-1} *or* MRayl) and hard boundaries around the outer boundaries (of the Pyrex glass).

iv) Soft boundary at the air | water interface, impedance of titanium at the walls of the ultrasonic probe and the impedance of glass at the Pyrex glass boundary (13 MRayl).

After establishing the boundary conditions, the acoustic pressure amplitudes were adjusted based on Equation 8 and inserted into the model. The pressure amplitude (p_o) of the system was calculated based on the intensities (I = power/area) of each system obtained calorimetrically (Section 3.1) using the equation:

$$I = \frac{p_0^2}{2\rho_o c} \qquad \textbf{(Equation 9)}$$

The sound wave profile used was plane wave radiation from the bottom of the ultrasonic probe. The total amount of elements[15] studied were adjusted based on the wave number, ω/c, which does not affect this study as the frequency remains constant.

6.1.2 515 kHz Ultrasonic Plate Transducer

Similar to the 20 kHz ultrasonic probe, the model built for the 515 kHz ultrasonic plate transducer was examined with various boundaries conditions, and compared to the actual experimental results showing the areas producing sonoluminescence.

[15] Divisions of the number of points (built as 'meshes' in the simulation process) taken within the model built for simulation process. (Refer to Figure 6.16).

Various boundary conditions were tested on the 2-D 515 kHz model:

i) Assuming all hard boundaries

ii) Hard boundaries at the vessel walls and soft boundary at the air | water interface

iii) Impedance of pyrex glass at the vessel walls and soft boundary at the air | water interface

The 515 kHz plate transducer was modeled in the 2-Dimensional model.

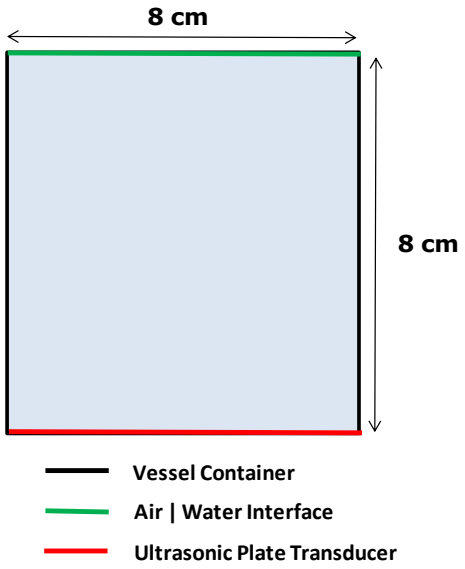

Figure 6.2: *Dimensions of the vessel and the ultrasonic source in the 2-Dimensional acoustic pressure model.*

Once the boundary conditions were established, the effects of changing the acoustic pressure amplitudes (based on Equation 8) and the height of the vessel (which is determined by the amount of water placed into the vessel) were assessed.

6.1.3 2-Dimensional Dental Tip Model

The dental tips used for previous experiments in Chapters 3, 4 and 5 were modelled as a rectangular void of 2.5 mm wide and 15 mm long, immersed into in a

rectangular vessel of 10 mm wide and 50 mm long (Figure 6.3). Ultrasound was set to emit through both sides of the rectangular void.

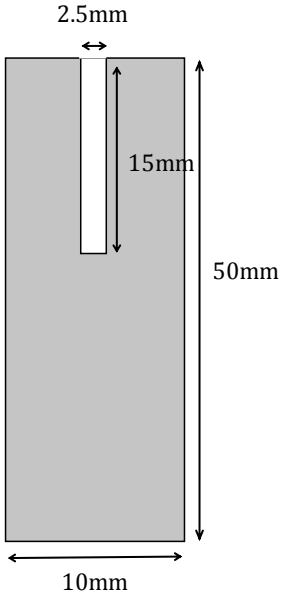

Figure 6.3: *Dimensions of the 2-D dental tip model.*

Similar to the previous sections, various boundary conditions of the model were examined:

i) All Hard Boundaries.
ii) All Hard Boundaries, Soft boundary at air | water interface.
iii) Hard wall boundaries, soft boundaries at air | water interface, stainless steel impedance (45.7 MRayl) at the bottom of the model tip.
iv) Glass impedance at the walls, soft boundaries at air | water interface, stainless steel impedance at the bottom of the tip.
v) Silicone rubber impedance (1.43 MRayl) at the walls, soft boundaries at air | water interface, stainless steel impedance at the bottom of the tip.

Upon deciding the suitable boundary conditions, the dental tip dimensions were altered to examine the effects of the dimensions on the acoustic pressure profiles. This was performed by adjusting:

i. Width of the dental tips (2.5 mm, 2.0 mm, 1.5 mm, 1.0 mm)
ii. Height of the dental tips (15 mm, 16 mm, 17 mm, 18 mm, 19 mm, 20 mm)

6.1.4 3-Dimensional Dental Tip Model

To bring the simulation work further, a 3-Dimensional model of the dental tips used was built, within which the novelty of this work lies as there has been little work done on 3-Dimensional pressure fields modeling, especially for ultrasonic dental instruments.

The 3-Dimensional dental tip models built based on a few stages:

Stage 1: Using a rectangular slab model.
Stage 2: Using a cylinder model.
Stage 3: Using a cone model.

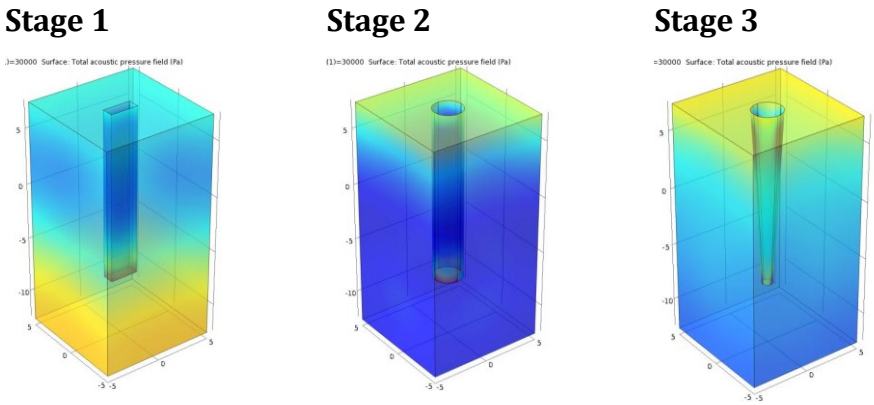

Figure 6.4: *An example of the 3-D model built to represent each stage of dental tip modeling.*

For each stage of the 3-D modeling process, the length and width of the dental tip was varied to examine the effects of acoustic pressure at different dimensions. The dimensions of the vessel remained unchanged in this study and were set to be 10 mm × 10 mm × 20mm. In general, the change of dimensions was performed as such (although slight changes have to be modified to cater for the different shapes of the model):

a) Width of the dental tips (2.5 mm, 2.0 mm, 1.5 mm, 1.0 mm)
b) Height of the dental tips (15.0 mm, 15.5 mm, 16.0 mm, 16.5 mm)

Boundary conditions used were similar to those developed in the previous sections in the 2-D models, where:

- Hard boundaries: Vessel walls and the dental tips. ($\frac{\partial p}{\partial n} = 0$)
- Soft boundaries: air | water interface. (p = 0, total sound reflection)

6.2 Simulation Results and Discussion

6.2.1 20 kHz Ultrasonic Probe

For all simulations performed on the 20 kHz ultrasonic probe, the initial pressure amplitude (p_o) value inserted into the model was based on the intensity supplied to the system, obtained calorimetrically (Section 3.1), which, was calculated to be:

i) 20 % on the power dial ≡ 5.10 W cm^{-2} ≡ 3.91 × 10^5 Pa
ii) 40 % on the power dial ≡ 9.72 W cm^{-2} ≡ 5.40 × 10^5 Pa
iii) 60 % on the power dial ≡ 13.06 W cm^{-2} ≡ 6.26 × 10^5 Pa
iv) 80 % on the power dial ≡ 16.17 W cm^{-2} ≡ 6.96 × 10^5 Pa

6.2.1.1 Effects of Various Boundary Conditions

Table 6.1: *Effect of various boundary conditions onto the sonicating system with a 20 kHz 'plane wave' ultrasonic source travelling into the system at an acoustic pressure amplitude (p_o) of 3.91 × 10^5 Pa.*

(i)	All hard boundaries 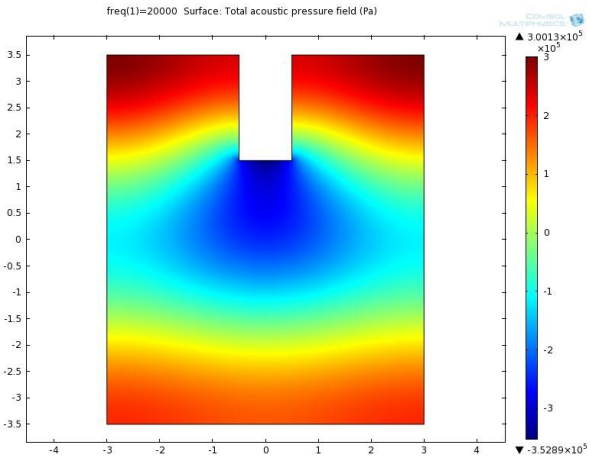
(ii)	All hard boundaries, soft boundaries at the air | water interface 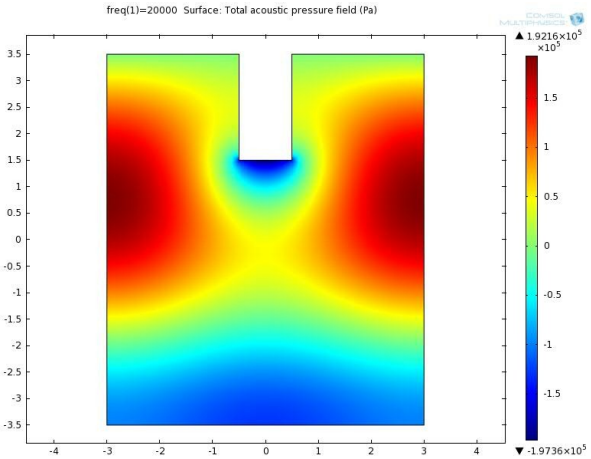

(iii)	Hard boundaries at the walls of the vessels, soft boundaries at the air | water interface, acoustic impedance of titanium at the sides of the titanium horn. 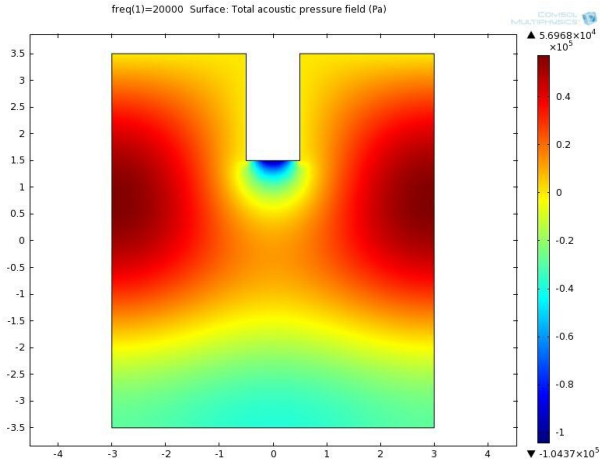
(iv)	Acoustic impedance of Pyrex glass at the walls of the vessels, soft boundaries at the air | water interface, acoustic impedance of titanium at the sides of the titanium horn. 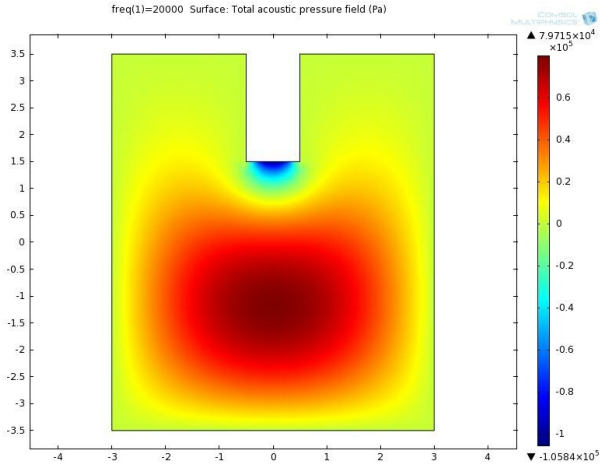

A longitudinal line was then drawn from the bottom of the ultrasonic horn model in a downwards direction for all the boundary conditions tested, to plot the total acoustic pressure produced along the longitudinal direction.

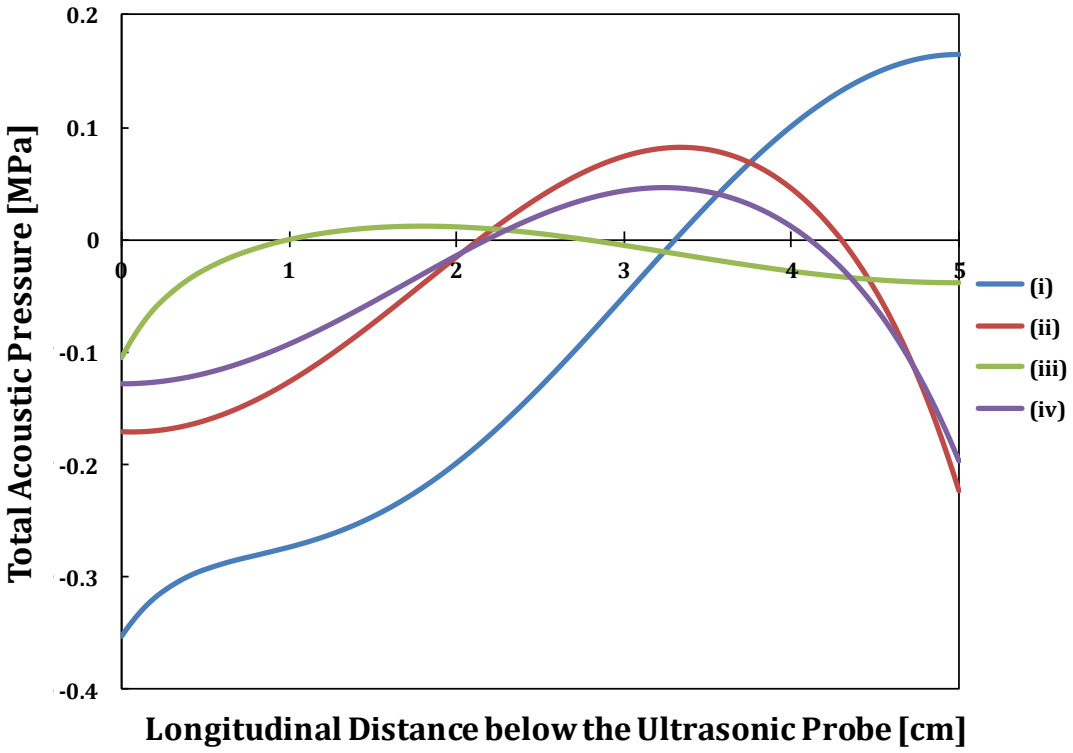

Figure 6.5: *Total acoustic pressure in the longitudinal direction below the ultrasonic probe model at various boundary conditions as stated in Table 6.1.*

It is interesting to see the effects of various boundary conditions on the total acoustic pressure fields produced in Table 6.1. Following to that, Figure 6.5 shows a big variation of acoustic pressure patterns when different boundary conditions were applied. Upon comparison with the actual sonoluminescence given out by the ultrasonic probe at the said settings, it was found that boundary condition (ii) and (iv) most closely matches with the experimental results obtained, where (ii) gives a higher maximum acoustic pressure at all the antinodal areas, as it assumes the wall boundaries as 100 % reflective boundaries and (iv) takes into account the acoustic impedance of those boundaries hence adjusting the acoustic pressure slightly. Klíma *et al.* (2007) found a similar trend of ultrasonic intensity obtained by a 20 kHz ultrasonic probe (Figure 6.6), which further strengthens our experimental results

obtained. It was therefore decided to use the boundary conditions (iv) to further our investigation, using the exact acoustic impedance of the material on the boundary conditions and treating the air | water interface as a soft boundary.

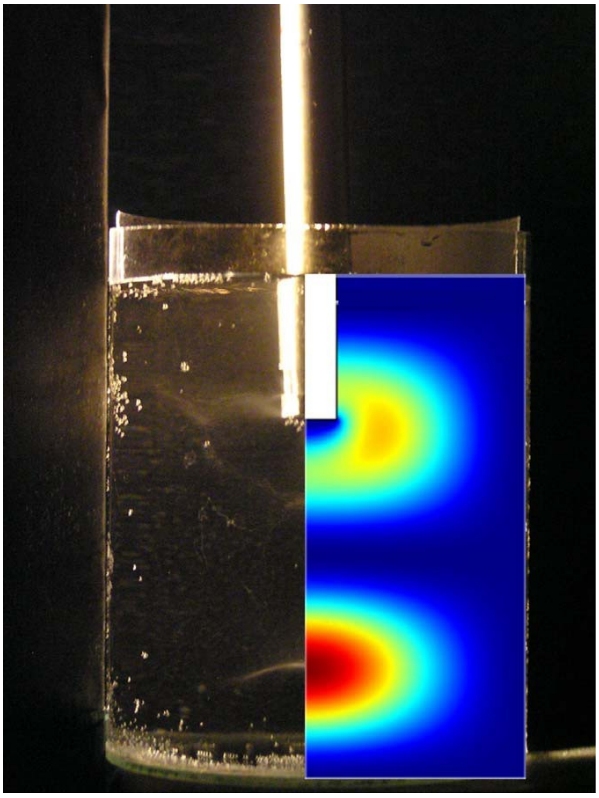

Figure 6.6: *Photograph of cavitating bubbles in a beaker under sonication of a 20 kHz ultrasonic probe at an ultrasonic power of 10 W, embedded with a simulated intensity distribution.*

Image taken from Klíma *et al.* (2007) with author's permission.

6.2.1.2 Effects of the Acoustic Pressure Amplitude

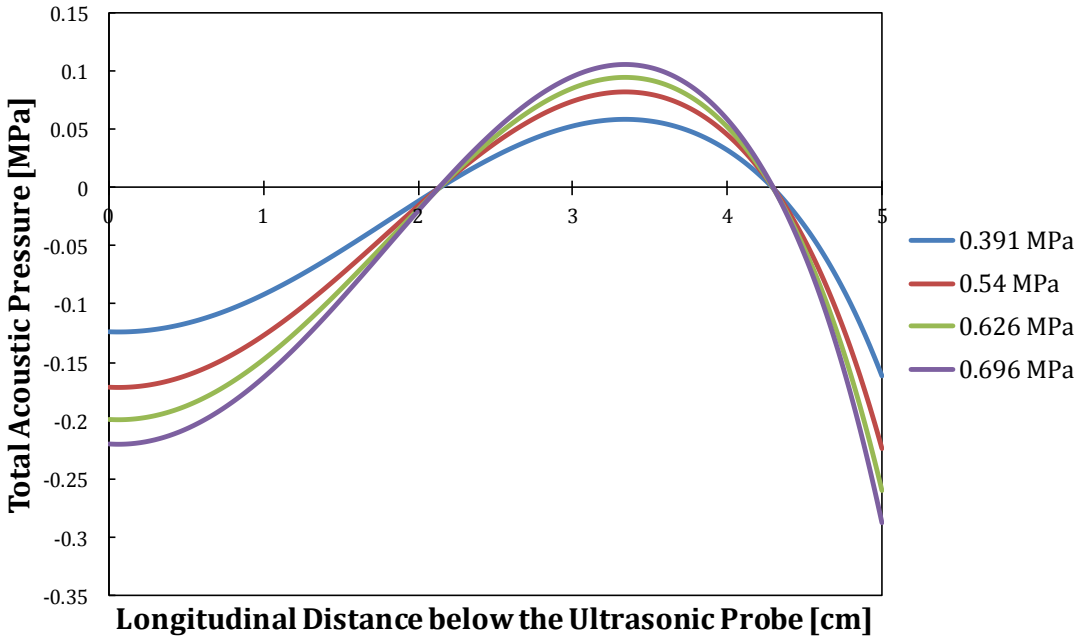

Figure 6.7: *Total acoustic pressure along the longitudinal direction below the ultrasonic probe model at various acoustic pressure amplitudes.*

Using the boundary conditions (iv), the ultrasonic probe model system was tested with different acoustic pressure amplitudes, obtained from the calorimetry results in Section 3.1. Based on Figure 6.7, when the acoustic pressure amplitude increases, the magnitudes of the total acoustic pressure increases as well, with an exception of the nodal points remaining the same for all the intensities tested. This indicates that there is no change in the acoustic pressure field patterns given the change in amplitude apart from the magnitude, which is supported by the sonoluminescence results on the 20 kHz ultrasonic probe at varying intensities (Figure 3.10) – which has also strengthen the reproducibility of the simulation work.

6.2.1.3 Effects of Vessel Dimensions

In this section, the effects of vessel dimensions were assessed based on the same acoustic pressure amplitude.

This can be separated into two sections:

a) increment of the width of the vessel
b) increment of the height of the vessel

Based on Table 6.2, it can be seen that there is a distinguishable change in acoustic pressure patterns as the width of the reaction vessel changes. In all cases, negative acoustic pressure is developed at the base of the ultrasonic probe, even though a different magnitude of total acoustic pressure is obtained when the vessel condition changes.

a) Increment in width of the vessel

Table 6.2: *Total acoustic pressure contour plots and their respective 1-dimensional acoustic pressure along the y-axis below the surface of the ultrasonic probe at various reactor vessel widths.*

(i)	6 cm width 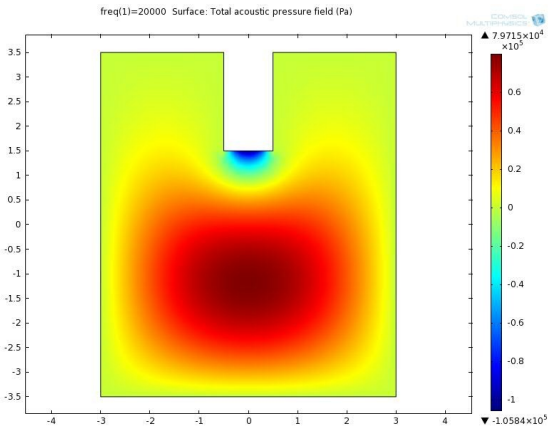	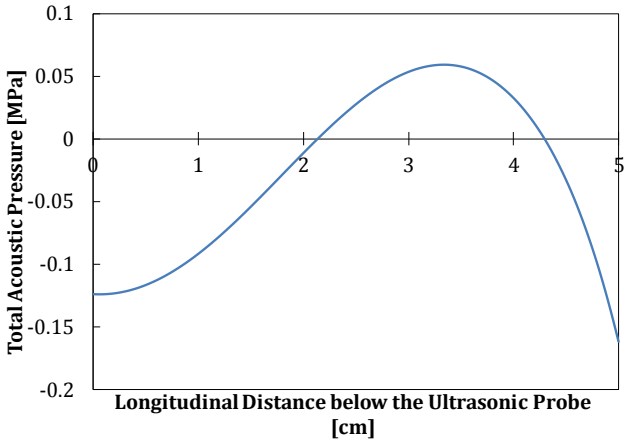

(ii)	8 cm width 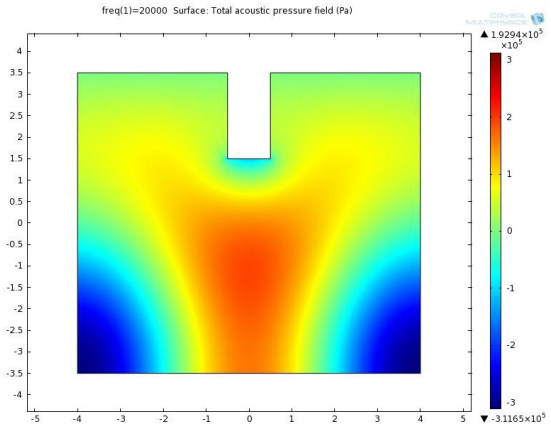	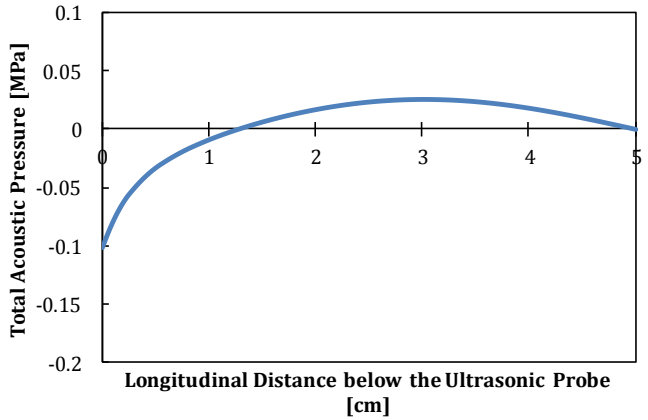
(iii)	10 cm width 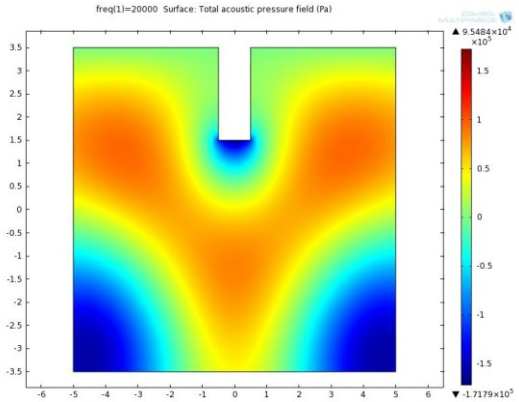	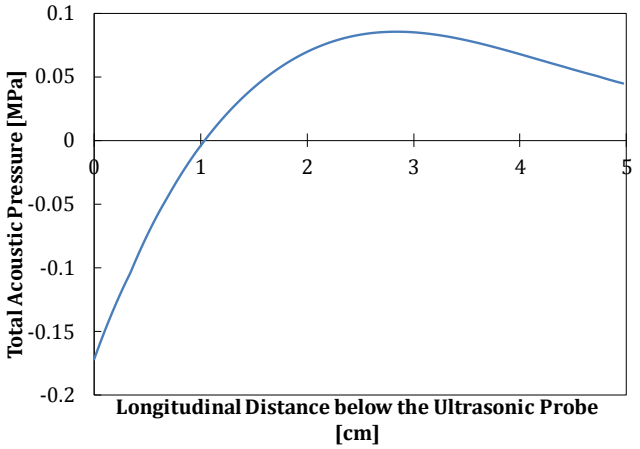

(iv)	12 cm width 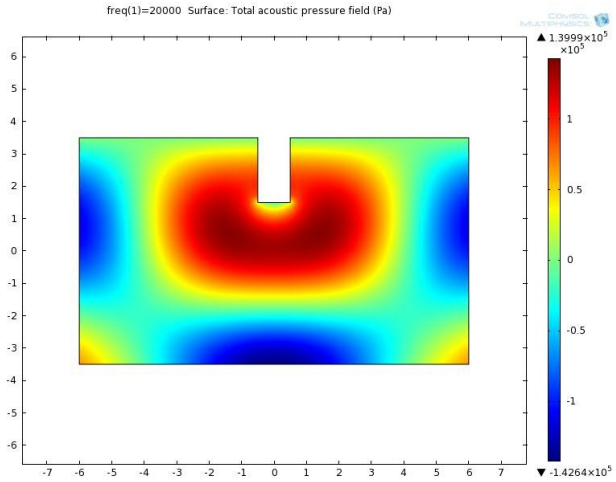	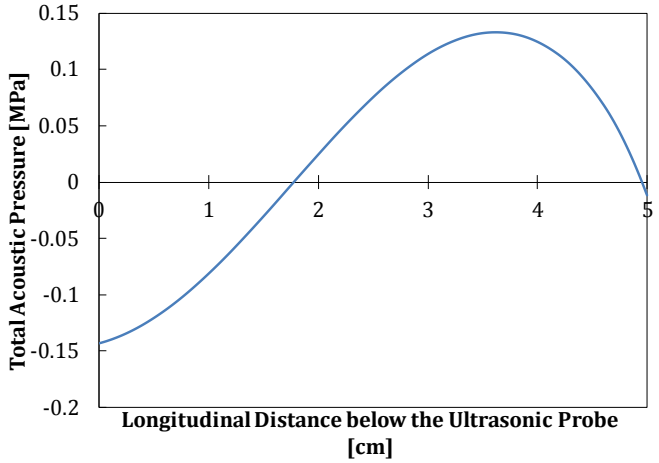
(v)	20 cm width 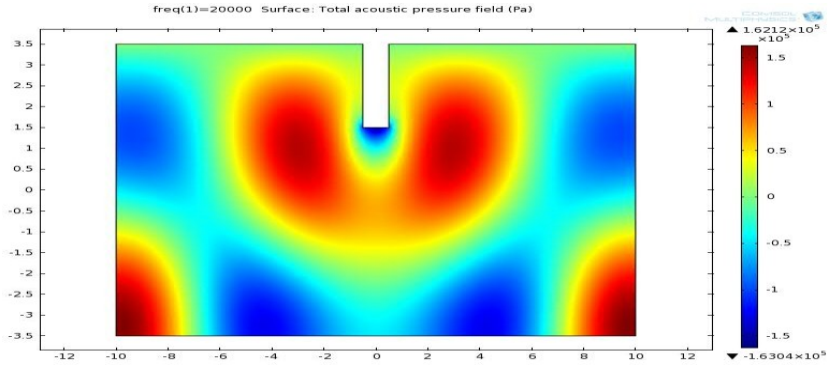	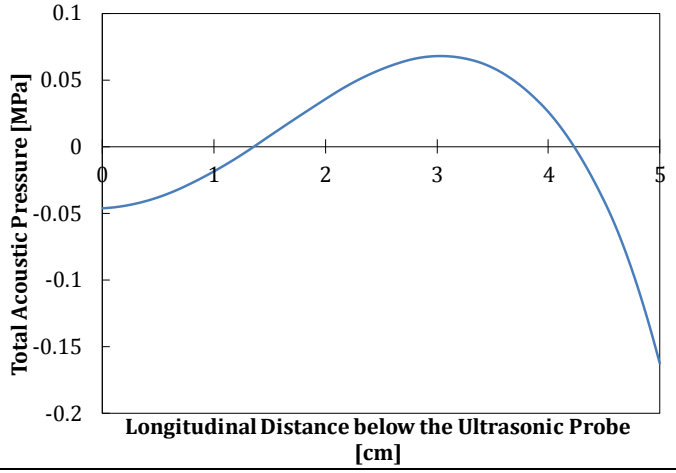

b) Increment in height of the vessel

Table 6.3: *Total acoustic pressure at a fixed amplitude contour plots and their respective 1-dimensional plots along the z-axis below the ultrasonic probe.*

(i)	7 cm height 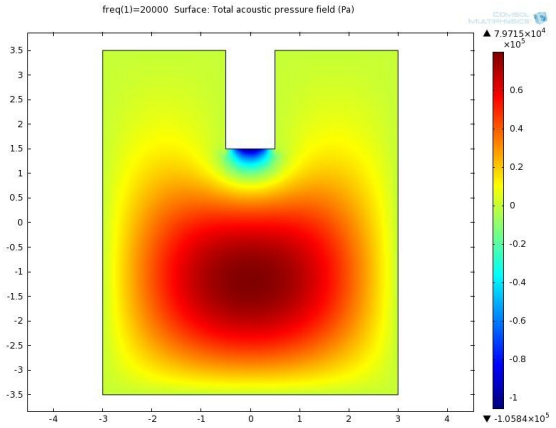	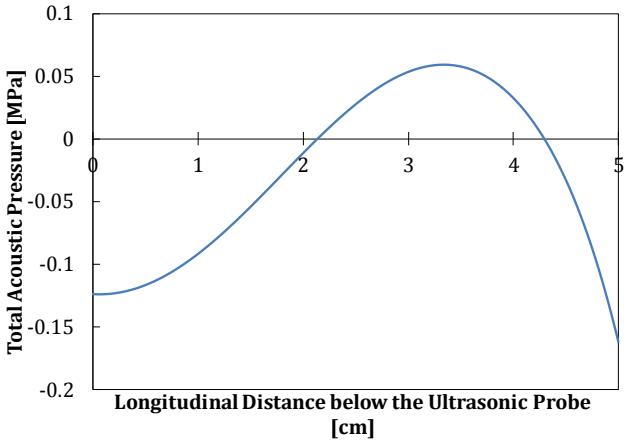

(ii)	8 cm height 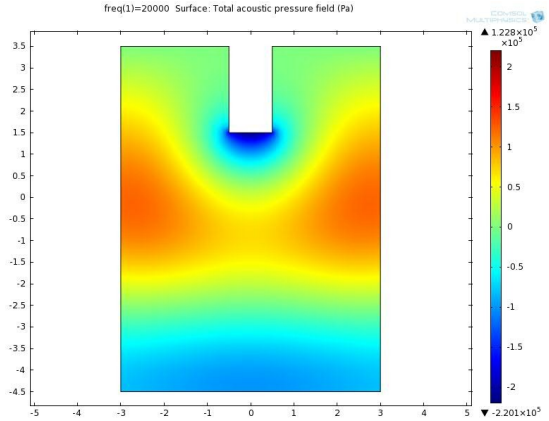	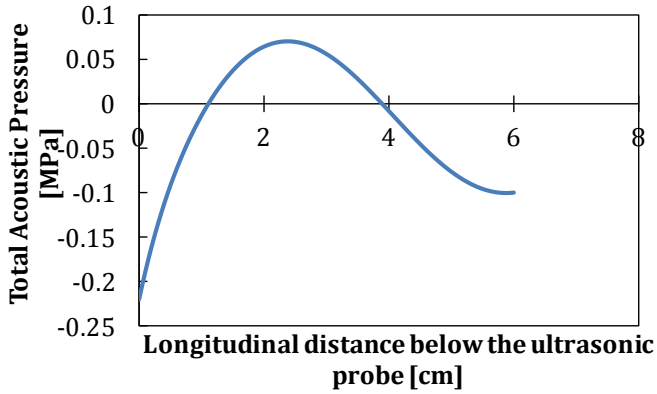
(iii)	10 cm height 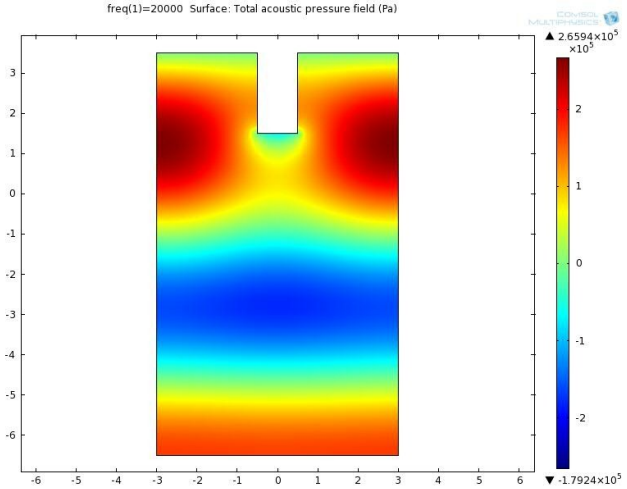	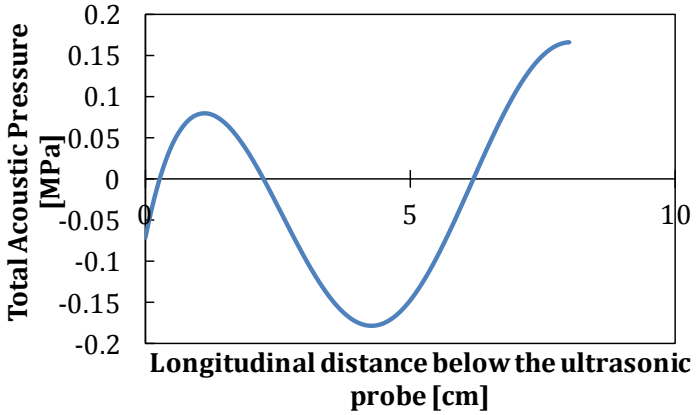

(iv)	12 cm height 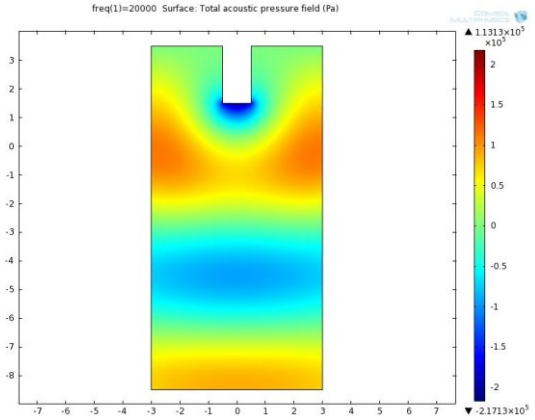	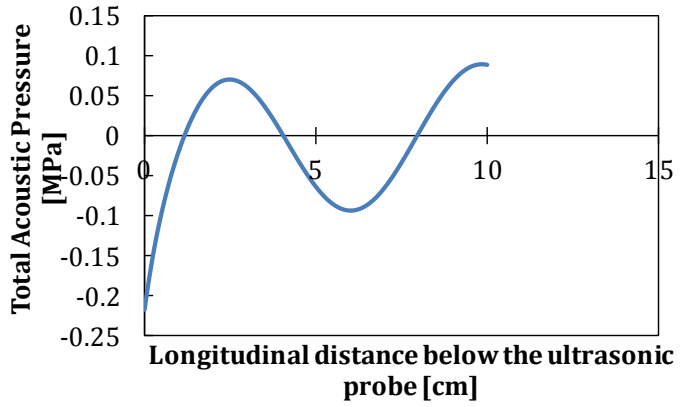
(v)	20 cm height 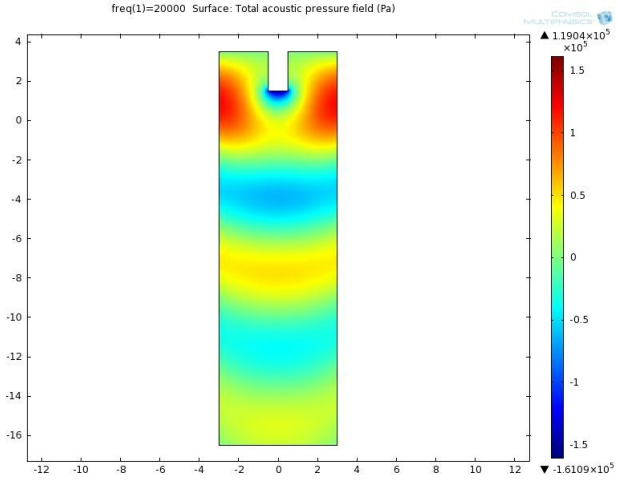	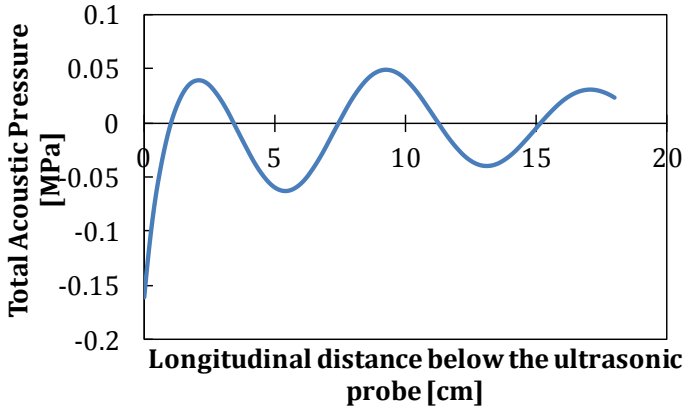

Based on Table 6.3, it can be seen that as the height of the vessel increases, a standing wave profile is produced, with a wavelength of 7.5 cm, corresponding to the wavelength of 20 kHz sound in water. From the sonoluminescence images, cavitation activity can only be detected at the areas closer to the tip of the ultrasonic source but not at the other antinodal points along the acoustic pressure wave profiles, indicating that other factors such as sound attenuation, together with the damping effect caused by bubble dynamics in the system, might also play a factor in the acoustic pressure profile but are not taken into account in this study.

The nature of this work is to predict the acoustic pressure fields around the ultrasonic devices. Experiments performed on the 20 kHz ultrasonic probe were to confirm and to have an established simulation method for further studies on the dental endosonic sources used. Based on the results obtained, there is a distinguishable change in the total acoustic pressure field patterns when the size of a vessel changes. Experiments on the characterisation of sonochemical cells performed by Birkin *et al*. (2003) and Vian *et al*. (2010) have found out that the sonochemical yield has strong dependence on the geometry of the reactors used, which has strengthened the simulated results obtained above. Comparable results were also obtained to those reported in the literature (Sáez *et al*., 2005, Raman *et al*., 2006, Klíma *et al*., 2007). This leads into the next part of the simulation study on the 515 kHz ultrasonic plate transducer to further strengthen the simulation methodology used.

6.2.2 515 kHz Ultrasonic Plate Transducer

Similar experiments were performed on the 515 kHz ultrasonic system as compared to the 20 kHz system. The boundary conditions of the system were first examined, and then a suitable boundary condition was chosen and compared to the actual experimental results on the sonoluminescence produced.

The pressure amplitudes used in this study was based on the intensities of the system, obtained calorimetrically and was found to be:

i)	Power 2/10	≡ 0.1028 W cm^{-2}	≡ 5.55×10^4 Pa
ii)	Power 4/10	≡ 0.2004 W cm^{-2}	≡ 7.75×10^4 Pa
iii)	Power 6/10	≡ 0.4137 W cm^{-2}	≡ 1.11×10^5 Pa
iv)	Power 8/10	≡ 0.6707 W cm^{-2}	≡ 1.41×10^5 Pa

6.2.2.1 Effects of Different Boundary Conditions

i) All hard boundaries.

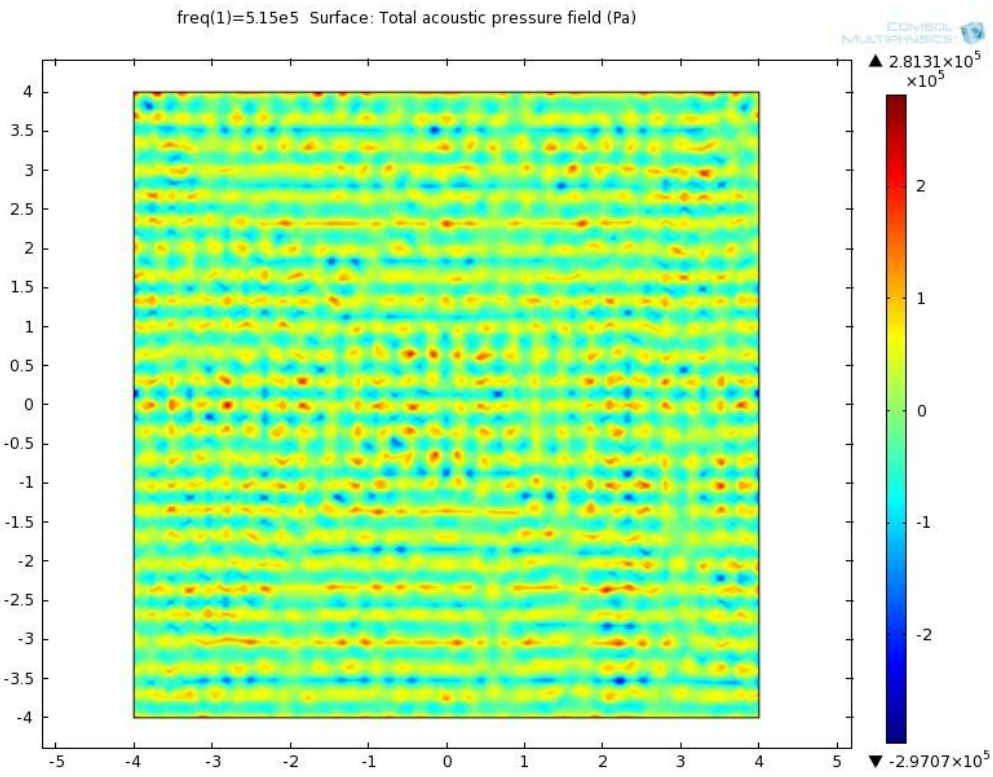

Figure 6.8: *Total acoustic pressure contour plot when all the boundaries were assumed to be hard wall boundaries, at an initial pressure amplitude of 5.55 × 10⁴ Pa.*

ii) Soft boundary at the air | water interface, hard boundaries at the vessel walls.

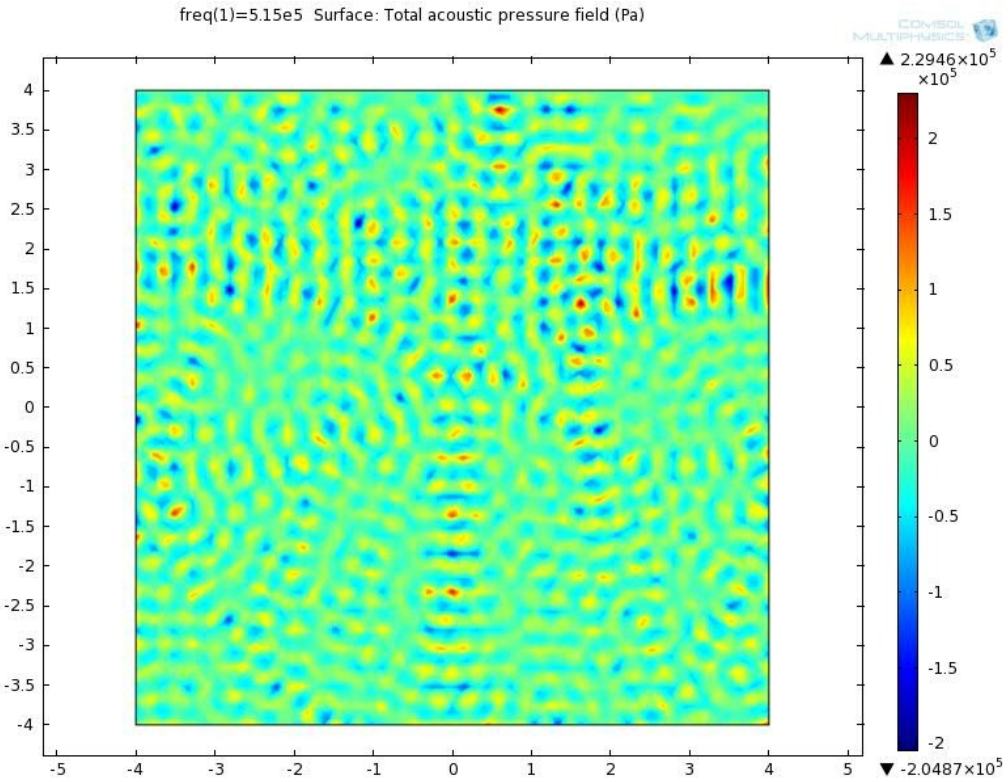

Figure 6.9: *Total acoustic pressure contour plot when the air | water interface was assumed to be a soft wall boundary, and hard wall boundaries at the vessel walls, at an initial pressure amplitude of 5.55 × 10⁴ Pa.*

iii) Soft boundary at the air | water interface, acoustic impedance of Pyrex glass at the vessel walls.

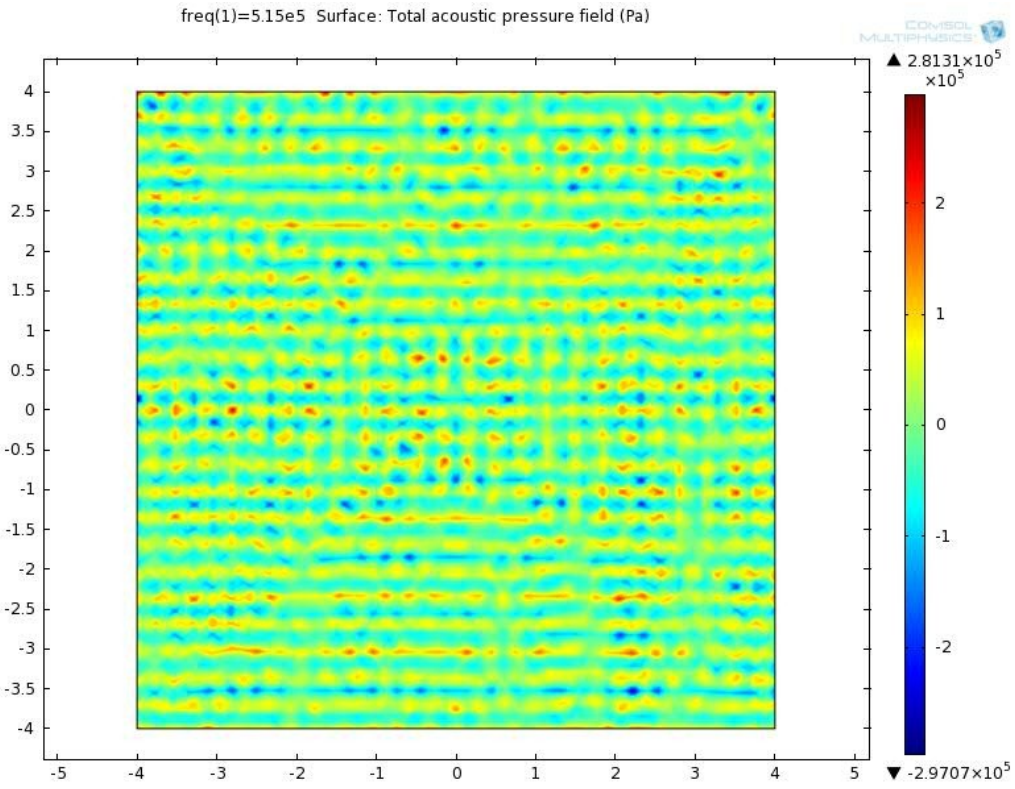

Figure 6.10: *Total acoustic pressure contour plot when the air | water interface was assumed to be a soft wall boundary, and the acoustic impedance of Pyrex glass at the vessel walls, at an initial pressure amplitude of 5.55 × 10⁴ Pa.*

From the results shown in Figures 6.8, 6.9 and 6.10, the change in the boundary conditions only changes the acoustic pressure field patterns slightly and there is not much difference in the magnitudes of the maximum and minimum acoustic pressures produced. Hence, in this case, boundary condition (iii) was chosen for further studies for the 515 kHz system to have a better match with the actual system used in practice.

6.2.2.2 Effects of Pressure Amplitudes

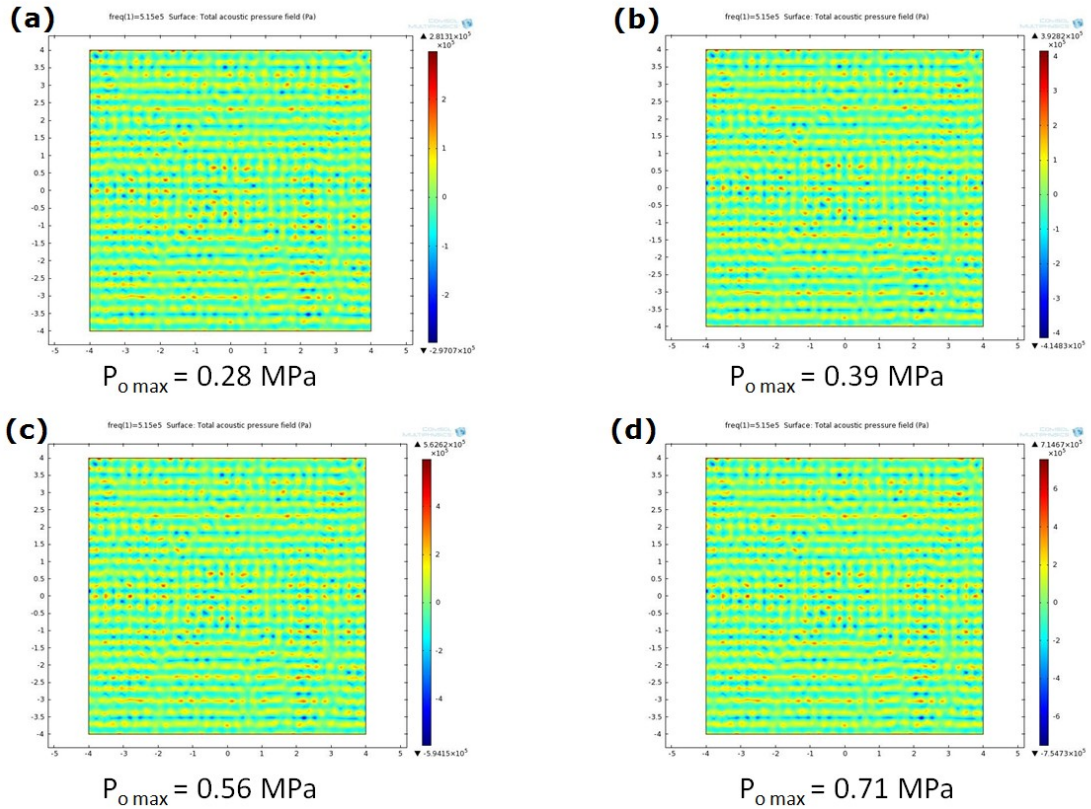

Figure 6.11: *Total acoustic pressure produced by a 515 kHz ultrasonic plate transducer at various pressure amplitudes employed. (a) 0.055 MPa; (b) 0.078 MPa; (c) 0.11 MPa; (d) 0.14 MPa.*

There is a formation of a standing wave profile in the 515 kHz plate transducer, with an increase in maximum acoustic pressure as the intensity (initial acoustic pressure amplitude) increases.

Henglein explained that the cavitation activities tend to appear at the acoustic pressure antinodes, as the cavitation bubbles were to be smaller than the resonant bubble size and were all driven by Primary Bjerknes force to be aligned along the antinodal points (Leighton, 1994). For a standing wave profile, the cavitation activities can be seen to occur at twice the acoustic frequency (or at $\lambda/2$) due to the adjacent pressure antinodes oscillating at π out of phase in time (Leighton, 1994).

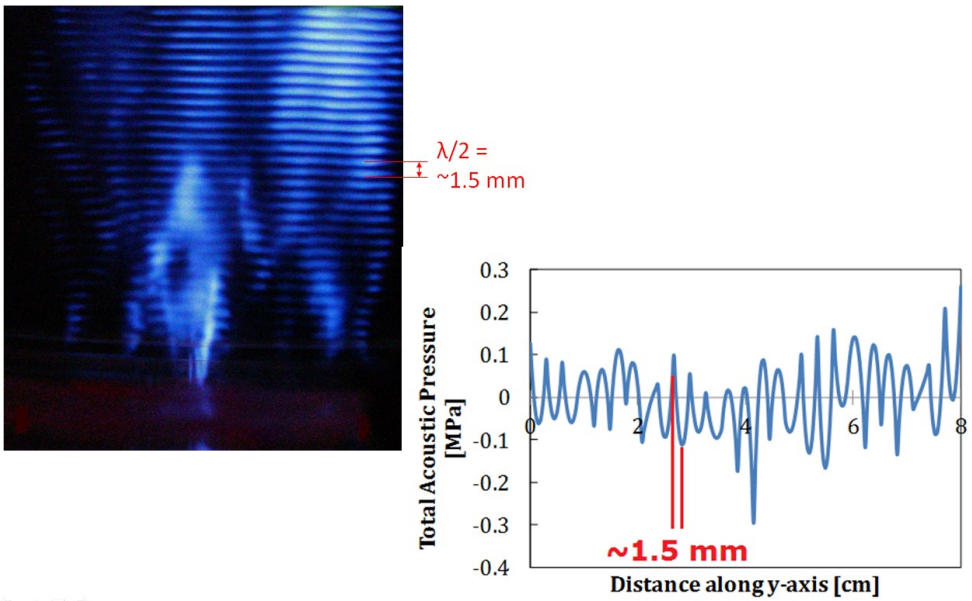

Figure 6.12: *(Left) Sono(chemi)luminescence image taken with the 515 kHz ultrasonic plate transducer upon exposure time of 30s at an intensity of 0.4 W cm^{-2}; (Right) An extracted 1-dimensional acoustic pressure along the y-axis in the middle of the simulated vessel.*

Figure 6.12 shows a correlated result on the sono(chemi)luminescence image taken upon sonication in luminol for 30 s at 0.4 W cm^{-2} (corresponding to 0.11 MPa of acoustic pressure amplitude in the simulation) and the total acoustic pressure plot along the y-axis in the middle of the simulated vessel. Results have shown that the light bands where sono(chemi)luminescence activity occurs correspond to half the wavelength of 515 kHz sound travelling in water, which correlates with the acoustic pressure profile obtained. With this, we can confirm that the methods used in the simulation, correlates to the experimental results and this then gains confidence to further simulation studies on the dental tip models.

6.2.3 2-Dimensional Dental Tip Model

Upon developing the ultrasonic model using appropriate equations and comparing the mathematical model results with the actual experimental observations and from the literature, a new 2-dimensional model of a dental tip was built based on the acoustic properties used in the previous sections.

Here, the dental tip was modelled as a rectangular void (Figure 6.3). The study was initiated by varying the boundary conditions, and followed by varying the width and height of the dental tip.

6.2.3.1 Boundary Conditions Study

Based on Table 6.4, it can be seen that changing the boundary conditions changes the pressure field patterns. In all cases, the maximum acoustic pressure field is present at the free end of the dental tip model, and with a slight negative acoustic pressure at the top of the dental tips (with an exception of boundary condition (iii)).

Further studies on the 2-dimensional dental tip model were based on boundary condition (v) as it mimics the actual experimental conditions most where silicone rubber was used as the walls of the vessel, which acts as a high sound absorber.

Table 6.4: *Total acoustic pressure plots for the 2-Dimensional dental tip model at a pressure amplitude of 0.39 MPa at various boundary conditions.*

i) All hard boundaries

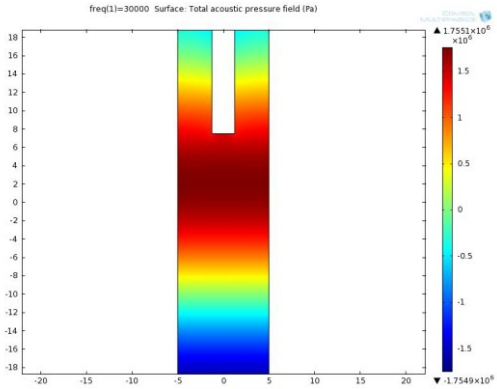

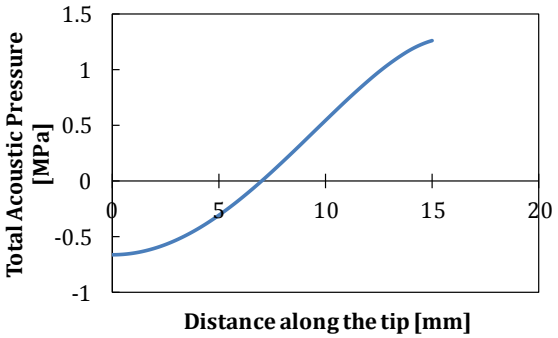

ii) Soft boundary at the air | water interface, hard boundaries everywhere else

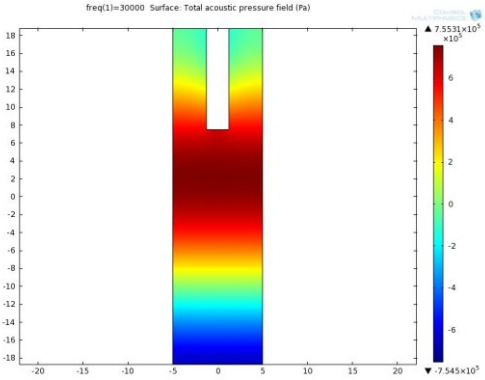

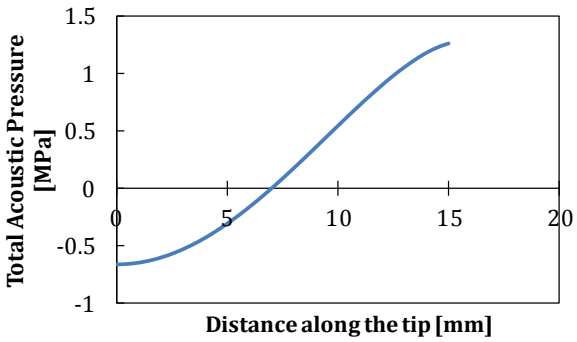

iii) Soft boundary at the air | water interface, impedance of stainless steel (45.7MRayl) at the bottom of the model tip, hard boundaries at the walls

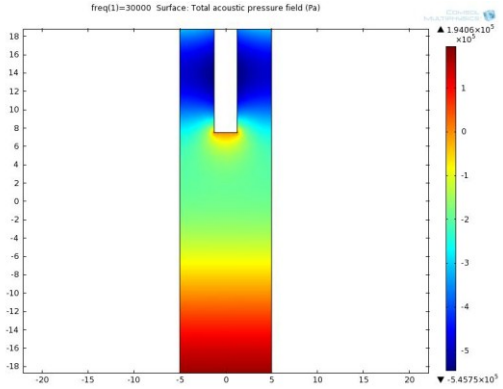

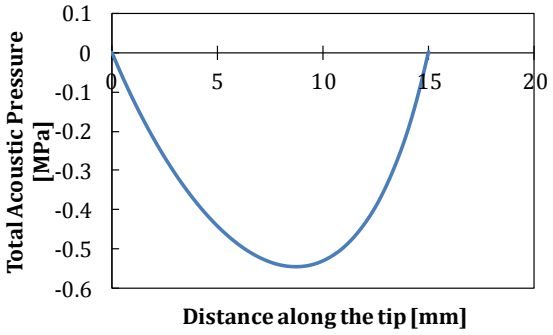

iv) Soft boundary at the air | water interface, impedance of stainless steel at the bottom of the tip, impedance of glass (13 MRayl) at the walls

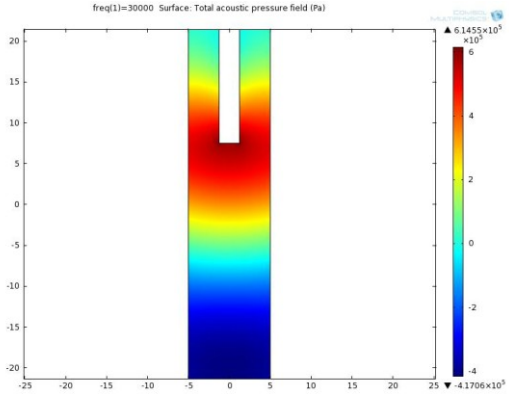

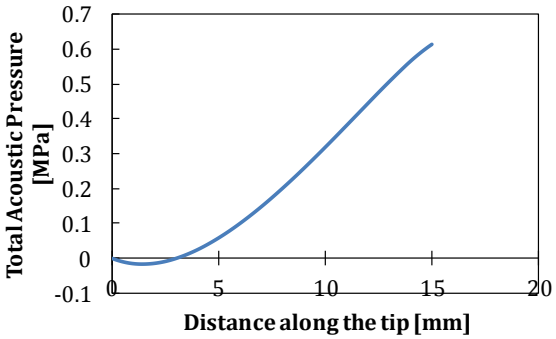

v) Soft boundary at the air | water interface, impedance of stainless steel at the bottom of the tip, impedance of silicone rubber (1.43 MRayl) at the walls

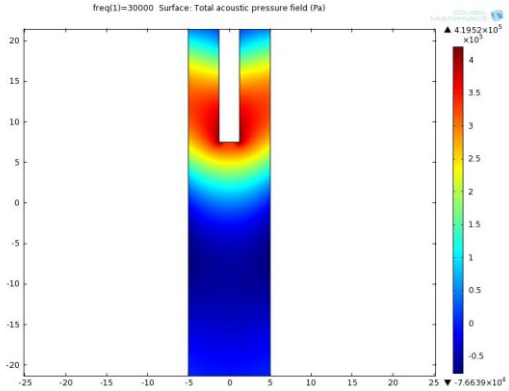

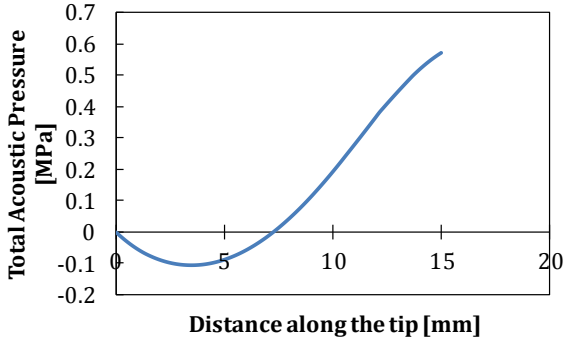

6.2.3.2 Effects of different dimensions of the dental tip

The results of changing the dimensions of the dental tip model were not very informative, where there is almost no detectable differences in the total acoustic pressure produced when there is a change in the width of the model tips (Figure 6.13).

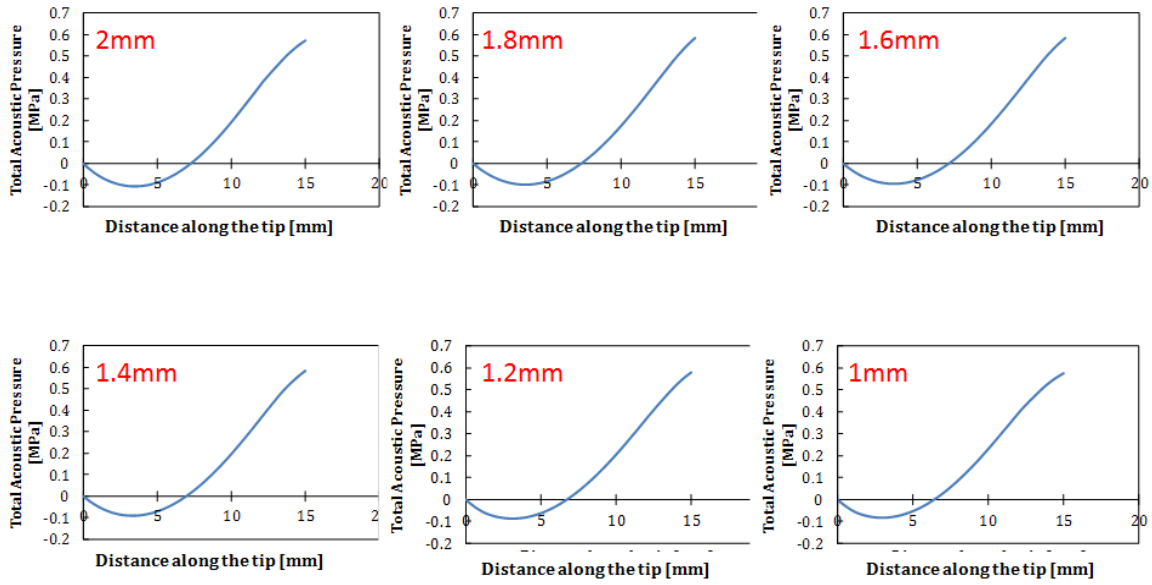

Figure 6.13: *Change in total acoustic pressure along the distance of the tip of different widths.*

The 2-dimensional model has its limitations where it assumes that the sound source is uniformly distributed throughout the entire dental tip, when in reality, is not the case. An example of the limitation of this model is showed in Figure 6.13, when the change of the width in the dental tip model should result to a significant change in acoustic pressure, but the simulated results show otherwise. This brings the need to establish a 3-dimensional model for the dental tip system to get a better illustration on the acoustic pressure field distributions.

6.2.4 3-Dimensional Dental Tip Model

As mentioned in the experimental section, the modeling of this 3-dimensional dental tip was performed in three different stages, first by using a rectangular slab model, which was then improved into a cylindrical model and finally a cone model – to mimic more closely the actual endosonic files.

In this study, we are interested in the acoustic pressure around the dental tip model. The main aim of the study was for comparison purposes, so the exterior wall boundary is not crucial in this study and was assumed to be hard wall boundaries, so were the dental tip models. The air | water interface was, like all previous studies, assumed to be a soft wall boundary, where all incident pressures to the surface are totally reflected.

Based on previous experimental results on the scanning laser vibrometry (SLV, Chapter 3, Section 3.5) of the dental tips, we assume that the production of acoustic pressure along the dental tips resulted in the vibration movements of the tips, and that was found to be dominated by the anterior-posterior movements of the dental tips as opposed to all directional oscillatory motion. We therefore developed a two-plane ultrasound emitter in the model (Figure 6.14), assuming that those were the planes that dominate the production of acoustic pressure in the system.

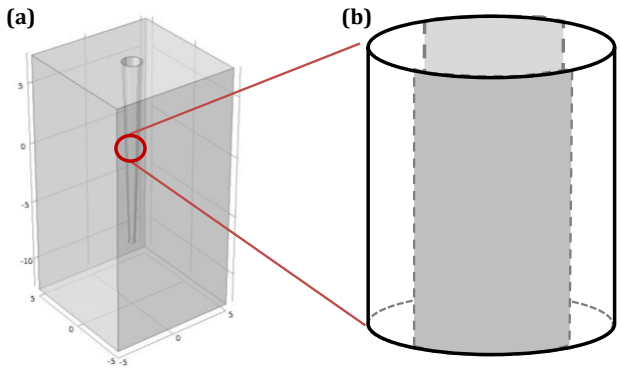

Figure 6.14: *(a) A 3-D cone model built in a vessel; (b) Magnified image of the cone model, with grey areas indicating the planes modelled as ultrasound emitter in the simulation process.*

6.2.4.1 Rectangular Slab Model

The 3-dimensional rectangular slab model has a dimension of 2.5 mm × 1 mm × 15 mm. This study was initiated by varying the width of the rectangular slab from 2.5 mm to 2.0 mm, 1.5 mm and 1.0 mm (Figure 6.15).

The initial acoustic pressure amplitude was set to be equivalent to the intensity of CT-4 at Power 10/10, which was calculated to be 0.39 MPa based on Equation 8. The generation of mesh represents the number of elements used for calculations, which, in this case, was chosen to be a physics controlled mesh from COMSOL, using a 'finer' mesh size with a total elements of 23981, totaling up the total degrees of freedom to solve to 34382 for a model with 2.5 mm width, 1mm depth and 15 mm height in a 1 cm × 1 cm × 2 cm vessel. An example of the number of meshes generated is shown in Figure 6.16.

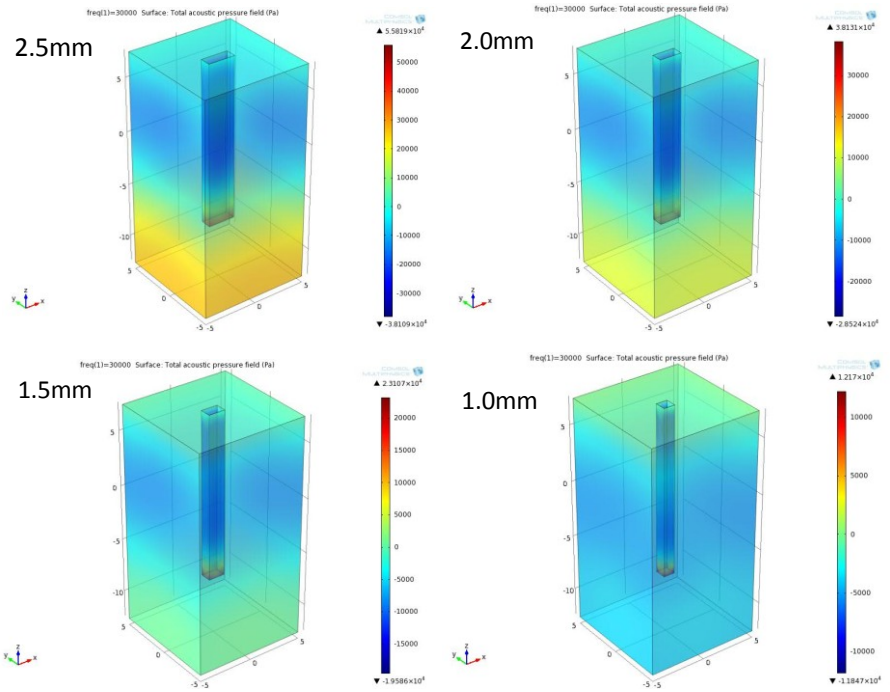

Figure 6.15: *Rectangular slab model of different widths in a vessel of 10 mm × 10 mm × 20 mm.*

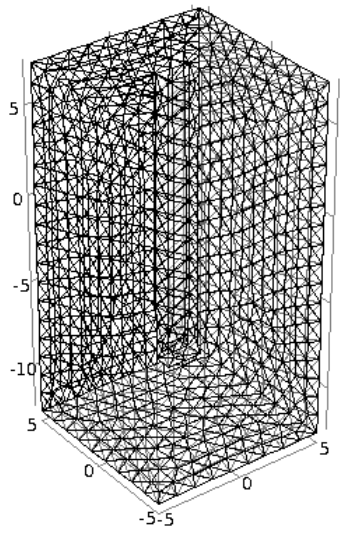

Figure 6.16: *An example of the tetrahedron meshes generated for a rectangular slab model in a vessel.*

The acoustic frequency for this model was set to 30 kHz, and the wave was emitted through two sides of the rectangular slab (front and back). The results obtained were analysed and plotted based on the total acoustic pressure produced along the length of the model dental file and also with a 3-dimensional illustration of the isosurface of the acoustic pressure fields in the entire vessel when varying the width of the model.

Figure 6.17 shows the pressure isosurface plots of varying widths for the rectangular slabs. It can be noted that there is a large area of negative pressure (shown in blue) in the middle of the slab for all cases, together with a very high positive acoustic pressure area at the bottom of the slabs. When the width of the model slab decreases, the area of negative acoustic pressure generated decreases significantly, and gets spread out throughout the model. When the width decreases to 1.0 mm, the trend shows two separate areas of negative acoustic pressure generated.

For a better illustration, a one-dimensional plot of the total acoustic pressure along the distance of the file is plotted in Figure 6.18. As shown, there is an expected decrease in magnitude of the acoustic pressure formed when the width is decreased from 2.5 mm to 1.0 mm. The negative acoustic pressure is more spread out for 1.0 mm along the file and becomes more focused on an area as the width increases. As

described earlier in the thesis, cavitation bubbles are formed upon achieving high enough negative acoustic pressure, which, for the case of the simulated results, is indicated by regions of high total acoustic pressure (as a standing wave profile is formed). This might be a factor that contributes to the cavitation activity shown in Chapter 3, Figure 3.25 showing differences in the areas of sono(chemi)luminescence (SCL) from one tip to another.

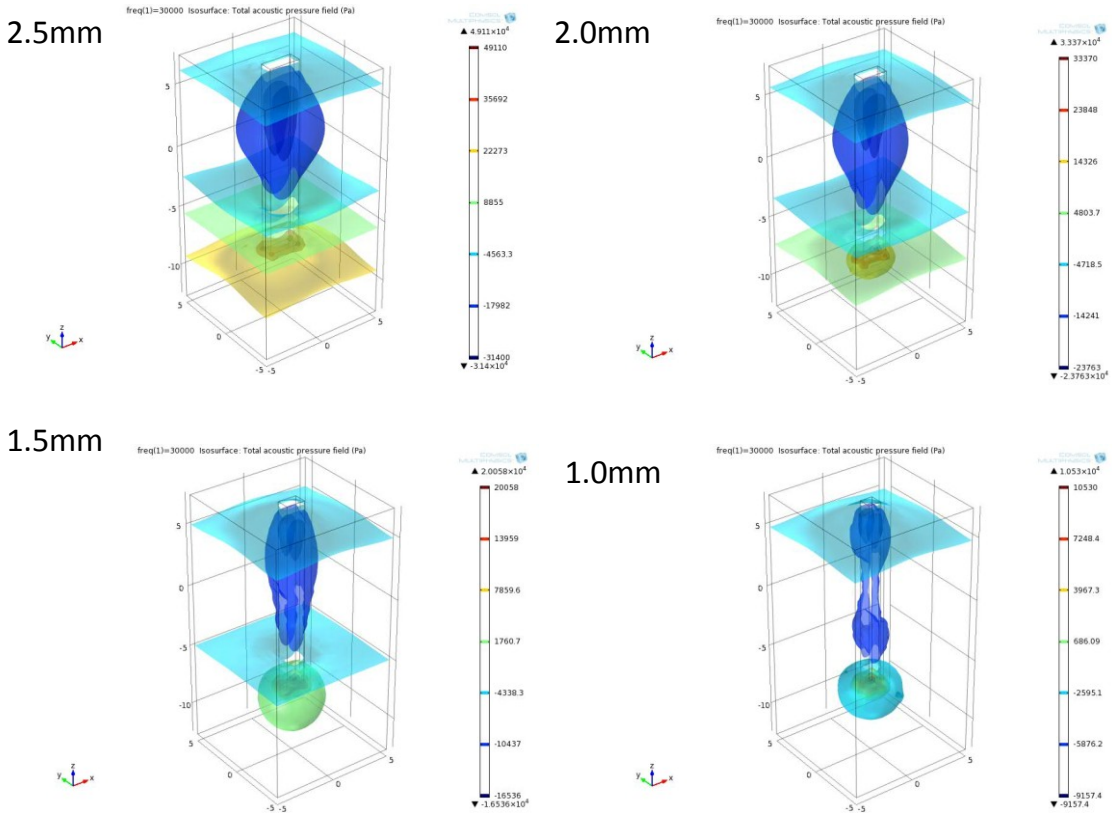

Figure 6.17: *Acoustic pressure isosurface plots for the slab model when decreasing the width of the models from 2.5 mm to 2.0 mm, 1.5 mm and 1.0 mm at a fixed acoustic pressure amplitude.*

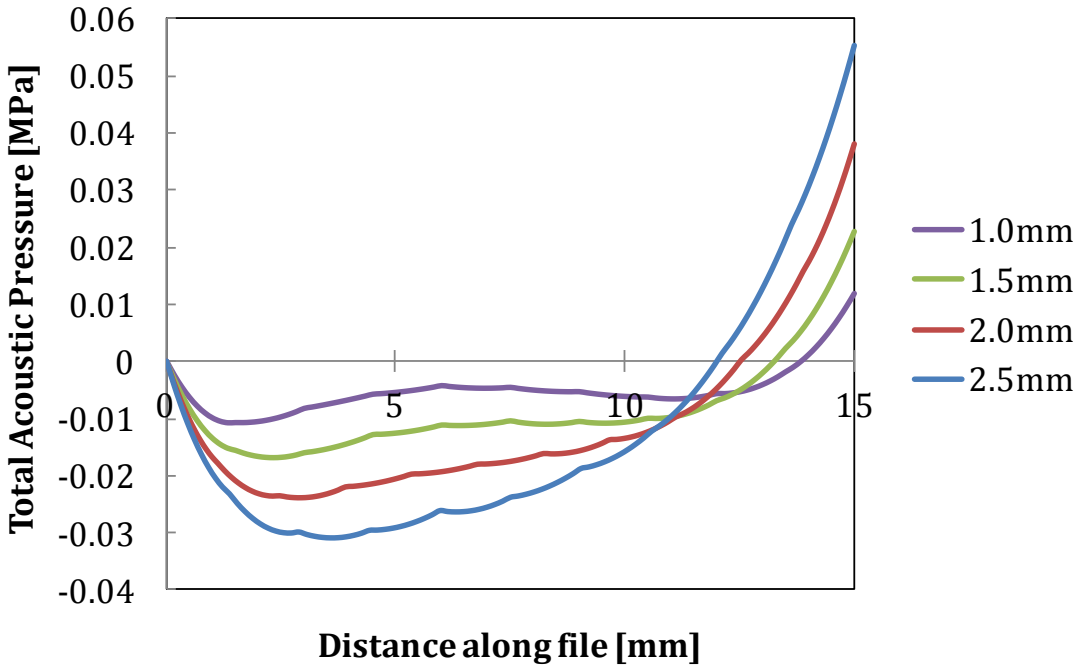

Figure 6.18: *1-dimensional plot of the total acoustic pressure along the length of the model 'file' of various widths.*

Further studies were performed to evaluate the differences in the acoustic pressure distribution upon increasing the length of the ultrasonic source. This was performed on all the rectangular slab model of various widths, by adjusting the length of the slab from 15 mm to 15.5 mm, 16 mm and 16.5 mm respectively.

Based on Figure 6.19, we can see that there is a decrease in negative pressure distributions upon increasing the length of the slab model, with a rectangular slab of 15 mm having a wider range of negative acoustic pressure generated from 0 to 12.5 mm along the model, but when the length was increased to 16.5 mm, the negative pressure generated along the tip reduces both in magnitude and also in the total distribution along the model. This might be a preliminary indication of the effects of the dimensions of the ultrasonic source in producing acoustic pressure in the liquid systems. Further studies were also performed on the rectangular slabs of various widths and the results all showed a similar decrease in the total negative acoustic pressure upon increasing the length of the model (See Appendix V).

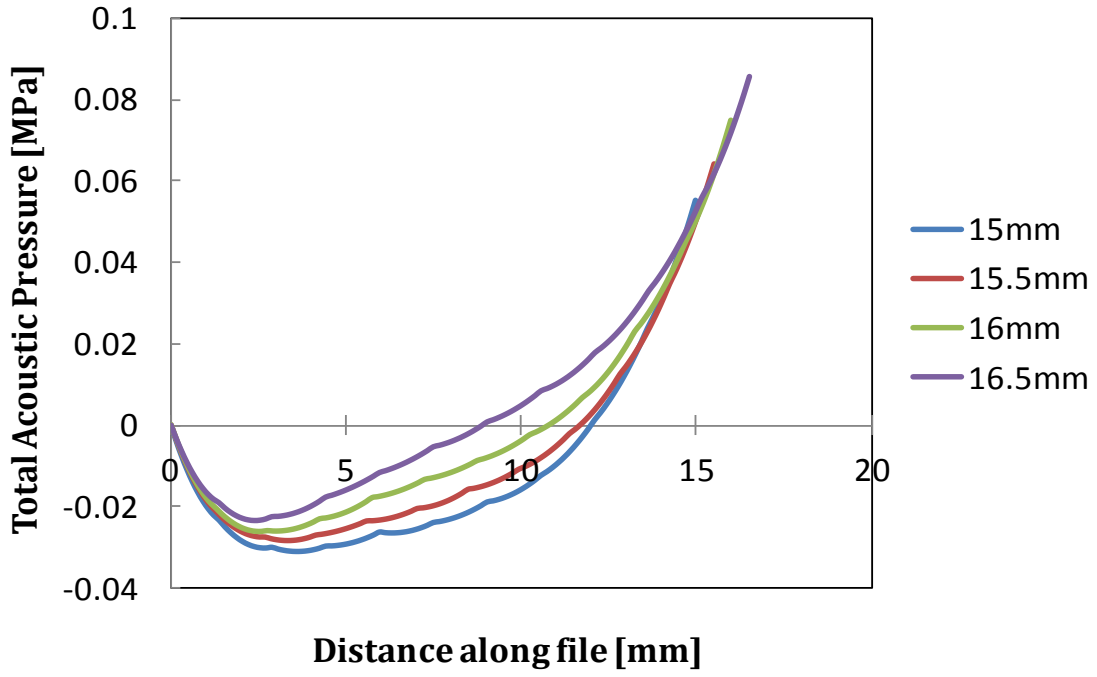

Figure 6.19: *Total acoustic pressure versus different length of the model rectangular slab of 2.5 mm × 1 mm.*

6.2.4.2 Cylinder Model

Upon developing the rectangular slab model, the second step in the 3-dimensional modeling was performed using a cylinder model to get a closer correlation to the actual dental endosonic files used in practice.

Similar to the previous section, the cylinder model was modeled with a fixed length of 15mm, with varying diameter ranging from 2.5 mm, 2 mm, 1.5 mm to 1 mm, in a vessel of 10 mm × 10 mm × 20 mm (Figure 6.20).

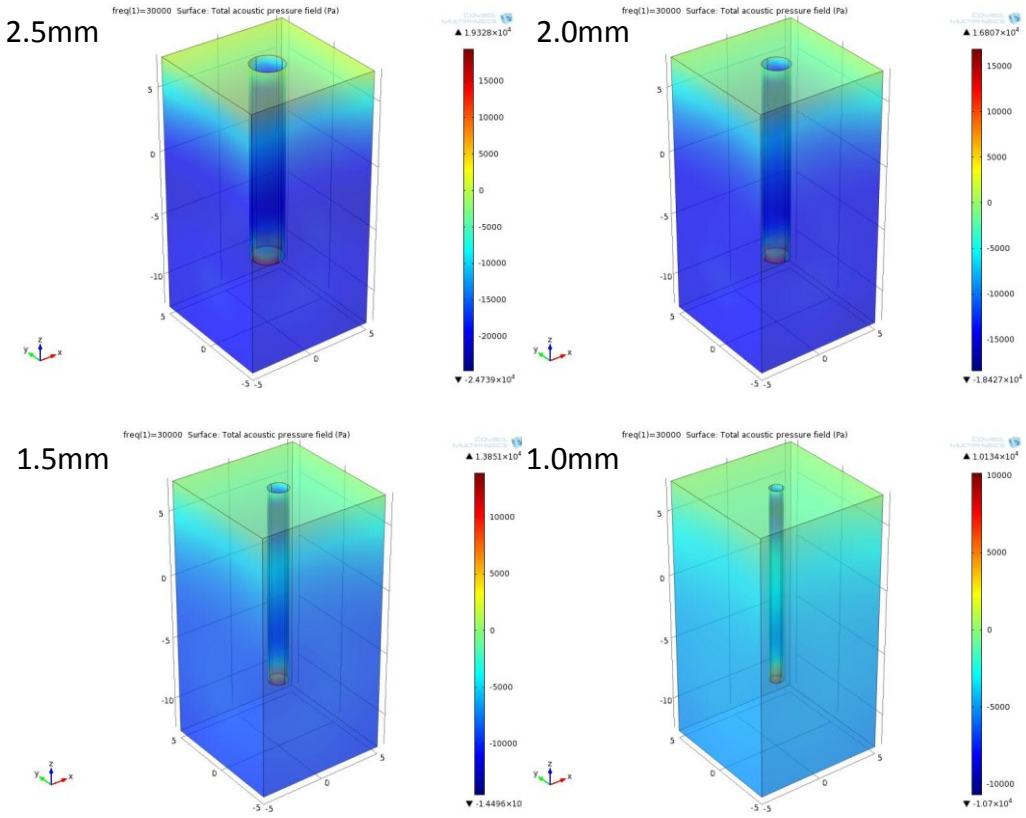

Figure 6.20: *Cylinder model of different diameters in a vessel of 10 mm × 10 mm × 20 mm.*

Mesh generations of the system was divided in a similar way as to those performed on the rectangular slab model (Section 6.2.4.1). Total elements of 28359 were built for the model of 2.5 mm diameter, 15 mm long cylindrical model. This totals up to 41109 degrees of freedom to solve, taking 9 s of simulation time to perform a single run. The ultrasonic source was modeled to be emitted from the anterior and posterior sides (Figure 6.16) of the cylinder, similar to those modeled for the rectangular slab.

Based on Figure 6.21, a small variation in the pressure field distribution can be seen as compared with the acoustic pressure fields obtained from the rectangular slab model. Here, there are still three distinguishable blobs of area showing maximum negative acoustic pressures (in blue) at various areas along the cylinder model. At the free ends of the model, the acoustic pressure generated near the model was shown to be highly positive acoustic pressure fields, but creates high negative acoustic

pressure in the liquid system (as shown in the isosurface plots), resulting in negative acoustic pressure in the surrounding liquid.

As this system was modeled to produce a standing wave profile along the ultrasonic source, the formation of a positive acoustic pressure will also result in acoustic pressure oscillating in the opposite direction at π out-of-phase which will produce negative acoustic pressure of the same magnitude (Leighton, 1994). That might be the reason for the formation of a area of negative pressure area at the end of the tip model.

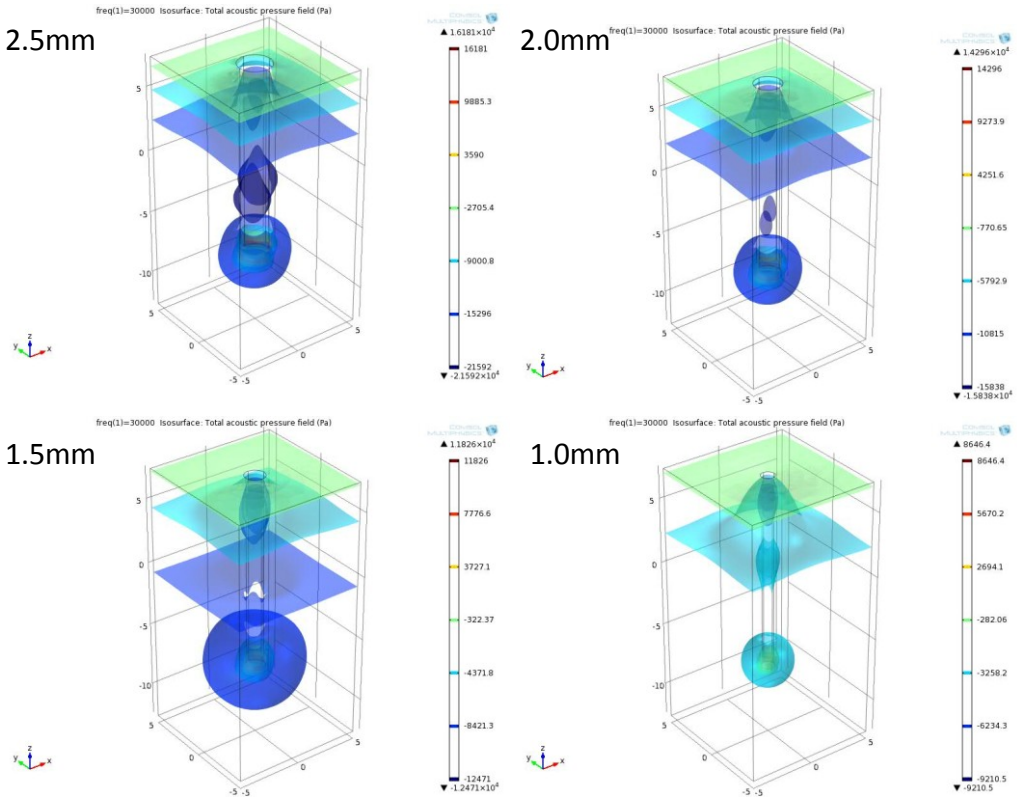

Figure 6.21: *Total acoustic pressure isosurface plots for the cylindrical model of 15mm length and various diameters at an initial acoustic pressure amplitude of 0.31 MPa.*

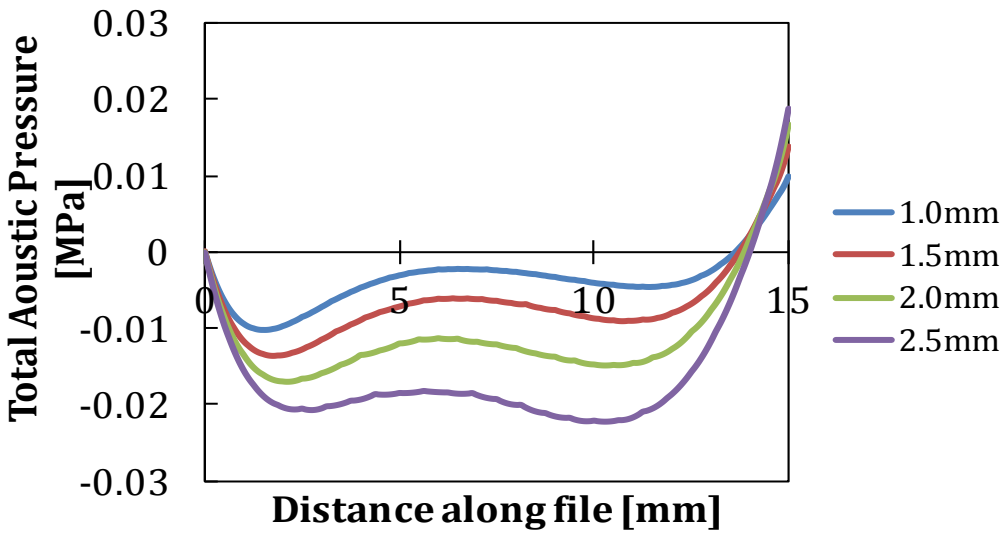

Figure 6.22: *1-dimensional acoustic pressure plot against the distance along the cylinder model of various diameter, at an initial acoustic pressure amplitude of 0.31 MPa.*

Based on Figure 6.22, we obtained a decrease in total acoustic pressure with the decrease in the diameter of the cylinder model. This showed a similar trend to those modeled as rectangular slab, apart from the overall distribution of the acoustic pressure along the entire model. This might be due to the fact that they both have different surface areas, resulting in difference in the acoustic pressure distribution.

For a fixed diameter model, when varying the length of the model, this affects the total acoustic pressure at the bottom end of the model tip. An example of the 1-dimensional pressure plots along the tip of different lengths is shown in Figure 6.23.

Increasing the length of the file in the cylinder model results in a decrease in acoustic pressure at the second half of the model, especially at the regions around 9 – 12 mm of the model. However, a slight increase in the acoustic pressure was observed at the end of the tip upon increasing its length. The plots from the cylindrical model indicate the areas of cavitation activity taking place in a sonicating system, where a wide distribution of cavitation activity is expected when the dental files are thicker and shorter; whereas a narrower distribution of the cavitation activity is expected for

longer and narrower dental files. Further simulated results of the same cylinder model with various dimensions are in Appendix V.

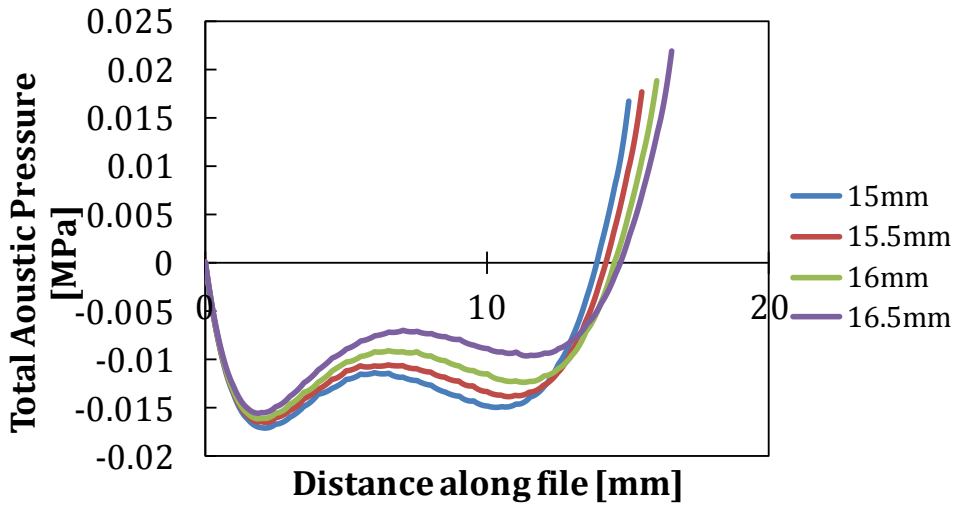

Figure 6.23: *Total acoustic pressure along the length of the cylinder model of 2.0mm diameter and various lengths, with an initial acoustic pressure amplitude of 0.31 MPa.*

6.2.4.3 Cone Model

Upon establishing and examining the differences in the 3-dimensional rectangular slab and cylindrical model, a cone-shaped model was built to have a better comparison with the real dental files used in practice. Similar to the previous sections, the model was examined by simulating several models of various dimensions for comparison. The cone model was simulated by changing a few parameters:

i) Different top diameter : 2.5 mm, 2.0 mm, 1.5 mm and 1.0 mm of 15 mm length.

ii) Different inclination angle: 3.0^{o}, 2.5^{o}, 2.0^{o} and 1.5^{o} at a constant 2.5mm top diameter and 15mm length.

iii) Different inclination angle: 1.8^{o}, 1.6^{o}, 1.4^{o}, 1.2^{o} and 1.0^{o} at a constant 1.0mm top diameter and 15mm length.

In the first attempt with the cone model, various top diameters of the cone were chosen: 2.5 mm, 2.0 mm, 1.5 mm and 1.0 mm respectively. Similar treatments were performed to the cone model as to all previous studies in this section. The number of meshes generated for a cone model of 2.5 mm was 40747, resulting in a total of 58313 degrees of freedom to solve.

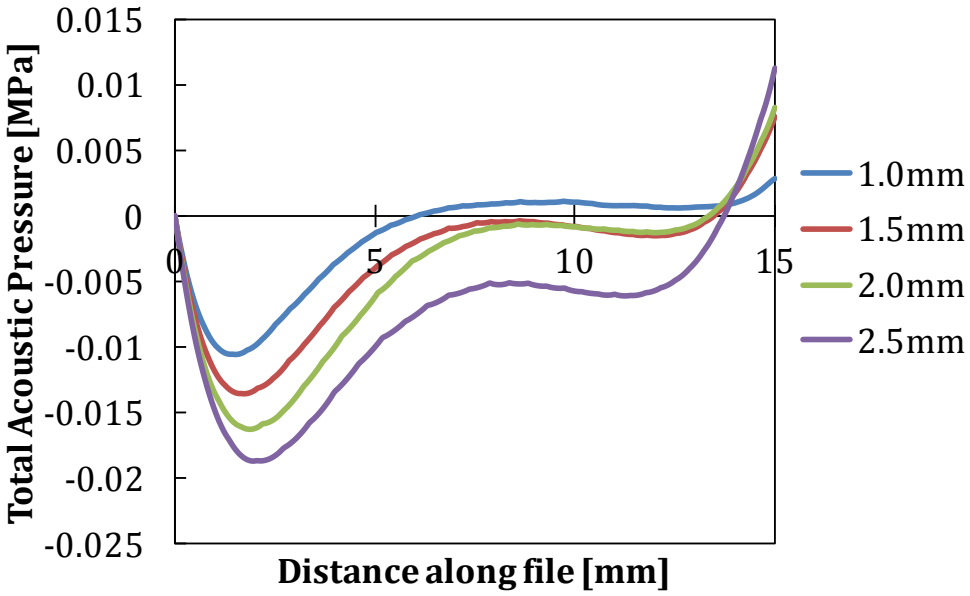

Figure 6.24: *Total acoustic pressure along the surface of the cone model of various top diameter, at an initial acoustic pressure amplitude of 0.31 MPa.*

Based on Figure 6.24, there is a reduction in the magnitude of the total acoustic pressure with the reduction of the diameter of the cone model. More interestingly, when the diameter of the cone model was reduced to 1.0 mm, there was a significant decrease in the total acoustic pressure, especially at the free end of the tip model. This showed similarities with the SCL experiments in Section 3.3 earlier, where endosonic files with thicker diameter (such as the CT-4) produced more SCL as compared to the thinner files (such as the UT-4).

Comparing the cylindrical and the cone models (Figures 6.22 and 6.24), it can be seen that, for the same top diameter and the same length, reducing the diameter in the tip of the cone model has resulted in great reduction in acoustic pressure produced. This indicates that the surface area of the emitter plays an important role

in displacing the surrounding liquid, which will then contribute to the production of cavitation bubbles.

The model was next built with a constant diameter of 2.5 mm and length of 15 mm, but with a different inclination angle, from 3°, 2.5°, 2° to 1.5°. Figure 6.25 illustrates the total acoustic pressure with various inclination angles. It can be seen that the cone model with a higher inclination angle will result in a lower magnitude of acoustic pressure produced at the lower half of the model tip, when there is no significant difference showed between 0 to approximately 4 mm along the model tip. This indication suggests that the production of acoustic pressure depends strongly on the surface area and is very dependent on the shape of the model, where places with thicker cone diameter create more acoustic pressure than the rest of the model tip. This strongly brings the need to have a better prototype model as the real endosonic file dimensions – and will be discussed further in Section 6.2.4.5.

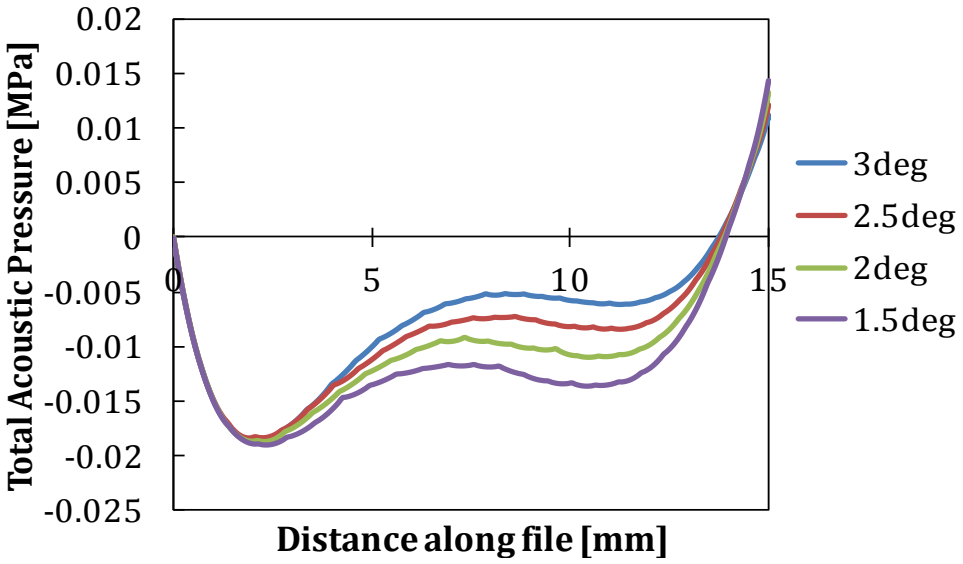

Figure 6.25: *Total acoustic pressure along the surface of the cone model of various inclination angle, fixed at 2.5 mm top diameter and 15mm length, at an initial acoustic pressure amplitude of 0.31 MPa.*

A similar experiment study was repeated with a top diameter of 1.0 mm, 15 mm length but with a variation of inclination angle from 1.8°, 1.6°, 1.4°, 1.2° and 1.0°. When the cone model had been reduced to 1.0 mm top diameter, the total acoustic

pressure reduced significantly at the bottom end of the model (Figure 6.26). When the inclination angle increases, the acoustic pressure at the bottom end of the model tip gradually increases to produce positive acoustic pressure. At an angle of 1.4° to 1.6°, there is almost no acoustic pressure formed between 7.5 and 12.5 mm along the tip.

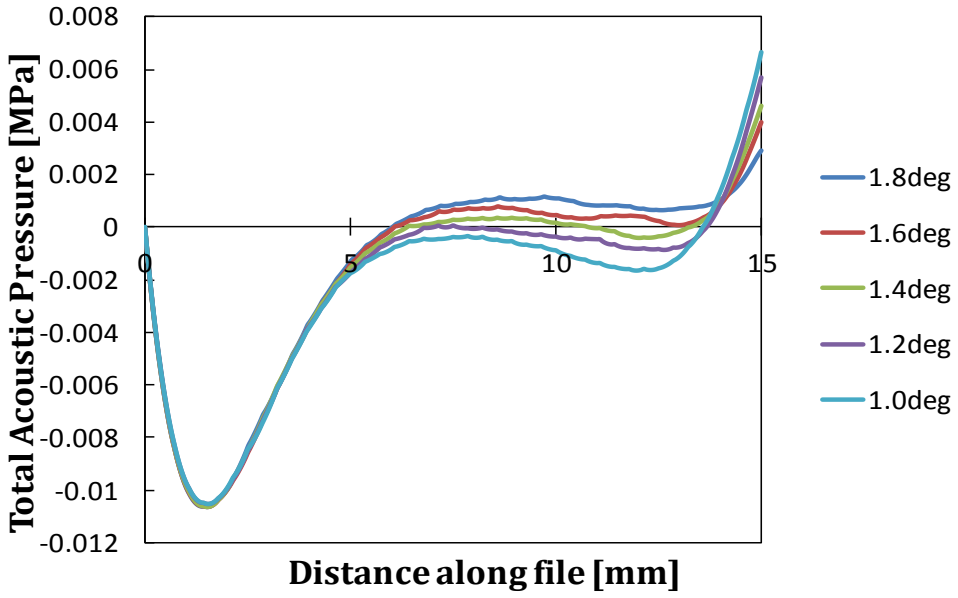

Figure 6.26: *Total acoustic pressure along the surface of the cone model of various inclination angle, fixed at 1.0 mm top diameter and 15 mm length, at an initial acoustic pressure amplitude of 0.31 MPa.*

From all previous experimental results on the endosonic files, such as the SCL (Section 3.3) and the vibrometry movements (Section 3.5) of the tips, we can deduce that, from the results patterns obtained, a standing wave profile is established when the tip vibrates, producing SCL at particular localised areas along the tips. Therefore, for the acoustic pressure profiles obtained, only the magnitudes of the acoustic pressure produced matters in this study, as there will be an opposite acoustic wave produced in π out-of phase with the original wave profile[16].

[16] Refer to Appendix I for illustration of a standing wave.

In the following section, the actual dimensions of three endosonic files used in this thesis will be discussed and correlated with all previous characterisation results obtained for the tips.

6.2.4.4 Acoustic Pressure Fields Prediction for the Endosonic Files Used

To bring the acoustic pressure field predictions further, the actual dimensions of three endosonic files (CT-4, CKT-1 and UT-4) were used to give better comparisons of the acoustic pressure fields predictions of the files used.

The dimensions of the tips were obtained using the methods mentioned in Section 2.1.2. The acoustic pressure amplitudes used were based on the calorimetry results obtained in Section 3.1 at the intensity equivalent to Power 10/10 on the power dial for all the tips. Table 6.5 below shows the dimensions and acoustic pressures of the dental tips used.

Table 6.5: *Dimensions and the acoustic pressure amplitudes of the three endosonic files used for pressure fields predictions.*

Dental Tips	Dimensions (mm)	Acoustic Pressure Amplitude at Power 10/10 (MPa)
CT-4	Length: 15.0 mm Top diameter: 1.5 mm Inclination angle: 2.0^{o}	0.313
CKT-1	Length: 15.0 mm Top diameter: 1.5 mm Inclination angle: 1.9^{o}	0.309
UT-4	Length: 15.0 mm Top diameter: 1.0 mm Inclination angle: 1.72^{o}	0.587

All three models were built for tips immersed in a vessel of 50 mm × 50 mm × 50 mm. Figure 6.27 shows the models built for CT-4, CKT-1 and UT-4 respectively.

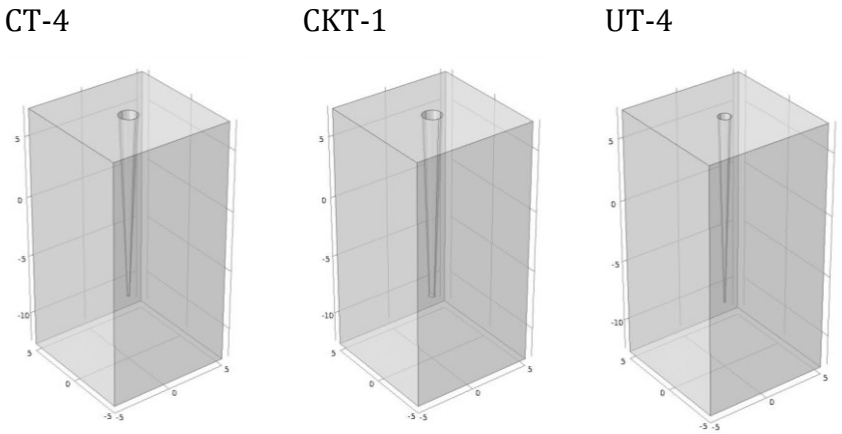

Figure 6.27: *Models of CT-4, CKT-1 and UT-4 built according to their respective dimensions in a vessel of 50 mm × 50 mm × 50 mm.*[17]

Figures 6.28, 6.29 and 6.30 illustrate the total acoustic pressure produced along the model tips for CT-4, CKT-1 and UT-4 respectively. It can be seen that the CT-4 produces the highest acoustic pressure in terms of magnitude, both in the negative and positive acoustic phases. This agrees with our experimental results (Chapters 3 and 4) where CT-4 were, among all the tips, had the best overall performance so far (in SCL, PIV and cleaning efficiencies experiments). On the contrary, UT-4 showed the smallest acoustic pressure, especially at the end of tip among the three tips examined (Figure 6.30), which, again, correlates well with the experimental results shown in Chapter 3 illustrating the lack of SCL produced at the end of UT-4 (Figure 3.14(c) and Figure 3.25(c)). The differences in SCL produced in CT-4 and CKT-1 cannot be distinguished from this model due to their similarities in dimensions within the working length. Further simulations have to be carried out to take into account the differences between them – which lie within the angle of contact between the tip and the hand piece.

[17] The dimensions of the vessel used in this figure are 10 mm × 10 mm × 20 mm for better illustration.

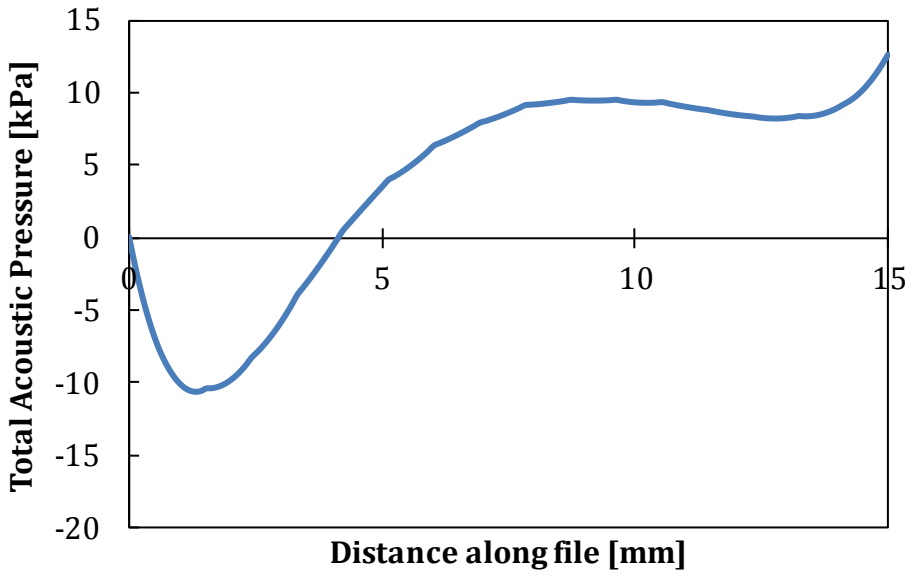

Figure 6.28: *Total acoustic pressure along the working length of* ***CT-4*** *at Power 10/10 (equivalent to acoustic pressure amplitude of 0.31 MPa).*

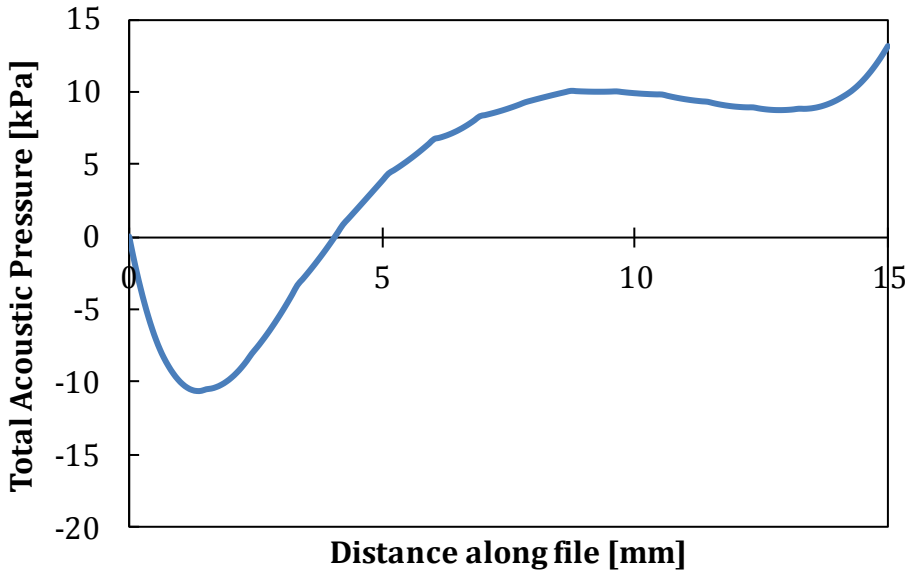

Figure 6.29: *Total acoustic pressure along the working length of* ***CKT-1*** *at Power 10/10 (equivalent to acoustic pressure amplitude of 0.31 MPa).*

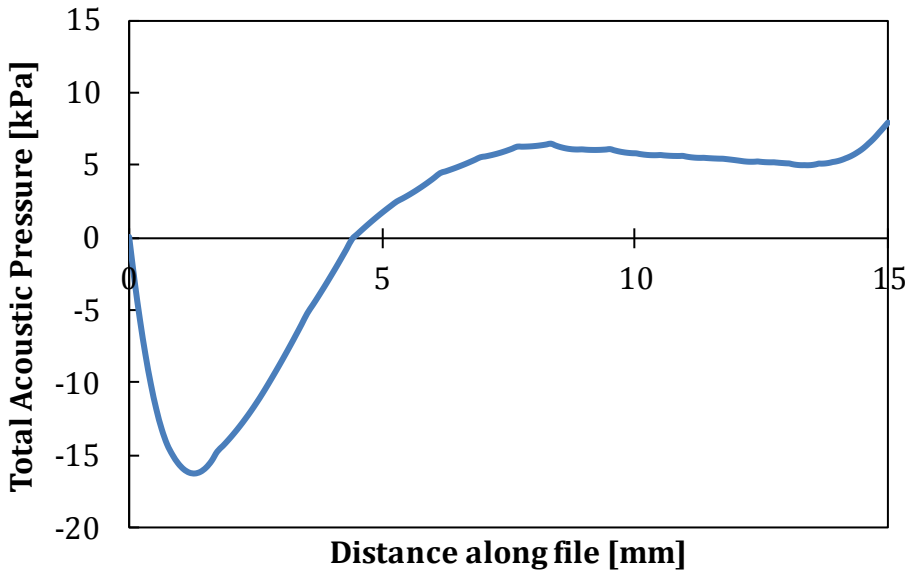

Figure 6.30: *Total acoustic pressure along the working length of* ***UT-4*** *at Power 10/10 (equivalent to acoustic pressure amplitude of 0.59 MPa).*

From the results obtained above, we can see that the acoustic pressure plays an important role in the formation of transient cavitation bubbles. It is important to note that the model built is solely based on the acoustic pressure formed in an infinite volume in comparison to the dimensions of the dental tips, in order to reduce other side factors such as acoustic streaming effects and also the bubble dynamics when transient cavitation is present in the system.

As noted previously, it is deduced that a standing wave profile is obtained based on the vibrometry motion (Section 3.5) of the dental tips. This means that the same is expected for the acoustic pressure predictions, where the nodal points of the acoustic pressure remain at the same position at all times, but the antinodes will change in phase with time. This explains the formation of positive acoustic pressure generated from the simulation even though in theory, only negative pressure fields generated will give rise to the formation of cavitation in the liquid system.

Table 6.6: *Images of sono(chemi)luminescence superimposed onto SLV results for CT-4, CKT-1 and UT-4 (Reproduced from Figure 3.25) together with the simulated pressure fields at the same settings superimposed onto the same SLV results, with the blue areas indiating pressure fields of <-5 kPa and >5 kPa.*

Tip	CT-4	CKT-1	UT-4
SLV *vs* SCL	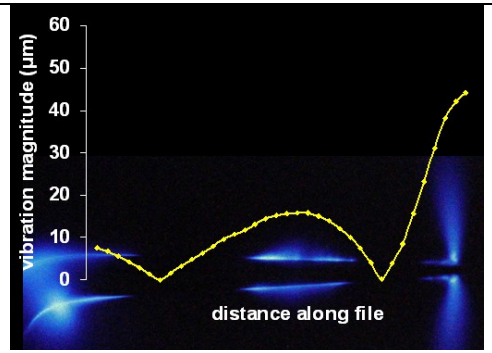	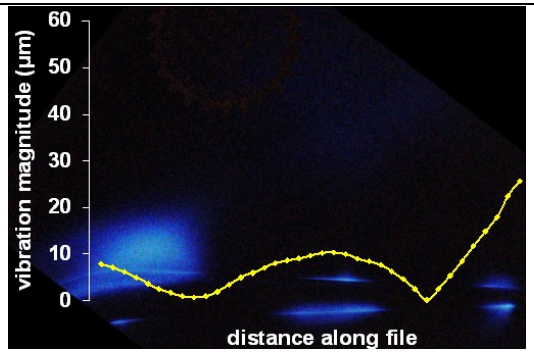	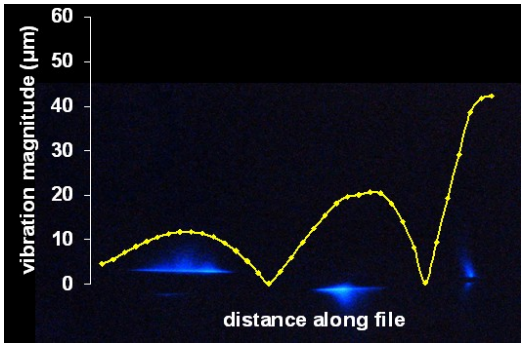
SLV *vs* Acoustic Pressure	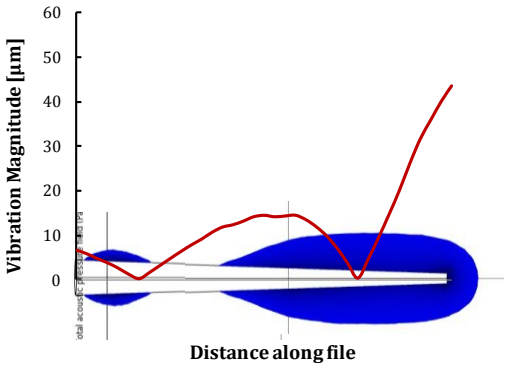	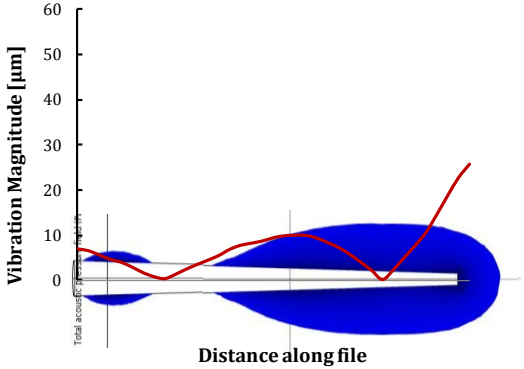	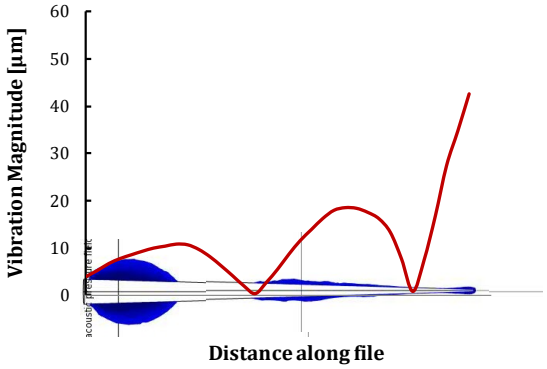

Table 6.6 illustrates the correlations between SCL, SLV and the predicted acoustic pressure fields for CT-4, CKT-1 and UT-4 at Power 10/10. It can be seen that, there is a distinct difference between UT-4 and the other two tips, where the maximum pressure produced is much lower than the other two tips, and producing much lower acoustic pressure in the surrounding liquid, though care must be taken that the magnitude of the total acoustic pressure obtained was just for comparison purposes and does not indicate the actual cavitation threshold of the system. On the contrary, CT-4 and CKT-1 were able to produce sufficient acoustic pressure in the surroundings, resulting in higher tendencies of transient cavitation production. There was only a slight difference in CT-4 and CKT-1 as shown in the model, where they both have almost similar dimensions, hence producing almost the same magnitude of acoustic pressure fields from the simulated results. However, when the vibration movements of the two tips were compared, CT-4 gave almost double in vibration displacement compared to CKT-1. This indicates that both production of acoustic pressure, coupled with sufficient amount of vibration displacement play a role in the production of transient cavitation – resulting in the formation of radicals.

This model built for pressure predictions gave a general idea of the reason why SCL is not produced much at the free end of the dental tips, especially for UT-4, even though the SLV measurements (Section 3.5) showed otherwise, where the free-end of the tip gave out the most vibration movements in comparison with other parts of the tips (see Figure 3.24).

However, it has to be noted that there are some dissimilarities in the tips above the working length, where it is not included in the model. For example, the CT-4 and CKT-1 have very similar designs and working lengths, but their contact angle is different. UT-4 on the other hand, has a longer 'bend' than the other two tips (Figure 3.30). In order to take these differences into account, the dental tips were modeled with the entire tip immersed into the liquid system, as shown Figure 6.31.

CT-4

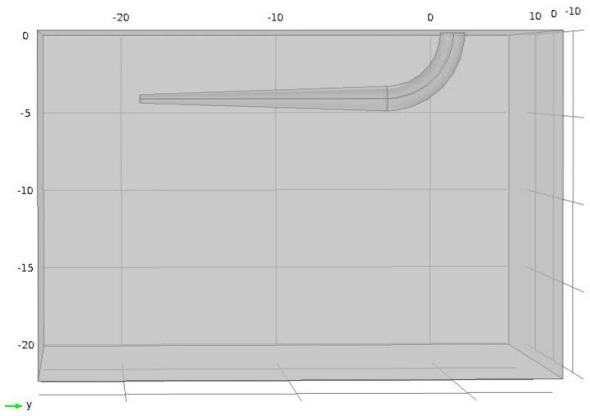

CKT-1

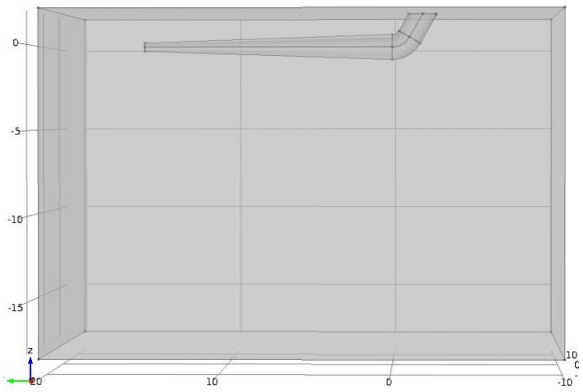

UT-4

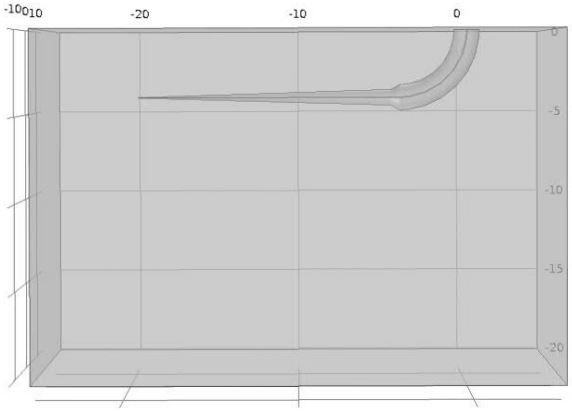

Figure 6.31: *3-dimensional model of the three dental tips used, fully immersed into a large volume of water of 3 cm × 3 cm × 2 cm.*

The boundary layers were set similar to the previous study (*i.e.* all hard boundaries except for the air | water interface, which is modeled as a soft boundary) and the total acoustic pressure fields were plotted against the total length of each dental tip – as appeared in the model. The initial acoustic pressure amplitude was adjusted according to the total intensity emitted into the system when the entire dental tip is immersed into water.

Figures 6.32, 6.33 and 6.34 show the total acoustic pressures of along the entire tip and their respective inset pictures showing the pressure distributions around the tips. There are two similarities that can be spotted in these models: the area close to the air | water interface always appears to be highest in producing negative acoustic pressure, and this phenomena can also be seen in the previous study using just rectangular slab, cylinder or cone shape models.

The air | water interface acts as a perfect sound reflector due to the difference in acoustic impedances, giving a reflective index of -0.999 (Blackstock, 2000). Due to this, the sound wave that travels towards the surface of the water gets fully reflected back, and this gives rise to the high acoustic pressure fields near the boundary of the water.

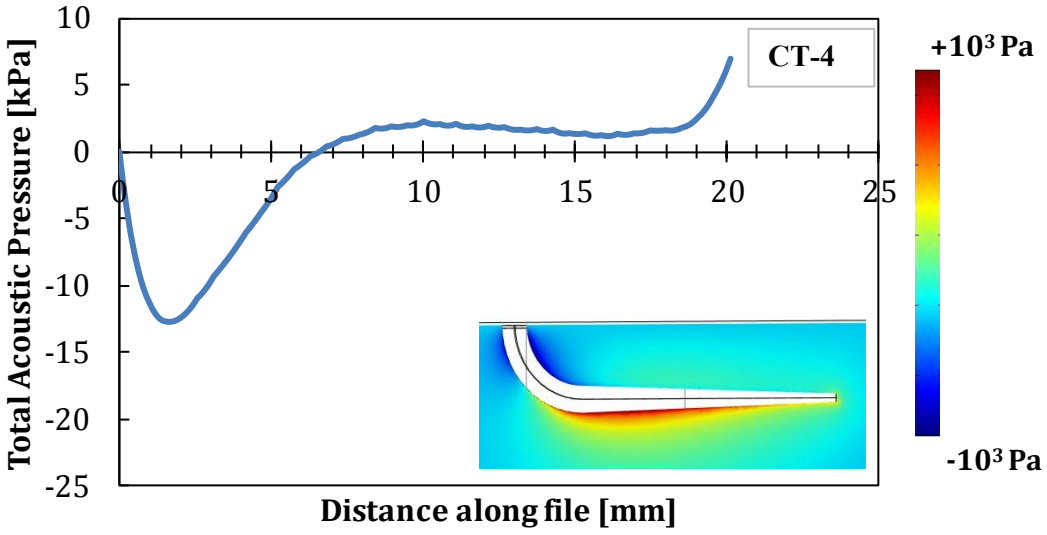

Figure 6.32: *Total acoustic pressure along the length of CT-4, with the inset picture showing the pressure distribution surrounding the tip at Power 10/10.*

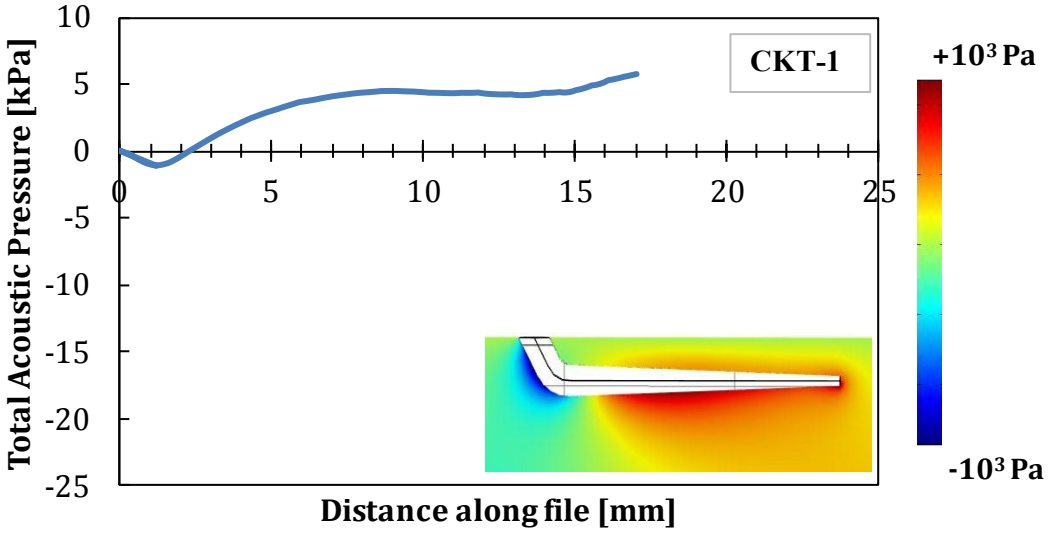

Figure 6.33: *Total acoustic pressure along the length of CKT-1, with the inset picture showing the pressure distribution surrounding the tip at Power 10/10.*

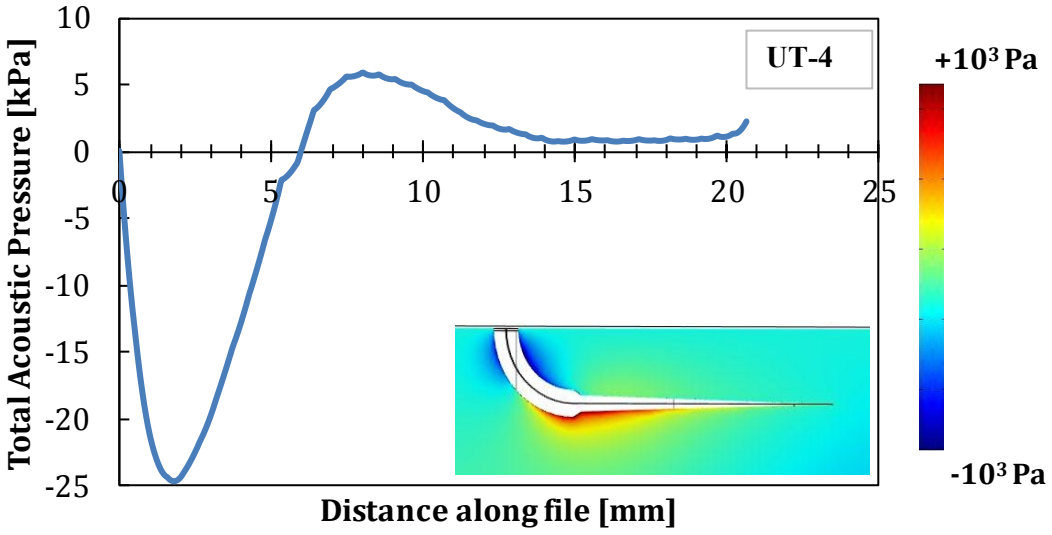

Figure 6.34: *Total acoustic pressure along the length of UT-4, with the inset picture showing the pressure distribution surrounding the tip at Power 10/10.*

The second similarity of the acoustic pressure profile for the three tips is that the acoustic pressure always comes to a maximum point at the free end of the tip, even though it might not show a maximum in acoustic pressure magnitude. This result correlates well with all previous experimental studies performed, showing that the free end of the tip gives the largest vibration amplitude, and also produces SCL.

By comparing the acoustic pressure profile of the CT-4 and CKT-1, it can be found that the angle of the tip plays a major role in producing acoustic pressure in a liquid. Though it can be seen that the total acoustic pressure along the working length (the final 15 mm of the plot) of CKT-1 remained constant above CT-4, the initial negative pressure produced at the bend of the tip was way lower than both CT-4 and UT-4, where the tips were connected at a 90^{o} angle to the hand piece. Though it is still immature to state a conclusion based on these pressure prediction findings, we can clearly see that there is a significant difference between the two simulated results, and that the contact angle between the working length of the tip and the hand piece does play a role in the total acoustic pressure emitted.

Based on Figure 6.34, when there is a step change in the diameter of the tip at approximately 5-6 mm along the entire length of UT-4, a very significant pressure peak is obtained. This slowly vanishes along the length of the file, and at the free end of the tip, only a little increment in acoustic pressure can be seen.

Overall, this model study gives a good overview of the pressure field predictions at various areas of the endosonic files, and it strongly depends on the way the tips were positioned into the liquid, shape and size of the tips. Though the areas where cavitation takes place depend strongly on the vibration profile of the tips, from this simulated model, it was unable to predict the exact location where sonoluminescence will take place.

As discussed previously in the beginning of the Chapter, there are limitations to this computational model built, and that the results obtained can only be used for comparison purposes. However, from this study, we can conclude that dental tips producing greater magnitude of acoustic pressure have higher tendency to produce

more transient cavitation, as obtained from the SCL results in Chapter 3. Further enhancements on the modelling can be performed by including the fluid dynamics module into the model, and possibly including bubble dynamics to account for the presence of cavitation bubbles in the system in order to get a closer total pressure approximation.

6.2.4.5 Effects of Various Boundary Conditions/ Volume/ Shape of Vessel

In this section, CT-4 was chosen to be the sample dental tip to be modeled under different conditions. The first part of the study was to simulate the pressure fields under various boundary conditions. Previous studies were simulated based on a hard wall property at the sides of the vessels. Here, a comparison on various boundary conditions, such as Pyrex glass, silicone rubber and human tissue were input as the boundary conditions of the vessel walls based on their acoustic impedances (Haynes, 2011).

Figure 6.35 illustrates the effects of boundary conditions on the total acoustic pressure produced by CT-4 under the same initial conditions. It can be seen that they all give similar wave profiles, showing peaks at the top, middle and the free end of the simulated dental tip. When a hard wall boundary is used, most of the acoustic pressure emitted gets reflected, but some gets transmitted outside the boundary, resulting in a relatively low acoustic pressure in comparison with the other boundary conditions used. Human tissue (Z = 1.53 MRayl) and silicone rubber (Z = 1.04 MRayl) had the closest acoustic impedance to water (Z = 1.5 MRayl) and will act as a good sound absorber ($R \approx 0$) (See Appendix I for derivation). A similar explanation applies for the Pyrex glass boundary, where it has an acoustic impedance of 13.1 MRayl, whilst it acts as a fairly good sound reflector (R = 0.63), there was also a huge amount of sound being transmitted into the boundary (T = 0.37) (See Appendix I for derivation).

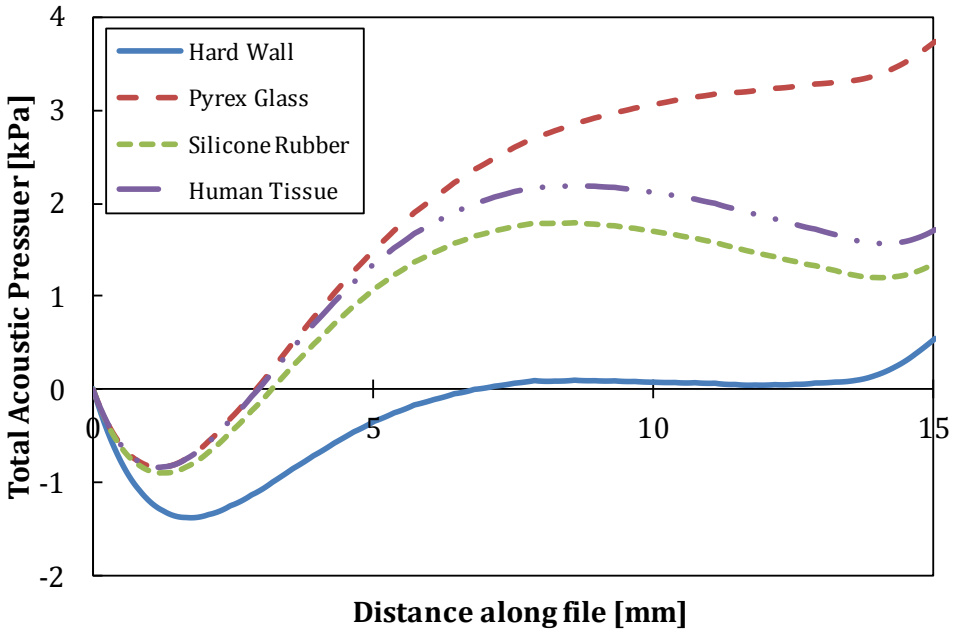

Figure 6.35: *Total acoustic pressure along the working length of CT-4 at Power 10/10 under various boundary conditions.*

As mentioned earlier in the section, all studies were performed in a 10 mm × 10 mm × 20 mm as an infinite volume vessel so as to reduce any possible side factors affecting the simulated results. In the next stage of the study, the effects of the volume of the vessel were assessed, using the boundary conditions of a silicone rubber for a closer comparison with the actual experimental work performed in a confined channel.

Figure 6.36 shows the effect of the vessel's width and depth on the total acoustic pressure produced. A significant, non-linear increment in acoustic pressure can be seen when both the width and depth of the vessel decrease, which is an expected phenomenon, as the chances of sound attenuation decrease and result in much higher, concentrated acoustic pressure produced in a more confined space. This suggests a much higher chance of transient cavitation production in a confined space, though one must note that there are still other factors affecting the production of transient cavitation which were not taken into account in this simulation.

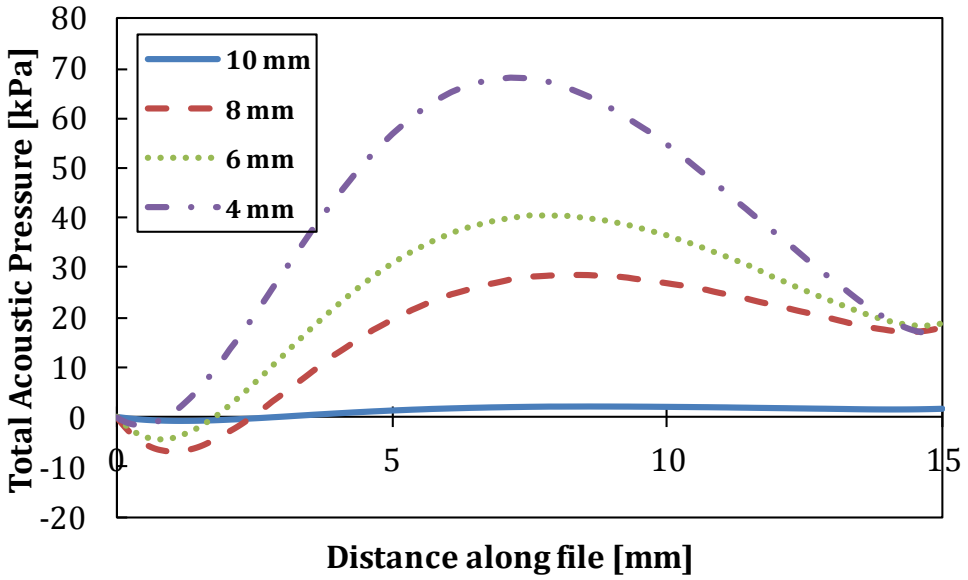

Figure 6.36: *Total acoustic pressure along the working length of CT-4 at Power 10/10 in a vessel of various widths and depths, with the outer boundary modelled according to the acoustic impedance of silicone rubber.*

In the last section of this study, several notches were simulated at various points along the sides of the vessels (drawn as pyramids of 2 mm tall, with a square base of 2 mm × 2 mm) (Figure 6.37). Various boundary conditions and vessel dimensions were used, with different numbers of notches around the vessel to examine the effects of non uniform surfaces to the acoustic pressure profile.

Based on Figures 6.38, 6.39 and 6.40, it can be seen that there is only a little effect from the notches on the total acoustic pressure profile, regardless of the dimension of the vessels and boundary conditions used. For the case of setting the vessel boundary as human tissue equivalent, the acoustic pressure profile did not have any significant difference (p-value > 0.05) and the surface plot of the acoustic pressure in the vessel showed very close similarities. Due to the absorbing nature of human tissue, there is little to no reflection of sound at the walls ($R \approx 0$), hence it does not affect the acoustic wave profiles in the entire vessel, as shown in Figure 6.41.

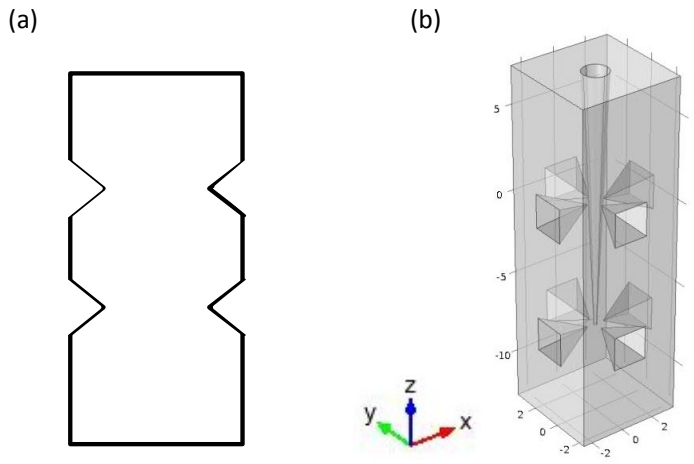

Figure 6.37: *(a) front and side view of the vessel with notches; (b) 3-dimensional model vessel with notches around.*

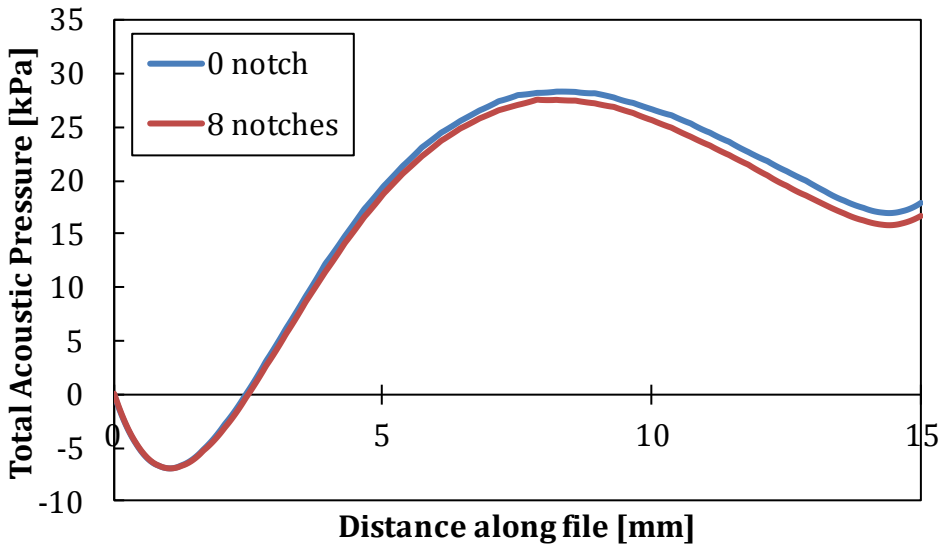

Figure 6.38: *Total acoustic pressure along the working length of CT-4 at Power 10/10 in a vessel of 8 mm × 8 mm × 20 mm, setting the vessel boundary as human tissue equivalent.*

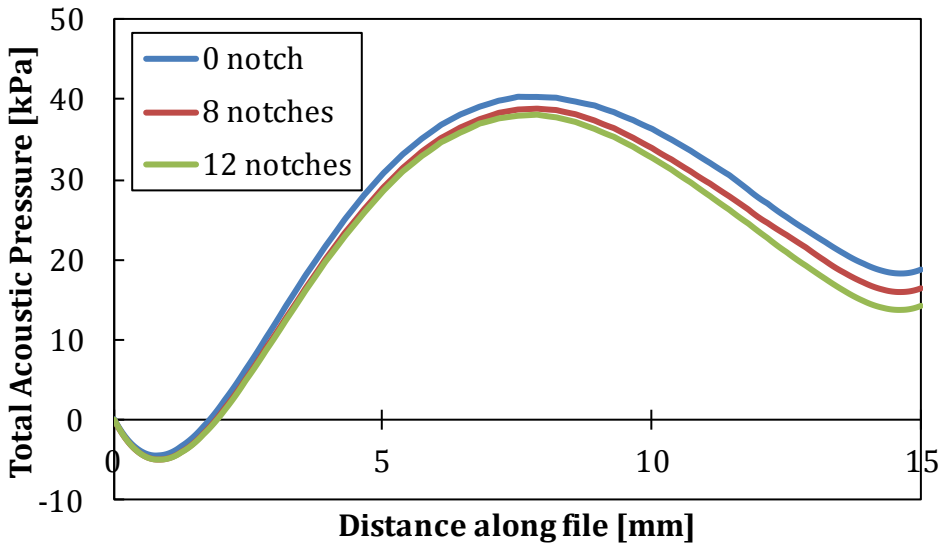

Figure 6.39: *Total acoustic pressure along the working length of CT-4 at Power 10/10 in a vessel of 6 mm × 6 mm × 20 mm, setting the vessel boundary as human tissue equivalent.*

On the other hand, when the vessel walls were simulated as hard walls, there is a slight change in total acoustic pressure profile (Figure 6.40). This illustration is more prominent when the isosurface pressure profile is being compared (Figure 6.42). The increase in number of notches from 0, 8 to 12 resulted in a wider spread of acoustic pressure at the middle of the dental tip. This could be explained by the nature of hard wall boundaries, reflecting sound wave produced towards it. By increasing the number of notches at the walls of the vessel increases the total surface area, hence increases the possibility of sound reflection in various directions.

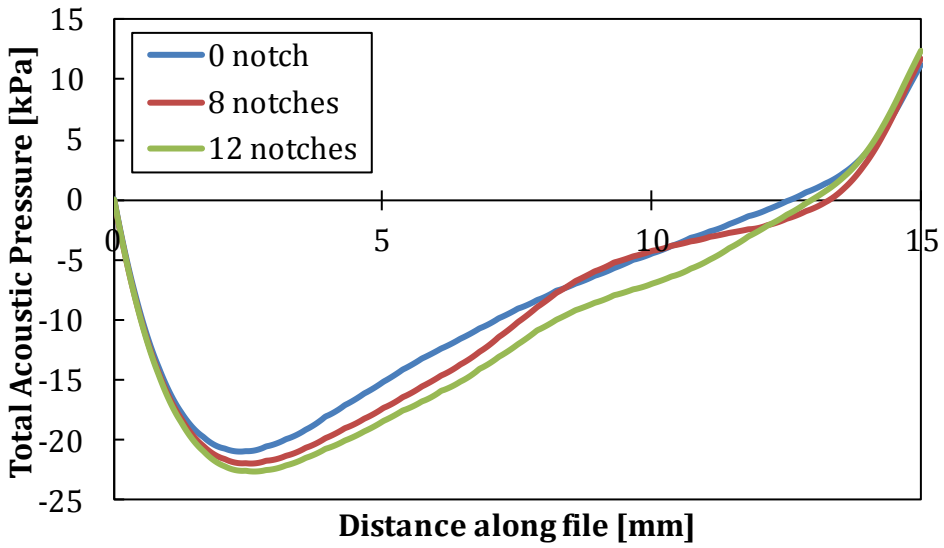

Figure 6.40: *Total acoustic pressure along the working length of CT-4 at Power 10/10 in a vessel of 6 mm × 6 mm × 20 mm, setting the vessel boundary as hard wall.*

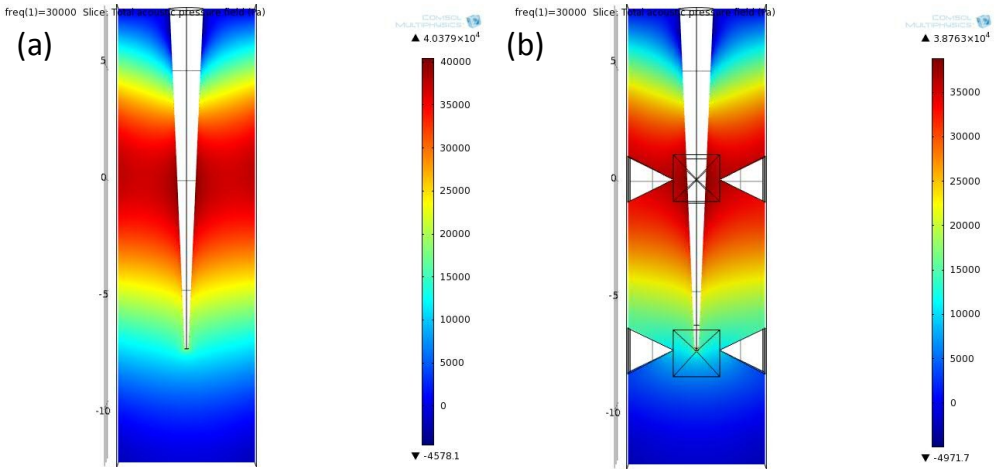

Figure 6.41: *Acoustic wave patterns across the middle of the vessel with boundary condition equivalent to human tissue (a) without notch; (b) with notches.*

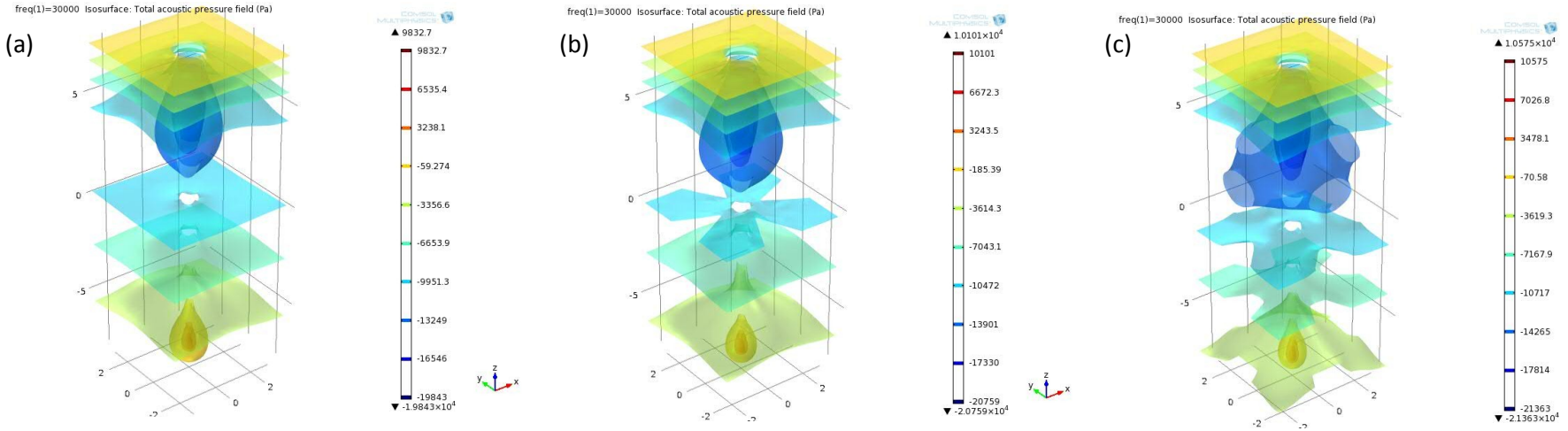

Figure 6.42: *Isosurface of the acoustic pressure produced when the vessel walls were simulated as hard walls: (a) without notch; (b) with 8 notches; (c) with 12 notches.*

6.3 Conclusions

This chapter gave an overview of the acoustic pressure fields in various ultrasonic systems. Based on the developments of the 2-dimensional model built on both the 20 kHz and 515 kHz ultrasonic devices, a reliable 3-dimensional model of the dental endosonic files was established and gave good comparative results among different endosonic files of various shapes. From this, it can be concluded that:

i) Reproducible results can be obtained from the 2-Dimensional model on the **20 kHz ultrasonic probe** and the acoustic pressure fields depend strongly on the size of the vessel and the boundary conditions.

ii) The **515 kHz ultrasonic plate transducer** model showed comparable results with the luminol photography obtained for the zones of cavitation activities, which strengthens the reliability of the methods used for the acoustic pressure fields prediction.

iii) The **2-dimensional model on the dental endosonic files** built gave insufficient information, which brought the need of building a 3-dimensional model for better pressure fields prediction.

iv) 3-dimensional model of a rectangular slab, cylinder and cone model showed that the **shape** and **dimension** play an important role in producing acoustic pressure fields in the surrounding under the same external conditions.

v) Acoustic pressure fields of the **3-dimensional model of CT-4**, **CKT-1** differ greatly to those produced by **UT-4**, but there was not much difference detected between the CT-4 and CKT-1 when only the working lengths of the dental tips were modeled.

vi) A good visualised correlation can be obtained from the **SLV**, **SCL** and the **predicted acoustic pressure fields**, indicating that all factors affect one another in the production of transient cavitation.

vii) The 3-dimensional models of the three endosonic files fully immersed in a bulk liquid showed similar results at the working length of the tips, with areas of high acoustic pressures producing high cavitational activities.

viii) Boundary conditions play an important role in the magnitude of acoustic pressure produced, where boundaries with acoustic impedances close to water acting as good sound absorbers and will produce higher acoustic pressure around the endosonic files compared to hard wall boundaries.

ix) Decreasing the volume of the vessel increases the surrounding acoustic pressure, but the presence of notches in the vessel does not affect the acoustic pressure field patterns when it was modeled as the walls equivalent to those of 'human tissue'.

With these conclusions, predictions of acoustic pressure in the surrounding liquid of the endosonic files can be used as a guideline to predict the possible areas of transient cavitation activities under different conditions, which will provide a better insight of the overall sonochemical performance of the endosonic instruments.

7. Conclusions

The work detailed in this thesis has illustrated the performances of the endosonic files assessed. This was divided into two main areas (refer to Section 1.5):

(i) characterisation of the endosonic files;
(ii) cleaning efficiencies of the endosonic files;

The output of this work was to correlate the factors affecting the cleaning efficiencies of the endosonic files, and to provide possible suggestions for the modification of the endosonic files for a better next generation endosonic files.

In Chapter 3, several characterisation methods were carried out on the endosonic files. Scheme 3.2 showed that the characterisation methods performed correlated to one another, where the energy output of the endosonic files (assessed calorimetrically) affects the vibration movements of the dental files, which, then affects the areas of sono(chemi)luminescence (SCL) produced. SCL produced with the cavitation counts using a cavimeter and the absorbance of Fe^{3+} from Fricke Dosimetry showed good correlations. Particle Image Velocimetry (PIV) of the fluid in an enclosed system affects the amount of SCL produced from the ultrasonically driven endosonic files.

The results obtained from Chapter 3 on various characterisation methods on the endosonic files were correlated with the cleaning efficiencies of the endosonic files in Chapter 4. The work on cleaning efficiencies was performed based on the emulsification, rate of dye removal with a dental irrigant, ink removal and hydroxyapatite (HA) paste removal. The results showed that endosonic files with high transient cavitation production and high streaming effects (based on PIV results in Chapter 3) were able to form emulsions with smaller oil-in-water droplets and remove dye, ink and hydroxyapatite paste more effectively.

Upon investigation into the sonochemical activities and the vibration movements of the endosonic files and correlation with the cleaning efficiencies, various factors that may contribute to the production of transient cavitation and vibration movements were investigated in Chapter 5. Results showed that SCL was more intense in a confined space, but the width of the channel and the positions of the files have little influence on the total SCL produced. Shape of the endosonic files played an important role in the formation of SCL (based on results on the Start-X tips). Though the vibration antinodes correspond to the areas where SCL is produced, the intensity of SCL produced was not affected by the magnitude of the vibration amplitudes of the files.

Computational simulation of the acoustic pressure fields in a liquid surrounding the endosonic files were performed in Chapter 6 to provide a better explanation of the experimental findings in Chapters 3, 4 and 5. Simulated results of the acoustic pressure showed that the shapes of the endosonic files affect the surrounding acoustic pressure. Endosonic files with a thicker diameter (*eg*. CT-4 and CKT-1) produced much higher acoustic pressure in the surrounding liquid as compared to the thinner files (*eg.* UT-4). Areas where high acoustic pressures were formed correspond to the areas where SCL is produced. This further strengthened the experimental results showing that the SCL produced was at localised areas along the file.

The work described in this thesis showed correlations of the sonochemical activities and the factors contributing to the cleaning efficiencies of the endosonic files. It has provided a thorough analysis of factors affecting the performance of the endosonic files, which has not been compared in detail in previous literature (van der Sluis *et al*., 2007a). It has shown that endosonic files with better acoustic streaming produce more SCL, which aids the removal of surface impurities and removal of dye in a confined environment. This has a strong relation to the shape of the endosonic files, where files with thicker diameters and greater vibration displacements will have better streaming effects in a liquid medium, producing more SCL – hence is more effective in cleaning.

Overall, this study has shown that the production of SCL is not solely dependent on the ultrasonic intensity produced by an endosonic file. Other factors such as sufficiently high vibration movement of the file and the ability to produce sufficiently high velocity fluid flow in a sonicating system are equally important. This provides useful suggestions to manufacturers and clinicians to assess the efficiency of an endosonic file based on the characterisation methods described in this thesis.

7.1 Future Work

The information on the characterisation of the endosonic files can be combined with simulation to improve the design of endosonic files which can cater for specific applications during endodontic treatments. Different characterisation methods described in this thesis can be performed on the endosonic files used in future dental practices, in order to evaluate their cleaning efficiencies.

It was concluded that the acoustic pressure distribution along the dental files play an important role in the formation of SCL. Hence it would be interesting to modify the shapes of the endosonic files based on the simulated results to provide an useful suggestion for future endosonic file designs.

Also, the cleaning performances of the endosonic files in *vivo* may be investigated based on their ability to remove dentin debris, and compared to the results obtained from the experiments conducted in an *in vitro* environment. As the root canal consists of complex micro-channels, it would be useful to perform a thorough computational simulation mimicking the size, shapes and boundary conditions of a root canal in order to provide more accurate information on the acoustic pressure distribution, which is vital to sonochemical cleaning.

Finally, based on the computational methods developed in this work, further investigation on the effects of cavitation bubbles and acoustic streaming in the computational model will provide more accurate information on the acoustic pressure distribution in the system.

Bibliography

AASIM, S. A., MELLOR, A. C. & QUALTROUGH, A. J. E. 2006. The effect of pre-soaking and time in the ultrasonic cleaner on the cleanliness of sterilized endodontic files. *International Endodontic Journal,* 39**,** 143-149.

ABISMAIL, B., CANSELIER, J. P., WILHELM, A. M., DELMAS, H. & GOURDON, C. 1999. Emulsification by ultrasound: drop size distribution and stability. *Ultrasonics Sonochemistry,* 6**,** 75-83.

ABRAMOFF, M. D., MAGALHAES, P. J. & RAM, S. J. 2004. Image processing with ImageJ. *Biophotonics Int.***,** 36-43.

AHMAD, M. 1989. Effect of Ultrasonic Instrumentation on Bacteroides-intermedius. *Endodontics & Dental Traumatology,* 5**,** 83-86.

AHMAD, M., FORD, T. R. P. & CRUM, L. A. 1987a. Ultrasonic debridement of root canals: acoustic streaming and its possible role. *Journal of Endodontics,* 14**,** 490-499.

AHMAD, M., FORD, T. R. P. & CRUM, L. A. 1987b. Ultrasonic debridement of root canals: an insight into the mechanism involved. *Journal of Endodontics,* 13**,** 93-100.

AHMAD, M., FORD, T. R. P., CRUM, L. A. & WALTON, A. J. 1988. Ultrasonic debridement of root canals - Acoustic cavitation and its relevance. *Journal of Endodontics,* 14**,** 486-493.

ASHOKKUMAR, M. 2011. *Theoretical and Experimental Sonochemistry Involving Inorganic Systems*, Springer.

ASHOKKUMAR, M., HODNETT, M., ZEQIRI, B., GRIESER, F. & PRICE, G. J. 2007. Acoustic Emission Spectra from 515 kHz Cavitation in Aqueous Solutions Containing Surface-Active Solutes. *Journal of the American Chemical Society,* 129**,** 2250-2258.

ATCHLEY, A. A., FRIZZELL, L. A., APFEL, R. E., HOLLAND, C. K., MADANSHETTY, S. & ROY, R. A. 1988. Thresholds for cavitation produced in water by pulsed ultrasound. *Ultrasonics,* 26**,** 280-285.

AZHARI, H. 2010. *Basics of Biomedical Ultrasound for Engineers*, Wiley-IEEE Press.

BAI, M. D. & JIAN, S. 2006. *The effect of hydroxyl radicals on photosynthesis pigments of phytoplankton in ship's ballast water,* Jilin, Jilin Sci Technol Publ House.

BAI, X. Y., ZHANG, Z. T., BAI, M. D., YANG, B. & BAI, M. B. 2005. Killing of invasive species of ship's ballast water in 20t/h system using hydroxyl radicals. *Plasma Chemistry and Plasma Processing,* 25**,** 41-54.

BALAMUTH, L. 1963. Ultrasonics and Dentistry. *Sound: Its Uses and Control,* 2**,** 15-19.

BARNABY, S. W. & PARSONS, C. W. 1897. *Trans. Inst. Naval Arch.,* 38**,** 232.

BARNABY, S. W. & THORNYCROFT, S. J. 1895. Torpedo boat destroyers. *Proc. Inst. Civ. Engrs,* 122.

BEER, R., BAUMANN, M. A. & KEIELBASSA, A. M. 2006. *Pocket Atlas of Endodontics*, Thieme Publishers.

BEHNAJADY, M. A., MODIRSHAHLA, N., TABRIZI, S. B. & MOLANEE, S. 2008. Ultrasonic degradation of Rhodamine B in aqueous solution: Influence of operational parameters. *Journal of Hazardous Materials,* 152**,** 381-386.

BEHREND, O., AX, K. & SCHUBERT, H. 2000. Influence of continuous phase viscosity on emulsification by ultrasound. *Ultrasonics Sonochemistry,* 7**,** 77-85.

BERGENHOLTZ, G., HORSTED-BINDSLEV, P. & REIT, C. 2010. *Textbook of Endodontology*, Wiley-Blackwell.

BIRKIN, P. R., LEIGHTON, T. G., POWER, J. F., SIMPSON, M. D., VINCOTTE, A. M. L. & JOSEPH, P. F. 2003. Experimental and theoretical characterization of sonochemical cells. Part 1. Cylindrical reactors and their use to calculate the speed of sound in aqueous solutions. *Journal of Physical Chemistry A,* 107**,** 306-320.

BITTON, G. 2005. *Wastewater microbiology*, John Wiley & Sons, Inc.

BLACKSTOCK, D. T. 2000. *Fundamentals of physical acoustics*, John Wiley & Sons, Inc.

BLUME, T. & NEIS, U. 2005. Improving chlorine disinfection of wastewater by ultrasound application. *Water Sci Technol,* 52**,** 139-144.

BOUTSIOUKIS, C., VERHAAGEN, B., VERSLUIS, M., KASTRINAKIS, E. & SLUIS, L. W. M. V. D. 2010a. Irrigant flow in the root canal: experimental validation of an unsteady Computational Fluid Dynamics model using high-speed imaging. *International Endodontic Journal,* 43**,** 393-403.

BOUTSIOUKIS, C., VERHAAGEN, B., VERSLUIS, M., KASTRINAKIS, E., WESSELINK, P. R. & VAN DER SLUIS, L. W. M. 2010b. Evaluation of Irrigant Flow in the Root Canal Using Different Needle Types by an Unsteady Computational Fluid Dynamics Model. *Journal of Endodontics,* 36**,** 875-879.

BROWN, D. C., MOORE, B. K., BROWN, C. E. & NEWTON, C. W. 1995. An in-vitro study of apical extrusion of sodium-hypochlorite during endodontic canal preparation. *Journal of Endodontics,* 21**,** 587-591.

CAMERON, J. A. 1987. The use of 4-percent sodium-hypochlorite, with or without ultrasound, in cleansing of uninstrumented immature root canals - SEM study. *Australian Dental Journal,* 32**,** 204-213.

CAPOTE, F. P. & CASTRO, M. D. L. D. 2007. *Analytical Applications of Ultrasound*, Elsevier Science.

CATUNA, M. C. 1953. Sonic Energy. *Annals of Dentistry,* 12**,** 100.

CHANDRAPALA, J., OLIVER, C., KENTISH, S., ASHOKKUMAR, M. 2012. Ultrasonics in food processing, *Ultrason. Sonochem.*, 5, 975-983.

CHEN, F., ZHAO, J. C. & HIDAKA, H. 2003. Highly selective deethylation of rhodamine B: Adsorption and photooxidation pathways of the dye on the TiO2/SiO2 composite photocatalyst. *International journal of photoenergy,* 5**,** 209-217.

CHEVALIER, F. L. 2002. *Principles of radar and sonar signal processing*, Artech House Publishers.

CLARK, J. & MACQUARRIE, D. 2002. *Handbook of Green Chemistry and Technology*, Blackwell Publishing.

CLARKE, W. B. 2009. *Hydrogen Peroxide*, University of Michigan Library.

CLARKSON, R. M. & MOULE, A. J. 1998. Sodium hypochlorite and its use as an endodontic irrigant. *Australian Dental Journal,* 43**,** 250-256.

COMSOL 2011. *COMSOL Multiphysics User's Guide*.

CRUM, L. A. 1979. Surface Oscillations and Jet Development in Pulsating Bubbles. *Journal De Physique,* 41**,** 285-288.

CRUM, L. A. 1984. Acoustic cavitation series: part five rectified diffusion. *Ultrasonics,* 22**,** 215-223.

CURRY, R. A. & TEMPKIN, B. B. 2010. *Sonography: Introduction to Normal Structure and Function* Sanders.

DE GROOT, S. D., VERHAAGEN, B., VERSLUIS, M., WU, M. K., WESSELINK, P. R. & VAN DER SLUIS, L. W. M. 2009. Laser-activated irrigation within root canals: cleaning efficacy and flow visualization. *International Endodontic Journal,* 42**,** 1077-1083.

DENTSPLY. 2010. *Start-X* [Online]. Available: http://www.dentsply.co.uk/Uploads/Files/start-x_brochure%20gb%20newcorrectedcodes.pdf [Accessed 4th December 2011].

DERYABIN, M., KASÝANOV, D., RODCHENKOV, I. & SERGEEV, D. 2010. Experimental Study of Acoustic Flows in a Focused Ultrasound Field. *Journal of Applied Mechanics and Technical Physics,* 51**,** 663-668.

DESTAILLATS, H., HOFFMANN, M. R. & WALLACE, H. C. 2003. Sonochemical Degradation of Pollutants. *In:* TARR, M. A. (ed.) *Chemical Degradation Methods for Wastes and Pollutants: Environmental and Industrial Applications.* CRC Press.

DRISCOLL, C. O., DOWKER, S. E. P., ANDERSON, P., WILSON, R. M. & GULABIVALA, K. 2002. Effects of sodium hypochlorite solution on root dentine composition. *Journal of Materials Science: Materials in Medicine,* 13**,** 219-223.

ERGAS, S. J., THERRIAULT, B. M. & RECKHOW, D. A. 2006. Evaluation of water reuse technologies for the textile industry. *Journal of Environmental Engineering-Asce,* 132**,** 315-323.

EULER, L. 1754. On the General and Fundamental Principle of all Mechanics whereon all other Principles Relative to the Motion of Solids or Fluids should be established. *Gentleman's Magazine.*

FELVER, B., KING, D. C., LEA, S. C., PRICE, G. J. & DAMIEN WALMSLEY, A. 2009. Cavitation occurrence around ultrasonic dental scalers. *Ultrasonics Sonochemistry,* 16**,** 692-697.

FENG, H., BARBOSA-CANOVAS, G. V. & WEISS, J. 2011. *Ultrasound Technologies for Food and Bioprocessing*, Springer.

FITZGERALD, M. E., GRIFFING, V. & SULLIVAN, J. 1956. Chemical Effects of Ultrasonics - "Hot Spot" Chemistry. *J. Chem. Phys.,* 25**,** 926-933.

FRANKE, M., BRAEUTIGAM, P., WU, Z. L., REN, Y. Z. & ONDRUSCHKA, B. 2011. Enhancement of chloroform degradation by the combination of hydrodynamic and acoustic cavitation. *Ultrasonics Sonochemistry,* 18**,** 888-894.

FREDERICK, J. R. 1965. *Ultrasonic Engineering*, John Wiley & Sons, Inc.

FRENKEL, V., GURKA, R., LIBERZON, A., SHAVIT, U. & KIMMEL, E. 2001. Preliminary investigations of ultrasound induced acoustic streaming using particle image velocimetry. *Ultrasonics,* 39**,** 153-156.

FRENZEL, J. & SCHULTES, H. 1934. *Zeit fur Phys. Chem.,* B27.

FRICKE, H. & HART, E. J. 1935. The Oxidation of Fe++ to Fe+++ by the irradiation with x-rays of solutions of Ferrous Sulfate in Sulfuric Acid. *J. Chem. Phys.,* 3**,** 60-61.

FROHLY, J., LABOURET, S., BRUNEEL, C., LOOTEN-BAQUET, I. & TORGUET, R. 2000. Ultrasonic cavitation monitoring by acoustic noise power measurement. *Journal of the Acoustical Society of America,* 108**,** 2012-2020.

FUCHS, F. J. 2002. *Ultrasonic Cleaning: Fundamental Theory and Application* [Online]. Blackstone~ney Ultrasonics. Available: http://www.blackstone-ney.com/pdfs/T_Fundamentals.pdf [Accessed 28th September 2011].

GAIKWAD, S. G. & PANDIT, A. B. 2008. Ultrasound emulsification: Effect of ultrasonic and physicochemical properties on dispersed phase volume and droplet size. *Ultrasonics Sonochemistry,* 15**,** 554-563.

GAO, D. R., QIAO, H. J. & LU, X. H. 2009. Finite Element Computational Simulation and PIV Measurement of Flow Field inside Metering-in Spool Valve. *Chinese Journal of Mechanical Engineering,* 22**,** 102-108.

GAQUERE-PARKER, A. C., AHMED, A., ISOLA, T., MARONG, B., SHACKLADY, C. & TCHOUA, P. 2009. Temperature effect on an ultrasound-assisted paper de-inking process. *Ultrasonics Sonochemistry,* 16**,** 698-703.

GARG, N. & GARG, A. 2010. *Textbook of Endodontics,* India, Jaypee Broters Medical Publishers.

GOGATE, P. R., SIVAKUMAR, M. & PANDIT, A. B. 2004. Destruction of Rhodamine B using novel sonochemical reactor with capacity of 7.5 1. *Separation and Purification Technology,* 34**,** 13-24.

GOLDBERG, B. B. & KIMMELMAN, B. A. 1988. *Medical Diagnostic Ultrasound: A Retrospective on its 40th Anniversary*, Eastman Kodak Company, New York.

GU, L. S., KIM, J. R., LING, J. Q., CHOI, K. K., PASHLEY, D. H. & TAY, F. R. 2009. Review of Contemporary Irrigant Agitation Techniques and Devices. *Journal of Endodontics,* 35**,** 791-804.

HAÏKEL, Y., SERFATY, R., BLEICHER, P., LWIN, T.-T. C. & ALLEMANN, C. 1996. Effects of cleaning, disinfection, and sterilization procedures on the cutting efficiency of endodontic files. *Journal of Endodontics,* 22**,** 657-661.

HARTY, F. J. & FORD, T. R. P. 2004. *Harty's Endodontics in Clinical Practice*, Wright, Elsevier Limited.

HATANAKA, S.-I., MITOME, H., YASUI, K. & HAYASHI, S. 2006. Multibubble sonoluminescence enhancement by fluid flow. *Ultrasonics,* 44, Supplement**,** e435-e438.

HAYNES, W. M. 2011. *CRC handbook of chemistry and physics: a ready-reference book of chemical and physical data*, CRC.

HEGDE, V. & SINGH, G. 2006. *Step by Step Root Canal Treatment*, Jaypee Brothers Medical Publishers.

HELING, I. & CHANDLER, N. P. 1998. Antimicrobial effect of irrigant combinations within dentinal tubules. *International Endodontic Journal,* 31**,** 8-14.

HENGLEIN, A. 1987. Sonochemistry: Historical developments and modern aspects. *Ultrasonics,* 25**,** 6-16.

HILAR, A. P. 1946. *Sonar : detector of submerged submarines* University of California Libraries.

HINZE, J. O. 1955. Fundamentals of the hydrodynamic mechanism of splitting in dispersion processes. *AIChE Journal,* 1**,** 289-295.

HODNETT, M., CHOW, R. & ZEQIRI, B. 2004. High-frequency acoustic emissions generated by a 20 kHz sonochemical horn processor detected using a novel broadband acoustic sensor: a preliminary study. *Ultrasonics Sonochemistry,* 11**,** 441-454.

HOROZOV, T. S., BINKS, B. P. & GOTTSCHALK-GAUDIG, T. 2007. Effect of electrolyte in silicone oil-in-water emulsions stabilised by fumed silica particles. *Physical Chemistry Chemical Physics,* 9**,** 6398-6404.

HUANG, J., HOLT, R. G., CLEVELAND, R. O. & ROY, R. A. 2004. Experimental validation of a tractable computational model for focused ultrasound heating in flow-through tissue phantoms. *Journal of the Acoustical Society of America,* 116**,** 2451-2458.

HUI, Y. H. & SHERKAT, F. 2005. *Handbook of Food Science, Technology, and Engineering.*, CRC Press.

HÜLSMANN, M. & HAHN, W. 2000. Complications during root canal irrigation - literature review and case reports. *International Endodontic Journal,* 33**,** 186-193.

HUQUE, J., KOTA, K., YAMAGA, M., IWAKU, M. & HOSHINO, E. 1998. Bacterial eradication from root dentine by ultrasonic irrigation with sodium hypochlorite. *International Endodontic Journal,* 31**,** 242-250.

IIDA, Y., YASUI, K., TUZIUTI, T. & SIVAKUMAR, M. 2005. Sonochemistry and its dosimetry. *Microchemical Journal,* 80**,** 159-164.

INGLE, J. I., BAKLAND, L. K. & BAUMGARTNER, J. C. 2008. *Ingle's Endodontics 6*, B. C. Decker Inc.

INGLE, J. I., BAKLAND, L. K., BEVERIDGE, E. E., GLICK, D. H. & HOSKINSON, A. E. 2002. *Endodontics*, BC Decker Inc.

INOUE, M., OKADA, F., SAKURAI, A. & SAKAKIBARA, M. 2006. A new development of dyestuffs degradation system using ultrasound. *Ultrasonics Sonochemistry,* 13**,** 313-320.

IRELAND, R. 2010. A Dictionary of Dentistry. *Oxford Dictionary of Dentistry.* Oxford University Press Inc.

JENSEN, S. A., WALKER, T. L., HUTTER, J. W. & NICOLL, B. K. 1999. Comparison of the cleaning efficacy of passive sonic activation and passive ultrasonic activation after hand instrumentation in molar root canals. *Journal of Endodontics,* 25**,** 735-738.

JIANG, L.-M., VERHAAGEN, B., VERSLUIS, M. & VAN DER SLUIS, L. W. M. 2010. Evaluation of a sonic device designed to activate irrigant in the root canal. *J Endod,* 36**,** 143-6.

JOHNSON, W. N. & WILSON, J. R. 1957. The Application of Ultrasonic Dental Units to Scaling Procedures. *Journal of Periodontology,* 28**,** 264-271.

JOULE, J. 1842. *Sturgeon's Annals of Electricity*.

KLÍMA, J., FRIAS-FERRER, A., GONZÁLEZ-GARCÍA, J., LUDVÍK, J., SÁEZ, V. & INIESTA, J. 2007. Optimisation of 20kHz sonoreactor geometry on the basis of computational simulation of local ultrasonic intensity and qualitative comparison with experimental results. *Ultrasonics Sonochemistry,* 14**,** 19-28.

KRATOCHVÍL, B., MORNSTEIN, V. & FORÝTKOVA, L. 2002. Sonochemical Effects on Descaler-produced Ultrasound In Vitro. *Scripta Medica,* 75**,** 21-28.

KREFTING, D., METTIN, R. & LAUTERBORN, W. 2004. High-speed observation of acoustic cavitation erosion in multibubble systems. *Ultrasonics Sonochemistry,* 11**,** 119-123.

KUIJPERS, M. W. A., KEMMERE, M. F. & KEURENTJES, J. T. F. 2002. Calorimetric study of the energy efficiency for ultrasound-induced radical formation. *Ultrasonics,* 40**,** 675-678.

LABORDE, J. L., HITA, A., CALTAGIRONE, J. P. & GERARD, A. 2000. Fluid dynamics phenomena induced by power ultrasounds. *Ultrasonics,* 38**,** 297-300.

LAUTERBORN, W. 1980. *Cavitation and Inhomogeneities in Underwater Acoustics*, Springer - Verlag.

LAUTERBORN, W. & BOLLE, H. 1975. Experimental investigations of cavitation-bubble collapse in the neighbourhood of a solid boundary. *Journal of Fluid Mechanics,* 72**,** 391-399.

LEA, S. C., LANDINI, G. & WALMSLEY, A. D. 2003. Displacement amplitude of ultrasonic scaler inserts. *Journal of Clinical Periodontology,* 30**,** 505-510.

LEA, S. C., LANDINI, G. & WALMSLEY, A. D. 2004. Assessing the vibrations of dental ultrasonic scalers. *Journal of Sound and Vibration,* 271**,** 1113-1120.

LEA, S. C., PRICE, G. J. & WALMSLEY, A. D. 2005. A study to determine whether cavitation occurs around dental ultrasonic scaling instruments. *Ultrasonics Sonochemistry,* 12**,** 233-236.

LEIGHTON, T. G. 1994. *The Acoustic Bubble*, Academic Press.

LEIGHTON, T. G. 2007. What is ultrasound? *Progress in Biophysics and Molecular Biology,* 93**,** 3-83.

LI, M. K. & FOGLER, H. S. 1978. Acoustic emulsification. Part 2. Breakup of the large primary oil droplets in a water medium. *J. Fluid Mech.,* 88**,** 513-528.

LIANG, J. S., JIN, Z. Z., MENG, J. P., DING, Y. & LI, L. 2004. Enhancement of rare earth elements on antibacterial property of composite phosphate inorganic antibacterial powders. *Rare Metal Materials and Engineering,* 33**,** 106-109.

LIFKA, J., ONDRUSCHKA, B. & HOFMANN, J. 2002. The use of ultrasound for the degradation of organic compounds in water: Aquasonolysis - A review. *Chemie Ingenieur Technik,* 74**,** 403-413.

LIONETTI, V. & PADDEU, S. 2009. Towards Ultrasound Molecular Imaging. *In:* PARADOSSI, G., PELLEGRETTI, P. & TRUCCO, A. (eds.) *Ultrasound contrast agents: Targeting and processing methods for theranostics.* Springer.

LOUISNARD, O. 2012. A simple model of ultrasound propagation in a cavitating liquid. Part II: Primary Bjerknes force and bubble structures. *Ultrasonics Sonochemistry,* 19**,** 66-76.

LUCHE, J.-L. & BIANCHI, C. 1998. *Synthetic organic sonochemistry*, Springer.

LUMLEY, P. J., LUCAROTTI, P. S. K. & BURKE, F. J. T. 2008. Ten-year outcome of root fillings in the General Dental Services in England and Wales. *International Endodontic Journal,* 41**,** 577-585.

MAKINO, K., MOSSOBA, M. M. & RIESZ, P. 1983. Chemical effects of ultrasound on aqueous solutions. Formation of hydroxyl radicals and hydrogen atoms. *The Journal of Physical Chemistry,* 87**,** 1369-1377.

MANDROYAN, A., DOCHE, M. L., HIHN, J. Y., VIENNET, R., BAILLY, Y. & SIMONIN, L. 2009. Modification of the ultrasound induced activity by the presence of an electrode in a sono-reactor working at two low frequencies (20 and 40 kHz). Part II: Mapping flow velocities by particle image velocimetry (PIV). *Ultrasonics Sonochemistry,* 16**,** 97-104.

MARSHALL, M., CANCRO, L. & FISCHMAN, S. 1995. Hydrogen peroxide - A review of its use in dentistry. *Journal of Periodontology,* 66**,** 786-796.

MARTIN, H., CUNNINGHAM, W., NORRIS, J. & COTTON, W. 1980. Ultrasonic versus hand filing of dentin - quantitative study. *Oral surgery, oral medicine, oral pathology, oral radiology and endodontics,* 49**,** 79-81.

MASON, T. J. 1991. *Practical Sonochemistry*, Ellis Horwood.

MCCALL, C. M. & SZMYD, L. 1960. Clinical Evaluation of Ultrasonic Scaling. *Journal of America Dental Association,* 60**,** 559-564.

MCMURRAY, H. N. & WILSON, B. P. 1999. Mechanistic and Spatial Study of Ultrasonically Induced Luminol Chemiluminescence. *The Journal of Physical Chemistry A,* 103**,** 3955-3962.

MCSKIMIN, H. J. 1965. Velocity of Sound in Distilled Water for the Temperature Range 20°–75° C. *Journal of Acoustic Society America,* 37**,** 325-328.

MEHRDAD, A. & HASHEMZADEH, R. 2010. Ultrasonic degradation of Rhodamine B in the presence of hydrogen peroxide and some metal oxide. *Ultrasonics Sonochemistry,* 17**,** 168-172.

MEROUANI, S., HAMDAOUI, O., SAOUDI, F. & CHIHA, M. 2010. Sonochemical degradation of Rhodamine B in aqueous phase: Effects of additives. *Chemical Engineering Journal,* 158**,** 550-557.

MILLER, M. W., MILLER, D. L. & BRAYMAN, A. A. 1996. A review of in vitro bioeffects of inertial ultrasonic cavitation from a mechanistic perspective. *Ultrasound in Medicine & Biology,* 22**,** 1131-1154.

MILLER, N. 1950. Chemical action of sound waves on aqueous solutions. *Transactions of the Faraday Society,* 46**,** 546-550.

MOAD, G. & SOLOMON, D. H. 2006. *The Chemistry of Radical Polymerization*, Elsevier.

MORRIS, J. C. 1966. The Acid Ionization Constant of HOCl from 5 to 35°. *The Journal of Physical Chemistry,* 70**,** 3798-3805.

MOSHE, I., JACKEL, S. & MEIR, A. 2003. Production of radially or azimuthally polarized beams in solid-state lasers and the elimination of thermally induced birefringence effects. *Optics Letters,* 28**,** 807-809.

NEGISHI, K. 1961. Experimental Studies on Sonoluminescence and Ultrasonic Cavitation. *Journal of the Physical Society of Japan,* 16**,** 1450-&.

NEPPIRAS, E. A. & NOLTINGK, B. E. 1951. Cavitation Produced by Ultrasonics: Theoretical Conditions for the Onset of Cavitation. *Proceedings of the Physical Society. Section B,* 64**,** 1032.

NEWTON, I. 1952. *Optiks*, Dover Publications, New York.

NG, K.-Y. 2005. Ultrasound-Mediated Drug Delivery *In:* WANG, B., SIAHAAN, T. J. & SOLTERO, R. A. (eds.) *Drug Delivery: Principles and Applications.* Wiley-Interscience.

NOWICKI, A., KOWALEWSKI, T., SECOMSKI, W. & WOJCIK, J. 1998. Estimation of acoustical streaming: theoretical model, Doppler measurements and optical visualisation. *European Journal of Ultrasound,* 7**,** 73-81.

OHARA, P., TORABINEJAD, M. & KETTERING, J. D. 1993. Antibacterial effects of various endodontic irrigants on selected anaerobic bacteria. *Dental Traumatology,* 9**,** 95-100.

PARK, S. 2008. *Mechanical properties of human tooth enamel: Patient age and spatial distribution.* Thesis: M.Sc., University of Maryland.

PASSARINHO-NETO, J. G., MARCHESAN, M. A., FERREIRA, R. B., SILVA, R. G., SILVA-SOUSA, Y. T. C. & SOUSA-NETO, M. D. 2006. In vitro evaluation of endodontic debris removal as obtained by rotary instrumentation coupled with ultrasonic irrigation. *Australian endodontic journal : the journal of the Australian Society of Endodontology Inc,* 32**,** 123-8.

PAULUS, W. 2005. *Directory of microbicides for the protection of materials: a handbook*, Springer.

PIZZOLATO, T. M., CARISSIMI, E., MACHADO, E. L. & SCHNEIDER, I. A. H. 2002. Colour removal with NaClO of dye wastewater from an agate-processing plant in Rio Grande do Sul, Brazil. *International Journal of Mineral Processing,* 65**,** 203-211.

PLESSET, M. S. & CHAPMAN, R. B. 1971. Collapse of an initially spherical vapour cavity in the neighbourhood of a solid boundary. *Journal of Fluid Mechanics,* 47**,** 283-290.

PLOTINO, G., PAMEIJER, C. H., GRANDE, N. M. & SOMMA, F. 2007. Ultrasonics in Endodontics: A Review of the Literature. *Journal of Endodontics,* 33**,** 81-95.

POLYTEC. 2000. *Polytec Scanning Vibrometer PSV 300* [Online]. Available: http://www-mech.eng.cam.ac.uk/dynvib/lab_facilities/vibrometer_hardware_manual.pdf [Accessed 3rd December 2011].

PRICE, G. J. 1992. *Current trends in sonochemistry*, Royal Society of Chemistry.

PRICE, G. J. & LENZ, E. J. 1993. The use of dosimeters to measure radical production in aqueous sonochemical systems. *Ultrasonics,* 31**,** 451-456.

PRICE, G. J., LENZ, E. J. & ANSELL, C. W. G. 2002. The effect of high intensity ultrasound on the synthesis of some polyurethanes. *European Polymer Journal,* 38**,** 1531-1536.

PRICE, G. J., SMITH, P. F. & WEST, P. J. 1991. Ultrasonically Initiated Polymerization of Methyl-methacrylate. *Ultrasonics,* 29**,** 166-170.

PRICE, G. J. & WALMSLEY, A. D. 2008. Joint Research Proposal: Optimising the Sonochemical and Ultrasonic Output of Dental Endosonic Instruments. University of Birmingham and University of Bath.

RAJKUMAR, D., SONG, B. J. & KIM, J. G. 2007. Electrochemical degradation of Reactive Blue 19 in chloride medium for the treatment of textile dyeing wastewater with identification of intermediate compounds. *Dyes and Pigments,* 72**,** 1-7.

RAMAN, V., ABBAS, A. & JOSHI, S. C. 2006. Mapping local cavitation events in high intensity ultrasound fields. *Proceedings of the COMSOL Users Conference November 2006, Bangalore*.

RANTANEN, N. W. 1986. *Diagnostic Ultrasound*, Jaypee Brothers Publishers.

REYNOLDS, O. 1873. The causes of the racing of the engines of screw steamers investigated theoretically and by experiment. *Inst. Naval. Arch.,* 14**,** 56.

RICHMAN, R. J. 1957. The use of ultrasonic in root canal therapy and root resection. *Med Dent J,* 12**,** 8.

RODENBUSH, W. H. & WAHL, M. H. 1933. The Reactions of the Hydroxyl Radical in the Electrodeless Discharge in Water Vapor. *J. Chem. Phys.,* 1**,** 696-702.

ROSSI-FEDELE, G., GUASTALLI, A. R., DOGRAMACI, E. J., STEIER, L. & DE FIGUEIREDO, J. A. P. 2011. Influence of pH changes on chlorine-containing endodontic irrigating solutions. *International Endodontic Journal,* 44**,** 792-799.

ROY, R. A., AHMAD, M. & CRUM, L. A. 1994. PHYSICAL-MECHANISMS GOVERNING THE HYDRODYNAMIC RESPONSE OF AN OSCILLATING ULTRASONIC FILE. *International Endodontic Journal,* 27**,** 197-207.

SÁEZ, V., FRÍAS-FERRER, A., INIESTA, J., GONZÁLEZ-GARCÍA, J., ALDAZ, A. & RIERA, E. 2005. Chacterization of a 20 kHz sonoreactor. Part I: analysis of mechanical effects by classical and computational methods. *Ultrasonics Sonochemistry,* 12**,** 59-65.

SANDER, L., WENZEL, A., HINTZE, H. & KARRING, T. 1996. Image homogeneity and recording reproducibility with 2 techniques for serial intra-oral radiography. *Journal of Periodontology,* 67**,** 1288-1291.

SANDERS, R. C. & WINTER, T. C. 2006. *Clinical Sonography: A Practical Guide*, Lippincott Williams & Wilkins.

SCHERZE, I., KNOFEL, R. & MUSCHIOLIK, G. 2005. Automated image analysis as a control tool for multiple emulsions. *Food Hydrocolloids,* 19**,** 617-624.

SCOTT, G. R. & TURNER, C. G. 1997. *The Anthropology of Modern Human Teeth: Dental Morphology and Its Variation*, The Press Syndicate of the University of Cambridge.

SHOCKWAVE THERAPY-BC. *General Information About Extracorporeal Shock Wave Therapy* [Online], Available: http://www.shockwavetherapy.ca/about_eswt.htm [Access 4 May 2012].

SILVERMAN, M., SILVERMAN, S., SILVERMAN, R. 2004. *Root Canal Treatment* [Online]. Silverman Family Dentistry. Available: http://www.silvermandental.com/new_site/pages/rootcanal.asp [Accessed 30 July 2009].

SINGLA, M., AGGARWAL, V., LOGANI, A. & SHAH, N. 2010. Comparative evaluation of rotary ProTaper, Profile, and conventional stepback technique on reduction in Enterococcus faecalis colony-forming units and vertical root fracture resistance of root canals. *Oral Surgery Oral Medicine Oral Pathology Oral Radiology and Endodontology,* 109**,** E105-E110.

SIVAKUMAR, M. & PANDIT, A. B. 2001. Ultrasound enhanced degradation of Rhodamine B: optimization with power density. *Ultrasonics Sonochemistry,* 8**,** 233-240.

SKINNER, S. 1904. *Philosophical Magazine,* 7**,** 329.

SOSTARIC, J. Z. & RIESZ, P. 2001. Sonochemistry of Surfactants in Aqueous Solutions: An EPR Spin-Trapping Study. *Journal of the American Chemical Society,* 123**,** 11010-11019.

SPENCER, H. R., IKE, V. & BRENNAN, P. A. 2007. Review: the use of sodium hypochlorite in endodontics - potential complications and their management. *Br Dent J,* 202**,** 555-559.

STEFANESCU, M.F. 2010. Ultrasounds Applications in Process Equipment. *Revista de Chimie,* 2**,** 113-117.

SURI, J. S., CHANG, R.-F. & KATHURIA, C. 2008. *Advances in Diagnostic and Therapeutic Ultrasound Imaging*, Artech House Publishers.

SUSLICK, K. S. 1990. Sonochemistry. *Science,* 247**,** 1439-1445.

SUSLICK, K. S., FANG, M. M., HYEON, T. & MDLELENI, M. M. 1999. Applications of sonochemistry to material synthesis. *In:* CRUM, L. A., MASON, T. J., REISSE, J. L. & SUSLICK, K. S. (eds.) *Sonochemistry and Sonoluminescence.* Kluwer Academic Publishers.

SUSLICK, K. S., GAWIENOWSKI, J. J., SCHUBERT, P. F. & WANG, H. H. 1983. Alkane sonochemistry. *The Journal of Physical Chemistry,* 87**,** 2299-2301.

SUSLICK, K. S., MDLELENI, M. M. & RIES, J. T. 1997. Chemistry Induced by Hydrodynamic Cavitation. *Journal of the American Chemical Society,* 119**,** 9303-9304.

TICHÝ, J., ERHART, J., KITTINGER, E. & PRÍVRATSKÁ, J. 2010. *Fundamentals of Piezoelectric Sensorics: Mechanical, Dielectric, and Thermodynamical Properties of Piezoelectric Materials* Springer.

TSOCHATZIDIS, N. A., GUIRAUD, P., WILHELM, A. M. & DELMAS, H. 2001. Determination of velocity, size and concentration of ultrasonic cavitation bubbles by the phase-Doppler technique. *Chemical Engineering Science,* 56**,** 1831-1840.

VAN DER SLUIS, L. W. M., VERSLUIS, M., WU, M. K. & WESSELINK, P. R. 2007a. Passive ultrasonic irrigation of the root canal: a review of the literature. *International Endodontic Journal,* 40**,** 415-426.

VAN DER SLUIS, L. W. M., WU, M. K. & WESSELINK, P. R. 2007b. The evaluation of removal of calcium hydroxide paste from an artificial standardized groove in the apical root canal using different irrigation methodologies. *International Endodontic Journal,* 40**,** 52-57.

VANHILLE, C., CAMPOS-POZUELO, C. & CONDE, C. 2004. A composed computational model applied to high amplitude ultrasonic resonators. *Acta Acustica United with Acustica,* 90**,** 376-379.

VIAN, C. J. B., BIRKIN, P. R. & LEIGHTON, T. C. 2010. Cluster Collapse in a Cylindrical Cell: Correlating Multibubble Sonoluminescence, Acoustic Pressure, and Erosion. *Journal of Physical Chemistry C,* 114**,** 16416-16425.

VIJAYKUMAR, S., GUNASHEKHAR, M. & HIMAGIRI, S. 2010. In vitro effectiveness of different endodontic irrigants on the reduction of Enterococcus faecalis in root canals. *Journal of Clinical and Experimental Dentistry,* 2**,** 169-172.

VINOTHKUMAR, T. S., KAVITHA, S., LAKSHMINARAYANAN, L., GOMATHI, N. S. & KUMAR, V. 2007. Influence of irrigating needle-tip designs in removing bacteria inoculated into instrumented root canals measured using single-tube luminometer. *Journal of Endodontics,* 33**,** 746-748.

VIVES, A. A. & ARNAU, A. 2004. *Piezoelectric Transducers and Applications*, Springer.

WALMSLEY, A. D. 1988. Applications of Ultrasound in Dentistry. *Ultrasound Medical Biology,* 14**,** 7-14.

WALMSLEY, A. D., LAIRD, W. R. E. & WILLIAMS, A. R. 1984. A model system to demonstrate the role of cavitational activity in ultrasonic scaling. *Journal of Dental Research,* 63**,** 1162-1165.

WALMSLEY, A. D., LAIRD, W. R. E. & WILLIAMS, A. R. 1988. Dental plaque removal by cavitational activity during ultrasonic scaling. *Journal of Clinical Periodontology,* 15**,** 539-543.

WALMSLEY, A. D. & WILLIAMS, A. R. 1989. Effects of constraint on the oscillatory pattern of endosonic files. *Journal of Endodontics,* 15**,** 189-194.

WAN, M.-W. 2006. *Development of a Portable, Modular Unit for the Optimization of Ultrasound-Assisted Oxidative Desulfurization of Diesel.* Thesis: Ph.D., University of Southern California.

WANG, C. T., CHOU, W. L., KUO, Y. M. & CHANG, F. L. 2009. Paired removal of color and COD from textile dyeing wastewater by simultaneous anodic and indirect cathodic oxidation. *Journal of Hazardous Materials,* 169**,** 16-22.

WEISSLER, A. 1959. Formation of Hydrogen Peroxide by Ultrasonic Waves: Free Radicals. *Journal of the American Chemical Society,* 81**,** 1077-1081.

WOHLFARTH, E. P. 1980. *Ferromagnetic Materials: A handbook on the properties of magnetically ordered substances*, Elsevier.

YOUNG, F. R. 1989. *Cavitation*, McGraw-Hill.

YOUNG, R. 2004. *Sonoluminescence*, CRC Press.

ZEHNDER, M. 2006. Root Canal Irrigants. *Journal of Endodontics,* 32**,** 389-398.

ZENG, Q.-F., FU, J., SHI, Y.-T. & ZHU, H.-L. 2009. Degradation of C.I. Disperse Blue 56 by Ultraviolet Radiation/Sodium Hypochlorite. *Ozone: Science & Engineering: The Journal of the International Ozone Association,* 31**,** 37 - 44.

ZEQIRI, B., GELAT, P. N., HODNETT, M. & LEE, N. D. 2003a. A novel sensor for monitoring acoustic cavitation. Part I: Concept, theory, and prototype development. *Ieee Transactions on Ultrasonics Ferroelectrics and Frequency Control,* 50**,** 1342-1350.

ZEQIRI, B., LEE, N. D., HODNETT, M. & GELAT, P. N. 2003b. A novel sensor for monitoring acoustic cavitation. Part II: Prototype performance evaluation. *Ieee Transactions on Ultrasonics Ferroelectrics and Frequency Control,* 50**,** 1351-1362.

ZINNER, D. D. 1955. Recent ultrasonic dental studies including periodontia without the use of an abrasive. *J. Dent. Res.,* 34**,** 748-749.

ZMENER, O., PAMEIJER, C. H. & BANEGAS, G. 2005. Effectiveness in cleaning oval-shaped root canals using Anatomic Endodontic Technology, ProFile and manual instrumentation: a scanning electron microscopic study. *International Endodontic Journal,* 38**,** 356-363.

8. Appendices

I) Definitions of Terms Used

Blake's nucleation threshold pressure, P_B (Atchley *et al.*, 1988):

$$P_B = p_o + 0.77\,\frac{\sigma}{R_o} \qquad \textbf{(Equation 10)}$$

when the surface tension dominates $\left(\frac{2\sigma}{R_o} >> p_o\right)$ and addition vapour pressure is neglected.

where,

p_o : hydrostatic pressure

σ : surface tension of the liquid

R_o : initial bubble radius

The equation assumes the following conditions:

i) Bubble obeys the ideal gas law

ii) The amount of gas within the bubble remains constant (*i.e.* no diffusion)

iii) The vapour pressure inside the bubble is constant

iv) The bubble remains spherical

v) Viscosity, inertial and gravitational effects are insignificant

vi) All processes are isothermal

Reflective and Transmission coefficients for longitudinal waves at normal incidence:

Every material has acoustic impedance, *Z*, which is the product of its density and speed of sound. When sound travels from one medium to another at a normal incidence, the amount of sound power that gets reflected and transmitted depends strongly on the acoustic impedances of the two medium (Blackstock, 2000), and can be summarised as:

$$R = \frac{Z_2 - Z_1}{Z_2 + Z_1} \qquad \textbf{\textit{(Equation 11)}}$$

and

$$T = \frac{2Z_2}{(Z_2 + Z_1)} \qquad \textbf{\textit{(Equation 12)}}$$

where Z_1 and Z_2 are the acoustic impedances of material where sound wave propagates from and travelling into.

For materials with similar acoustic impedances, such as water and silicone rubber, $R = 0$ and $T = 1$; where sound is totally transmitted from medium 1 to medium 2. On the other hand, when sound travels from water (Z = 1.5 MRayl) to Pyrex glass (Z = 13.1 MRayl), part of the sound waves gets reflected (R = 0.63) and partly gets transmitted.

For the case of air | water interface, air has much lower acoustic impedance (Z = 411.6 Rayl); all sound wave that passes through liquid into air gets reflected (R = -0.999) and little/none gets transmitted over (Blackstock, 2000).

Boundary conditions:

i) Hard wall boundary:

When a sound wave hits a rigid wall (*i.e.* $Z_2 >> Z_1$), particle velocity totally vanishes at the boundary ($u = 0$). This results in no flux difference between the two medium, hence $\delta p/\delta n = 0$, where p is the pressure incident to a plane normal to it (n). This yields $R = 1$ (from Equation 11), where the sound wave gets totally reflected in the same direction as the incident signal (Blackstock, 2000).

ii) Soft wall boundary:

When a sound wave travels from a hard medium to an infinitely soft medium (*i.e.* $Z_2 << Z_1$), then, from Equations 11 and 12, $T = 0$ and $R = -1$. Similar to the previous condition for rigid walls, this will have no transmission into the next medium, but the reflection of the sound wave will be in an opposite direction to the incident wave. To achieve this, at the interface of the two boundaries, the resulting pressure, p will be equal to zero as the two waves (incident and reflection waves) cancel each other out.

Standing wave:

It is a wave that remains in a constant position, which is formed due to two identical travelling waves travelling in opposite directions superimposed to one another (Leighton, 1994). This is caused by impedance mismatch between the two mediums (where the wave becomes highly reflective) and there is no net flow of energy.

For the case of a dental endosonic file immersed in water, the sound wave travels from the dental file (made of stainless steel, Z = 45.7 MRayl) into water (Z = 1.5 MRayl). Given these two impedances, the reflective coefficient (Based on Equation 11) gives R = 0.88, which is a high reflector. Due to this, most of the sound wave that travels along the dental endosonic file gets reflected back at half a period later, resulting in the formation of a standing wave (Figure 8.1).

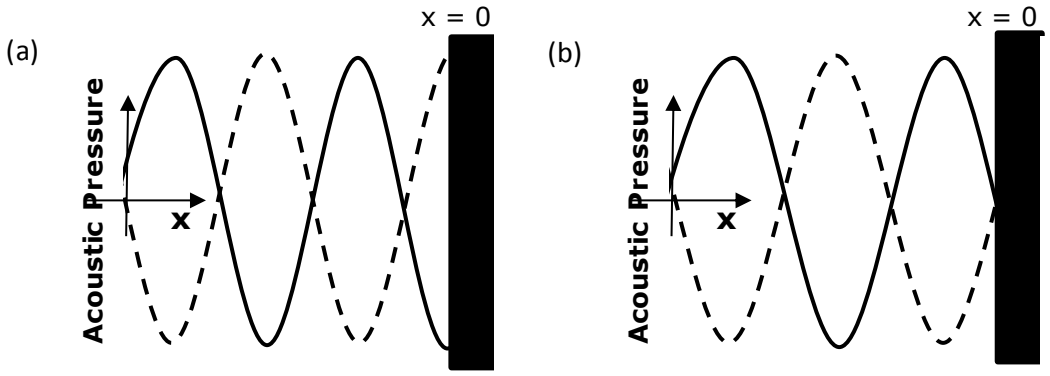

Figure 8.1: *A standing wave system along the x-axis, formed by (a) reflection of a pressure wave from a rigid boundary; (b) reflection of a pressure wave from a free boundary. (Solid line represents the parameter at the start of the period, dotted line is the situation half a period later.)*

Image reproduced from The Acoustic Bubble (Leighton, 1994).

II) Vibration displacement profiles of dental files

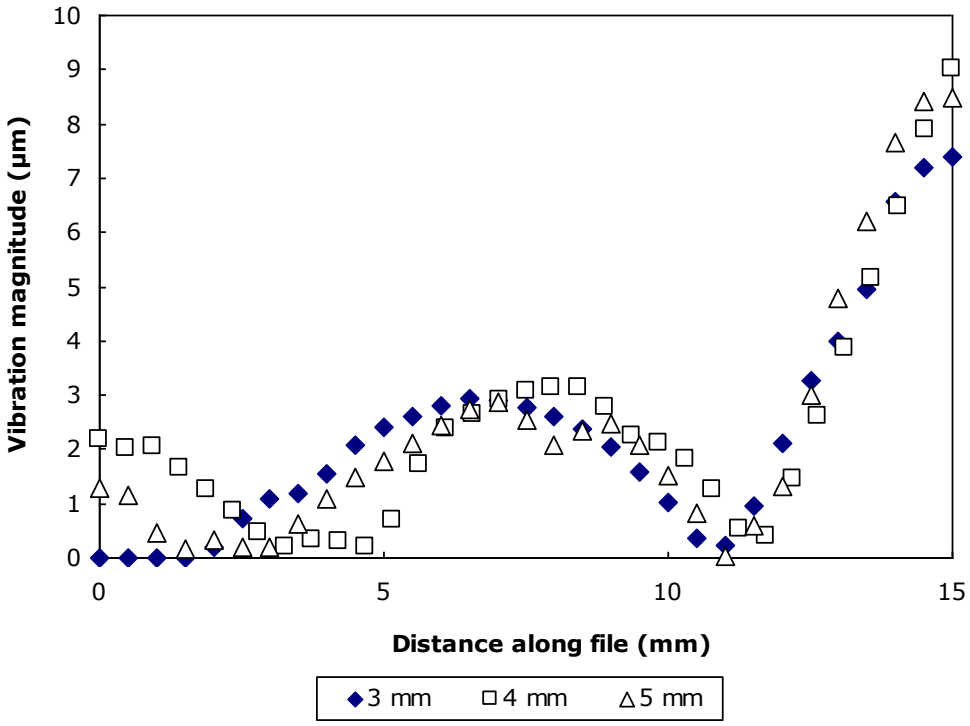

Figure 8.2: *Vibration displacement profile for CKT-1 at Power 1/10 in a confined space of different channel widths.*

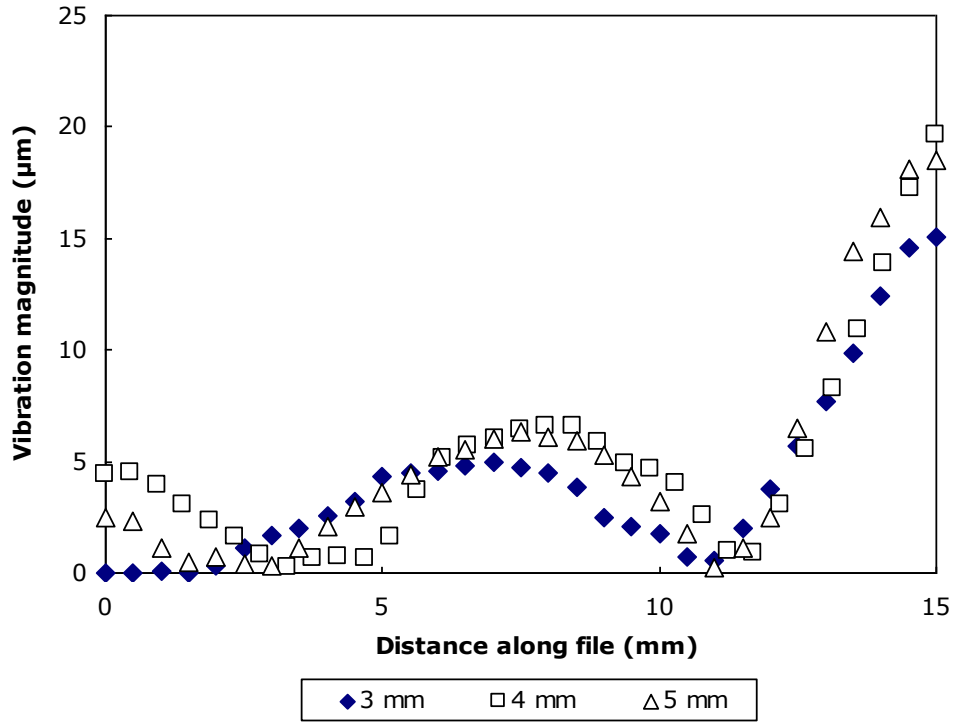

Figure 8.3: *Vibration displacement profile of CKT-1 at Power 5/10 in a confined space of different channel widths.*

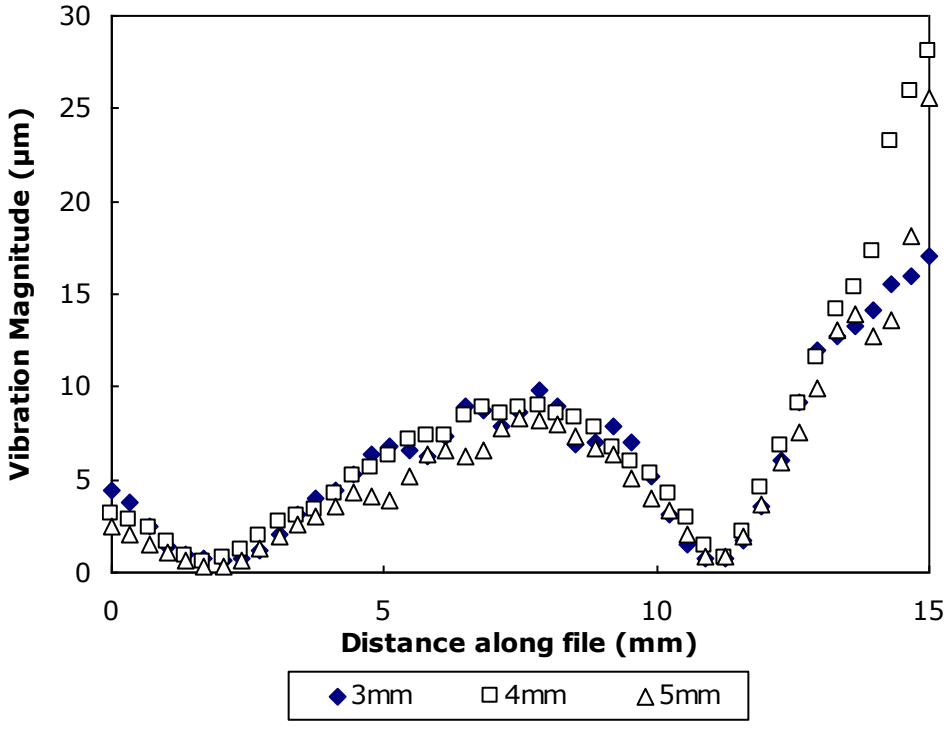

Figure 8.4: *Vibration displacement profile of CKT-1 at Power 10/10 in a confined space of different channel widths.*

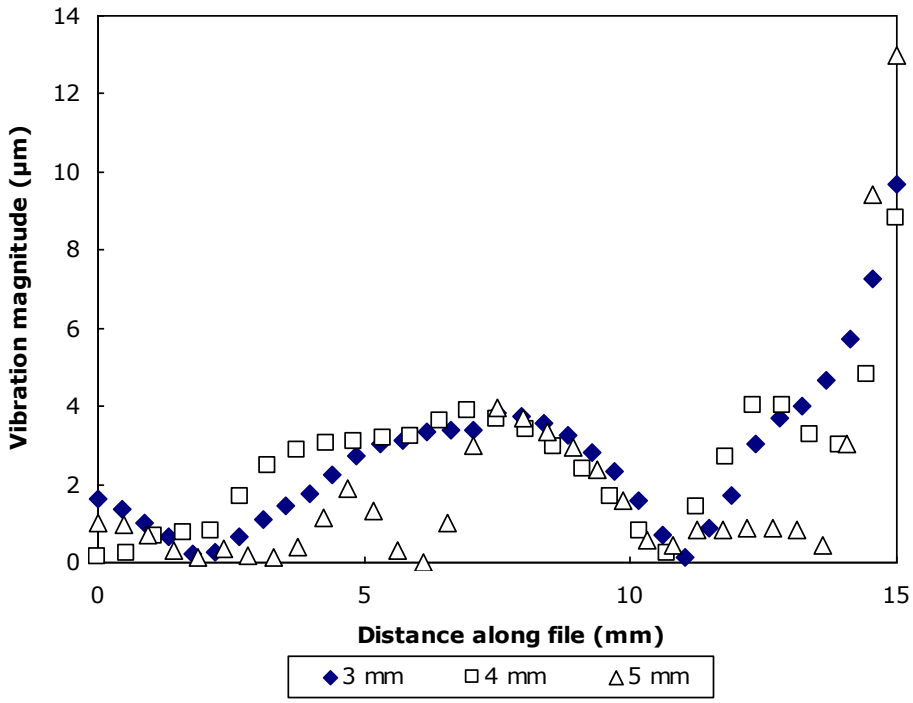

Figure 8.5: *Vibration displacement profile of CT-4 at Power 1/10 in a confined space of different channel widths.*

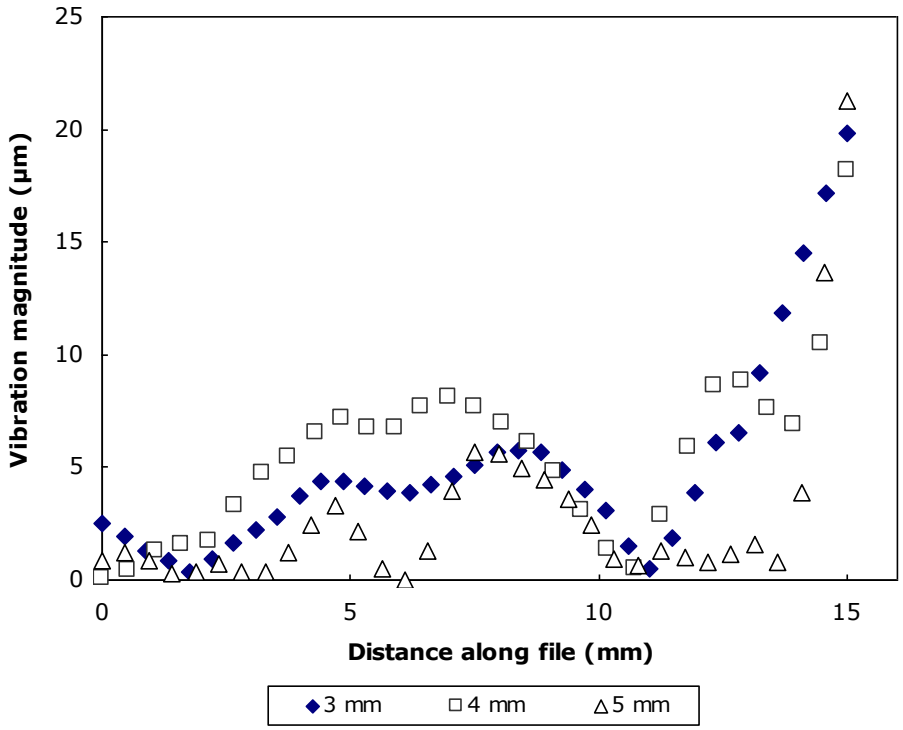

Figure 8.6: *Vibration displacement profile of CT-4 at Power 5/10 in a confined space of different channel widths.*

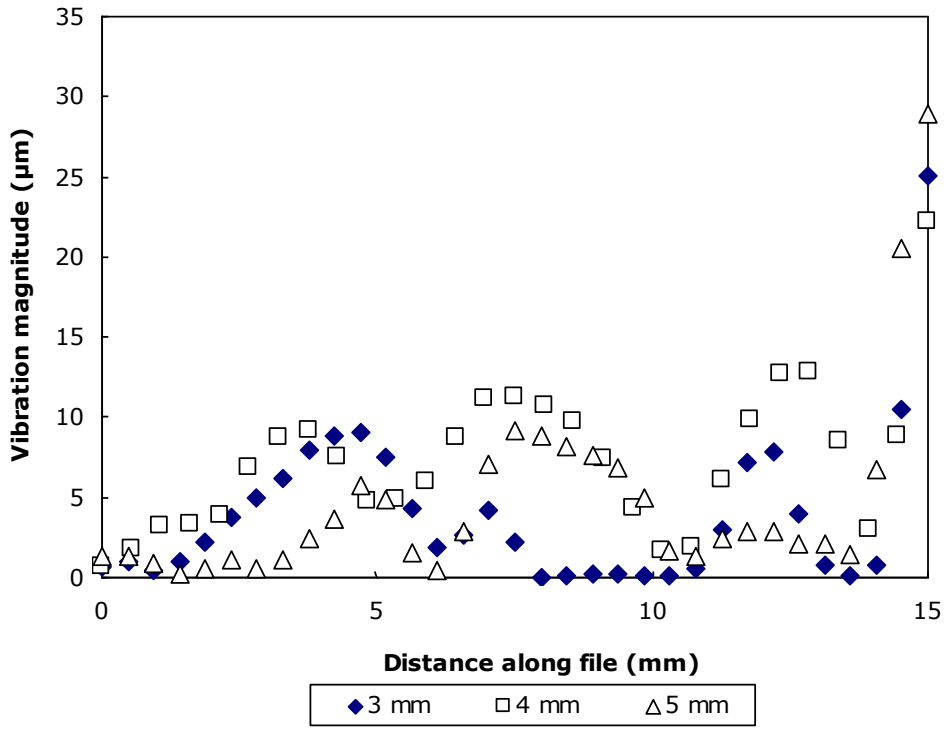

Figure 8.7: *Vibration displacement profile of CT-4 at Power 10/10 in a confined space of different channel widths.*

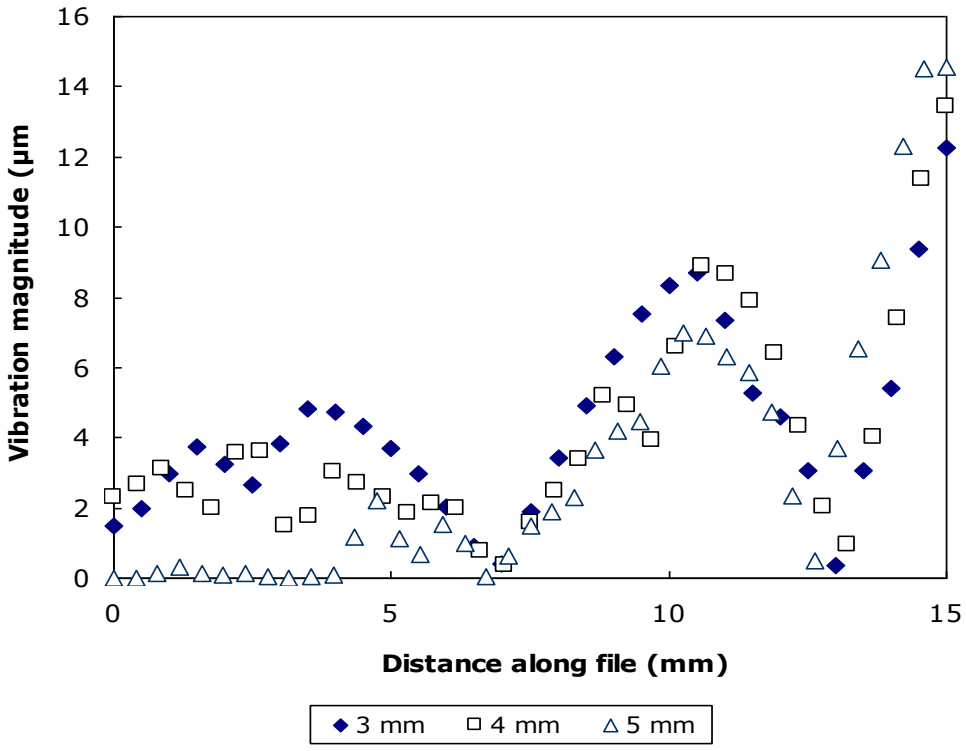

Figure 8.8: *Vibration displacement profile of UT-4(2) at Power 1/10 in a confined space of different channel widths.*

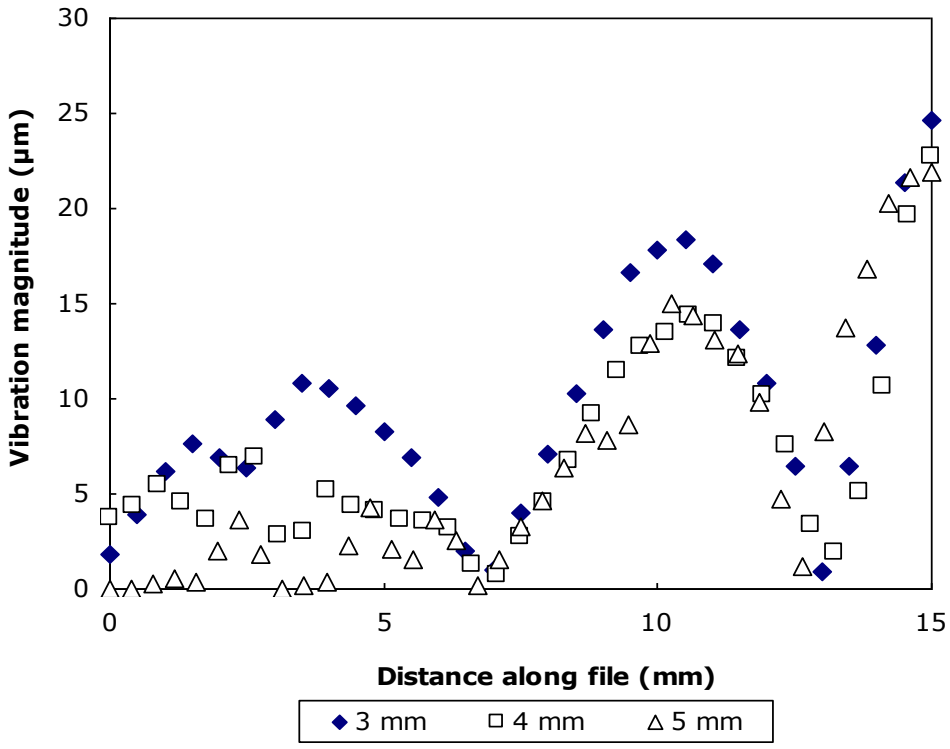

Figure 8.9: *Vibration displacement profile of UT-4(2) at Power 5/10 in a confined space of different channel widths.*

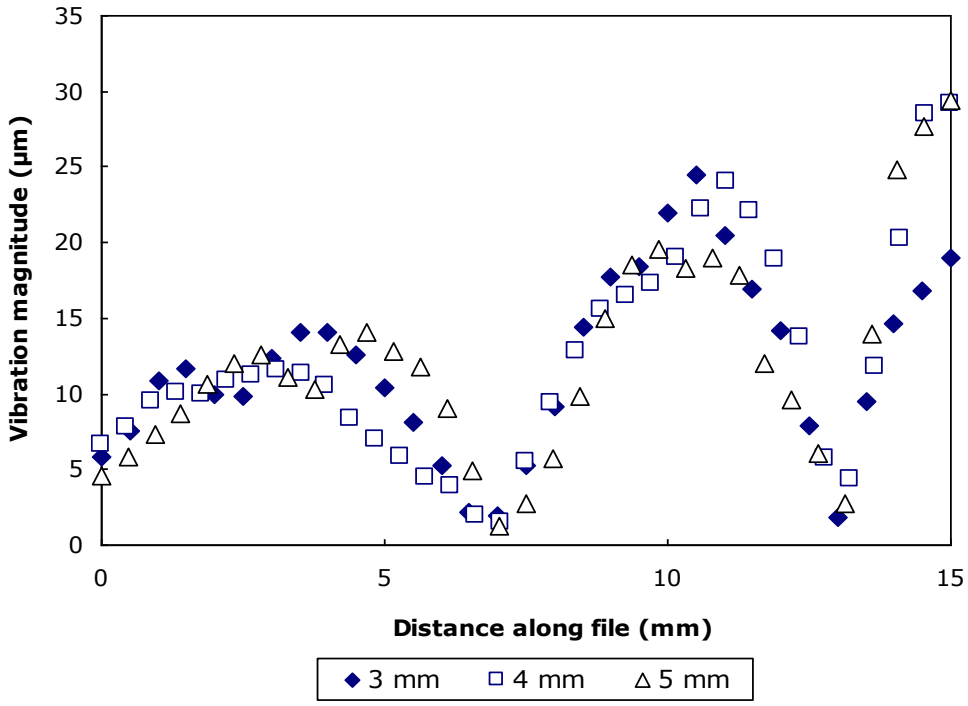

Figure 8.10: *Vibration displacement profile of UT-4(2) at Power 10/10 in a confined space of different channel widths.*

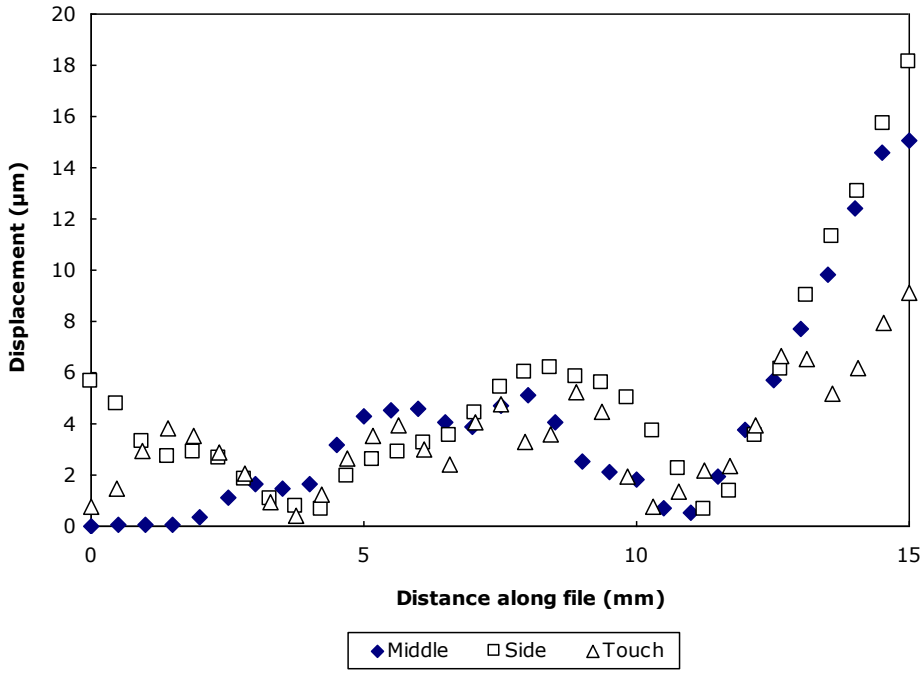

Figure 8.11: *Vibration displacement profile of CKT-1 at Power 5/10 in a confined space at different positions.*

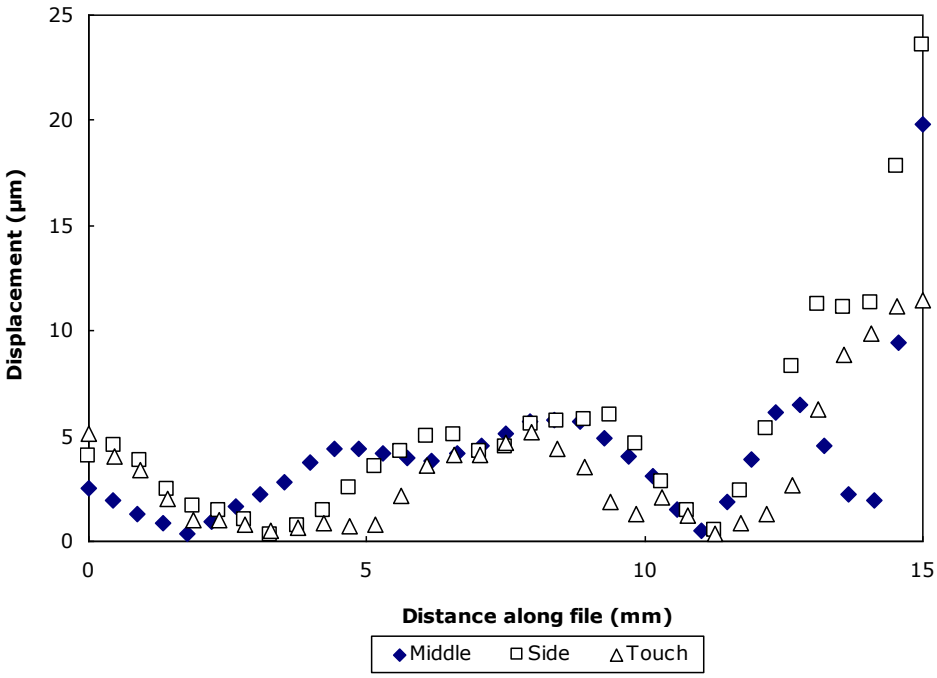

Figure 8.12: *Vibration displacement profile of CT-4 at Power 5/10 in a confined space at different positions.*

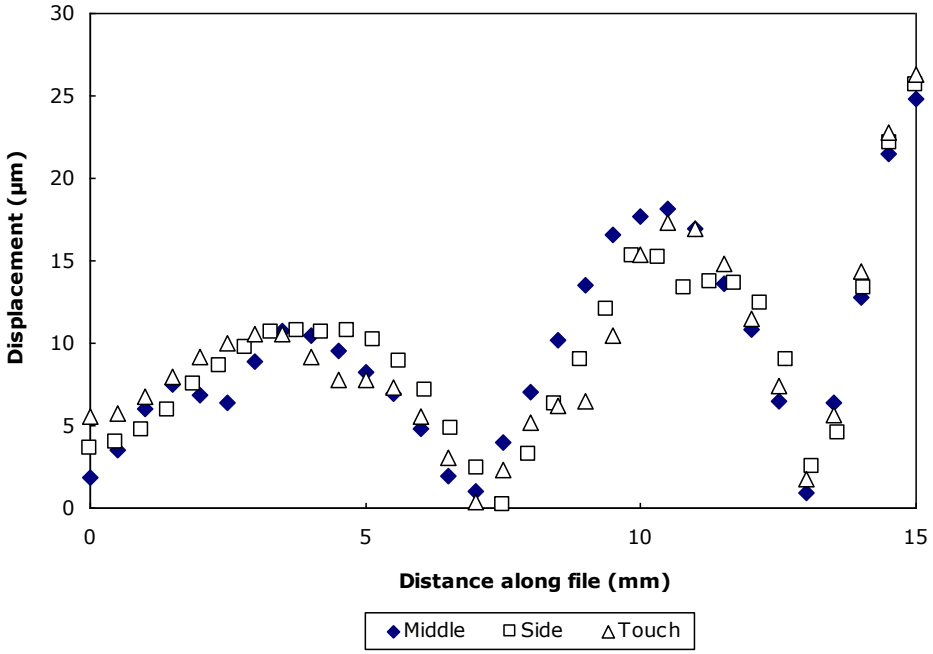

Figure 8.13: *Vibration displacement profile of UT-4(2) at Power 5/10 in a confined space at different positions.*

III) Sono(chemi)luminescence in a channel

Table 8.1: *Sono(chemi)luminescence in a 3-mm-wide channel upon sonication at Powers 1/10, 5/10 and 10/10 for CT-4, CKT-1 and UT-4(2) tips.*

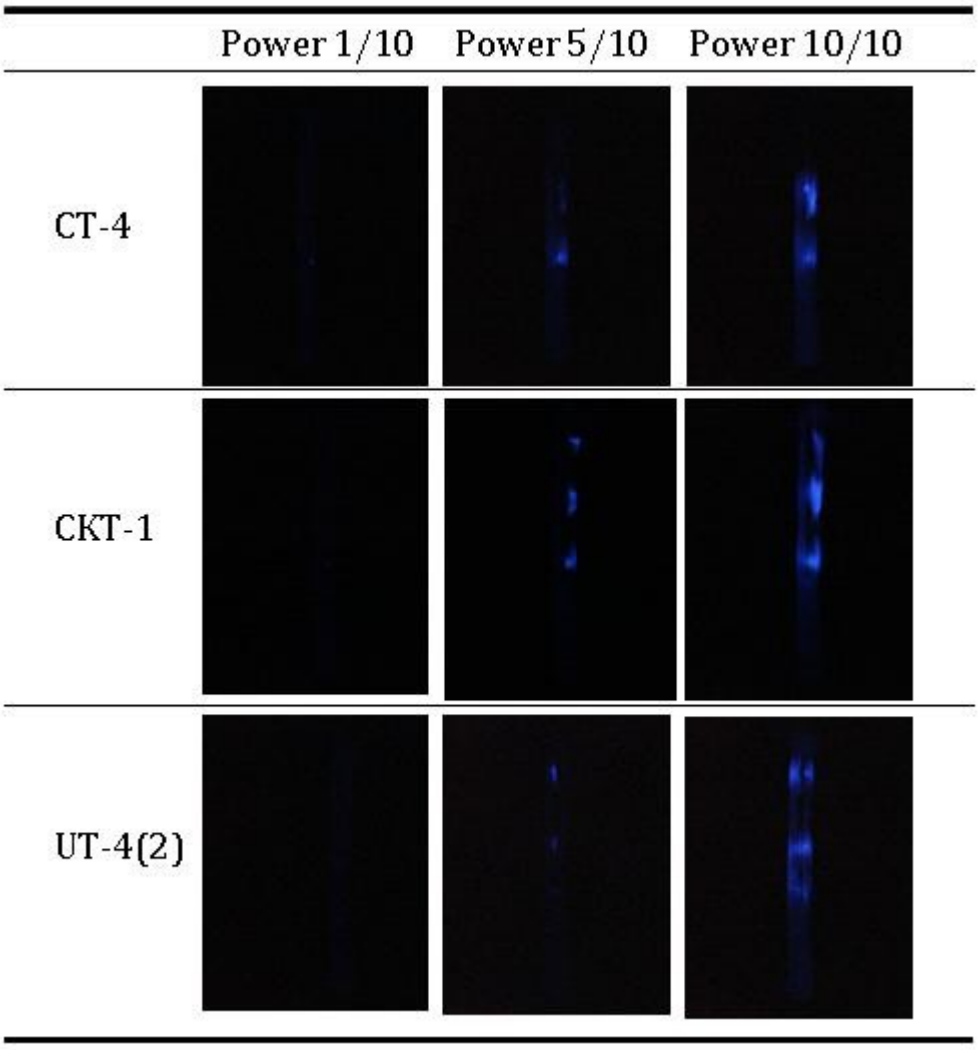

Table 8.2: *Sono(chemi)luminescence in a 4-mm-wide channel upon sonication at Powers 1/10, 5/10 and 10/10 for CT-4, CKT-1 and UT-4(2) tips.*

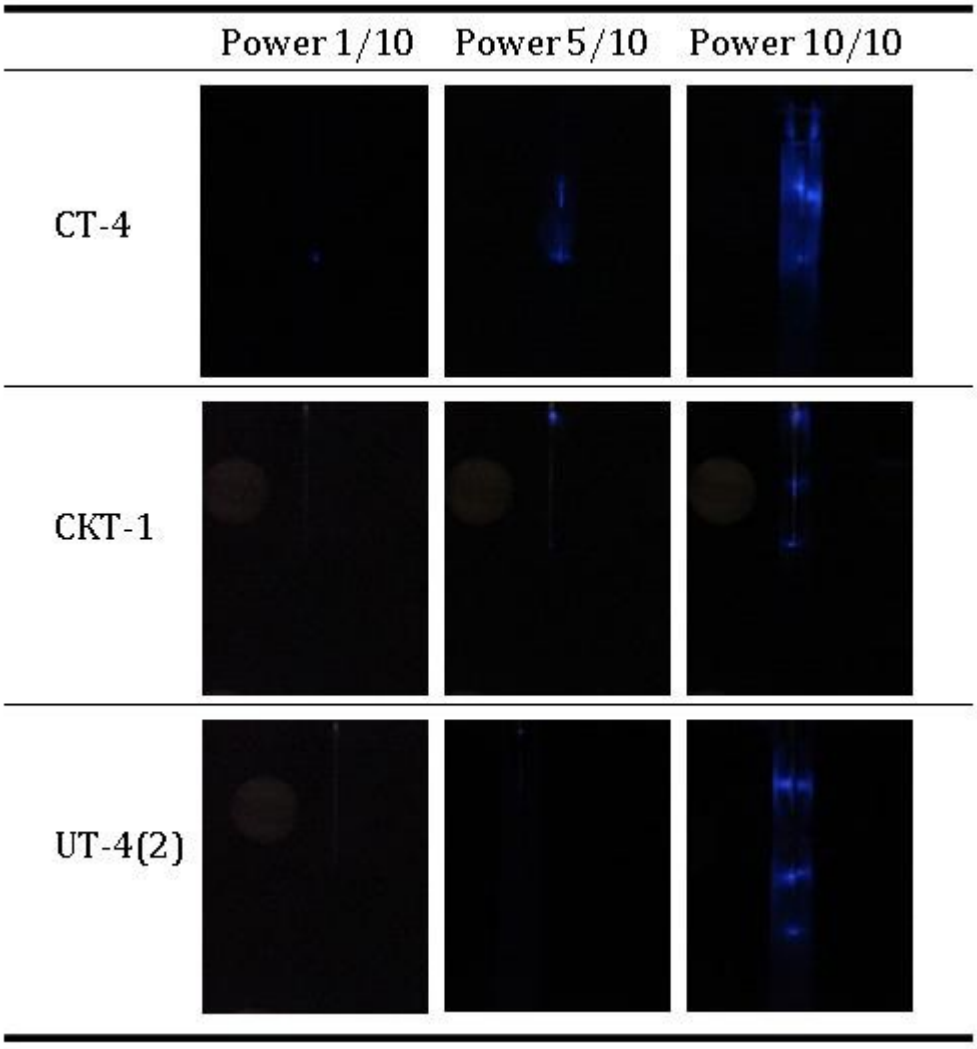

Table 8.3: *Sono(chemi)luminescence in a 5-mm-wide channel upon sonication at Powers 1/10, 5/10 and 10/10 for CT-4, CKT-1 and UT-4(2) tips.*

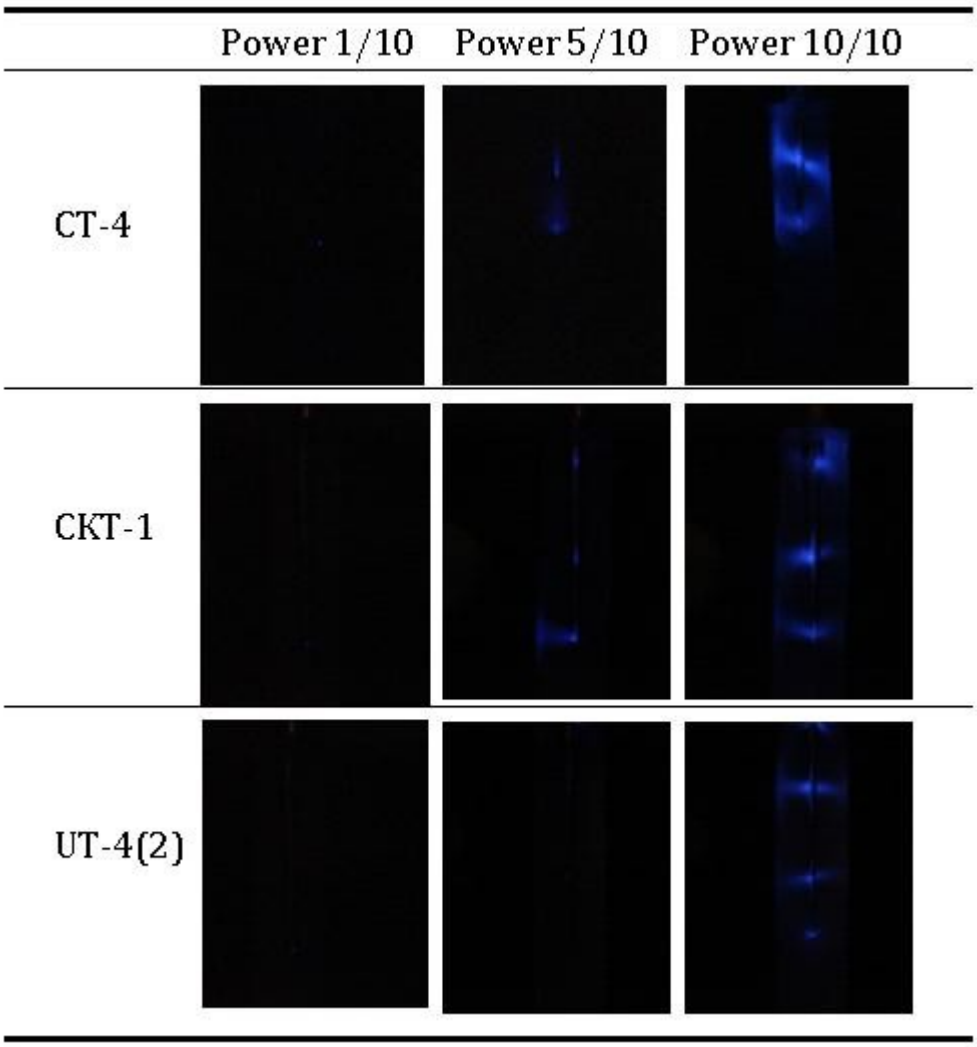

IV) Results on the Start-X Tips

Table 8.4: *Sono(chemi)luminescence images taken at various power settings for the Start-X tips used.*

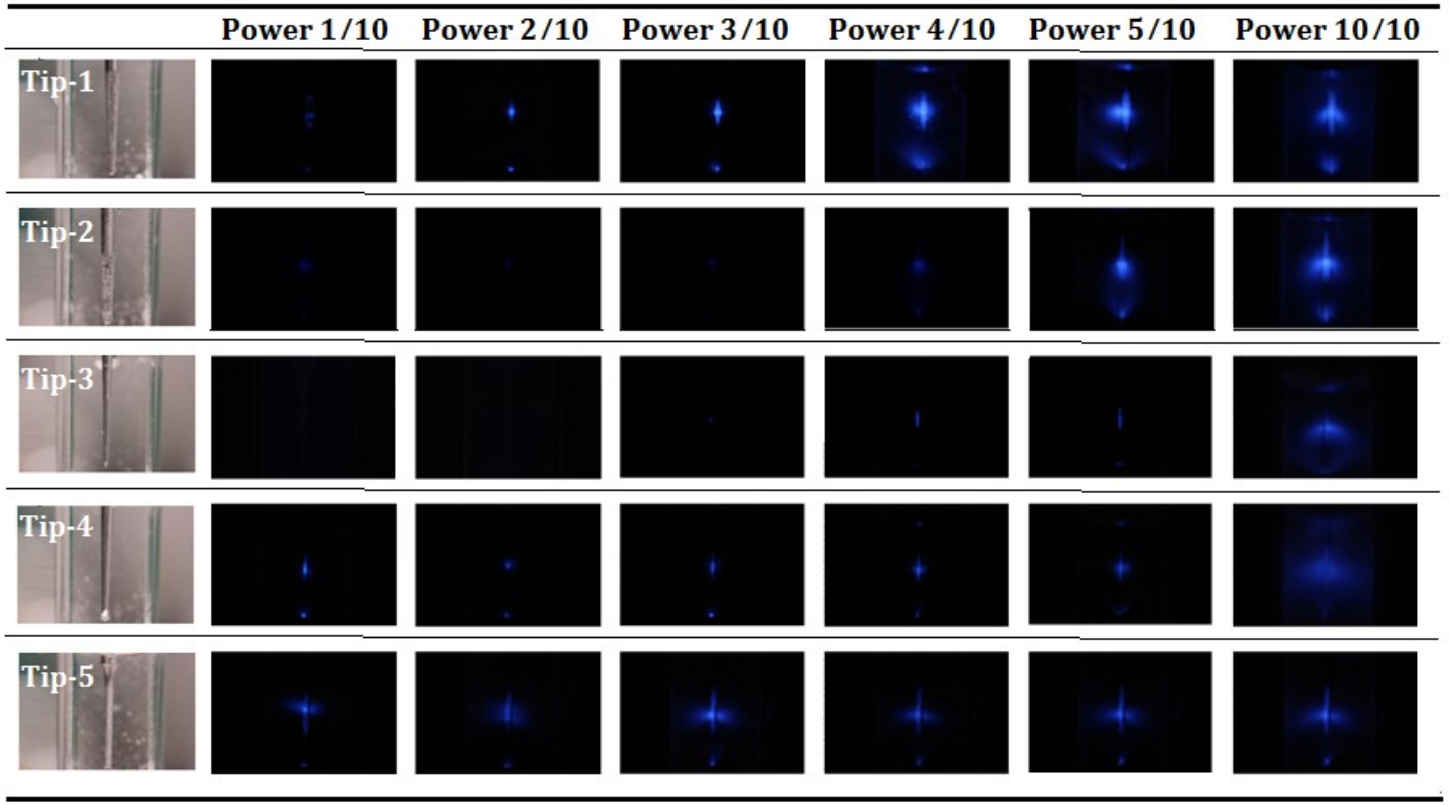

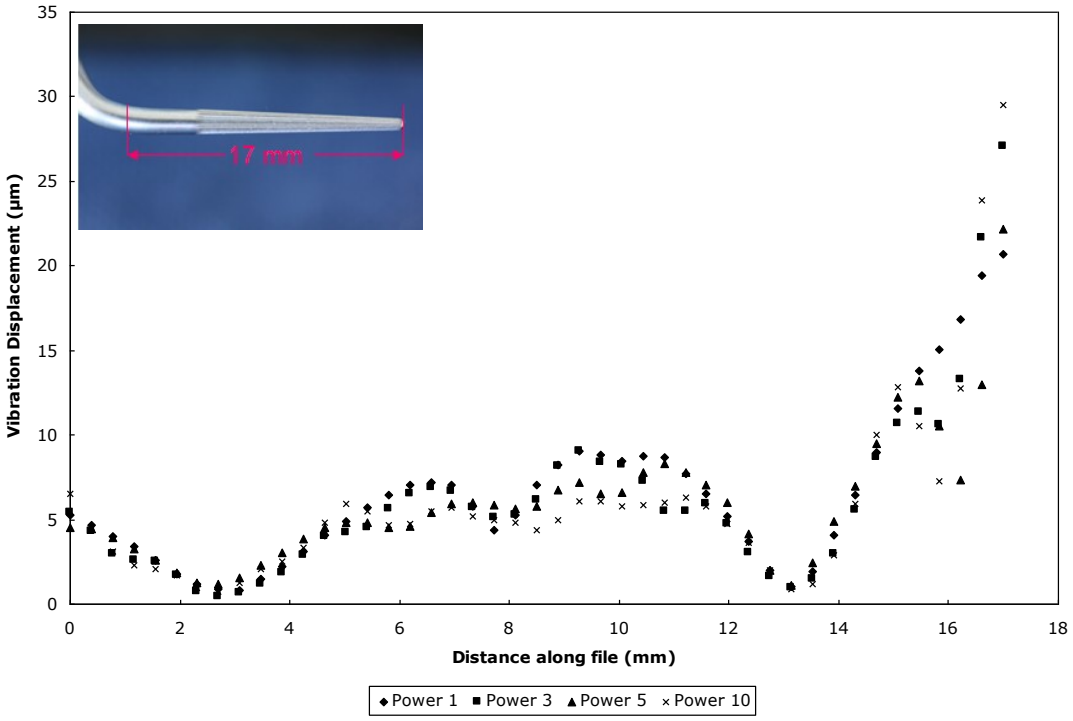

Figure 8.14: *Vibration profile along Tip-1 at Powers 1, 3, 5 and 10, with an inset image of Tip-1 indicating its working length.*

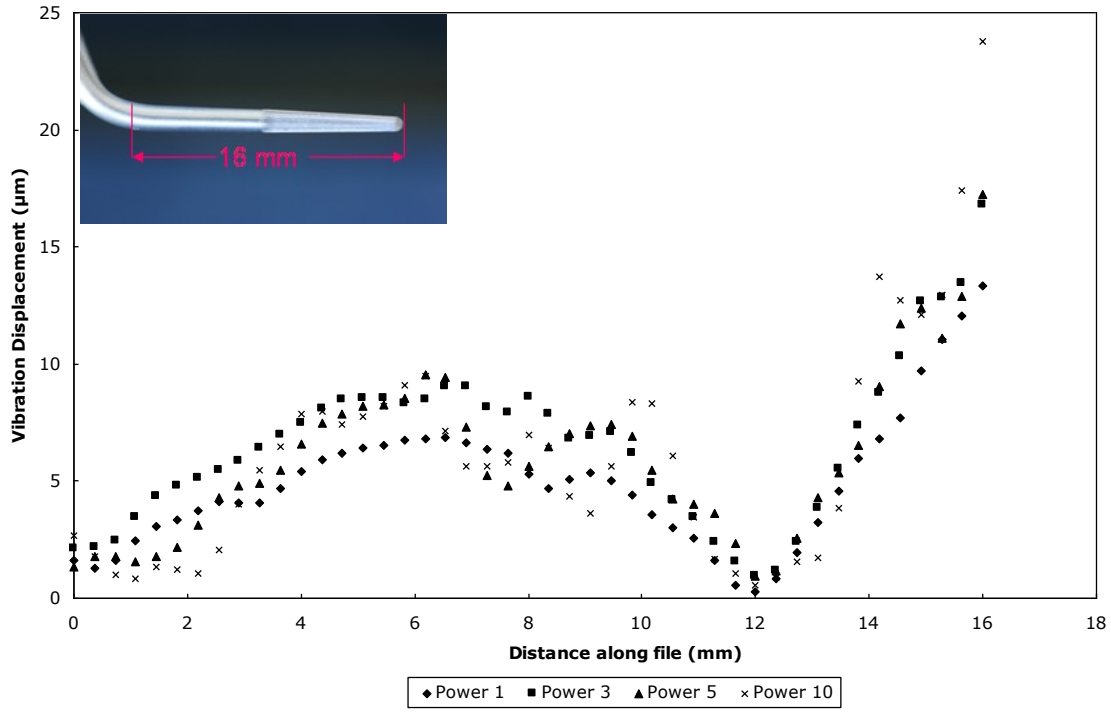

Figure 8.15: *Vibration profile along Tip-2 at Powers 1, 3, 5 and 10, with an inset image of Tip-2 indicating its working length.*

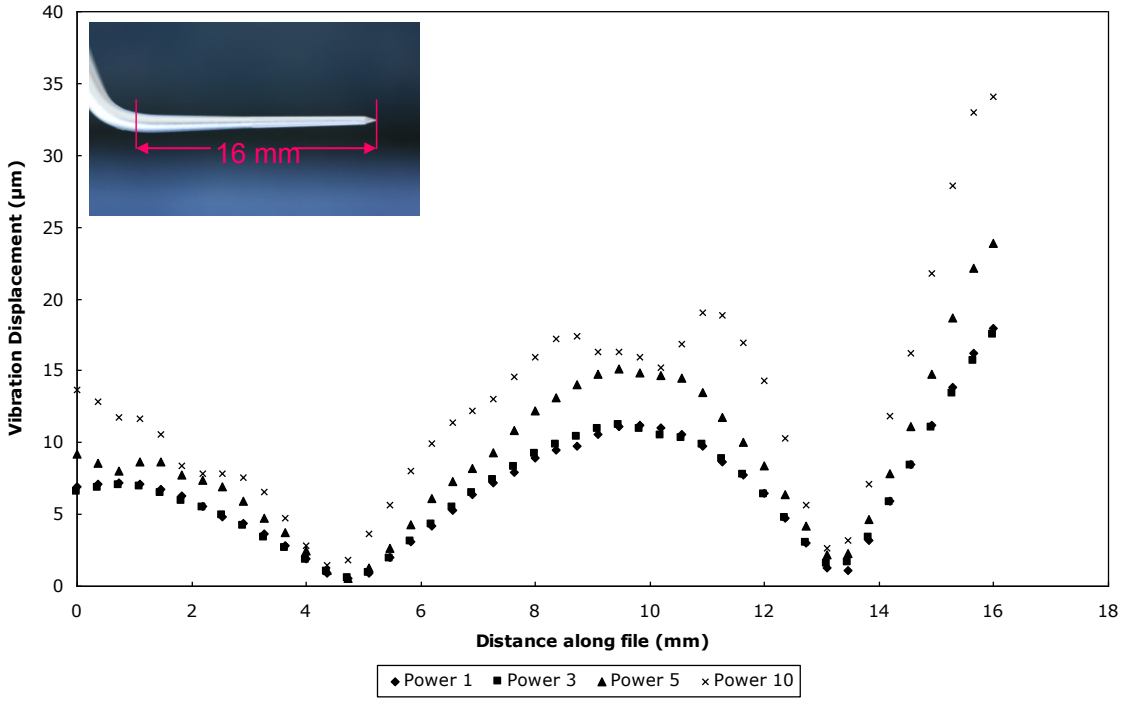

Figure 8.16: *Vibration profile along Tip-3 at Powers 1, 3, 5 and 10, with an inset image of Tip-3 indicating its working length.*

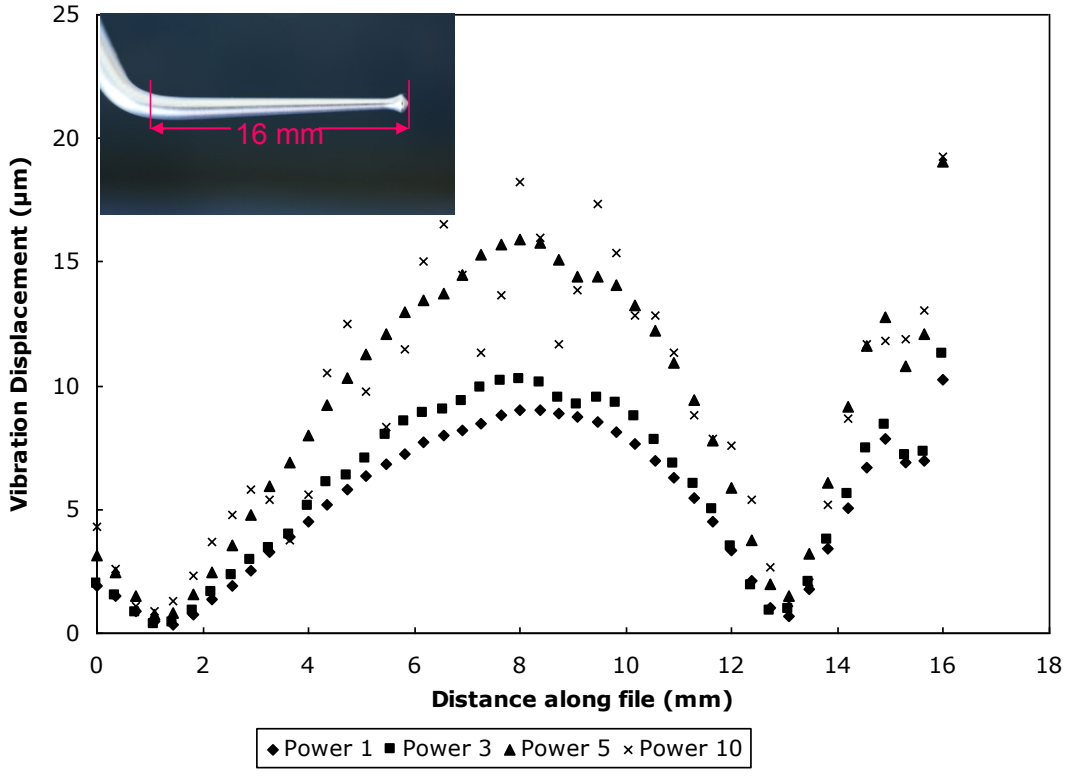

Figure 8.17: *Vibration profile along Tip-4 at Powers 1, 3, 5 and 10, with an inset image of Tip-4 indicating its working length.*

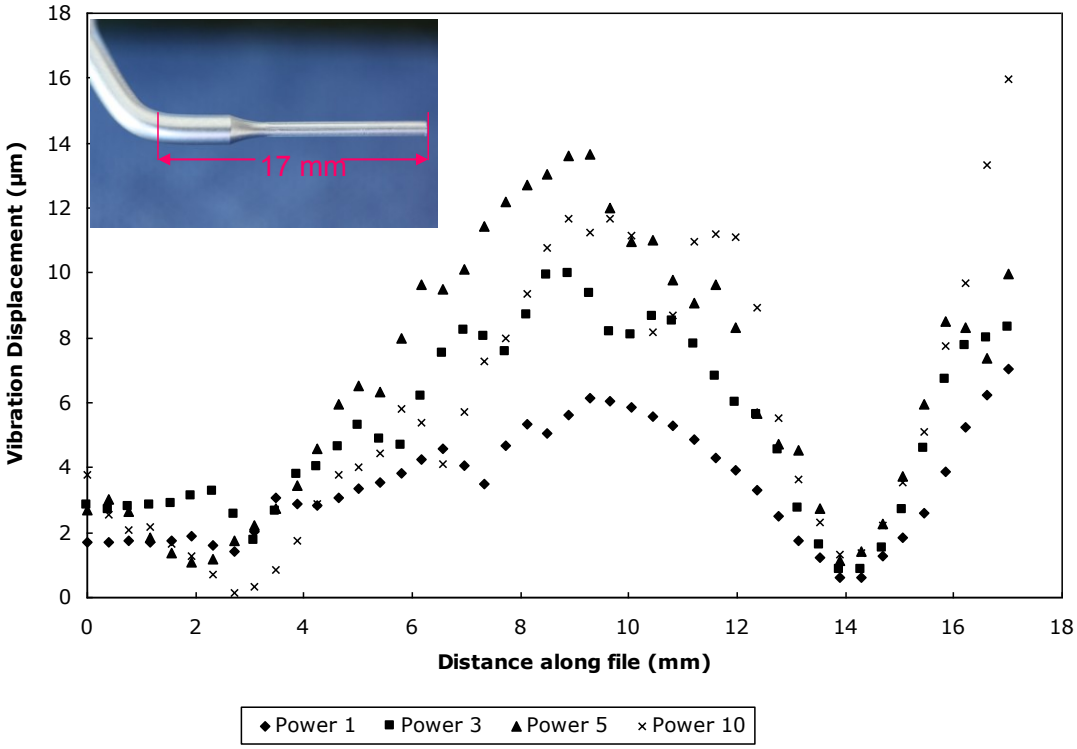

Figure 8.18: *Vibration profile along Tip-5 at powers 1, 3, 5 and 10, with an inset image of Tip-5 indicating its working length.*

V) 3-D Acoustic Pressure Field Prediction

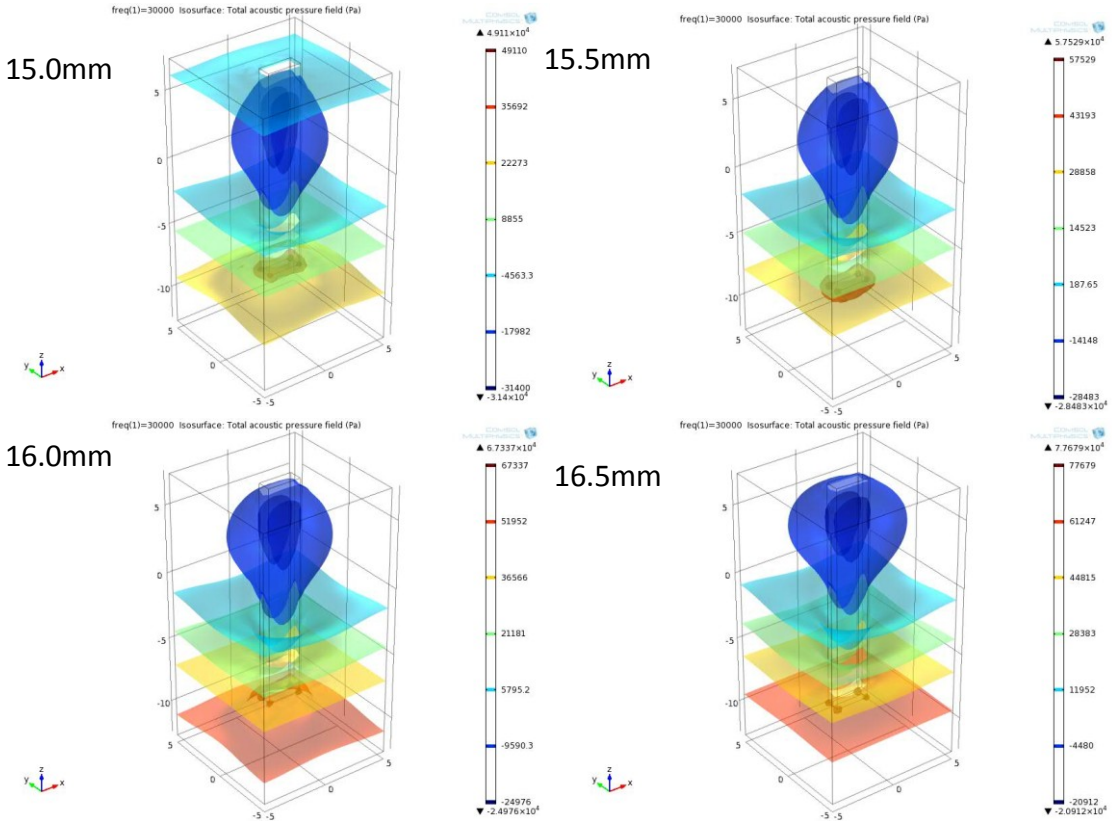

Figure 8.19: *Acoustic pressure isosurface plots for a rectangular slab model at pressure amplitude of 0.31 MPa, with a constant width of 2.5 mm and depth of 1.0 mm but varying length from 15 mm, 15.5 mm 16 mm to 16.5 mm.*

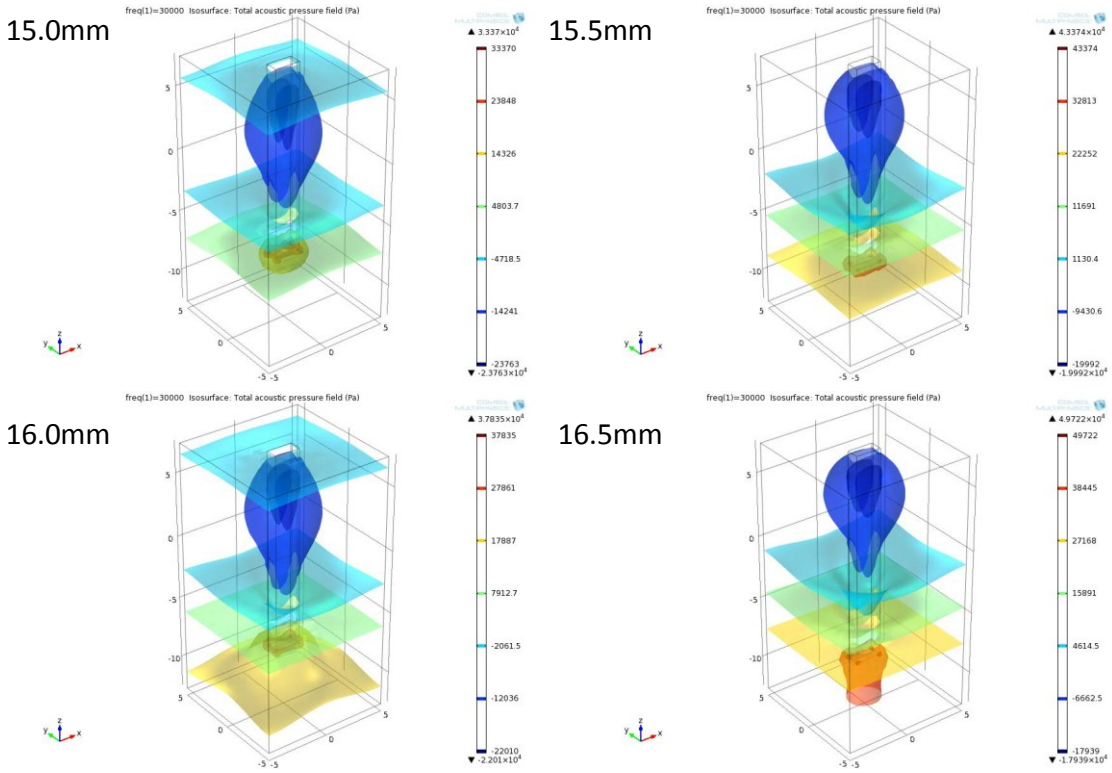

Figure 8.20: *Acoustic pressure isosurface plots for a rectangular slab model at pressure amplitude of 0.31 MPa, with a constant width of 2.0 mm and depth of 1.0 mm but varying length from 15 mm, 15.5 mm 16 mm to 16.5 mm.*

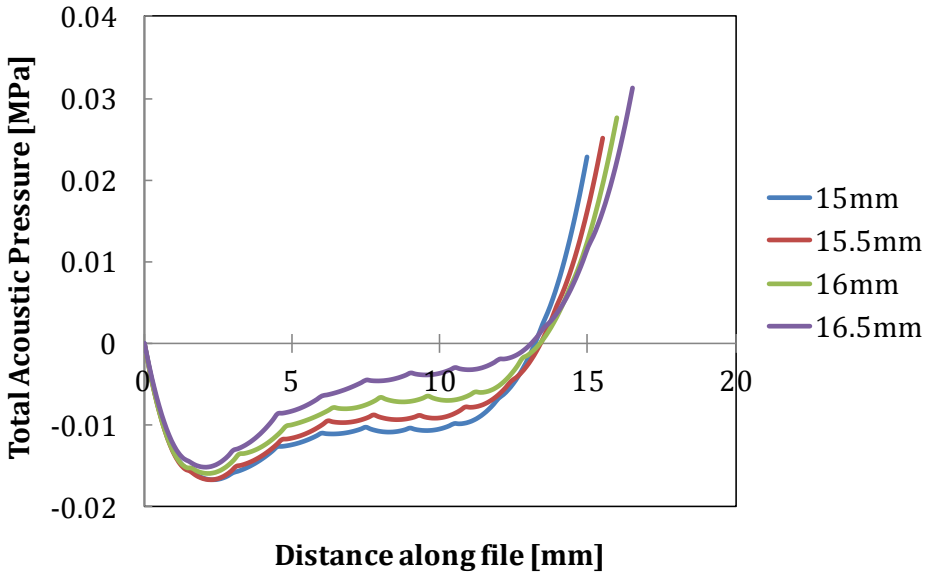

Figure 8.21: *Acoustic pressure plots for a rectangular slab model along the length of the model at pressure amplitude of 0.31 MPa, with a constant width of 2.0 mm and depth of 1.0mm but varying length from 15 mm, 15.5 mm 16 mm to 16.5 mm.*

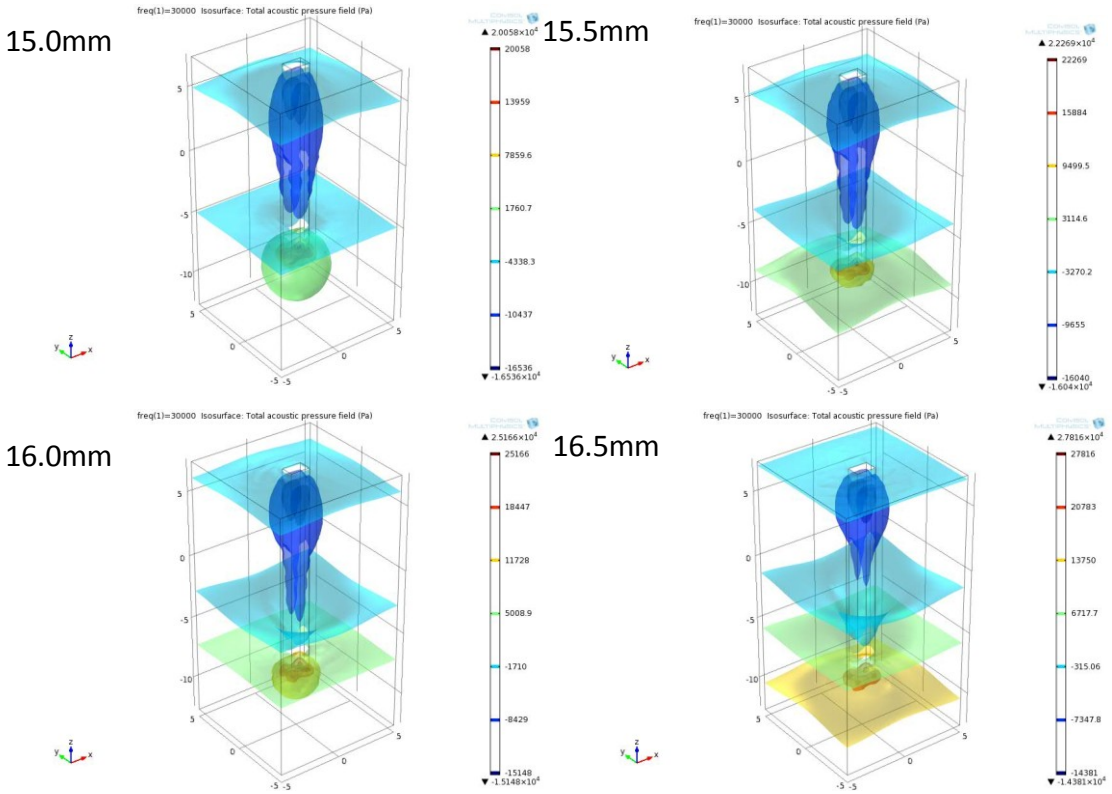

Figure 8.22: *Acoustic pressure isosurface plots for a rectangular slab model at pressure amplitude of 0.31 MPa, with a constant width of 1.5 mm and depth of 1.0 mm but varying length from 15 mm, 15.5 mm 16 mm to 16.5 mm.*

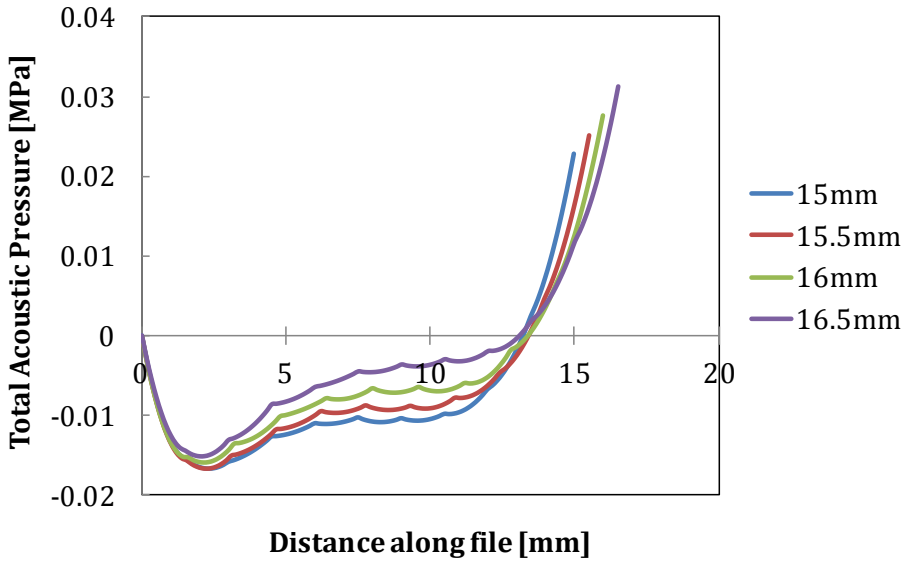

Figure 8.23: *Acoustic pressure plots for a rectangular slab model along the length of the model at pressure amplitude of 0.31 MPa, with a constant width of 1.5 mm and depth of 1.0mm but varying length from 15 mm, 15.5 mm 16 mm to 16.5 mm.*

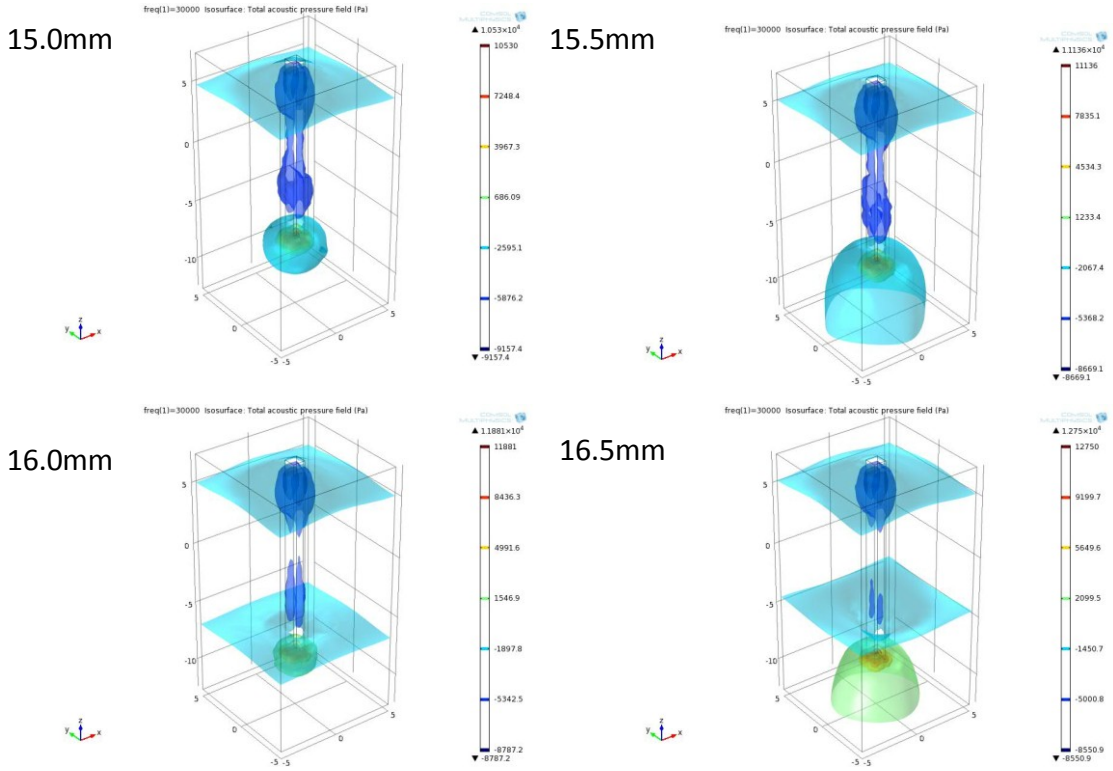

Figure 8.24: *Acoustic pressure isosurface plots for a rectangular slab model at pressure amplitude of 0.31 MPa, with a constant width of 1.0mm and depth of 1.0 mm but varying length from 15 mm, 15.5 mm 16 mm to 16.5 mm.*

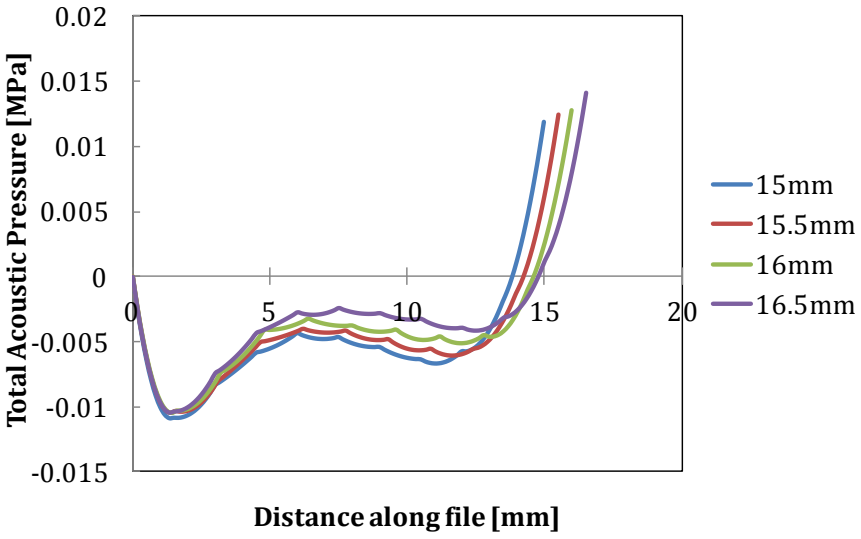

Figure 8.25: *Acoustic pressure plots for a rectangular slab model along the length of the model at pressure amplitude of 0.31 MPa, with a constant width of 1.0 mm and depth of 1.0mm but varying length from 15 mm, 15.5 mm 16 mm to 16.5 mm.*

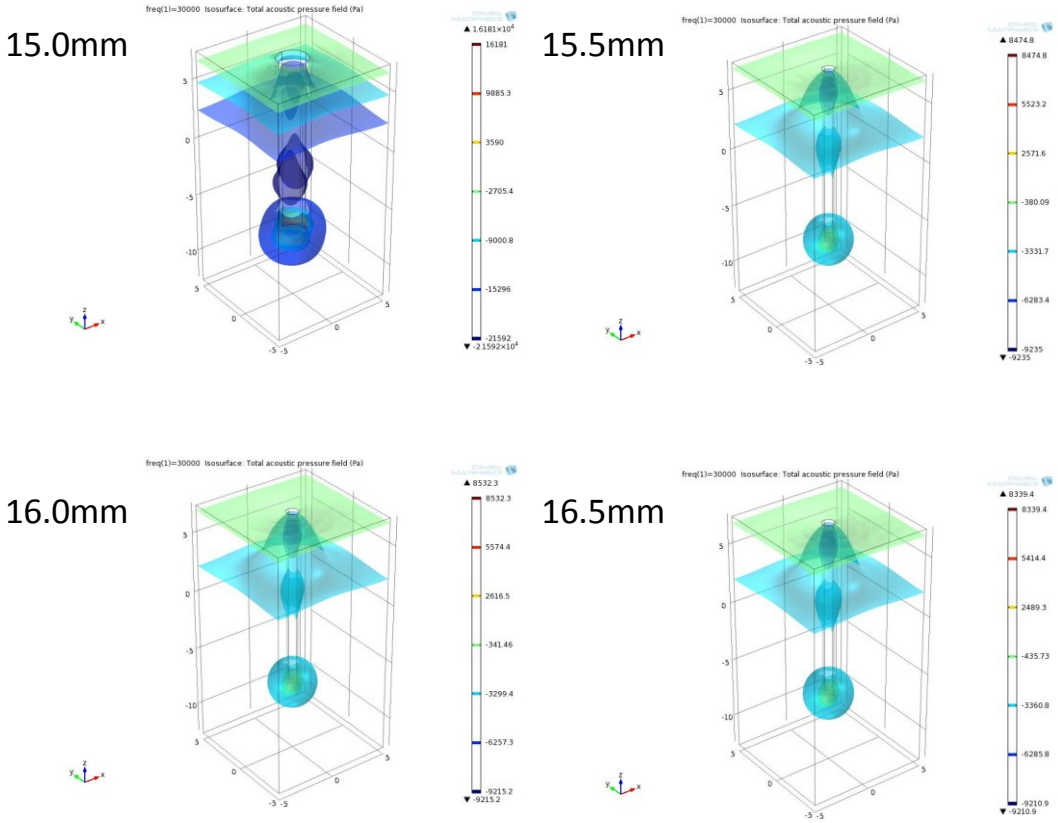

Figure 8.26: *Acoustic pressure isosurface plots for a cylindrical model at pressure amplitude of 0.31 MPa, with a constant diameter of 2.5 mm but varying length from 15 mm, 15.5 mm 16 mm to 16.5 mm.*

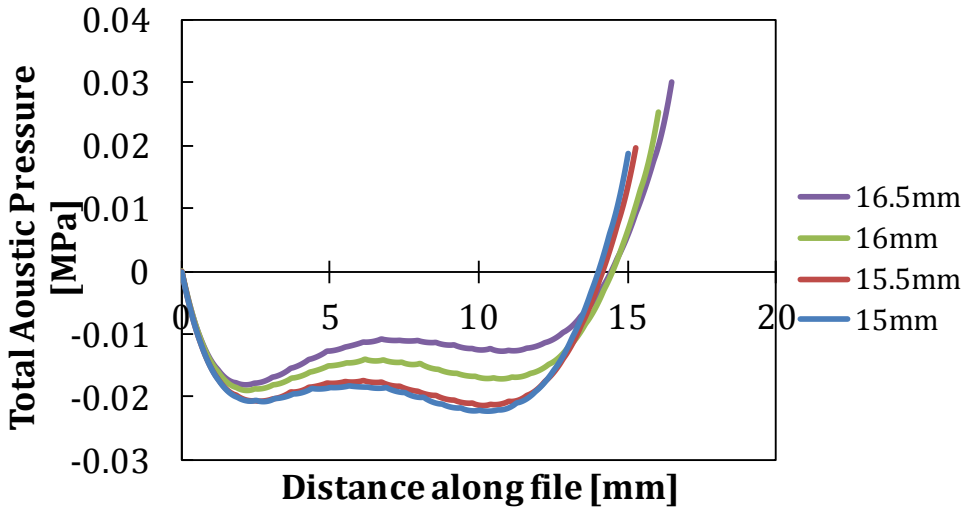

Figure 8.27: *Acoustic pressure plots for a cylindrical model along the length of the model at pressure amplitude of 0.31 MPa, with a constant diameter of 2.5 mm but varying length from 15 mm, 15.5 mm 16 mm to 16.5 mm.*

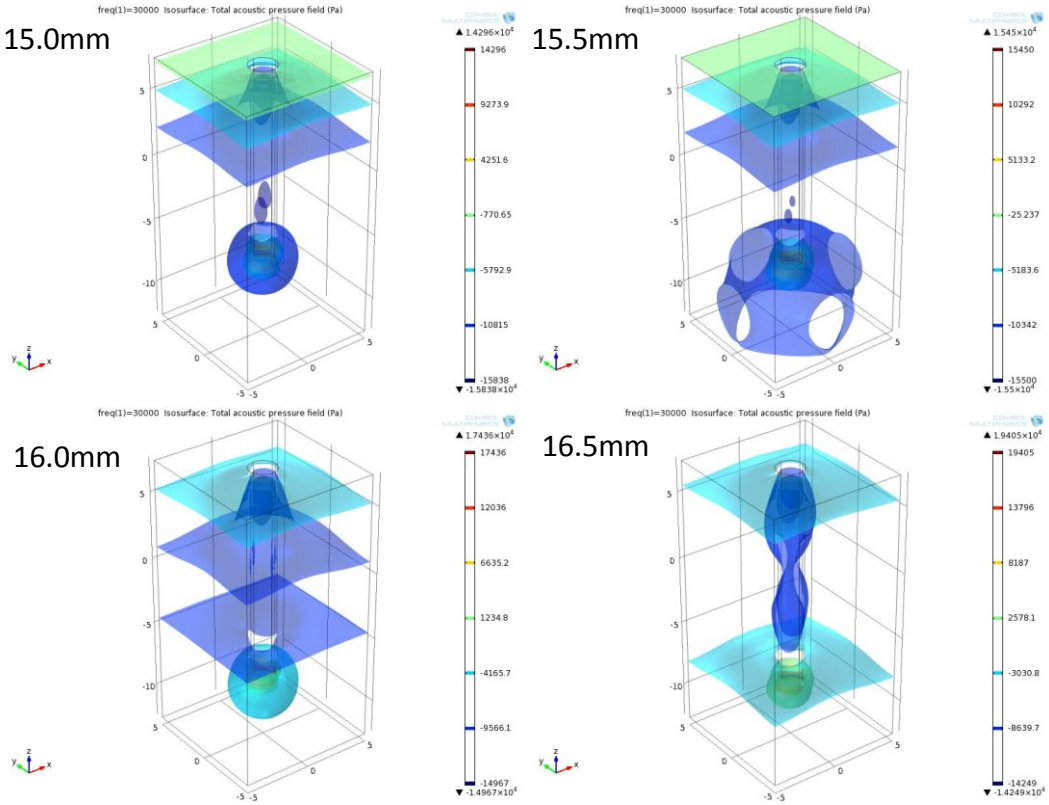

Figure 8.28: *Acoustic pressure isosurface plots for a cylindrical model at pressure amplitude of 0.31 MPa, with a constant diameter of 2.0 mm but varying length from 15 mm, 15.5 mm 16 mm to 16.5 mm.*

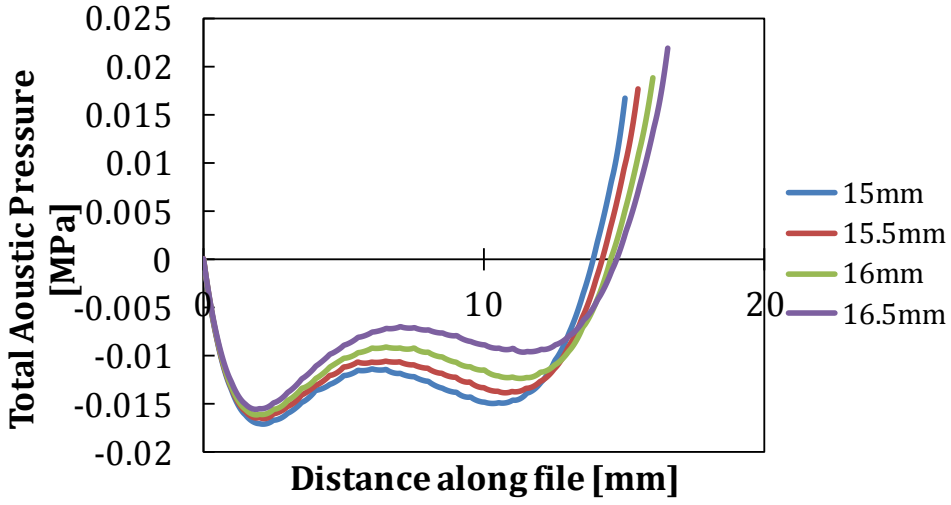

Figure 8.29: *Acoustic pressure plots for a cylindrical model along the length of the model at pressure amplitude of 0.31 MPa, with a constant diameter of 2.0 mm but varying length from 15 mm, 15.5 mm 16 mm to 16.5 mm.*

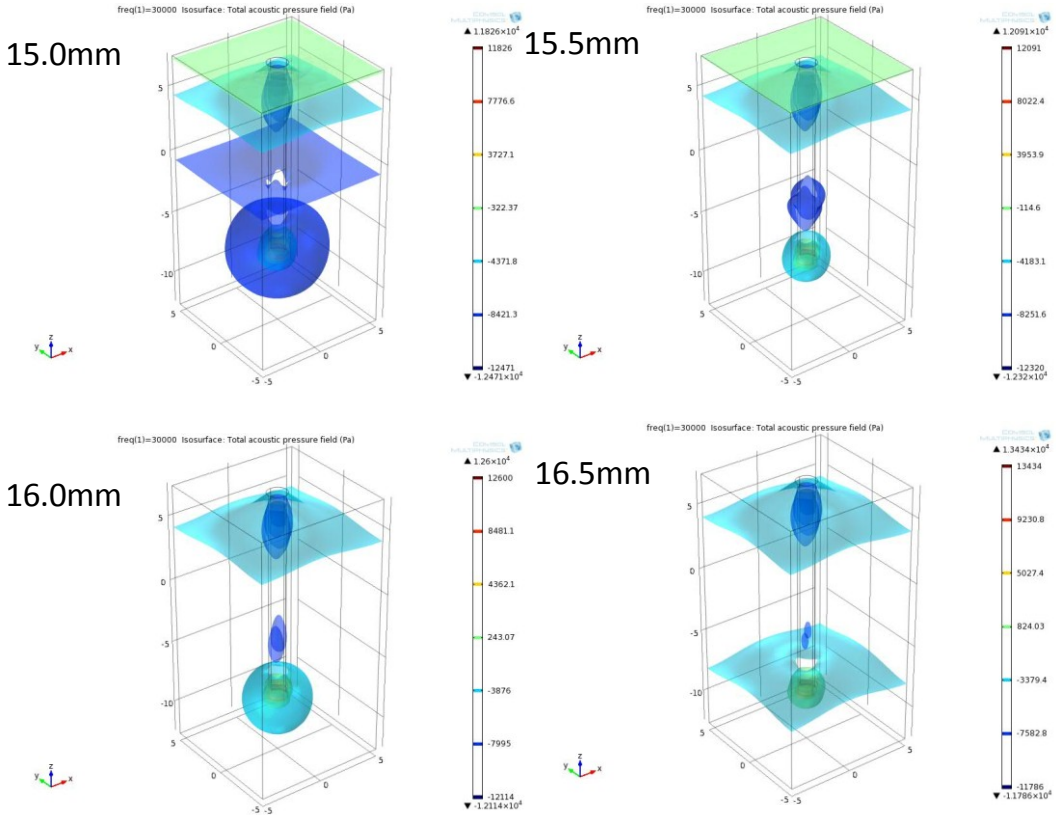

Figure 8.30: *Acoustic pressure isosurface plots for a cylindrical model at pressure amplitude of 0.31 MPa, with a constant diameter of 1.5 mm but varying length from 15 mm, 15.5 mm 16 mm to 16.5 mm.*

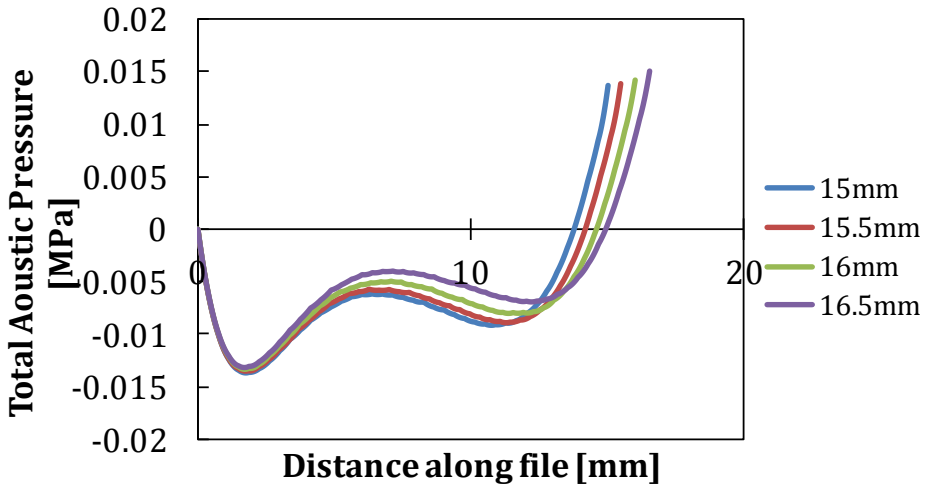

Figure 8.31: *Acoustic pressure plots for a cylindrical model along the length of the model at pressure amplitude of 0.31 MPa, with a constant diameter of 1.5 mm but varying length from 15 mm, 15.5 mm 16 mm to 16.5 mm.*

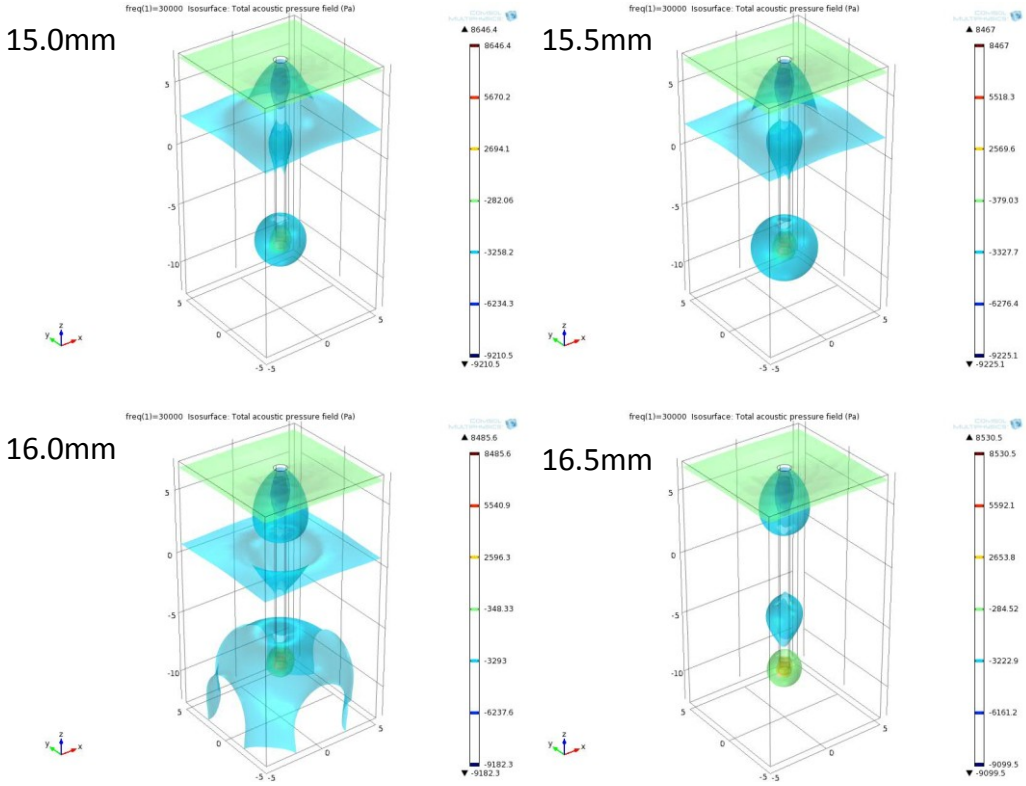

Figure 8.32: *Acoustic pressure isosurface plots for a cylindrical model at pressure amplitude of 0.31 MPa, with a constant diameter of 1.0mm but varying length from 15 mm, 15.5 mm 16 mm to 16.5 mm.*

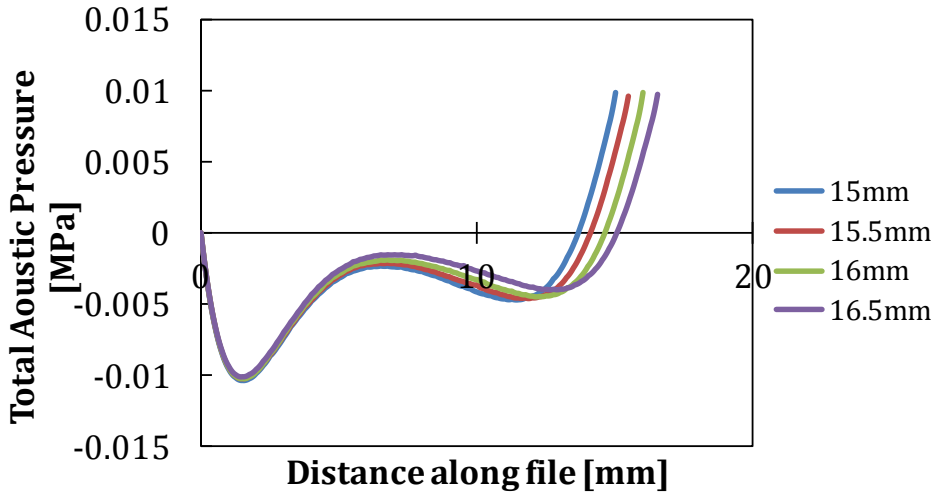

Figure 8.33: *Acoustic pressure plots for a cylindrical model along the length of the model at pressure amplitude of 0.31 MPa, with a constant diameter of 1.0 mm but varying length from 15 mm, 15.5 mm 16 mm to 16.5 mm.*